Design Process
for a Highly-Efficient
Low-Noise Propeller

Entwurfsprozess
für einen hocheffizienten, geräuscharmen Propeller

Von der Fakultät für Maschinenwesen der Rheinisch-Westfälischen Technischen Hochschule Aachen zur Erlangung des akademischen Grades eines Doktors der Ingenieurwissenschaften genehmigte Dissertation

vorgelegt von

Ole Bergmann

Berichter: Univ.-Prof Dr.-Ing. Eike Stumpf
Univ.-Prof Dr.-Ing. Kai-Uwe Schröder

Tag der mündlichen Prüfung: 27. November 2025

Danksagung

An dieser Stelle möchte ich mich herzlich bei meinen Mentoren, Kollegen, Freunden sowie meiner Familie für ihre Unterstützung bedanken.

Mein erster Dank gilt meinen Mentoren und Doktorvätern. Ohne Prof. Dr.-Ing. Eike Stumpf und Prof. Dr.-Ing. Kai-Uwe Schröder von der RWTH Aachen wäre diese spannende Reise nicht möglich gewesen. Sie haben mir Ihr Vertrauen geschenkt und sämtliche Hürden einer externen Promotion aus dem Weg geräumt – dafür danke ich Ihnen von Herzen. Ebenso möchte ich mich bei meinen Doktorvätern an der FH Aachen, Prof. Dr.-Ing. Carsten Braun und Prof. Dr.-Ing. Frank Janser, bedanken. Ihr habt mir die Möglichkeit gegeben, mich über sechs Jahre hinweg intensiv mit einem Thema zu beschäftigen. Dabei standet Ihr mir mit Rat und Tat zur Seite und habt das Beste aus mir und meiner Arbeit herausgeholt. Danke, Carsten, für dein exzellentes Feedback in unzähligen Jour-fixes. Danke, Frank, dass du mir diesen Weg nach meiner Bachelorarbeit aufgezeigt und ihn mit mir gemeinsam bestritten hast.

Ein besonderer Dank geht an meinen Weggefährten Felix Möhren, der mich seit dem Bachelorstudium begleitet. Wir haben nicht nur während des Studiums, sondern auch während der Promotion Hand in Hand gearbeitet und etwas Großartiges geschaffen. Ohne unseren ständigen Austausch und dein wertvolles Feedback wäre der Weg deutlich steiniger gewesen. Als nächstes danke ich Nils Böhnisch für die sportlichen und fachlichen Diskussionen sowie das Korrekturlesen meiner Arbeiten. Darüber hinaus danke ich Henry Page für seinen unermüdlichen Einsatz im Büro, in der Werkstatt und in den Windkanälen. Du bist die gute Fee im Büro und warst bei den Messungen von unschätzbarem Wert. Die Arbeit an der FH Aachen war für mich eine einmalige Chance, die die Kollegen, die zu Freunden wurden, zu einer unvergesslichen Zeit gemacht haben. Mein Dank geht daher auch an Robert Plante, Andreas Thoma, Joscha Mayntz und Jona Keimer. Ob Pizza-Dienstag, Döner-Donnerstag, Konferenzen oder Flugmesswochen – ihr habt hunderte schöne Erinnerungen hinterlassen.

Zum Schluss danke ich meiner Familie, die mir immer den Rücken freigehalten hat. Mit euch konnte ich aufreibende und anstrengende Tage schnell vergessen und neue Kraft schöpfen. Die größte Unterstützung jedoch habe ich von meiner geliebten Partnerin Katrin Sowinski erhalten. Du bist für uns nach Aachen gezogen, hast mich tagtäglich unterstützt, gestärkt und warst immer für mich da. Wenn die Tage wieder lang wurden, hast du meine Aufgaben übernommen und für mein großes Ziel zurückgesteckt. Dafür danke ich dir aus tiefstem Herzen.

Krefeld, Juli 2025 *Ole Bergmann*

Zusammenfassung

Die Elektrifizierung der Luftmobilität stellt Propellerhersteller vor neue Herausforderungen und ermöglicht zugleich neuartige Lufttransportkonzepte. Diese Disseration analysiert und optimiert elektrisch angetriebene Propeller mit dem Fokus auf Propeller der allgemeinen Luftfahrt, Auftriebs- und Kipp-Propeller. Die Herausforderung besteht darin, Lärm und Energiebedarf über verschiedene Betriebsbedingungen hinweg gegeneinander abzuwägen.

Zu Beginn wird eine erweiterte Blatt-Elemente-Impuls Theorie (BEMT) zur Leistungsprognose bewertet und validiert, indem sie mit Windkanalversuchen und CFD RANS Simulationen verglichen wird. Die Validierung zeigt, dass die BEMT Schub und Drehmoment mit einer Genauigkeit von 10% vorhersagt.

Anschließend werden verschiedene aeroakustische Modellierungsansätze vorgestellt. Das tonale Lärmmodell von Farassat sowie das Breitbandlärmmodell von Brooks, Pope und Marcolini (BPM) werden anhand experimenteller Daten validiert und erreichen eine Genauigkeit von ±7 dB. Die tonalen Lärmmodelle von Gutin und Hanson werden unter verschiedenen Flugbedingungen untersucht und mit dem vorab validierten Farassat-Modell verglichen. Die Bewertung zeigt, dass die Modelle von Gutin und Hanson tonalen Lärm nicht zuverlässig vorhersagen.

Darauf folgend wird die BEMT mit den Modellen von Farassat und BPM sowie einem genetischen Algorithmus zu einer multidisziplinären Optimierungsverfahren (MDO) kombiniert. Die MDO balanciert die Lärmemissionen und den Energieverbrauch über eine gesamte Flugmission hinweg. Ergänzt wird sie durch Modelle zur Abschätzung des Motorwirkungsgrads, der Motor- und der Propellermasse. Im ersten Schritt werden Blattzahl und Durchmesser optimiert, im zweiten Schritt folgen Sehnenlängen- und Verwindungsverteilung.

Die MDO wird auf eine generische Flugmission mit Schwebe-, Transitions- und Reiseflugphase angewendet. Nacheinander werden die Einflüsse der verschiedenen Modelle auf die Optimierungsergebnisse bewertet. Die Bewertung unterstreicht die Notwendigkeit eines multidisziplinären, mehrstufigen Verfahrens zur Optimierung von Lärmemissionen und Energieverbrauch. Der Vergleich eines Fest- mit einem Verstellpropeller zeigt, dass letzterer nur 6,5% effizienter ist.

Diese Dissertation leistet einen Beitrag zur Weiterentwicklung elektrisch angetriebener Propeller durch die Einführung eines validierten Optimierungsverfahren und zeigt notwendige Schritte zur weiteren Verbesserung des Optimierungsprozesses auf.

Schlagworte: *Doktorarbeit, Propeller, Aerodynamik, Akustik, Optimierung*

Abstract

The electrification of air mobility presents challenges for propeller manufacturers while enabling new air transport concepts. This dissertation analyses and optimises electrically driven propellers, focusing on general aviation propellers, lift propellers, and tilt propellers - those that benefit the most from the electrification. A central challenge is balancing noise emissions and energy consumption across varying operating conditions.

The thesis begins by evaluating and validating an extended blade element momentum theory (BEMT) for performance prediction by comparing it with wind tunnel tests and CFD RANS simulations. The validation demonstrates that the BEMT predicts thrust and torque with an accuracy of 10%.

Subsequently, different aeroacoustic modelling approaches are introduced. Farassat's tonal noise model and the broadband noise model of Brooks, Pope, and Marcolini (BPM) are validated against experimental data, demonstrating reliable noise predictions within an accuracy of ±7 dB. The tonal noise models by Gutin and Hanson are assessed under various flight conditions and compared to the previously validated Farassat model. The assessment reveals that Gutin's and Hanson's model do not reliably predict the tonal noise emissions.

A genetic algorithm is used for multidisciplinary optimisation (MDO), combining BEMT with Farassat's tonal and BPM broadband noise models. The MDO compares noise emissions and energy consumption over a flight mission to identify the optimal balance between them. The MDO is extended to include models for the motor efficiency, the motor mass, and the propeller mass prediction. In the first step, blade number and diameter are optimised followed by the optimisation of chord and twist distribution.

The MDO is applied to a generic flight mission comprising hover, transition, and cruise phases. The influence of each model is assessed individually. The assessment highlights the need for a multidisciplinary, step-wise approach to optimise noise emissions and energy consumption. Comparing fixed- and variable-pitch propellers for the reference mission shows that the variable-pitch propeller is only 6.5% more efficient.

This dissertation advances the development of electrically driven propellers by introducing a validated optimisation framework and outlines the necessary steps to further improve the optimisation process.

Keywords: *PhD-Thesis, Propeller, Aerodynamics, Acoustics, Optimisation*

Contents

List of Figures

List of Tables

List of Symbols

General Symbols

A	area	[m^2]
a_a	axial induction factor	[$-$]
a_t	tangential induction factor	[$-$]
b_c	chord length to diameter ratio	[$-$]
c_r	chord length of radial station	[m]
D	drag	[N]
D_P	propeller diameter	[m]
F	tip and root loss funciton	[$-$]
f	frequency	[Hz]
FC	force alignment factor (tangential displacement)	[m]
J	advance ratio	[$-$]
J_{mb}	Bessel's function of first kind	[$-$]
K	section length of blade element	[m]
k	wave number	[$-$]
L	lift	[N]
L/D	lift-to-drag ratio	[$-$]
L_I	sound intensitiy	[dB]
L_p	sound pressure level	[dB]
L_W	sound power	[dB]

M	Mach number	[–]
m	harmonic number	[–]
MAC	mean aerodynamic chord	[m]
$\dot{m}$	mass flow	[kg/s]
N_B	number of blades	[–]
o	observer distance	[m]
p	pressure	[Pa]
$\tilde{p}$	sound pressure	[Pa]
p_0	reference sound pressure (2e−5 Pa)	[Pa]
P	power	[W]
Q	torque	[Nm]
Q_s	Q-Factor	[dB]
R	radius	[m]
Re	Reynolds number	[–]
RF	radiation function	[–]
R_T	time scale ratio	[–]
St	Strouhal number	[–]
T	thrust	[N]
t	time	[s]
t_b	non-dimensional thickness	[–]
u	circumferential velocity	[m/s]
v	velocity	[m/s]
w	resulting velocity	[m/s]
w_a	axial induced velocity	[m/s]
w_t	tangential induced velocity	[m/s]

x_G	Gutin's argument of Bessels's function	[$-$]
x_H	Hanson's argument of Bessels's function	[$-$]

Greek Symbols

α	angle of attack (AoA)	[deg]
β	twist	[deg]
Γ	circulation	[$\mathrm{m^2/s}$]
δ	boundary layer thickness	[m]
η	efficiency	[$-$]
Θ	cross sectional area	[$\mathrm{m^2}$]
θ	observer angle	[deg]
Λ	sweep	[deg]
λ	wave length	[m]
μ_x	helicopter advance ratio	[$-$]
ν	kinematic viscosity	[$\mathrm{m/s^2}$]
Φ	phase alignment factor	[$-$]
ϕ	helix angle	[deg]
Ψ	non-compactness factor	[$-$]
ρ	density	[$\mathrm{kg/m^3}$]
σ	solidity	[$-$]
τ	total mission time	[s]
ω	rotational frequency	[rad/s]

Subscripts

0	static conditions	[$-$]
a	axial	[$-$]

B	blade parameter	[−]
d	drag	[−]
e	edge	[−]
Glo	global parameters	[−]
hub	hub	[−]
∞	free stream conditions	[−]
l	lift	[−]
Loc	local parameters	[−]
lod	loading	[−]
n	normalised	[−]
P	propeller parameter	[−]
r	radial dependent variable	[−]
ret	retarded	[−]
t	tangential	[−]
thi	thickness	[−]
tip	blade tip	[−]

Superscripts

¯	mean part (of a time-dependent quantity)	[−]
ˆ	amplitude (of a time-dependent quantity)	[−]
˜	route mean square (of a time-dependent quantity)	[−]
˙	time derivative	[−]

Coefficients

C_d	drag coefficient	[−]
C_f	friction coefficient	[−]

C_l	lift coefficient	[–]
C_P	power coefficient	[–]
C_Q	torque coefficient	[–]
C_T	thrust coefficient	[–]

Abbreviations

AoA	angle of attack	[deg]
AAM	advanced air mobility	[–]
AF	activity factor	[–]
AR	aspect ratio	[–]
BB	broadband	[–]
$BEMT$	blade element momentum theory	[–]
BET	blade element theory	[–]
$BLVS$	boundary layer vortex shedding	[–]
BPF	blade passing frequency	[–]
BPM	Brooks Pope Marcolini	[–]
BSO	blade shape optimisation	[–]
BVS	blunt vortex shedding	[–]
CFD	computational fluid dynamics	[–]
CST	class shape transformation	[–]
$DDES$	delayed detached eddy simulation	[–]
DES	detached eddy simulation	[–]
DNS	direct numerical simulation	[–]
DoF	degrees of freedom	[–]
Dop	Doppler factor	[–]
ESC	electronic speed controller	[–]

F1A	Farassat's formulation 1A	[–]
FF	far-field	[–]
FAA	Federal Aviation Administration	[–]
FoM	figure of Merit	[–]
FW-H	Ffowcs Williams - Hawking	[–]
GA	general aviation	[–]
GMT	general momentum theory	[–]
GPPO	global propeller parameter otpimisation	[–]
LE	leading-edge	[–]
LES	large eddy simulation	[–]
LLT	lifting line theory	[–]
MDO	multidisciplinary optimisation	[–]
MIL	minimum induced loss condition	[–]
MRF	moving reference frame	[–]
NextGen	Next Generation Air Transportation System	[–]
NF	near-field	[–]
OASPL	overall sound pressure level	[dB]
PDA	pre-deflection analysis	[–]
PSD	power spectral density	[–]
PTL	Prandtl tip and root loss correction	[–]
RANS	Reynolds-averaged Navier–Stokes	[–]
RBM	rigid body motion	[–]
RQ	research question	[–]
SC	sweep correction	[–]
SMT	simple momentum theory	[–]

SPL	sound pressure level	[dB]
$STOL$	short take-off and landing	[–]
TE	trailing-edge	[–]
TtP	thrust to power ratio	[N/kW]
TV	tip-vortex	[–]
UAM	urban air mobility	[–]
UNF	ultra-near field	[–]
VLM	vortex lattice method	[–]
VPM	vortex particle method	[–]
$VTOL$	vertical take-off and landing	[–]
$WMLES$	wall modelled large eddy simulation	[–]
WT	wind tunnel	[–]

1 Introduction

Challenges of climate change, advancements in battery technology, and the European Commission's "Flightpath 2050" initiative [47] are driving the transition towards the electrification of air mobility. The "Flightpath 2050" initiative and the corresponding initiative of the Federal Aviation Administration (FAA) "Next Generation Air Transportation System" (NextGen) [44] both aim to significantly reduce noise pollution and greenhouse gas emissions. Electrification eliminates direct CO_2 emissions and has the potential to reduce noise emissions [126]. Moreover, it has opened new possibilities for air mobility, such as advanced air mobility (AAM), which involves unmanned and manned aerial vehicles for transport within cities, between city centres and between mobility hubs [101, 119]. AAM vehicles share the common characteristic of short or vertical take-off and landing capabilities (STOL or VTOL) and are mainly driven by propellers.

In order to achieve the emission reduction targets of the "Flightpath 2050" and NextGen initiative, highly efficient, low-noise propellers are required, as the propellers are key contributors to both the noise emissions and energy consumption. The electrification comes with challenges in energy storage and nowadays results in lower energy density compared to conventional combustion engines [29, 149]. Furthermore, the electrification of general aviation (GA) and AAM demands new propeller designs tailored to the specific requirements of electric motors, as the electric motors have different characteristics then combustion engines [62]. Electric motors and combustion engines differ not only in their mode of operation but also in the following aspects [84]:

- The rotational speed range
- The torque - rotational speed relationship
- The efficiency map
- The motor mass and size
- The scalability capabilities

The propeller converts the rotation generated by a motor into thrust by accelerating a fluid. This principle is used for remote controlled micro-drones up to large helicopters and transport aircraft. Within this thesis, propellers are categorised in groups to handle these different kinds of applications. The following enumeration describes typical characteristics of each propeller category. The descriptions are by no means complete and there are propellers which could be sorted in different categories. These categories are created by the author based on the assessment of the requirements for different kind of propellers and rotors.

1. **Low Reynolds number propellers** operates at Reynolds numbers below 50,000. They are typically used for small drones with high thrust-to-weight ratios.[1] Due to the low Reynolds numbers, these propellers often use flat-cambered plates as airfoils. Deformations are less important, but weight is crucial, as drones are controlled by adjusting rotational speed. Therefore, moment of inertia is essential. Typical diameters are below 50 cm.

2. **Lift propellers** are similar to low Reynolds number propellers in the application, with diameters ranging from 1 m to 4 m. The higher Reynolds numbers require typical airfoils instead of flat plates. This type of propeller must operate at the limits of its design envelope in terms of deformation, weight, aerodynamic performance, and noise emissions for optimal efficiency and compliance with operational requirements. Therefore, these propellers have high aspect ratios and typically two blades for optimal aerodynamic performance. Due to the critical system mass, lift propellers generally have fixed roots. Lift propellers are used for controlling the aircraft, which is achieved through (sudden) variations in rotational speed. Therefore, the moment of inertia of the lift propellers must be kept low.

3. **GA propellers** are well known and must provide sufficient thrust for both take-off and high-speed operations. The aspect ratio of GA propellers is significantly smaller than that of lift propellers. Conventional GA propellers can be operated as fixed-pitch, variable-speed propellers or as variable-pitch, fixed-speed propellers. Electrification allows for variable-pitch, variable-speed GA propellers. System mass is less critical than in VTOL operations, which is why ground-adjustable pitch propellers are feasible.

4. **Tilt propellers** combine the requirements of both lift and GA propellers, regardless of the tilting mechanism (tilt-wing, tilt-prop, tail-sitter). Recent developments show that tilt propeller have multiple blades with moderate blade solidity compared to lift propellers. Additionally, the opposing design goals of cruise and hover are addressed by a variable-pitch system.

5. **Turbo propellers** (or turbo-props) are highly loaded propellers designed for high-speed aircraft. The tips of the propeller blades may operate in the transonic regime, necessitating blade sweep to reduce wave drag. Since turbines do not allow for significant changes in rotational speed, variable pitch propellers are required.

6. **Open-fans** (or open-rotors) represent a transition from a typical propeller with high aspect ratio and low solidity to a fan. Propeller blades can be considered as independent of each other, while fan blades interact with each other, requiring all blades to be designed together to account for all relevant effects.[2]

---

[1] There is a range of applications in other planet's and moon's atmospheres where low Reynolds number propellers are limited in performance. For such applications, accurate prediction and high-fidelity simulations are required.

[2] If the ratio of blade spacing (s) to chord length (c), ($\frac{s}{c}$), is less than 3, the blades interact with each other. This value can be derived from potential theory.

7. **Rotors** are similar to a lift propeller. However, the key difference between a lift propeller and a rotor is the rotor's elastic hub connection, which allows for heave and lead-lag motion, while the propeller has a rigid hub connection. This makes rotors more complex than propellers. Helicopters are controlled by cyclic and collective pitch adjustments rather than by changes in rotational speed, as is the case with lift propellers.

This work focuses on the categories **lift propeller**, **GA propeller**, and **tilt propeller**, as these fields are most relevant for the GA and AAM. Turbo-props and open-fans are typically analysed with high-fidelity simulations and are less affected by electrification. Rotors usually operate at a constant rotational speed, so they do not benefit as much as other propellers from electric motors, which can operate at variable speeds. Low Reynolds number propellers, mainly used in small drone applications, face fewer performance limitations than other propellers, as the effective capacity of the batteries decreases with power consumption, resulting in higher relative battery-to-aircraft mass ratios [6, 151]. Therefore, they do not require prediction methodologies as accurate as those needed for the other categories.

Fig. 1.1 depicts an exemplary aircraft for each relevant propeller category. The aircraft on the left side of fig. 1.1 is the VoloCity from Volocopter GmbH, which uses lift propellers for VTOL missions. The VoloCity flies with 18 two-bladed fixed-pitch propellers with diameters of around 2.1 m. The aircraft in the middle of fig. 1.1 is the GA aircraft Velis Electro of Pipistrel d.o.o. with an electric-driven propeller. The Velis Electro flies with a three-bladed fixed-pitch propeller that has a diameter of approximately 1.65 m. The third aircraft on the right side of fig. 1.1 is the VTOL Joby S4 aircraft with a tilt-propeller configuration by Joby Aviation Inc. The propeller are tilted for VTOL and cruise. The Joby S4 flies with six five-bladed variable-pitch propellers, each with a diameter of approximately 1.85 m.

Lift propeller:
Volocopter – VoloCity

GA propeller:
Pipistrel –Velis Electro

Tilt propeller:
Joby Aviation – Joby S4

© *Martina Heintzen*

© *Ole Bergmann*

© *United States Air Force*
230920-F-CC248-1015

Figure 1.1: Exemplary aircraft representing the relevant propeller categories

Fig. 1.1 highlights the diverse electric-driven AAM propeller applications. All three vehicles are airborne and either already certified or undergoing certification. These novel propeller systems introduce novel challenges [79], which we will outline in the next sections.

1.1 Motivation

Albert Betz is considered the pioneer of numerical propeller design [13, 95]. He was the first to publish what's known as the "minimum induced loss" (MIL) condition which states the relationship of parameters for an optimal propeller blade. The key parameters for optimal propeller design are the twist and chord distributions, which can be determined by applying the MIL condition. The required thrust, blade number, diameter, and operational condition must be specified as input in order to solve the MIL condition for obtaining the twist and chord distributions. The required thrust and diameter are usually specified by the aircraft manufacturer, while the remaining design parameters must be defined using appropriate engineering methods.

However, Betz considered only aerodynamic constraints, whereas propeller design is inherently a multidisciplinary task. As Ohad Gur states, *"Only by harnessing all analyses into a holistic design framework* ***might*** *the designer find an optimised design."* [63], underscoring the necessity of a multidisciplinary optimisation approach. A comprehensive design process must account for aerodynamic performance, noise emissions, structural integrity, mass, motor efficiency, system complexity, costs, producibility, and integration into the overall aircraft concept.

This comprehensive list of requirements demonstrates that propeller design is a complex venture, which must be tackled using multi physical solvers that account for different engineering disciplines. NASA has compiled a summary of propeller design procedures in three reports [2, 18, 135]. These reports from 1973 present state-of-the-art procedures with a focus on propellers for GA and civil aviation. At that time, the oil crisis drove the need for more efficient open-rotor concepts [83]. Propellers were primarily made of steel, and research efforts were directed towards increasing the speed and efficiency of propeller-driven aircraft, while noise was considered less important.

Nowadays, manufacturing techniques, materials, applications, simulation capabilities, and design requirements have significantly evolved. However, a comprehensive new report series that considers all of these factors is not yet available. The aim of this thesis is to present a design procedure for highly-efficient low-noise propellers.

On the one hand, most propeller manufacturers supply the GA market, where they have extensive knowledge of pairing specific engine types with propellers for specific speed ranges and diameter requirements. This experienced-based matching is possible because only a few combustion engines are available for the GA, which operate in known speed ranges. Therefore, the number of possible combinations between motors and propellers is manageable. However, the emerging field of electric-driven AAM presents challenges beyond the experience of these established manufacturers. Electric engines can be easily tailored to different torque and rotational speed requirements, resulting in a wider variety of electric engines than combustion engines [35, 105]. Thereby, the number of possible combinations between motors and propellers increases drastically. As a consequence, the applicability of traditional design approaches is uncertain for the new requirements placed on propellers by novel electric-driven AAM vehicles, emphasising the need to re-evaluate conventional design methods.

On the other hand, electric aircraft must be tailored to specific missions due to the significantly lower energy density of batteries compared to conventional fuels [29, 149]. As a result, each flight mission requires a dedicated aircraft, and each aircraft, in turn, requires a mission-specific propeller. Such a propeller is only optimal for that particular mission, which is why a unique propeller should be designed for every AAM vehicle. Since propeller performance directly impacts overall vehicle performance, a novel propeller design methodology is essential to support decision-making during the aircraft's conceptual design phase.

Summarising both sides leads to the following findings. The propeller manufacturers cannot provide the needed information for the conceptual design of an aircraft, due to the lack of experience in the field of electric-driven air mobility. This gap of experience can be covered by a suitable design environment, which provides the required information within a reasonable time-frame during the concept phase, without relying on high-fidelity simulations. One possible solution is a multidisciplinary optimisation (MDO) approach, comprising the following three disciplines:

1. Aerodynamics
2. Structural mechanics
3. Aeroacoustics

The first aspect of a multidisciplinary optimisation framework must cover the aerodynamic design. The external shape of the propeller, which is described by the diameter, the number of blades and the distribution of airfoils, twist, chord, lean and sweep distributions, determines the aerodynamic performance. These parameters must be optimised within a design approach in appropriate time, as the aerodynamic performance is required in the aircraft's conceptual phase. An aerodynamic optimisation is required, as the reduced energy density requires highly efficient propellers over the flight mission. Methods for the purely aerodynamic optimisation in the conceptual design exists [17, 20, 22], but they are not coupled with the following two disciplines.

The aerodynamic efficiency of propellers can be significantly improved by increasing the aspect ratio of the blades. Propellers with higher aspect ratios exhibit increased aerodynamic and structural coupling [143], which necessitates structural considerations in the design process. This is only one of several reasons why structural considerations are required. The structure can only sustain the loads if the aerodynamic design of the propeller provides sufficient space for the structural layout.

Therefore, the second aspect must cover the structural analysis. Loads during operation can lead to significant deformations, impacting aerodynamic performance [142, 152]. The close coupling of aerodynamic and structural considerations enables the analysis of the interaction between structural deformations and aerodynamic response. This interaction is known as aeroelasticity and must be taken into account to ensure structural integrity at all operating points. The structural design of propellers is addressed in the NASA designed reports mentioned before [2]. To determine the aeroelastic performance of propellers, coupled aeroelastic simulation codes were developed by several researchers or industrial groups [14, 67, 90]. However, these approaches are coupled with higher-fidelity aerodynamic solvers, which are too time-consuming for optimisation procedures. Furthermore, they do not account for the third discipline.

The third important aspect is the noise emissions and the human perceptions. Flightpath 2050 postulated a 65% reduction in perceived noise emissions. The linkage between human perception and noise emissions, which are described in engineering metrics like sound pressure level (SPL), is under investigation. An appropriate noise weighting is required to translate noise emissions into perceived noise. Recent studies show that annoyance is a key measure for AAM noise and is closely related to loudness [4]. Therefore, the SPL as a metric for loudness is an appropriate indicator for annoyance and the human perception. Furthermore, hovering is the phase of a VTOL flight mission associated with the highest noise pollution [4], though other phases also contribute. Therefore, noise emissions of a VTOL should be evaluated mainly in hover conditions. Nevertheless, noise reduction is also important for GA, which operates in lower airspace near residential areas. Electrification eliminates engine noise, leaving propeller noise as the primary noise source for the GA. Aeroacoustic optimisation can be employed to reduce propeller noise [31, 146, 153]. These methods manipulate the twist and chord distribution using a numerical scheme to reduce propeller noise. Another approach is the use of swept blades [34, 74, 76, 106]. However, propeller sweep is effective in case of high blade passing frequencies (appendix D.2). The benefit of sweep is therefore limited in both AAM and GA applications, as the blade number is comparatively low and the rotational speed should be low to minimise noise. Furthermore, sweep introduces strong aeroelastic coupling effects that must be considered in the design process [10, 114]. Even if sweep may not contribute significantly to noise reduction of GA or AAM propellers, the acoustic optimisation should be able to consider sweep, as swept blades may offer other benefits[3] [27, 80, 87].

In conclusion, a coupled aeroelastic and aeroacoustic optimisation, or aero-elasto-acoustic optimisation, has not yet been developed or described in the literature. A first attempt was made by Ref. [67], involving the optimisation of a fixed-pitch propeller with constant diameter and blade number, considering a combustion engine. However, it does not address the wide variety of electrically driven propellers with varying sizes and blade numbers. Further studies have shown interactions between aeroelastic effects and noise emissions in helicopter rotors [52, 78] and open-fan concepts [40]. On the one hand, helicopter studies were conducted under flight manoeuvres or oblique inflow conditions. However, their findings are limited to rotor systems and cannot directly be applied to the emerging field of electrically driven propellers. On the other hand, open-fan concepts are applied in the civil aviation. Open-fans differs from conventional propellers in terms of operational and structural requirements as well as the required analysis tools.

---

[3] Reduction of vibrations; Reduction of blade vortex interactions; Improved aerodynamic efficiency

The author, together with collaborator Felix Möhren, addresses the complex challenge of developing a novel optimisation approach for the analysis and design of electrically driven propellers. The focus is on reduced-order models to enable fast turnaround times during the conceptual aircraft design phase. Complexity is reduced by considering freely rotating propellers without interaction with the aircraft itself. The co-thesis of collaborator Felix Möhren [112] focuses on aeroelastic design, while this thesis concentrates on the aeroacoustic design and optimisation of propellers. Accordingly, this study investigates appropriate aerodynamic and aeroacoustic methods, with their constraints detailed in the next section.

1.2 Research Questions

The author addresses three research questions (RQ) in this thesis regarding the aeroacoustic and aeroelastic optimisation of electrically driven propellers for the selected categories: lift-propeller, GA-propeller, and tilt propeller.

RQ 1 - How applicable are reduced order aerodynamic simulation methods for electrically driven GA and AAM propellers in conceptual design?
In conceptual design, various geometries must be analysed within a reasonable time frame to identify optimal solutions. Thus, a robust and accurate calculation method is necessary, capable of predicting performance across different flight conditions and types of propellers. This question focuses on the integrated variables thrust and torque, which results in the power consumption and propulsive efficiency. The prediction method must yield accurate results not only at the propeller's design point but also under off-design conditions.

On the one hand, an accurate aerodynamic prediction methodology is required for aeroelastic and aeroacoustic simulations, as these disciplines are coupled. In aeroelastic simulations, the aerodynamic and structural models are closely coupled, whereas in aeroacoustic simulations, the aerodynamic and acoustic models are loosely coupled. The reduced aerodynamic simulation model provides the input for the acoustic simulation, which is why the answer of the first RQ is required for the continuing aeroacoustic analysis. On the other hand, the reduced-order model must be reliable across multiple geometries and operating conditions, as it is intended for integration into an multidisciplinary optimisation (MDO) approach.

RQ 2 - Which aeroacoustic simulation method enables accurate prediction of noise from electrically driven GA and AAM propellers in conceptual design?
Accurate noise prediction is essential in conceptual propeller design to control noise emissions, primarily influenced by loudness. A range of noise prediction methods is available, from empirical correlations to high-fidelity simulations. Each method demands different levels of aerodynamic simulation fidelity. Therefore, this question seeks a method that is accurate for noise emission prediction over multiple operating points and geometries, computational efficient for conceptual design application, and does not increase the required aerodynamic fidelity.

The second RQ delivers an acoustic method which could be applied in an MDO. The accuracy of the method is known, which is important to quantify the results of the third RQ.

RQ 3 - How can electrically driven propellers be designed with aerodynamic, aeroacoustic, and aeroelastic considerations for a complete flight mission during conceptual design?
Performance and noise prediction represent only one side of the challenge. The other side involves designing the propeller for the mission requirements. AAM missions bring new design conflicts that must be solved to achieve efficient, low-noise aircraft. A novel design strategy for electrically driven propellers is needed, as there is no procedure describes in literature.

The answer to the third RQ outlines how an MDO approach should be structured, and which effects must be considered to optimise the propeller for a specific flight mission.

1.3 Thesis Structure

The present thesis is structured in five main chapters. The introduction has outlined the needs for a novel optimisation and design framework and has focused the research scope to open propellers for the GA and the AAM.

Chapter 2 provides the physical and operational background of propellers in section 2.1. The reference propeller, introduced in section 2.2, serves as a basis for evaluating the effects of different physical models. It is analysed both numerically and experimentally in two-, three-, and four-bladed configurations, as well in hover and cruise conditions. The aerodynamic modelling of propellers is presented in section 2.3. A blade element momentum theory (BEMT) with tip loss correction and sweep correction is presented as a reduced-order model for the aerodynamic analysis of propellers. Different high fidelity CFD RANS simulation approaches are described and compared against each other. Finally, the reduced order model and the CFD RANS simulations are validated against wind tunnel tests in section 2.4. The wind tunnel tests, conducted by the author, are described in section 2.4. Chapter 2 addresses the first RQ. The derived reduced-order model is used in subsequent calculations.

Chapter 3 continues with the acoustic modelling of propellers. Similar to chapter 2, it begins by discussing the physical background of sound, followed by an examination of various noise sources and their characteristics. In section 3.1, three different tonal noise models are described in detail, and subsequently, a strategy for modelling the broadband noise is presented in section 3.2, addressing the second RQ. Farassat's formulation 1A (F1A) for tonal noise modelling and the Brooks, Pope, and Marcolini (BPM) broadband noise model are validated against three experimental data sets from literature in section 3.3. Gutin's and Hanson's tonal noise models are analysed under different operational conditions using the validated tonal noise model of Farassat. Chapter 3 addresses the second RQ and presents a suitable noise model for use in subsequent calculations.

Chapter 4 discusses the propeller design process. Section 4.1 outlines the state-of-the-art aerodynamic design procedure for a single operating point. The procedure is applied to redesign the introduced reference propeller. Section 4.2 provides a brief overview of the propeller's structural design.

A comparison between the reference propeller and a redesigned version highlights the benefits and drawbacks of single-point optimisation. These drawbacks demonstrate the need for a multidisciplinary optimisation (MDO) approach, which is detailed in section 4.3. This new method considers the effects of the electric motor, propulsion system mass, and pitch system.

Chapter 5 presents two different design studies for a mission based propeller design. In section 5.1, the influence of different design parameters on the aerodynamic and aeroacoustic performance is assessed. In section 5.2 and 5.3, the MDO approach is applied to find the optimal geometry for a generic mission. In the MDO study, different models are applied stepwise, to assess the influence of different modelling approaches. This assessment is utilised in section 5.4 to answer RQ3.

Chapter 6 concludes this thesis by summing up all findings and answering the related RQ's, followed by an outlook including recommendations for related future work.

2 Propeller Aerodynamics

This chapter summarises the aerodynamic behaviour of propellers and presents an accurate and efficient performance prediction modelling approach. This approach is later used for aeroacoustic simulations and optimisation. First, the fundamental mode of action is discussed. Different operational modes and their impact on propulsive efficiency are explained.

Secondly, a reference propeller is introduced, which serves both for validation and for assessing the impact of different modelling approaches. This propeller is utilised in experimental investigations conducted in a wind tunnel as well as in numerical simulations using different CFD RANS methods to evaluate the modelling strategies and validate their accuracy.

Third, the different performance modelling approaches are discussed. The discussion is separated into three sections.

1. The blade element momentum theory (BEMT), along with its correction methods, is explained, and the impact of the different correction methods is assessed.
2. The influence of 2D airfoil data on performance prediction is evaluated. Two modelling approaches (XFOIL and 2D RANS) are compared, and the effects of two different stall model are examined.
3. High-fidelity CFD RANS simulations are presented, and the results of various modelling approaches are compared.

Finally, wind tunnel experiments are conducted for validation. The predictions of both RANS and BEMT method are compared to the wind tunnel results.

2.1 Basic Propeller Theory

As explained in section 1.2, a propeller converts rotational movement into thrust T. The rotation generates a moment around the propeller axis, known as torque Q. The engine must overcome this torque to maintain the propeller's rotational speed. The required shaft power, to sustain the propeller's speed, is calculated by multiplying the angular velocity ω by the torque:

$$P = Q \cdot \omega = Q \cdot 2\pi \cdot n \tag{2.1}$$

where n represents the rotational speed in Hz.

In simple terms, the propeller sucks air and accelerates it to generate thrust. Fig. 2.1 illustrates the ideal streamlines around a propeller in cruise conditions, from far upstream (section 0) about the propeller plane (section 1) to far downstream (section 2). Upstream, in the far-field of the propeller (section 0), the incoming air has a uniform velocity distribution and the static pressure is p_∞. The acceleration of the air can be explained by a pressure jump across the propeller plane (section 1), resulting in accelerated airflow across the plane due to the pressure difference Δp. According to free-stream theory, the pressure returns to p_∞ far downstream (section 2). However, the air has been accelerated to a higher velocity v_2. This theoretic approach was first described by Rankine [128] and finalized by Froude [48]. By applying the momentum theory in axial direction, the resulting thrust can be calculated using eq. (2.2):

$$\dot{I}_2 - \dot{I}_1 = \sum F = T \tag{2.2}$$

The lower part of fig. 2.1 presents the ideal velocity and pressure distribution along the propeller axis. The air accelerates smoothly from section 0 to section 2, while the pressure experiences a jump Δp across the propeller disk. Since the static pressure in the far field must remain at p_∞ and the propeller introduces a pressure jump Δp, the pressure distribution along the axis can be derived. Directly in front of the propeller disk the static pressure must be lower than p_∞, whereas behind the disk, the static pressure is higher than p_∞. The principle sketch further shows the axial induced velocity w_a in the propeller plane, which is a measure for the sucked air by the propeller.

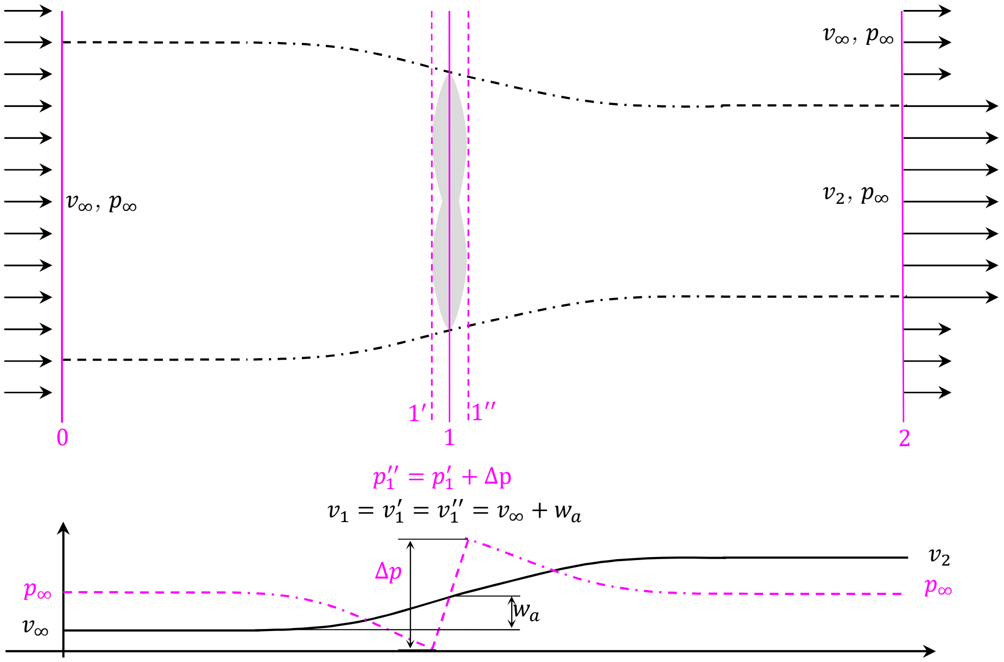

Figure 2.1: Principle sketch of the propeller's mode of action

Applying momentum theory from section 0 (far upstream) to section 2 (far downstream), as described by eq. (2.2), allows for the calculation of thrust based on the velocity in the propeller's wake. The area swept by the propeller is given by:

$$A_P = \frac{\pi}{4} R^2 \tag{2.3}$$

where R is the propeller radius. Using this, the thrust equation can be expressed as:

$$T = \dot{m} \cdot \Delta v = \rho_\infty \cdot A_P \cdot v_1 \cdot (v_2 - v_\infty) \tag{2.4}$$

where ρ_∞ represents the free field air density, v_1 is the velocity in the propeller plane, v_2 is the velocity in the far-field wake, and v_∞ is the upstream velocity.

The momentum theory can also be applied more locally, specifically from a section just before the propeller disk (section 1') to a section just after the propeller disk (section 1"). This approach, expressed in (eq. (2.5)), yields a thrust calculation based on the propeller area multiplied by the pressure jump across the propeller disk.

$$T = A_P \cdot \Delta p = A_P \cdot (p_1^{''} - p_1^{'}) \tag{2.5}$$

The static pressure terms can be replaced with velocity terms by applying Bernoulli's principle from section 0 (far upstream) to 1' as well as 1" to 2 (far downstream). Bernoulli's principle can be derived from the conservation of energy under the assumption of incompressible, frictionless, and steady flow. This allows the static pressures to be related to the upstream free-stream and downstream wake velocities. Both derived equations can be used to calculate the propeller's thrust.

$$T = \frac{\rho_\infty}{2} \cdot A_P \cdot (v_2^2 - v_\infty^2) \tag{2.6}$$

By equating the thrust expressions derived from momentum theory applied from section 0 to section 2 (eq. (2.4)) and from section 1' to section 1" (eq. (2.5)), a relationship between the velocity in the propeller plane and the far-field velocities can be established (eq. (2.7)). Eq. (2.7) enables the calculation of one set of velocities given the other, ensuring a comprehensive understanding of how the propeller interacts with the surrounding airflow to generate thrust.

$$v_1 = \frac{1}{2}(v_2 + v_\infty) \tag{2.7}$$

$$v_2 = 2v_1 - v_\infty \tag{2.8}$$

As shown in the lower part of fig. 2.1, the velocity in the propeller plane can be divided into the axial induced velocity w_a and the free-stream velocity v_∞.

$$v_1 = v_\infty + w_a \tag{2.9}$$

Substituting the wake velocity into eq. (2.4) leads to the final thrust equation in eq. (2.10).

$$T = 2\rho_\infty \cdot A_P \cdot v_1(v_1 - v_\infty) \tag{2.10}$$

Eq. (2.10) is reformulated to obtain the axial velocity in the propeller plane (eq. (2.11)).

$$v_1 = +\frac{v_\infty}{2} \pm \sqrt{\left(\frac{v_\infty}{2}\right)^2 + \frac{T}{2\rho A_P}} \tag{2.11}$$

In case, that the propeller operates in static or hover conditions, eq. (2.11) simplifies to eq. (2.12).

$$v_{1,hover} = \sqrt{\frac{T}{2\rho A_P}} \tag{2.12}$$

To compare the key performance indicators of propellers, it is necessary to normalise the generated forces and moments. The key performance indicators of propellers are the thrust coefficient, torque coefficient, and propulsive efficiency. In addition to the conventional normalisation methods used in classical aerodynamics, it is essential to normalise the propeller speed. This is because propeller performance is influenced by two key velocities: the rotational speed of the propeller and the free-stream velocity of the incoming air.

Fig. 2.2 provides an overview of the geometry (r, c, β), velocity components (v_∞, v_t, v_a, w, ω), and resulting aerodynamic forces (L', D', T, Q) relevant for the following explanations. The parameters shown are partially already defined, and relevant for the description of the propeller performance. The geometric parameters include the local blade radius r, chord length c, and twist angle β. Fig. 2.2 also illustrates the tangential velocity v_t at radius r, resulting from blade rotation at angular velocity ω and the resulting velocity w from the superposition of axial and tangential velocity. In addition, fig. 2.2 shows the aerodynamic forces acting on the blade section at r: the two-dimensional lift L' and drag D'. Finally, the propeller generates not only thrust T, but also torque Q, both indicated along the propeller axis.

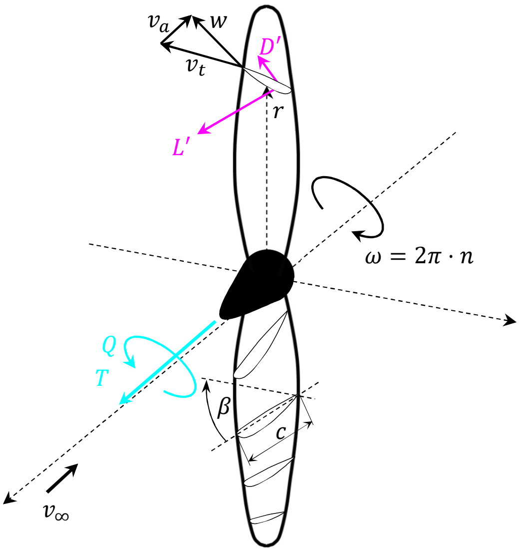

Figure 2.2: Overview about the propeller geometry, velocities and resulting forces and moments

In propeller and rotor applications, this dual velocity dependence is managed through the use of the advance ratio (J). The advance ratio is a dimensionless parameter that normalises the free-stream velocity relative to the rotational velocity of the propeller (eq. (2.13)). This normalisation enables consistent comparisons of propeller performance across different operating conditions and configurations.

$$J = \frac{v_\infty}{n \cdot D_P} \tag{2.13}$$

Where D_P is the propeller diameter. In helicopter applications, the advance ratio is normalized with the tip speed leading to the following equation:

$$\mu_x = \frac{v_\infty}{\pi \cdot n \cdot D_P} \tag{2.14}$$

The advance ratio describes the distance a propeller or rotor travels per revolution.

Various definitions for this normalisation exist in the literature; however, in this thesis, thrust, torque, and power consumption are normalised according to the following equations. In these equations, the respective quantity is divided by the air density, a reference measure for the propeller area, and a measure for the blade tip speed. These chosen normalisation methods ensure dimensional consistency.

The dimensionless coefficients for thrust c_T, torque c_Q, and power c_P are defined as follows:

$$c_T = \frac{T}{\rho(\pi R^2)(R\omega)^2} \tag{2.15}$$

$$c_Q = \frac{Q}{\rho(\pi R^2)(R\omega)^2 R} \tag{2.16}$$

$$c_P = \frac{P}{\rho(\pi R^2)(R\omega)^3} \tag{2.17}$$

However, since power P equals the torque Q times the rotational frequency ω, the torque and power coefficients have equivalent values.

The propulsive efficiency η of the propeller is described by eq. (2.18). This efficiency metric indicates how effectively the propeller converts power into forward motion, essentially representing the advancing velocity per unit of power consumption, or how far a propeller or aircraft travels for a given amount of power used.

$$\eta = \frac{(v_\infty \cdot T)}{P} = \frac{(v_\infty \cdot T)}{2\pi n \cdot Q} = \frac{J}{\pi} \cdot \frac{C_T}{C_Q} \tag{2.18}$$

In helicopter applications, the efficiency is expressed as the Figure of Merit (FoM), stated in eq. (2.19). It is calculated as the ratio of ideal power consumption to actual power consumption. The FoM is derived for hover conditions, meaning the free-stream velocity is zero ($v_\infty = 0$), which simplifies the calculation of the induced power to eq. (2.12). The FoM expression can be further simplified by substituting eq. (2.15) and (2.17). Eq. (2.19) indicates that higher disk loadings result in higher FoM.

$$FoM = \frac{P_{\text{ideal}}}{P_{\text{real}}} = \frac{(T \cdot v_{1,hover})}{P_{\text{real}}} = \frac{T}{P}\sqrt{\frac{T}{2\rho A_P}} = \frac{C_T^{3/2}}{\sqrt{2} \cdot c_P} \tag{2.19}$$

The comparison of the propeller performance is typically done by plotting the torque or power coefficient, thrust coefficient, and propulsive efficiency against the advance ratio as presented in fig. 2.3. The torque coefficient is typically two orders of magnitude smaller than the thrust coefficient, so it is multiplied by 100 for better visibility. The propulsive efficiency reaches its maximum at approximately 80% of the advance ratio range in which the propeller produces thrust. In this case, the propeller is producing thrust up to an advance ratio of 0.76. Beyond this advance ratio, the propeller is producing drag. At an advance ratio of 0.76, the torque coefficient and therefore the power consumption is still positive, which means the propeller is consuming energy to maintain the zero thrust condition, while it does not further accelerate the air. The operating point where the torque coefficient crosses zero is known as wind-milling. The propeller rotates solely due to incoming airflow without engine power.

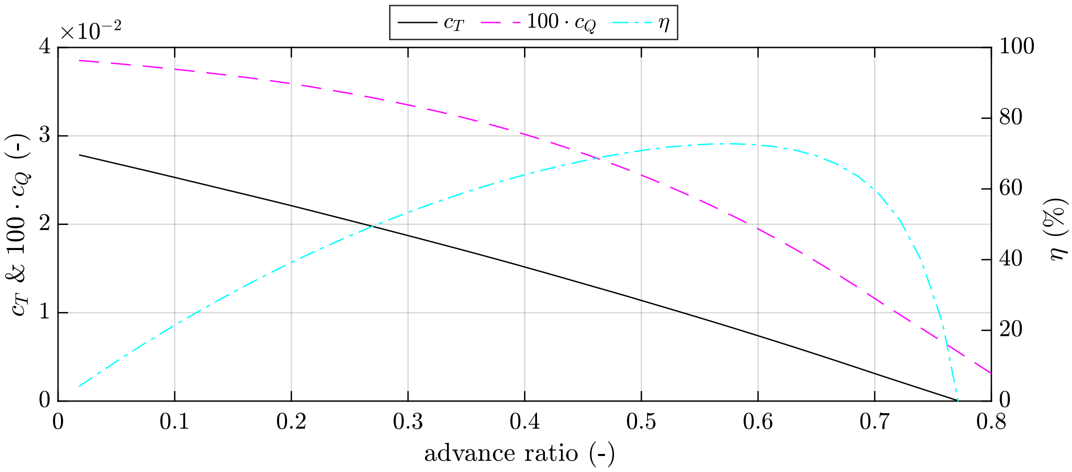

Figure 2.3: Generic propeller performance

The reference propeller used in this analysis is a three-bladed design with a diameter of 74 cm, operating at a nominal rotational speed of 4500 rpm and a pitch of 5°. Details of the propeller can be found in section 2.2. To expand the propeller's operational range, two potential modifications can be made. The first involves adjusting the propeller pitch, resulting in a variable-pitch propeller. By altering the pitch, the propeller can achieve higher advance ratios, enhancing its performance across a wider range of operating conditions. As illustrated in fig. 2.4, the operational range increases as the propeller pitch is varied between -5° and 25°. At higher pitch settings, the propeller's optimal operating point shifts toward higher advance ratios, which is crucial for aircraft that need higher top speeds. This ensures that the propeller delivers sufficient thrust and maintains efficiency throughout the entire operational range.

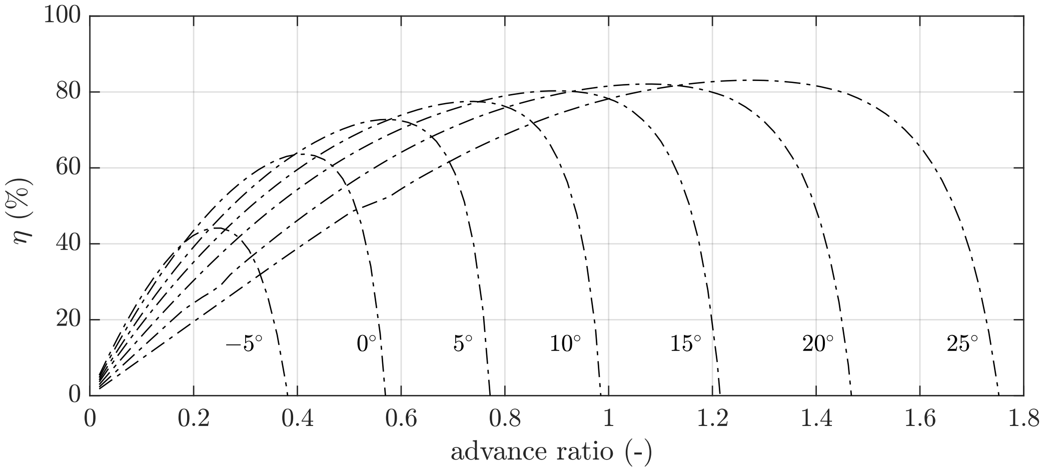

Figure 2.4: Generic variable-pitch constant-speed propeller performance

The second method to expand the operational range involves adjusting the rotational speed, resulting in a variable-speed propeller. This approach is particularly feasible with electric motors, as they allow for a wide range of operational rotational speeds. However, since the advance ratio is normalised with the rotational speed, efficiency plots remain unchanged when represented against the non-dimensional velocity. Consequently, the efficiency of variable-pitch propellers must be shown in relation to the flight speed. Fig. 2.5 displays the efficiency against the flight speed for rotational speed settings ranging from 3000 to 6000 rpm. As the rotational speed increases, compressibility effects begin to reduce the propeller's maximum propulsive efficiency.

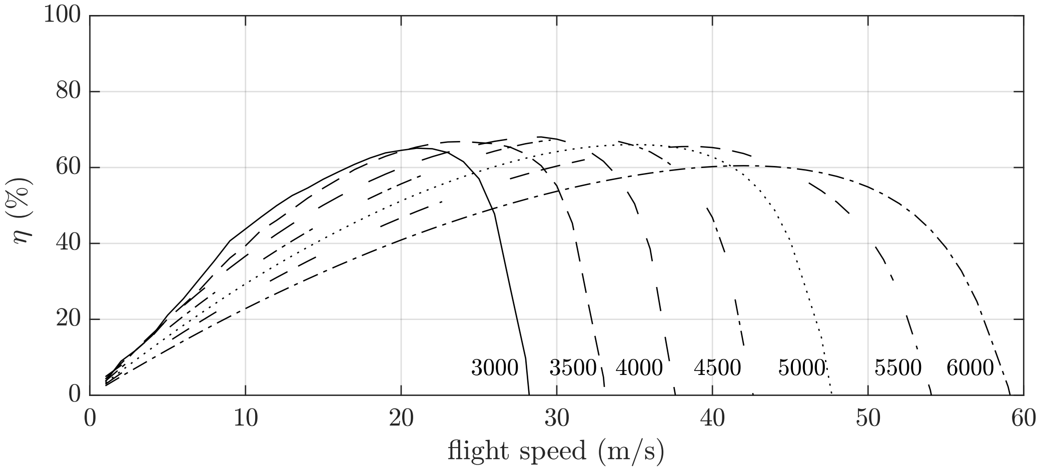

Figure 2.5: Generic variable-speed fixed-pitch propeller performance

2.2 Reference Propeller

In the aerodynamic validation and assessment of the prediction methodology, three propellers from Helix carbon GmbH are used as references. The reference propeller is a subscale model of a GA propeller. All three propellers have the same blade geometry but use two, three and four blades respectively, with a diameter of 74 cm. The diameter and thrust levels fit the wind tunnel of FH Aachen University of Applied Sciences, which is why the propellers are selected for validation purposes.

Fig. 2.6 shows the planform of the reference blade (cf. diagram a)) and its twist, chord and thickness distribution (cf. diagram b)). Diagram a) depicts the leading-edge (LE), quater-chord line (c/4) and trailing-edge (TE). Additionally, the 75% radius section location is visualized in diagram a). The airfoil of this section is shown in fig. 2.15.

Twist reduces from 22° at the hub to 7° at the tip of the blade. The chord length is approximately 5 cm along the complete radius and the thickness reduces from 15% at the root to 10% at the tip. The propeller was designed by the Helix Carbon GmbH as a reference propeller for comparisons between experimental tests and numerical simulations. The LE of the reference propeller has an S-shape. The S-shape increases complexity in the assessment of the numerical approaches.

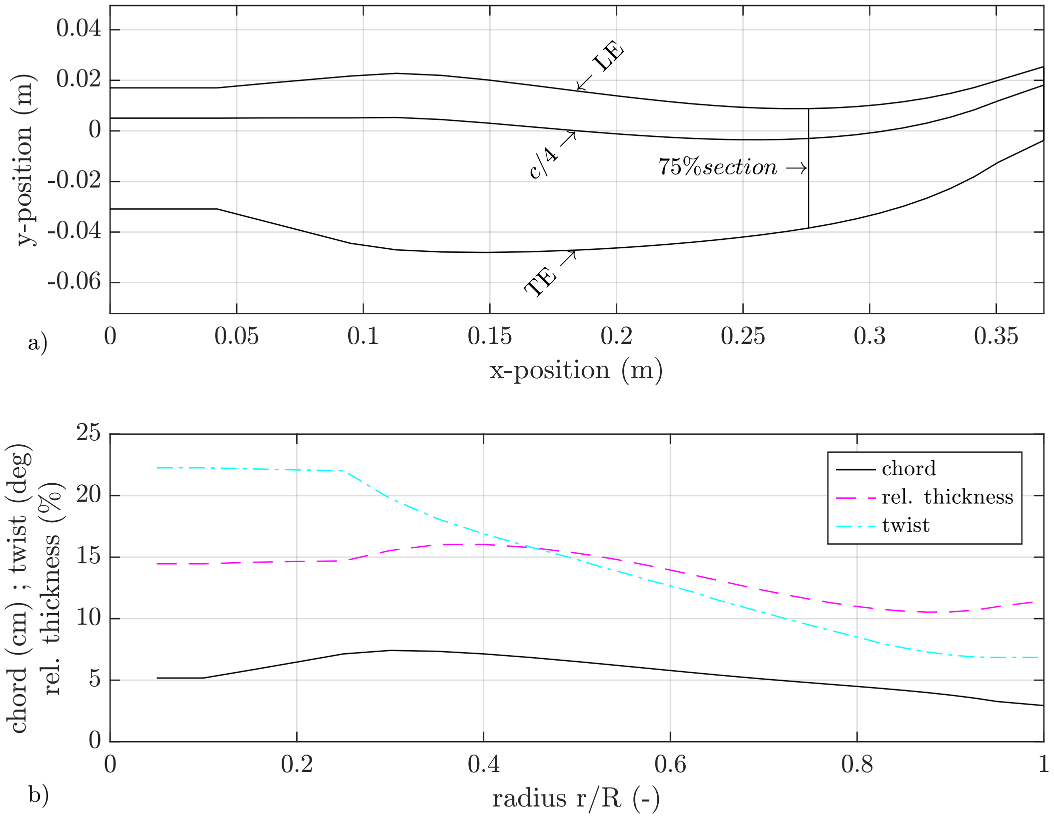

Figure 2.6: Reference propeller's planform and properties

The reference condition for the analysis is a rotational speed of 3500 rpm at standard atmospheric conditions:

- Reference temperature: $T = 288.15$ K
- Reference pressure: $p = 1013.25$ hPa
- Reference density: $\rho = 1.225$ kg/m^3
- Reference kinematic viscosity: $\mu = 1.48\ 10^{-5}$ m^2/s

These standard settings are used for all further calculations and analyses except in case of wind tunnel experiments.

An accurate description of the geometry is essential for the comparison of different propellers. In this work, the geometric parameters are divided in global and local propeller parameters. The global propeller parameters are the blade number and diameter. These two parameters are crucial for the overall performance of a propeller, but they are often dictated by the aircraft manufacturer. However, propellers with the same diameter and blade number can be designed for different applications, such as AAM or GA. Therefore, the intended operation of the propeller is essential for its design.

The local propeller parameters defines the shape of the propeller. The most important aspects are the twist, chord, and thickness distribution, which drive the overall aerodynamic performance, acoustic emissions and structural integrity. Further details about the airfoil, sweep and lean distribution are essential for a detailed analysis of the propeller performance.

2.3 Propeller Performance Modelling

Propeller performance modelling covers a wide range of applications. The specific application determines the requirements for the modelling approach. Fig. 2.7 shows an overview of typical simulation approaches and gives quick information about the modelling effort, the level of physics modelled, and the level of physics resolved by the methods. The list is not complete but offers an overview of the most commonly used approaches for propeller performance prediction. Multi-fidelity methods are also available, coupling different levels of fidelity.

The suitable simulation method depends on the design phase of the aircraft, the operating environment, and the parameters to be determined. These parameters include the pressure field in the wake, the pressure on the blades, the forces at the hub, the pressure field induced by the propeller on other structures, and structural, or aeroacoustic analyses. In the following paragraphs, the main advantages and disadvantages of the most common models are presented.

The first stage of the pyramid shown in fig. 2.7 consists of blade element theory methods (BET). The BET is typically coupled with a momentum approach to predict the axial induced velocity resulting in the blade element momentum theory (BEMT). BEMT methods are easy to implement, fast, and accurate for freely spinning propeller, as shown in Ref. [23, 28, 65]. Details about the BEMT are provided in subsection 2.3.1. Therefore, BEMT is used in early design stages and multi-disciplinary optimisation. The BEMT requires 2D airfoil data to predict propeller performance. The 2D data can capture viscous effects, which is an advantage compared to potential flow solvers. However, BEMT does not resolve the flow field, which can be both an advantage and disadvantage. Since they do not resolve the flow field, the BEMT is fast and robust, but on the other hand, BEMT methods:

1. cannot physically capture interactions with surrounding structure
2. cannot capture 3D effects on the blade

However empirical or other correction models can be easily implemented to improve performance prediction under these conditions.

The second to fourth stages are potential flow solvers. Potential flow solvers can capture interactions between the propellers and surrounding structures such as struts, ducts, other propellers, or stator blades. They require some kind of wake description to solve the potential flow problem. Different types of wake models are used in the literature. The most common ones are the fixed wake, semi-prescribed wake, free wake, and vortex particle wake [65]. These first three wake models describe the wake by non-viscous vortex sheets. Therefore, these wake models cannot account for dissipation, which is important for the calculation of the propeller wake. In the case of the fixed wake, the propeller's wake is prescribed by the rotational speed and the flight velocity. For a semi-prescribed wake, the wake's form is prescribed by the rotational speed but it can be stretched depending on the operational conditions and therefore the axial movement of the wake screw. A free wake model allows complete distortion of the wake sheet. A second drawback of these wake models is singularities at the tip vortex, making them numerically unstable [141].

A fourth way to describe the propeller wake is the vortex particle method (VPM). The VPM describes the wake as free vortex particles, which move independently from each other. Therefore, the VPM allows more complex wake interactions compared to vortex sheet methods, as they have fewer problems with singularities. Furthermore, VPM allows for viscous dissipation, enhancing the prediction accuracy [96]. Additional wake models e.g. for helicopter applications in horizontal flight, or other flight states also exist, but are less relevant for the propeller performance prediction [134].

Stage two of the pyramid is the lifting line theory (LLT) method. LLT's advantage lays in its direct use of a wake model compared to the BEMT. Appropriate wake models capture many kinds of interactions. Blade-vortex interactions are of particular interest for performance prediction in hover conditions. Similar to the BEMT, the LLT requires 2D airfoil polars and can thereby account for viscous effects. The increase in simulation effort compared to the BEMT varies depending on the wake model. However, LLT, like BEMT, cannot predict 3D effects on the blade [5]. The disadvantages of LLT compared to BEMT are the increased simulation effort, reduced robustness, and greater overall complexity. LLT and BEMT are strip theories that discretise a blade along its span into small strips. At these strips the flow is assumed to be 2D.

Stage three of the pyramid is the vortex lattice method (VLM). VLM is the first stage that can resolve 3D flow on the blade. VLM does not require 2D airfoil data, but 2D data can be used to take viscosity effects into account. The computational effort is further increased because the VLM requires a certain panel density in chord-wise direction [20].

The fourth stage is an extension of the potential flow solver to a 3D panel method that resolves the complete propeller geometry. This model does not need 2D airfoil data. Modern 3D panel methods use boundary layer correction methods to consider viscous flow effects [20]. A 3D method is able to capture differences between suction and pressure side, which is not possible with the VLM, as VLM uses only one vortex sheet for both sides [133].

The fifth stage of the pyramid consists of CFD RANS methods. RANS-based CFD methods solve the Navier–Stokes equations by applying turbulence models alongside spatial and temporal discretisation. Turbulence models average the viscous effects in time and space, and provide information about velocity fluctuations [140]. In comparison to the previous stages, RANS requires not only the discretisation of the blade geometry, but also a sufficient fine discretisation of the complete flow field around the propeller. Therefore, the numerical effort increases significantly. RANS methods offer varying levels of fidelity, as they can be performed as steady or unsteady simulations, and they can resolve the blade or uses surrogate models to represent the blade. Furthermore, the propeller motion can be modelled in multiple ways, depending on the scope of interest. The applied CFD RANS methods are presented in 2.3.3.

The final two stages of the pyramid include large eddy simulations (LES) and direct numerical simulations (DNS). Many other simulation methods exist but won't be discussed here in detail, such as wall-modelled large eddy simulations (WMLES), detached eddy simulations (DES), delayed detached eddy simulations (DDES), and Lattice-Boltzmann methods [82]. LES replaces classical turbulence models and resolve parts of the turbulent structures. Small turbulent structures are still modelled by turbulence models. Therefore, the flow field needs to have a much finer discretisation compared to RANS simulations. In short, WMLES, DES, and DDES differ in how they divide the flow into into resolved and modelled turbulent kinetic energy. Therefore, DNS solves the Navier–Stokes equations without any turbulence modelling by resolving all relevant spatial and temporal scales of the flow. Therefore, DNS needs no modelling of any kind of turbulent phenomena, and therefore forms the top of the pyramid. Unlike RANS methods, which solve averaged forms of the Navier–Stokes equations, Lattice-Boltzmann methods recover the Navier–Stokes equations in the macroscopic limit of a mesoscopic particle model. The Lattice-Boltzmann method models fluid motion at the mesoscopic scale and computes macroscopic flow quantities from particle distributions, while the RANS method solves time-averaged Navier–Stokes equations using turbulence models [111]. However, these higher-order models are of limited relevance for propeller performance prediction due to their intensive computational cost.

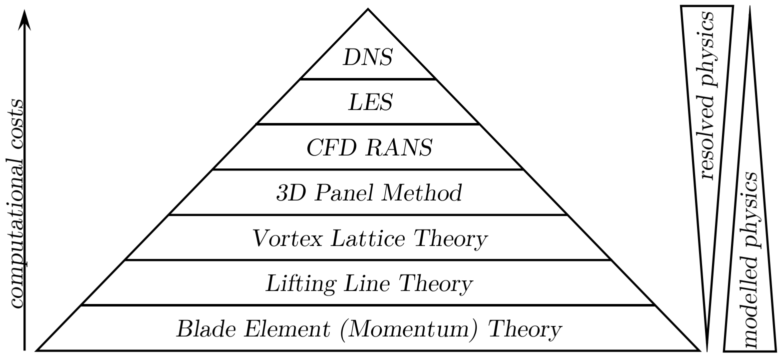

Figure 2.7: Aerodynamic simulation methods for propeller performance prediction

Moreover, empirical methods [37, 71] and methods based on the momentum theory exist. However, these methods do not resolve the blade geometry, which is why they are not suitable for detailed propeller performance modelling.

This study utilises BEMT for analysing propeller performance, multidisciplinary optimisation, and aero-elasto-acoustic coupling. BEMT offers the shortest run time while maintaining high accuracy in the prediction of integrated forces and moments. Higher-order models do not necessarily yield better accuracy in this regard, but they require significantly more computational time [23, 28, 65]. Therefore, the BEMT is described in detail in the following section.

Section 2.3 is organised in three subsections. Subsection 2.3.1 provides insights into the blade element method. The modelling approach with its required correction schemes is explained. Subsection 2.3.2 assesses the influence of 2D airfoil data on the overall performance prediction, including insights into correction schemes for performance modelling. The 2D modelling and its influence are assessed in this step, because a basic understanding of the applied BEMT is required to evaluate the influence of the data on the performance prediction. Subsection 2.3.3 presents different blade-resolving RANS approaches, which will be used for validation purposes.

2.3.1 Blade Element Theory

In a first step, the propeller blades can be treated as rotating wings, as Froude did in 1878 [49]. In this rotary wing approach, each propeller blade is analysed individually. The propeller blades are sliced radially into 2D airfoil sections with each strip treated as an infinite wing.

At each section, the tangential velocity v_t due to rotation is calculated. The axial velocity v_a known from the flight state corresponds to the free-stream velocity v_∞. The axial and tangential velocity are superposed to determine the resulting velocity w (eq. (2.20)).

$$w = \sqrt{v_a^2 + v_t^2} \tag{2.20}$$

The information about axial and tangential velocitiy are used to determine the helix angle Φ, which represents the angle of the wake screw. Φ represents the angle of the wake screw. It can be approximated by substituting the advance ratio (eq. (2.13)) into eq. (2.22). However, this approximation is only valid as a first-order estimation.

$$\Phi = \arctan \frac{v_a}{v_t} \approx \arctan \frac{J}{\pi} \tag{2.21}$$

Next, the angle of attack α (AoA) relative to the airfoil section is calculated (eq. (2.22)). The local section's twist β and the helix angle Φ (eq. (2.21)) results in the AoA.

$$\alpha = \beta - \Phi \tag{2.22}$$

These parameters are used to calculate the sectional airfoil forces, lift L' (eq. (2.23)) and drag D' (eq. (2.24)). Reynolds and Mach number effects are considered by the used 2D airfoil polars. The AoA-dependent 2D lift coefficients c_{l_α} and drag coefficients c_{d_α} are applied to calculate the sectional lift L' and drag D' of the blade element.

$$L' = \frac{\rho}{2} \cdot w^2 \cdot c_{l_\alpha} \cdot c_r \tag{2.23}$$

$$D' = \frac{\rho}{2} \cdot w^2 \cdot c_{d_\alpha} \cdot c_r \tag{2.24}$$

Fig. 2.8 depicts the relationships between the present velocities, resulting angles, and resulting sectional forces. To contextualise the 2D section, the simplified 3D illustration from fig. 2.2 is also shown. The illustrated 2D section corresponds to the section on the upper blade at radius r, with the local velocity u resulting from the rotation at frequency n.

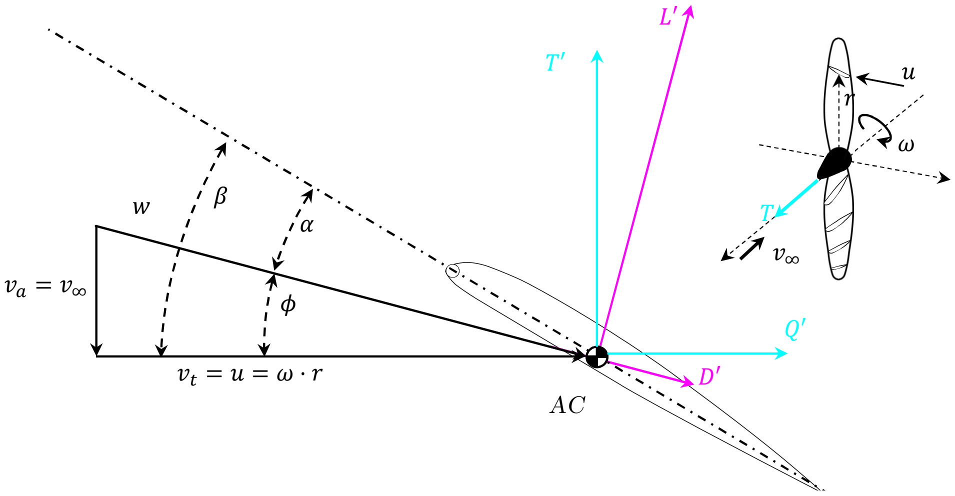

Figure 2.8: Velocities and forces at a 2D blade section

L' and D' are transformed into sectional thrust T' (eq. (2.25)) and sectional force Q' in the propeller plane (eq. (2.26)). As shown in fig. 2.8, T' and Q' are normal and tangential forces relative to the propeller axis.

$$T' = L' \cdot \cos(\phi) - D' \cdot \sin(\phi) \tag{2.25}$$

$$Q' = L' \cdot \sin(\phi) + D' \cdot \cos(\phi) \tag{2.26}$$

The propeller thrust T is obtained by integrating T' over the span multiplied by the number of propeller blades N_B (eq. (2.27)). The final torque is obtained by integrating Q' multiplied by the section radius and the number of blades (eq. (2.28)).

$$T = N_B \cdot \int_{r_{\text{hub}}}^{r_{\text{tip}}} T'_r \, dr \tag{2.27}$$

$$Q = N_B \cdot \int_{r_{\text{hub}}}^{r_{\text{tip}}} Q'_r \cdot r \, dr \tag{2.28}$$

For the structural analysis of the propeller, the torsional moment along the propeller blade is necessary and can be derived from the moment coefficient of the 2D airfoil. Additionally, structural and aerodynamic sweep and lean effects must be considered when analysing curved propellers. Lift and drag forces act at the aerodynamic centre (AC) of the blade section as shown in fig. 2.8.

2D aerodynamic data of an airfoil are required for the application of the BEMT theory. These data can be obtained through experiments, high-fidelity, or low-fidelity CFD simulations, or basic assumptions based on potential flow theory. The potential flow theory shows that the maximal lift slope of an infinite wing is 2π. This lift slope is frequently used in unsteady airfoil theories, or unsteady simulations for rough estimations of the dynamic response.

As in CFD RANS simulations, spatial discretisation is required for the aerodynamic predictions with BEMT methods. To achieve reliable results, a mesh independence study is necessary to determine the number of sections needed for a mesh-independent solution.

Fig. 2.9 shows the thrust and torque coefficients for the reference propeller at a rotational speed of 3500 rpm and an inflow velocity of 10 m/s. The x-axis represents the number of sections, while the left y-axis shows the thrust coefficient, and the right y-axis displays the torque coefficient.

This comparison demonstrates that a minimum of 32 sections is required to achieve a mesh-independent solution.

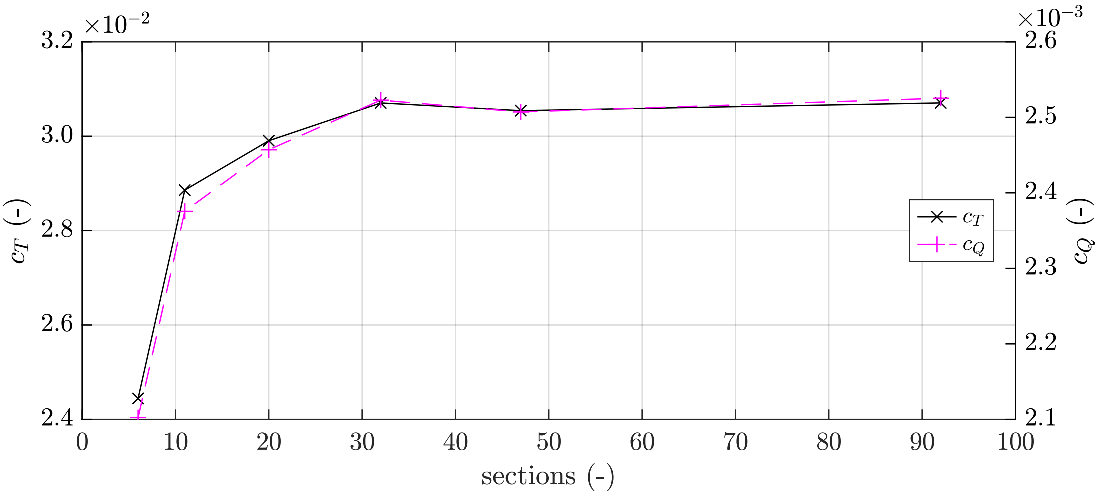

Figure 2.9: Spatial discretisation independence study for BEMT simulations

The BEMT does not consider any cross-flow between sections, which is the major drawback of this method. Accurate three-dimensional flow can only be predicted by high fidelity CFD simulations. However, the BEMT can be improved by different correction methods, which are presented in the following subchapters:

1. The correction of the induced velocities
2. The tip loss correction
3. The sweep correction model
4. The influence of different 2D airfoil data

2.3.1.1 Momentum Correction

The most important step in the performance prediction using BEMT is calculating the induced velocities, as these affect the AoA. The induced velocities w_t and w_a can be determined using momentum theory. Blade element theory (BEMT) with momentum corrections leads to the blade element momentum theory (BEMT).

The momentum theory can be applied in two forms. A closed scheme iterates the momentum produced by the propeller thrust and torque with the induced velocities. The simple momentum theory calculates only the axial induced velocity, while the general momentum theory calculates both axial and tangential induced velocities.

Fig. 2.10 shows the modified 2D velocities, angles, and segment forces under the assumption of axial and tangential induced velocities.

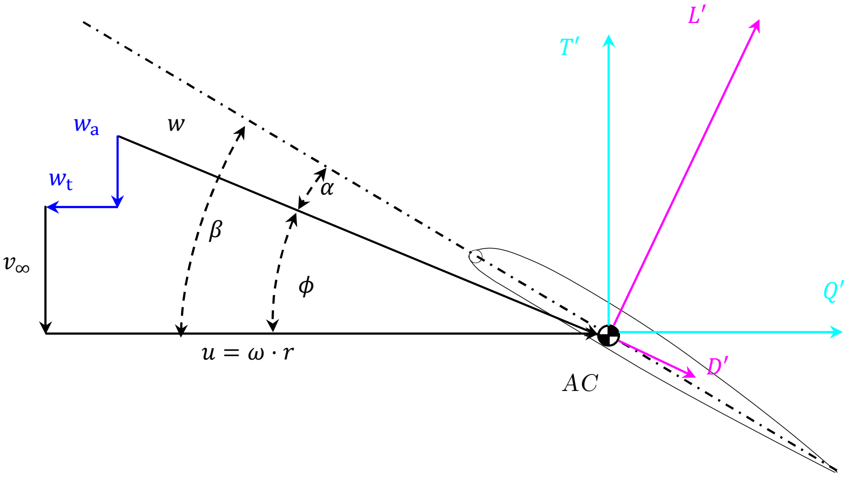

Figure 2.10: Velocities and forces at a 2D blade section with induced velocities

The induced velocities w_a and w_t arise from the forces acting on the fluid and the distortion of the streamlines. The momentum theory was introduced in eq. (2.11) and is reformulated to express the axial induced velocity in eq. (2.29). It is called simple momentum theory (SMT) and assumes that the tangential induced velocity is zero.

$$w_a = -\frac{v_\infty}{2} \pm \sqrt{\left(\frac{v_\infty}{2}\right)^2 + \frac{T}{2 \cdot \rho \cdot (\pi R^2)}} \tag{2.29}$$

The application of the momentum theory to each section results in the general momentum theory. The general momentum theory determines radial-dependent axial and tangential induced velocities for each section. The solidity σ is introduced in eq. (2.31) to simplify the relations of the axial and induced velocity factors eq. (2.34) and 2.33. The mean solidity $\bar{\sigma}$ quantifies the propeller's projected area.

$$\sigma_r = \frac{N_B \cdot c_r}{2\pi r} \tag{2.30}$$

$$\bar{\sigma} = \frac{N_B}{2\pi} \int_{R_{\text{hub}}}^{R_{\text{Tip}}} \frac{c}{r}\, dr \tag{2.31}$$

The derivation of the axial and tangential induction factors a_a (eq. (2.32)) and a_t (eq. (2.33)) is presented in detail in appendix A, along with insights into the governing equations. The complete derivation is not found in the literature, which is why it is stated in appendix A. The induction factors are derived under hover conditions rather than cruise conditions to enhance prediction accuracy.

$$a_a = (1 + a_a)\frac{\sigma \cdot [c_l \cos(\phi) - c_d \sin(\phi)]}{4 \sin^2(\phi)} \tag{2.32}$$

$$a_t = (1 + a_a)\frac{\sigma \cdot [c_l \sin(\phi) + c_d \cos(\phi)]}{4 \sin^2(\phi)} \cdot \frac{v_\infty}{u} \tag{2.33}$$

The axial and tangential velocities, multiplied by the induction factors, result in the induced velocities (eq. (2.35) and (2.34)).

$$w_a = v_\infty \cdot a_a \tag{2.34}$$

$$w_t = u \cdot a_t \tag{2.35}$$

The new induced velocities result in new relative velocities and, consequently, lead to new relations between the angles, as shown in fig. 2.10. Φ and AoA are determined using eq. (2.21) and (2.22) along with the modified velocities given by eq. (2.36) and (2.37).

$$v_a = v_\infty + v_a \tag{2.36}$$

$$v_t = u + v_t \tag{2.37}$$

$$w = \sqrt{(v_\infty + w_a)^2 + (u + w_t)^2} \tag{2.38}$$

At this point, it is important to note that alternative theories can be applied to calculate the induced velocities. Potential flow theory, particularly the LLT, is frequently used for this purpose. The LLT provides a method for calculating 3D induced velocities. However, in potential flow theory, all propeller blades and the complete wake must be modelled, which increases significantly the calculation effort. The section-wise bound circulation is calculated using eq. (2.39).

$$\Gamma = \frac{1}{2} \cdot c_{l_\alpha} \cdot c_r \cdot w \tag{2.39}$$

The circulation of a segment $\vec{dl}$ induces, according to the Biot-Savart law (eq. (2.40)), a vectorial induced velocity at an arbitrary point located at the distance $\vec{r_l}$. The induced velocities of all circulation filaments must be summed to determine the total induced velocity at a specific point.

$$\vec{w_i} = \frac{\Gamma}{4 \cdot \pi} \frac{\vec{dl} \times r_l}{|\vec{r_l}|^3} \tag{2.40}$$

2.3.1.2 Tip and Hub Loss Corrections

The BEMT assumes that all sections act like infinite wings. However, vortices at the tip and root of the blade violate the infinite wing assumption. Hub and tip losses need to be considered to enhance the simulation results of the BEMT. Due to the vortex formations at the blade tip and hub, the propeller's lift is altered. This reduction in lift must be accounted for to increase prediction accuracy. Prandtl first developed a tip loss correction in 1919. The model was derived from the interactions between staggered vortex filaments.

Eq. (2.41) defines the tip loss factor as a function of the radial position, the blade number, and the helix angle. The tip loss factor is normalised to the peak value of 1.

$$F_{\text{tip}} = \frac{2}{\pi} \cdot \text{acos}\left(\exp\left(-\frac{N_B}{2}\frac{R_{\text{tip}} - r}{r\sin(\phi)}\right)\right) \tag{2.41}$$

Similarly, the model is extended to account for hub losses. However, the hub loss extension is less relevant due to the lower loading at the hub. Eq. (2.42) defines the hub loss factor.

$$F_{\text{hub}} = \frac{2}{\pi} \cdot \text{acos}\left(\exp\left(-\frac{N_B}{2}\frac{r - R_{\text{hub}}}{r\sin(\phi)}\right)\right) \tag{2.42}$$

The overall correction factor is defined by combining both factors in eq. (2.43).

$$F = F_{\text{tip}} \cdot F_{\text{hub}} \tag{2.43}$$

The tip and hub loss factor manipulates the axial and tangential velocities according to Prandtl and Glauert as stated in eq. (2.44).

$$w_{a_{PTL}} = w_a \cdot F \tag{2.44a}$$

$$w_{t_{PTL}} = w_t \cdot F \tag{2.44b}$$

However, the author observes a better correlation to wind tunnel data when the lift coefficient of the propeller is adjusted instead of the induced velocities. Applying the loss factor directly to the forces results in a reduction in propeller thrust and torque. However, the reduction of the of the axial induced velocity increases the AoA and therefore might increase the loading at the tip, even if the resulting velocity w is reduced. Airfoil drag remains unchanged because pressure and friction drag are less affected as long as flow separation is not accounted for. Therefore, only the airfoil lift is corrected by the loss factor, as stated in eq. (2.45).

$$c_{l_{PTL}} = c_l \cdot F \tag{2.45}$$

2.3.1.3 Sweep Correction Method

Propeller noise can be mitigated through various measures. One feasible approach to reducing propeller noise for a fixed diameter and a fixed number of blades, which are often specified as top-level aircraft requirements, is to apply a sweep variation. Additionally, sweep can be used to reduce dynamic loads caused by propeller-wing interactions or oblique inflow.

Propeller noise evaluation using a computational acoustic solver requires precise aerodynamic performance data. However, the classical BEMT cannot accurately model swept propellers due to theoretical limitations. As a result, sweep correction models become essential for the accurate analysis of swept propellers and the effective conduction of noise emission optimisations.

The author developed a geometric correction model for BEMT methods presented in [8]. Busemann's swept wing correction model [21] is adapted for application to swept propellers. In the fixed-wing model, the reference axis for the sweep correction is the aircraft fixed y-axis. In the propeller application, however, the reference axis must be the section's radius vector. Therefore, the reference axis changes due to sweep, as shown in fig. 2.11. Fig. 2.11 illustrates the differences between a straight (unswept) and a swept propeller blade. Furthermore, the global Cartesian coordinate system is defined with the x-axis pointing radially and the z-axis pointing in the thrust direction. The right blade represents a straight blade, while the left blade represents a swept blade. The circumferential velocity u_{Loc} results from the rotational movement and can be calculated with eq. (2.46).

$$\vec{u} = \vec{\omega} \times r\vec{_{Loc}} \tag{2.46}$$

Therefore, the rotational velocity is altered for the swept blade compared to the unswept blade, because it must be orthogonal to the local radius vector (r_{Loc}) and is no longer orthogonal to the global x-axis. The subscript *Loc* is related to the local sweep.

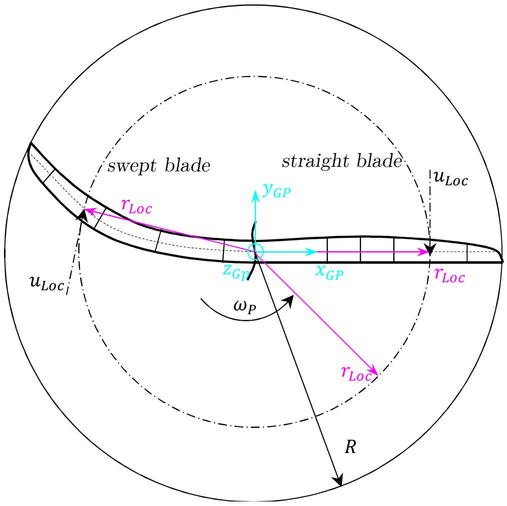

Figure 2.11: Difference between a straight blade and a swept blade (front view)

Fig. 2.12 illustrates the sweep definitions of the section at r_{Loc}. The author introduces the global sweep Λ_{Glo} and the local sweep $\Lambda_L oc$. The global sweep is defined as the angle between the global propeller x-axis and the local radius vector pointing towards the quarter-chord point of the airfoil. The local sweep is defined as the angle between the local radius vector and the tangent of the quarter-chord line – the connection of all quarter-chord points.

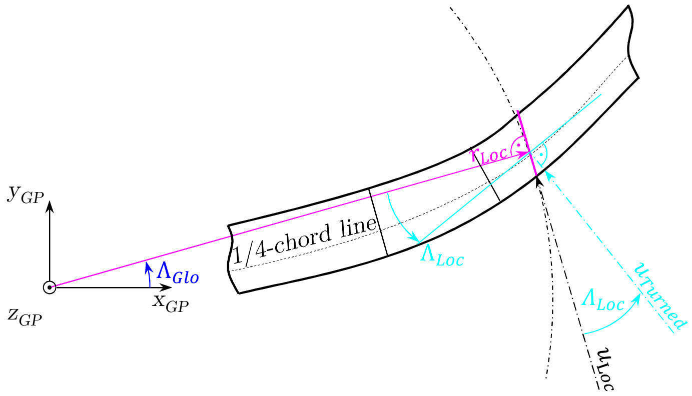

Figure 2.12: Sweep definition at a blade section (front view)

According to Busemann's derivation, the inflow velocity has to be turned to be normal to the quarter chord line of a wing. Therefore, the tangential velocity must also be turned accordingly as shown in eq. (2.47).

$$u_{t_{Loc}} = u_t \cdot \cos(\Lambda_{Loc}) \tag{2.47}$$

The turned velocity results in a quadratic change of the acting forces. The change in velocity is transformed into a change of c_l and c_d. Eq. (2.48) and (2.49) show the cosine square dependency of the resulting coefficients due to sweep.

$$c_{l_{Loc}} = c_{Loc} \cdot \cos^2(\Lambda_{Loc}) \tag{2.48}$$

$$c_{d_{Loc}} = c_d \cdot \cos^2(\Lambda_{Loc}) \tag{2.49}$$

The forces in the rotation plane act, by definition, in the turned velocity system. This leads to Q_{Loc} acting normal to the quarter-chord line instead of normal to the local radius. It is calculated using the adopted coefficients and eq. (2.50).

$$Q'_{Loc} = L'_{Loc} \cdot \sin(\phi_{Loc}) + D'_{Loc} \cdot \cos(\phi_{Loc}) \tag{2.50}$$

As the Q_{Loc} force was calculated in the turned system it does not directly result in the torque (which acts globally). For the torque prediction, the Q_{Loc} force must be transformed to be normal to the local radius by eq. (2.51).

$$Q' = Q'_{Loc} \cdot \cos(\Lambda_{Loc}) \tag{2.51}$$

Fig. 2.13 depicts the dependencies between the resulting tangential force due to the swept velocity and the tangential force relative to the radius. Furthermore, fig. 2.13 reveals that a radial force is introduced due to sweep.

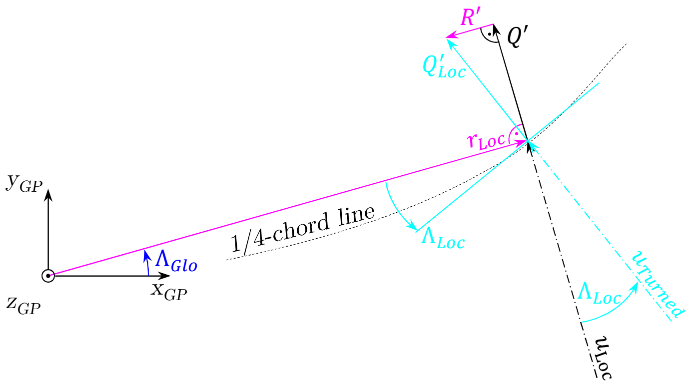

Figure 2.13: Action of tangential forces at a swept blade (front view)

The radial force does not affect the overall performance but could influence deformations. Axially acting forces are not influenced by the local sweep, except for the changes in the coefficients.

The results of the presented model are detailed and validated through CFD RANS simulations in [8].

2.3.1.4 Influence of Correction Methods on Performance Prediction

The influence of the different correction methods on the performance prediction is analysed in the following paragraphs. The impact of the correction methods is assessed through a comparison of the performance predictions for the four-bladed reference propeller presented in section 2.2.

The comparison in fig. 2.14 shows the predicted performance curves of the reference propeller. The left side of fig. 2.14 presents the thrust curves, while the right side displays the predicted torque curves. The black curve represents the prediction using the simple momentum theory (SMT) according to eq. (2.11). With the application of the higher-order general momentum theory (GMT), along with the Prandtl tip loss correction (PTL) and the sweep correction (SC), as described in section 2.3.1.1 - 2.3.1.3, thrust and torque are reduced. The correction models are applied sequentially, leading to a combination of GMT with PTL, as well as GMT with PTL and SC. PTL and SC primarily reduce the lift by manipulating c_l. The reduction in c_l decreases the thrust, as described in eq. (2.25), and torque, as described in eq. (2.26). Additionally, the SC further reduces the predicted torque.

The GMT changes the slope of the performance curves and results in a less pronounced curvature in the mid-range of the advance ratio. The PTL further reduces the loading, thereby decreasing both thrust and torque. The zero-thrust crossing remains unaffected by all models, as a reduction in loading also decreases the induced velocities and subsequently reduces c_l.

In the given case, the SC has only a minor effect on the overall performance due to the small propeller sweep. However, previous studies demonstrate the model's effectiveness for propellers with greater sweep [8, 9].

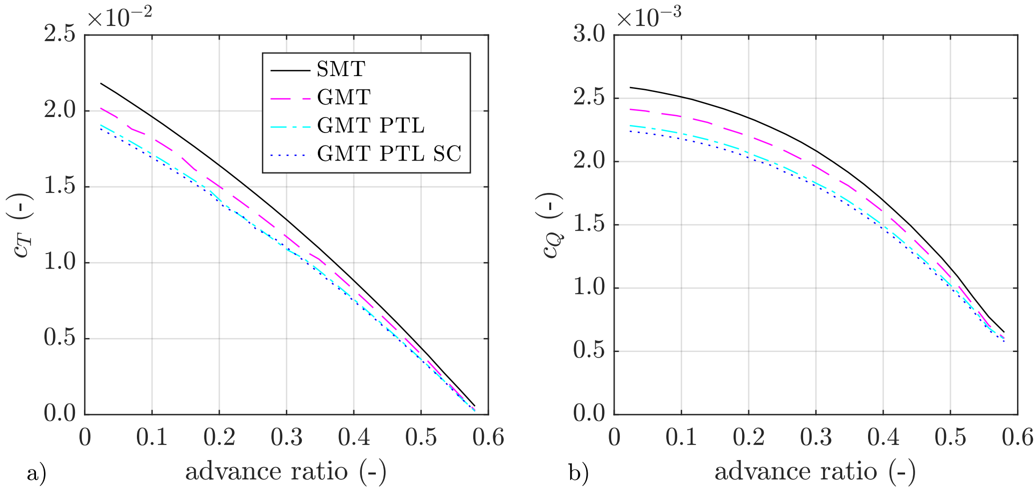

Figure 2.14: Performance predictions of the four-bladed reference propeller with different correction methods

The comparison of the different correction methods for performance prediction reveals significant deviations in thrust and torque estimations. The deviation in thrust and torque predictions between the highest and lowest results is approximately 10% at an advance ratio of 0.1. This error remains nearly constant across the entire advance ratio range. Further studies comparing BEMT modelling approaches with various induced velocity corrections report similar levels of deviations [23, 65, 107].

In the following thesis, blade element momentum theory (BEMT), which combines blade element theory with general momentum theory, is applied unless stated otherwise.

2.3.2 2D Airfoil Data for Blade Element Methods

The infinte wing slices of the blade, require aerodynamic data. The airfoil coefficients c_l, c_d, and c_m of the infinite wings can be calculated using 2D aerodynamic solvers. Simple BEMT methods, or those applied within the framework of aeroelasticity, often utilise the 2π assumption for the calculation of unsteady phenomena [32]. However, BEMT always requires 2D aerodynamic data as input to calculate thrust, power, and efficiency.

The 2D airfoil data directly affects performance prediction. During in-flight operations of a propeller, some sections of the propeller may operate under stalled conditions. In such stalled conditions, the accurate prediction of lift and drag becomes crucial for determining the overall propeller performance.

The 2D aerodynamic data can be estimated using various tools, ranging from potential flow theory to higher-fidelity CFD simulations or wind tunnel tests. Potential flow theory is fast and provides reliable accuracy under moderate Reynolds and Mach number conditions, as well as in unstalled conditions. CFD RANS simulations improve predictions in stalled regions but require significantly more computational time compared to potential flow results.

Wind tunnel tests, however, face challenges in covering a wide range of Reynolds and Mach numbers. Furthermore, wind tunnel tests have inherent accuracy limitations that must be well understood. Due to these constraints, wind tunnel tests cannot be performed for every airfoils needed in a numerical analysis, as more than 30 sections (and therefore 30 airfoils) must be characterised for mesh independent solutions (cf. fig. 2.9). However, wind tunnel tests are essential for validating the tools, as demonstrated in Ref. [7].

Furthermore, the boundary layer properties can significantly influence aerodynamic performance predictions, which have to be defined for reduced order potential flow solvers, high fidelity CFD simulations as well as wind tunnel test. Laminar boundary layers tend to separate earlier and more abruptly than turbulent ones, which resist separation longer due to enhanced momentum exchange. Typically, a laminar boundary layer has lower drag coefficients compared to a turbulent boundary layer. These phenomena must be accurately captured by the airfoil data prediction methodology.

The following subchapters introduce different modelling and correction methods and compare their prediction results. First, section 2.3.2.1 presents the results of 2D RANS simulations for tripped and untripped conditions. Second, section 2.3.2.2 discusses the XFOIL results for tripped and untripped conditions. Third, section 2.3.2.3 introduces a 2D and 3D airfoil polar correction. Finally, section 2.3.2.4 compares the propeller performance predictions derived from the different airfoil data sources.

The results are provided for the airfoil at the reference propeller's 75% section. Fig. 2.15 illustrates the selected airfoil geometry, which is analysed with XFOIL and RANS simulations. Since the airfoil was cut from a CAD file, details such as its family, thickness ratio, camber, and the positions of maximum camber and maximum thickness are unknown.

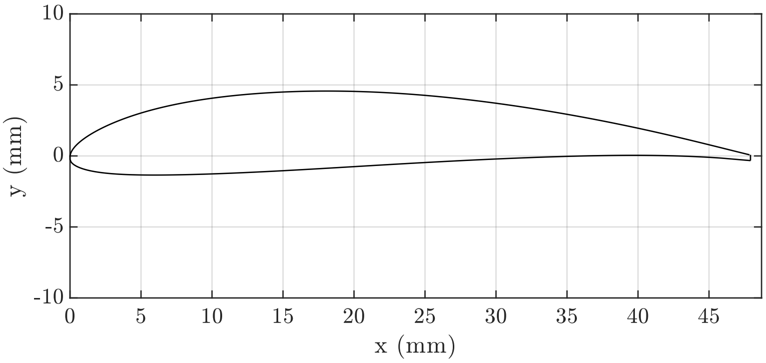

Figure 2.15: Reference airfoil at 75% of the radius

2.3.2.1 2D RANS Airfoil Simulation

One way to obtain the required 2D force and moment coefficients is through RANS simulations. RANS is not limited to attached flow regions, but for deep stall conditions, unsteady RANS (URANS) or large eddy simulations (LES) are necessary. LES must be applied to finite-width strips rather than purely 2D elements, since eddies are inherently three-dimensional and cannot be captured in 2D. The same applies to other methods that resolve eddies. While direct numerical simulation (DNS) is possible for airfoil studies, its high resolution is unnecessary for computing force and moment coefficients [136].

The 2D RANS airfoil simulations are conducted with the commercial CFD solver `Simcenter Star-CCM+`. The physics is modelled by a compressible coupled flow solver, incorporating Menter's Shear Stress Transport (SST) model [109], non-linear constitutive relationships, and controlled turbulence decay [144]. Additionally, a comparison is made between a fully turbulent simulation and a simulation using the $\gamma - Re - \theta$ transition model [110]. Further details on the mesh settings, the mesh independence study, and the validation of the applied approach can be found in Ref. [7, 41, 58].

The boundary layer is resolved using a low-y+ approach with 40 prism layer cells. Boundary layer settings are determined based on the following equations and Schlichting's skin-friction correlation [137].

$$Re_x = \frac{\omega R c}{\nu} \tag{2.52}$$

$$\sigma_{99,turb} = \frac{0.37c}{Re_x^{0.2}} \tag{2.53}$$

$$c_f = (2\log_{10}(Re_x) - 0.65)^{-2.3} \tag{2.54}$$

$$u_* = \sqrt{\frac{\tau_w}{\rho}} \tag{2.55}$$

$$y = \frac{y^+ \nu}{u_*} \tag{2.56}$$

The resulting near wall thickness y is the height of the first cell in the prism layer.

The reference velocity is calculated using the distance from each airfoil section to the rotation point and the rotational speed. The reference Reynolds number is determined using the airfoil's chord length and the circumferential velocity.

The reference parameters for the given airfoil are listed below and are calculated using standard atmospheric conditions.

- Chord length $c = 4.8 \quad cm$
- Reynolds number $Re_x = 333{,}000$
- Mach number $Ma = 0.3$
- Displacement thickness $\sigma_{99,turb} = 1.4 \quad mm$
- Near wall thickness $y = 3.1 \quad nm$

The first step of all RANS simulations is a mesh independence study to ensure that the simulation results are not influenced by its spatial discretisation. A polyhedral unstructured mesh is generated using the integrated meshing tool in `Simcenter Star-CCM+`. A temporal discretisation study is unnecessary because the solution converges to a static result, making the time step irrelevant to the outcome. This assumption is valid in the attached flow regime without significant flow separation. Similarly, a study about different turbulence models is unnecessary because the SST model has demonstrated its accuracy in numerous simulations [41, 88, 132].

Fig. 2.16 illustrates the mesh independence study for the given airfoil. The x-axis represents the number of cells in increments of 100,000, while the y-axis shows the relative error of c_l and c_d compared to the predictions obtained with the finest mesh. Mesh independence is achieved at 1 million cells. The c_l converges significantly faster compared to c_d. To the left of the vertical line, the results are mesh-dependent, whereas to the right of the vertical line, the results are mesh-independent. These results are obtained using the reference velocity and a 0° AoA. To ensure comparability across different AoA values, the same mesh settings are used for each AoA.

However, the wake refinements are attached to the surface of the airfoil, aligned with the AoA, and have a spread angle of 10°. Therefore, the mesh is updated for each AoA.

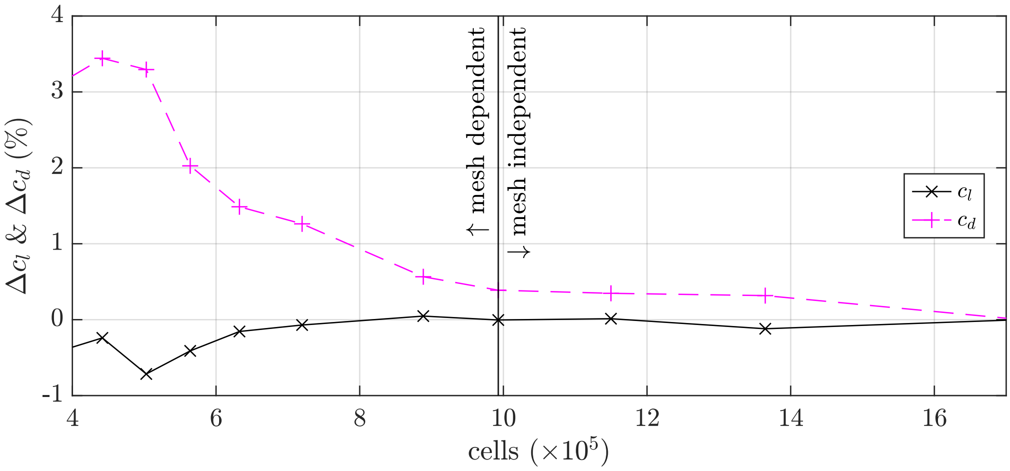

Figure 2.16: Mesh independence study of 2D RANS simulations

Fig. 2.17 compares the fully turbulent and $\gamma - Re - \theta$ 2D RANS simulations. Diagram a) of fig. 2.17 displays the $c_l - \alpha$ polars, while diagram b) shows the $c_l - c_d$ polars. The black curves represent the fully turbulent flow, and the cyan curves correspond to the simulation with $\gamma - Re - \theta$ transition model. The fully turbulent simulations run for 5,000 iterations, while the simulations with transition models run for 8,000 iterations. The convergence with the $\gamma - Re_\theta$ model is worse compared to the fully turbulent simulation and the simulation is less stable.

The figure includes error bars, indicating the maximum and minimum values over the final 1,000 iterations of the RANS simulation. These error bars represent the fluctuations in the converged solutions. As separation on the airfoil increases, the fluctuations become more pronounced. Consequently, the error bars are larger in the stalled regions. Complete flow separation occurs on the suction side at angles of attack below -8° and above 17°, which leads to large c_l and c_d fluctuations. However, in the linear region of the c_l polar, the fluctuations about the last 1,000 iterations are negligible.

Diagram a) shows that in the linear region of the airfoil lift curve, both the fully turbulent and the transitional simulations predict nearly identical values of c_l. Although the transition point does not visibly affect the results in this region, it's worth noting that a turbulent boundary layer causes a slight decambering effect, which can slightly reduce c_l. A comparison between the lift predictions with and without th e$\gamma - Re_\theta$ transition model confirms this effect, though the difference remains below 0.005. The transition model also predicts earlier stall, occurring at around 11° AoA, compared to 13° without it. A similar trend appears at negative AoA, where stall begins about 0.5° earlier when the transition model is used. In the negative AoA region, c_l exhibits an upward jump caused by flow separation. This jump in the transient simulation occurs 1° earlier compared to the fully turbulent simulation. As the AoA decreases further, c_l continues to decline.

The highest lift is reached at an angle of attack (AoA) of 13° for the turbulent simulation, with a c_l of 1.55, and at 12° with a c_l of 1.47 for the simulation with transition. Beyond this AoA, the lift decreases and breaks down suddenly at 19° and 16° AoA, respectively. With further increase in AoA, the lift begins to rise again, an effect known as secondary lift. This secondary lift corresponds to the behaviour of a flat plate, which generates lift primarily through pressure on the lower surface, rather than suction on the upper surface.

Diagram b) reveals that drag is reduced in the linear region of the polar due to decreased skin friction drag. At the c_l of 0.5 the c_d of the transient simulation $5e-3$ smaller than of the fully turbulent simulation. In contrast, the error bars indicate that the transition model leads to fluctuations in drag about the last 1,000 iterations. The fully turbulent simulations show no drag fluctuations in the region of attached flow. Fluctuations occur only in stalled conditions, but this region lies beyond a c_d of 0.1.

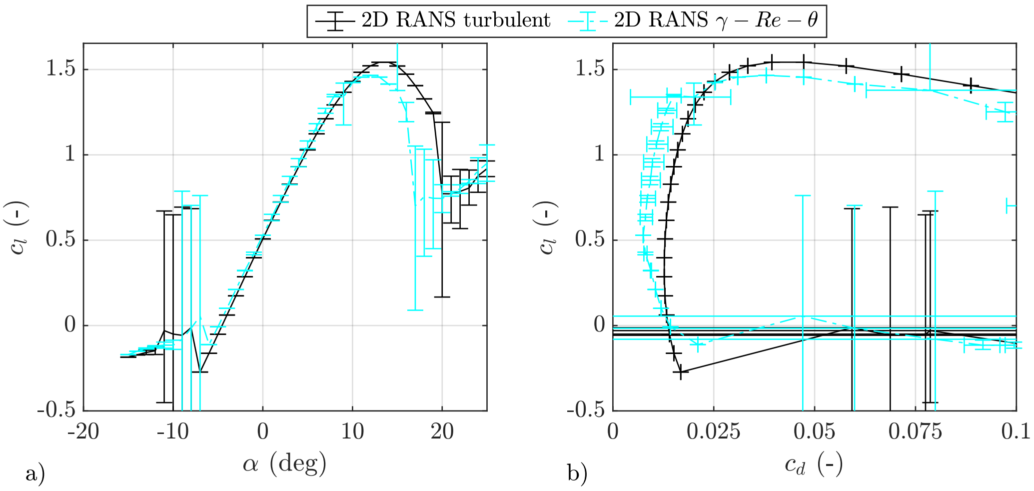

Figure 2.17: Comparison of 2D RANS simulations with and without transition model

The comparison of both models shows that, in the current case, the $\gamma - Re - \theta$ model slightly affects the drag prediction and the separation point. Lift prediction, however, remains almost unaffected in the attached flow regime. This suggests that transition modelling under the given operational conditions might not significantly influence the overall performance prediction, as it mainly depends on the lift curves. Therefore, transition modelling is not further investigated in this thesis.

2.3.2.2 XFOIL Simulation

XFOIL is a two-dimensional potential flow solver, enhanced with viscid models. It incorporates the compressibility correction based on the Kármán-Tsien approach and includes a boundary layer model to account for friction drag and separation. The boundary layer model employs the displacement thickness concept, while transition prediction relies on the e^n approach [129]. XFOIL allows the analysis of both laminar and turbulent airfoil behaviour within the BEMT calculation scheme, although it is restricted to purely subsonic operations. The BEMT procedure limits the propeller's tip Mach number to 0.7 to address this constraint. The transition model estimates the laminar-turbulent transition, which influences stall behaviour [33, 38, 39] However, the laminar-turbulent transition can also be fixed at a specified location on the airfoil surface. In simulations of fully turbulent flow, the transition is set at the LE of the airfoil.

Due to the inherent characteristics of potential flow solvers, XFOIL remains limited to regions of attached flow, even when the boundary layer model provides stall predictions. Studies conducted on various airfoils indicate an accuracy of approximately 10% for c_l predictions in the unstalled region [33, 58]. The accuracy for c_d predictions is comparatively lower. To enhance the potential flow solver's simulation accuracy, XFOIL offers options to adjust boundary layer settings. The empirical n factor in the e^n model, which depends on the airfoil shape and Reynolds number, plays a critical role in these adjustments. The presented results use an n factor of 8, as recommended in the XFOIL manual.

Fig. 2.18 shows the comparison of the XFOIL results (with and without transition) to the 2D RANS (cf. fig. 2.17) simulations. As in fig. 2.17, diagram a) shows the $c_l - \alpha$ polars and diagram b) shows the $c_l - c_d$ polars. However, the RANS simulations are presented without error-bars.

The comparison between XFOIL and RANS results reveal that XFOIL predicts a higher c_l slope than RANS. The c_l polars align closely around the zero lift coefficients. However, the curves' slopes differ significantly. While the RANS simulation shows the decambering effect as a reduction in c_l between laminar-turbulent transitional and fully turbulent results, XFOIL does not show this behaviour. Furthermore, XFOIL predicts a more favourable flow separation than the RANS simulations, featuring a pronounced plateau of constant c_l in the high AoA regime. XFOIL does not exhibit the jump in c_l observed in the negative AoA stall region. Despite this, the post-stall slope of c_l is similar to that predicted by RANS. The c_l variation due to laminar-to-turbulent transition is of reduced magnitude in both methods. However, the XFOIL transition model does not influence the stall characteristics, whereas the RANS transition model affects the stall region. The XFOIL transitional model slightly reduces c_l in the linear region, whereas the RANS transitional model slightly increases c_l.

Diagram b) illustrates that the c_d in XFOIL remains unaffected by the transition model, as the laminar-turbulent transitional and fully turbulent c_d are equivalent. Therefore, the comparison reveals that the natural laminar-turbulent transition is located at the LE according to XFOIL, and therefore fully turbulent. The RANS prediction, in contrast, shows a higher c_d in case of the fully turbulent simulation, suggesting that the boundary layer is not fully tripped. The XFOIL c_d predictions match the RANS predictions with laminar-turbulent transition in the linear region. This discrepancy indicates an incorrect tripping location in XFOIL, which may be influenced by the n factor in the e^n method.

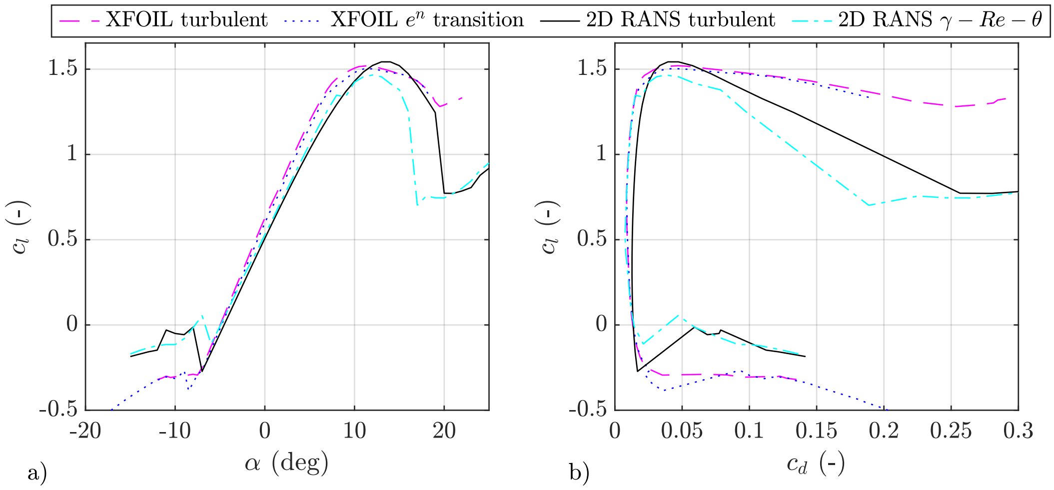

Figure 2.18: Comparison of 2D RANS and XFOIL simulations

2.3.2.3 Pre- and Post-Stall Modelling

A wide AoA range is required for the performance modelling of propellers to cover various operational conditions. For GA propellers in particular, stall typically occurs at low advance ratios during take-off. In helicopter applications, reverse flow at the hub is a common phenomenon during high-speed cruise conditions. Therefore, airfoil polars in the stalled region are essential. However, XFOIL cannot provide airfoil coefficients in the stalled and post-stall regions. Thus, a model is required to extend the unstalled airfoil polars into the stalled region.

An empirical stall model based on [145] is employed for this purpose. This model is derived from wind tunnel experiments conducted on a variety of airfoils. It predicts post-stall behaviour using the airfoil's thickness ratio and the propeller blade's aspect ratio. In addition to these ratios, the model requires specific polar characteristics as inputs, including:

- zero-lift AoA $\alpha_{c_{l,0}}$
- linear slope of the $c_l - \alpha$ polar $(dc_l/d\alpha)$
- maximum and minimum c_l and c_d and their respective AoA $(c_{l,min/max}, \alpha_{c_l,min/max}, c_{d,min/max}, \alpha_{c_d,max/min})$

These parameters are used to predict the theoretical maximum lift coefficient at $\alpha_{c_l,max}$ without stall. Adjustments based on additional empirical parameters are used to determine the post-stall region. For stability purposes, the model truncates the airfoil polars beyond its maximum lift coefficient. Since XFOIL is known to perform poorly in the stalled region, the model limits the polars at this point.

A second correction adjusts the airfoil data in the pre-stall region to account for the finite aspect ratio. This model is referred to as the 3D stall model (3D stall) [118]. Similar to fixed-wing applications, the finite aspect ratio modifies the linear slope of the 2D airfoil $c_l - \alpha$ polar, with lower aspect ratios resulting in reduced slopes.

Fig. 2.19 shows the airfoil polars of XFOIL without transition, the stall model, and the 3D stall model for the reference propeller and a propeller with an infinite aspect ratio. The black curve in fig. 2.19 represents the previously presented XFOIL polar from fig. 2.18.

The cyan dash-dotted curves illustrate the post-stall correction, which begins at the maximum c_l predicted by the XFOIL simulation. The model does not modify the pre-stall region but introduces adjustments to the post-stall region. The reference propeller's aspect ratio significantly influences the post-stall behaviour. Diagram a) shows that beyond the maximum c_l, the curves drop abruptly. After this sudden breakdown, the curve transitions smoothly into a sinusoidal shape, a feature added by the author to improve the model. The sinusoidal curve extends the airfoil polars to cover the full 360°. Diagram b) depicts the corresponding increase in drag.

The model does not perfectly fit the negative stall region, but this area is typically irrelevant during propeller operations.

The magenta dashed lines in diagram a) and b) represent the 3D stall corrected results for an infinite aspect ratio. The infinite wing assumption does not affect the pre-stall c_l in diagram a). However, the c_d increases quadratically with c_l. The infinite aspect ratio also raises the height of the second post-stall c_l maximum compared to the cyan post-stall correction.

Finally, the blue dash-dotted lines represent the 3D stall corrected polars for the reference propeller with an aspect ratio $\Lambda = 11.5$. Due to the finite aspect ratio, the c_l slope is reduced. The second c_l maximum returns to the level of the cyan post-stall peak. The quadratic c_d increase in diagram a) exceeds that of the infinite wing assumption.

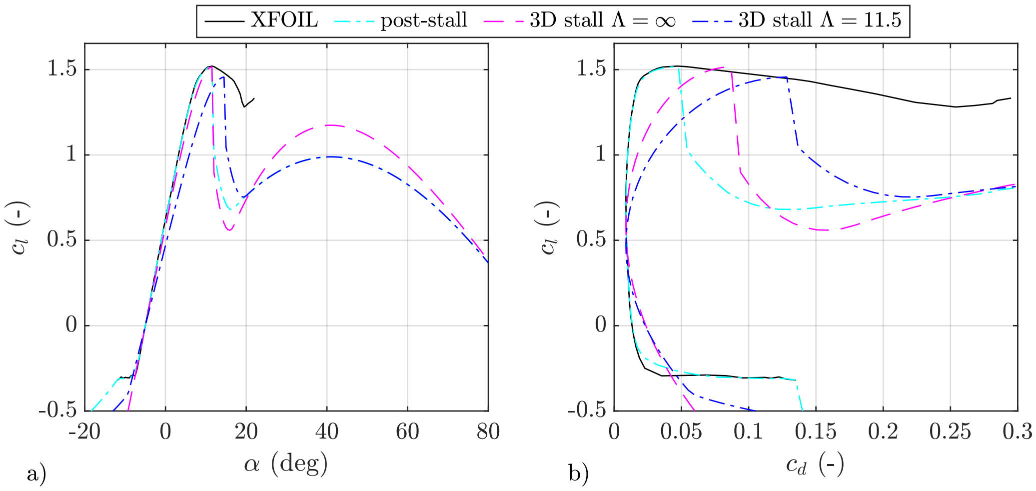

Figure 2.19: Comparison of 2D XFOIL results with post-stall and 3D stall corrections

2.3.2.4 Influence of 2D Data on Performance Prediction

The correction models are evaluated through a performance prediction comparison using different 2D databases. The performance calculations are conducted using the same radial sections. The bottleneck for the number of radial sections are the CFD RANS simulations, which limit the calculations to only 17 sections.

Fig. 2.20 illustrates the thrust and torque coefficients in diagrams a) and b) based on the various 2D datasets. The black curves show the performance prediction using the 2D RANS data, which was obtained as described in section 2.3.2.1, without applying the $\gamma - Re - \theta$ transition model. The magenta dashed lines correspond to XFOIL simulations without transition. The cyan dash-dotted line represents the post-stall model, which matches the representation in fig. 2.19. The blue dotted line depicts the 3D stall prediction using the propeller's real aspect ratio. The vertical line represents the advance ratio at which detailed blade distributions are shown in fig. 2.21.

Initially, 2D RANS and XFOIL results are compared. The thrust prediction with 2D RANS polars is significantly lower compared to the XFOIL polars. The same trend applies to the torque prediction, except in the high advance ratio region. The slope of the torque prediction differs between RANS and XFOIL polars. With XFOIL polars, the torque prediction's slope increases significantly, while with RANS polars, it remains unchanged. Consequently, RANS polars result in higher torque values during high advance ratio operations compared to XFOIL polars. This is caused by increased drag values in the low AoA region.

The post-stall extension does not modify the XFOIL results, indicating that the propeller operates in unstalled conditions across its entire advance ratio range. The 3D stall model significantly reduces thrust and torque due to adjustments in c_l. At an advance ratio of 0.1, the 3D stall model predicts a 15% reduction in both thrust and torque compared to XFOIL results. However, it slightly changes the slope of the torque curves, resulting in higher torque values at high advance ratios compared to predictions based on XFOIL polars.

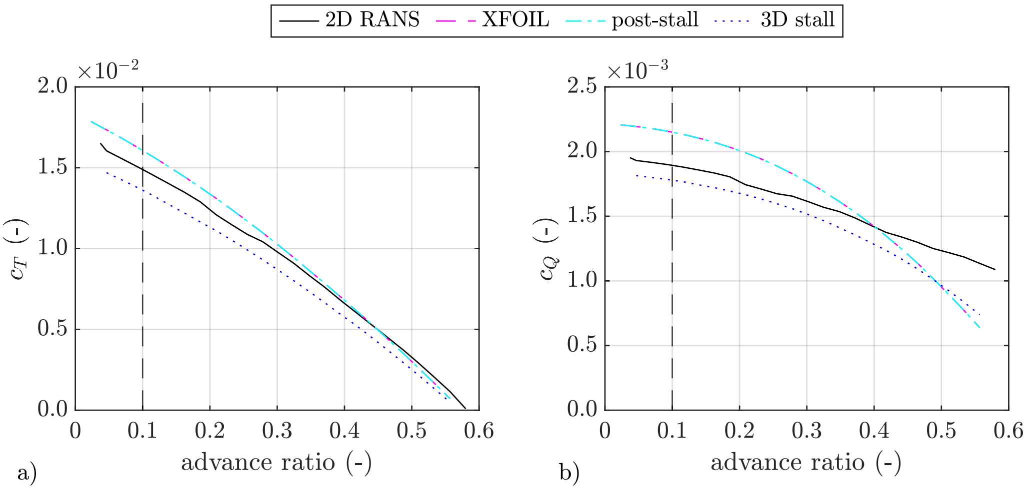

Figure 2.20: Performance predictions of the four-bladed reference propeller with different 2D data bases

The c_l is a key parameter in overall propeller performance, playing a crucial role in torque and thrust predictions, as detailed in Ref. [7]. Fig. 2.21 illustrates detailed information along the blade radius for all four airfoil polar types at an advance ratio of 0.1. The first row shows the axial induced velocity (w_a), the second row presents the AoA, the third row illustrates the c_l distribution, and the fourth row depicts the c_d distribution along the non-dimensional radius. The c_d in diagram d) is displayed on a logarithmic y-axis to enhance readability. The vertical line marks the position of the presented airfoil polars.

The w_a, AoA, c_l, and c_d are selected for comparison because they are interdependent and collectively influence propeller performance. The w_a serves as a direct measure of the propeller thrust.

Fig. 2.21 shows that, in all four diagrams, the trends between the 2D data sources are closely aligned. At an advance ratio of 0.1, the propeller root exhibits a positive w_a even though the AoA at the root is negative. Due to the highly cambered airfoils, c_l remains positive even in the AoA region below -7°. The small AoA leads to a reduced c_l and a significantly increased c_d. Towards the tip, w_a decreases, the AoA increases, and c_l approaches zero as a result of the PTL correction.

The reasons for the differences in performance predictions can be derived from comparing the 2D data sources in each diagram. XFOIL and the post-stall distribution aligns from the hub to the tip in all four diagrams, resulting in equivalent aerodynamic performance.

The 3D stall model significantly reduces c_l along the entire blade, leading to lower w_a and higher AoA. The c_d differs at the tip compared to XFOIL but remains approximately the same along the rest of the blade.

The differences between the 2D RANS and XFOIL simulations are most pronounced at the tip and root of the propeller, with smallest variation in the middle part of the blade. The 2D RANS simulation produces a lower w_a distribution, resulting in an increased AoA but still lower c_l due to differences in the 2D polars, as shown in fig. 2.18. The c_d distribution is higher at the root but approximately half as large from a non-dimensional radius of 0.4 to the tip.

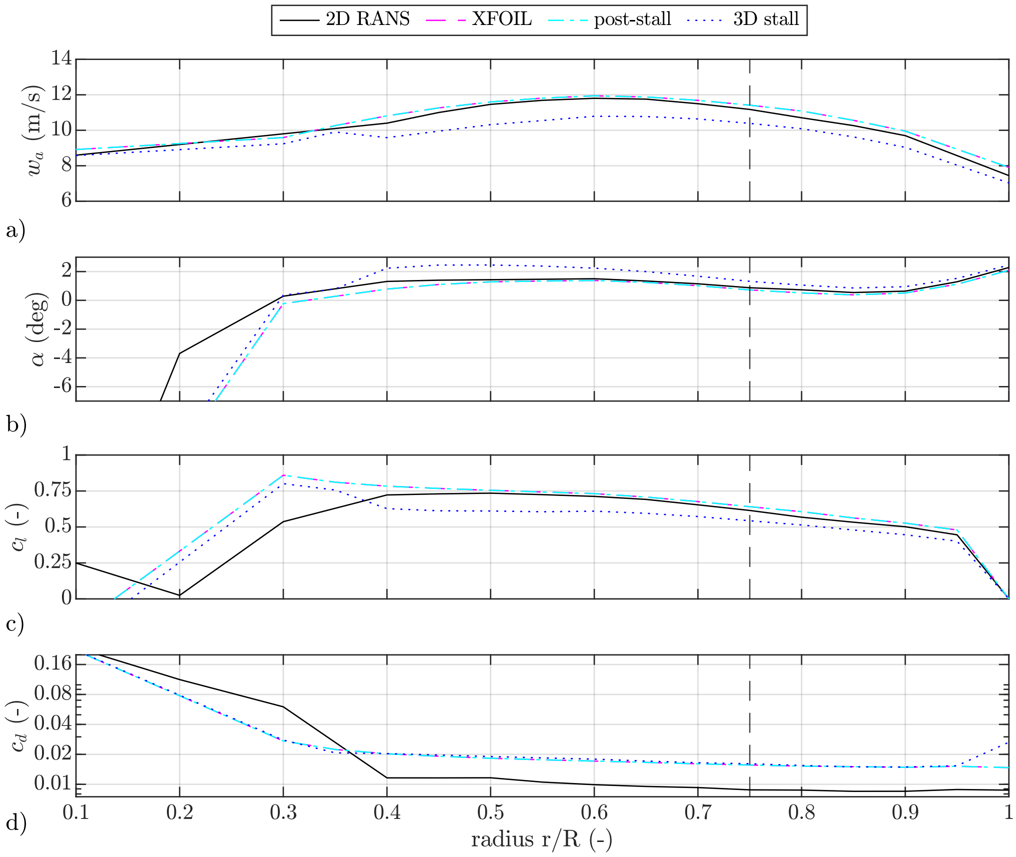

Figure 2.21: Influence of 2D data bases at the advance ratio of 0.1

The dominance of lift over drag is evident in eq. (2.25) and (2.26). The c_l is two orders of magnitude higher than the c_d across most of the propeller. Additionally, drag is multiplied by $sin(\Phi)$ in the thrust prediction, where the helix angle Φ is typically small in the advance ratio region below 1[1]. As a result, variations in drag have a reduced impact on thrust prediction.

For torque prediction, a clear dependency on lift or drag cannot be directly inferred from eq. (2.26) because the sine and cosine terms are swapped, balancing the differences in magnitude between c_l and c_d. However, fig. 2.21 illustrates that c_d is nearly identical between the XFOIL, post-stall, and 3D-stall predictions. This observation suggests that at an advance ratio of 0.1, the c_l predominantly influences torque prediction.

---

[1] Φ can be approximated using eq. (2.21), with the advance ratio. An advance ratio of 1 corresponds to a helix angle of approximately 20°.

A sensitivity study on c_d is performed in Ref. [7, 61] and in fig. 2.22. Fig. 2.22 quantifies the influence of c_l and c_d changes on the performance prediction. The XFOIL results are artificially manipulated to show the influence of the 2D data prediction on performance. Three manipulations are applied:

1. The c_d is set to zero.
2. The c_d is set to a constant value of 0.05, approximately doubling it compared to the XFOIL prediction (cf. fig. 2.21).
3. The c_l is increased by 10%.

Diagram a) of fig. 2.22 shows the relative changes in c_T, while diagram b) shows the changes in c_Q, both relative to the XFOIL prediction in fig. 2.20. Since zero thrust is reached at $J = 0.55$, the relative errors escalate at the zero crossing. Torque reaches its zero crossing at a higher advance ratio, reducing the divergence.

Diagram a) illustrates that setting c_d to 0 has a minor influence on c_T prediction at low advance ratios. The error due to $c_d = 0$ remains below 5% up to $J = 0.45$. A similar trend is observed when c_d is increased to 0.05. However, c_T decreases instead of increasing. Increasing c_l by 10% results in a 5% increase in c_T across a wide range of advance ratios. The c_T of 5% compared to the 10% c_l increase highlights the impact of higher induced velocity, which reduces AoA along the blade and, consequently, c_l.

Diagram b) shows the influence of manipulated 2D data on torque prediction. Unlike the thrust prediction, drag manipulation significantly impacts torque prediction. Setting c_d to zero results in a 10% reduction in torque. The relative deviation grows with higher advance ratios. The constant c_d of 0.05 raises c_Q by 30% at the advance ratio of 0.1. Once again, the deviation grows with the advance ratio. The 10% larger c_l results in an increase of c_Q, similar to the effect of c_T. At $J = 0.05$, c_Q increases by 8%, and at $J = 0.4$ by 5% due to the c_l manipulation. The higher induced velocities result in a larger helix angle, which rotates the lift vector further into the propeller plane. These observations have also been reported in Ref. [7].

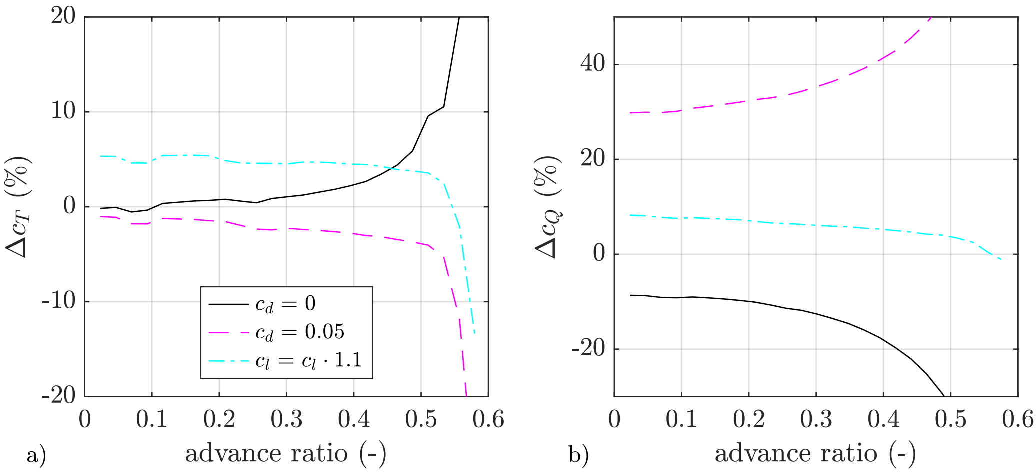

Figure 2.22: Influence of artificial c_l and c_d changes on the performance prediction

The comparison of different 2D data sources reveals that significant differences in prediction results arise depending on the source and stall modelling approach. The deviation between the lowest and highest prediction results at an advance ratio of 0.1 is 18.5% for both thrust and torque predictions.

2.3.3 3D Blade Resolving RANS Simulations

In the field of RANS methods, various modelling approaches are available. These include blade-resolving approaches and virtual propeller model approaches. Virtual models, such as actuator disc or actuator line models, do not resolve the blade geometry but are useful for simulating interactions with other structures. However, for propeller performance modelling, only blade-resolving approaches can be used.

The commercial CFD RANS solver Simcenter STAR-CCM+ offers several blade-resolving propeller modelling approaches. The following paragraphs describe these strategies in order of increasing simulation effort.

1. Moving reference frame (MRF) with defined interfaces
2. Moving reference frame with periodic boundaries (Periodic MRF)
3. Rigid body motion (RBM) with defined interfaces
4. Overset mesh with overlaying meshes

In general, RANS simulations can be conducted as time-dependent (unsteady) or time-independent (steady) simulations. Operating conditions with detached flow require time-dependent simulations, as discussed in section 2.3.2.1. In contrast, for attached flow, stationary simulations can be performed if the chosen modelling approach supports them. For a rotating propeller with mesh motion, a time-dependent simulation is required, even if the flow is mainly attached.

As outlined in the introduction of chapter 2, this section focuses on the most commonly used approaches. Other methods, such as morphing mesh or multi-fidelity approaches, exist but are of less relevance for propeller performance modelling.

The MRF technique requires two mesh domains. One domain is static, while the other is rotating. The mesh domains are connected by interfaces. Within the rotating mesh domain, the airflow rotates around the propeller, defined by a rotating coordinate system. Therefore the mesh domain does not move, and as a result, no unsteady simulation is required. Information from the moving reference frame domain is transported cell-by-cell across the mesh interface between the rotating and non-rotating regions. A steady simulation approach reduces computational effort but does not resolve unsteady effects. This procedure enables steady-state simulations, significantly reducing computational costs. A more comprehensive review of RANS and URANS propeller simulations is provided in Ref. [7].

The drawback of this method is that helical slipstream velocity information becomes smeared across the interfaces. As a result, this simulation technique cannot model any kind of interactions, and the wake in the non-rotating domain is not accurately represented. However, the MRF approach can also be solved using a time-marching simulation method, which is required in cases of severe flow separation on the propeller blade.

The MRF technique simplifies the problem of propeller performance modelling significantly by reducing it to stationary flow conditions. Additionally, it can be further simplified by utilising the axial symmetries of the propeller through the use of so-called periodic boundaries. In this approach, a sector (or "piece of cake") is extracted from the rotating moving reference frame. This results in two cut surfaces between one blade and the neighbouring blade. These cut surfaces (or interfaces) are linked in such a way that the flow entering one interface exits the other in the same manner. This approach significantly reduces the mesh domain's size.

The sliding mesh technique with rigid body motion (RBM) is used to simulate the real motion of the rotating mesh domain. As with the MRF technique, a part of the flow domain around the propeller is separated. However, unlike MRF, this part performs a mesh motion, requiring a time-marching unsteady simulation approach. For each time step, new interpolation between the rotating and non-rotating domains is necessary. This interpolation is not necessary in the MRF approach, as the cell dependencies are already defined.

The advantage of the RBM over the MRF method is that information are not smeared across the interfaces. As a result, the propeller wake is transported into the non-rotating flow domain without loss of information.

Alternatively, an overset mesh technique (also known as the Chimera approach) can be used instead of the sliding mesh technique. While the sliding mesh approach relies on defined interfaces at specific surfaces, the overset mesh utilises a background mesh combined with a local mesh surrounding the propeller. Information is exchanged through overlapping volumina, enabling the transfer of flow quantities between the non-rotating and rotating domains without relying on predefined interfaces. At each time step, new overlapping volumina are calculated, enabling the seamless exchange of information between the non-rotating and rotating regions.

Tab. 2.1 provides a comparison of these CFD RANS methods against each other. It compares simulation results for a single operating point, including the required computational effort. The computational effort depends on the number of cells, the number of iterations, and the time required per iteration step. Time-resolving schemes, which capture the propeller wake dynamics, require significantly more iterations compared to steady approaches, as the wake must develop.

The four-bladed reference propeller operates at a rotational speed of 3500 rpm with a free-stream velocity of 21.55 m/s, corresponding to an advance ratio of $J = 0.5$ under standard conditions. The aerodynamic performance is presented in absolute values.

As shown in Tab. 2.1, the MRF approach predicts the highest thrust. The periodic approach predicts slightly less thrust compared to the MRF approach, but with slightly higher torque. Both the sliding mesh and overset mesh approaches predict the same mean thrust.

The RANS simulations were conducted on a workstation with 265 GB RAM and 128 AMD EPYC Rome CPU cores, using Simcenter STAR-CCM+ Version 2306. The time per iteration depends on the available computational power.

Appendix B provides details on the physical settings for all four simulation approaches, along with additional insights into the mesh domains and mesh independence studies. The base mesh size for all simulations is equivalent to that of the MRF approach, ensuring consistent spatial discretisation and minimising discretisation errors.

Table 2.1: Overview about blade resolving 3D RANS methods

		MRF	**Periodic MRF**	**RBM**	**Overset mesh**
Steady		Yes	Yes	No	No
Wake interactions		No	No	Yes	Yes
Req. Cells	(mio.)	60	49	52	39
Iteration time	(s)	32	30	29	18
Req. iterations	(k)	3	4	18	18
Req. time	(h)	27	33	145	90
Pred. thrust	(N)	11.87	10.60	10.50	10.25
Pred. torque	(Nm)	3.28	3.33	3.49	3.532

Fig. 2.23 shows the vorticity in the propeller plane for all four modelling approaches. Mathematically, as stated in eq. (2.57), vorticity is the curl of the flow, indicating where turbulence and vortices are generated:

$$vorticity = \nabla \times v \tag{2.57}$$

The vorticity is presented on a logarithmic scale in fig. 2.23.

The results of all four simulation approaches are combined by extracting one quarter of each simulation and rejoining the sections into a composite image. For the periodic simulation, only one quarter of the propeller was simulated. The left section represents the MRF results, the upper section shows the periodic MRF results, the right section represents the RBM results, and the lower section shows the overset mesh results.

In all four diagrams, the vorticity within the propeller radius is significantly increased. However, the MRF and RBM approaches exhibit additional vorticity generation within the moving frame but outside the propeller radius. The diagrams clearly show the tip vortex leaving the blade tip with high vorticity, which decreases as the vortex travels further before interacting with the next blade. Increased vorticity is also observed along the blades, though these vorticity sheets disappear from the evaluation plane as they move downstream.

The comparison reveals that increased modelling effort leads to increased vortex generation. The periodic MRF approach, which requires the highest modelling effort, shows significant interactions at the periodic boundaries and the static/rotating MRF boundary. In the standard MRF simulation, these static/rotating MRF boundary interactions are reduced compared to the periodic MRF approach. This artificial vorticity generation is further reduced in the RBM approach but still persists. Only the overset mesh approach shows no significant artificial vorticity production.

The results within the propeller disk are similar across all four approaches. A comparison of the MRF approaches with and without periodic boundaries shows no significant differences. However, the RBM and overset mesh simulations exhibit significantly lower blade vortex interactions[2]. The tip vortex in the overset mesh simulation is the smallest, resulting in reduced interactions. Furthermore, the vorticity along the blade is lower compared to the other three simulation approaches.

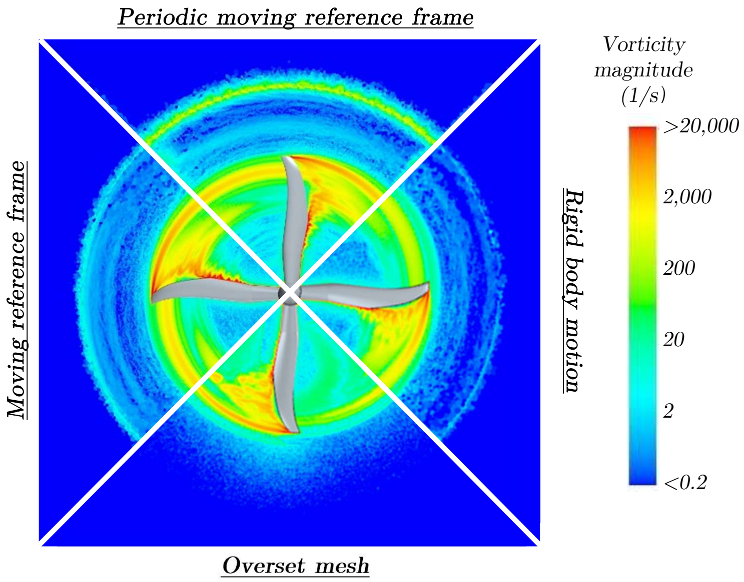

Figure 2.23: Comparison of vorticity in the propeller plane for the RANS approaches in hover conditions

While table 2.1 presents the results for a single operating point, fig. 2.24 shows the results across different advance ratios. As for each unsteady simulation only three operating points are simulated, the points are not connected by a line. The MRF simulation is represented in the black solid line, while the period simulation is displayed in the magenta dashed dotted line. The RBM simulation is displayed with triangles and the overset mesh simulation with diamonds. The RBM and overset simulations fit together perfectly, which is why they cannot be differentiated in the diagram.

---

[2] Blade vortex interactions are visible in front of the blades in each quarter section.

The comparison reveals that the MRF and the periodic MRF approach predicts a similar performance. Thrust and torque of the periodic approach is slightly lower compared to the standard MRF approach.

As the unsteady simulation approaches consider time-dependent results, error bars must be shown. The time-dependent flow separation cannot be accurately captured with a steady approach, which is why error bars are not shown for the MRF approaches. The error bars represent the fluctuations over the last two revolutions of the propeller. However, fig. 2.24 shows that the error bars are negligible.

The RBM and overset mesh simulations align perfectly. At an advance ratio of 0.1, the thrust predictions from the unsteady approaches are significantly higher compared to the steady approaches. With the increased thrust, the torque also increases. At an advance ratio of 0.5, the thrust prediction of all simulations matches, but the torque of the unsteady approaches remains higher.

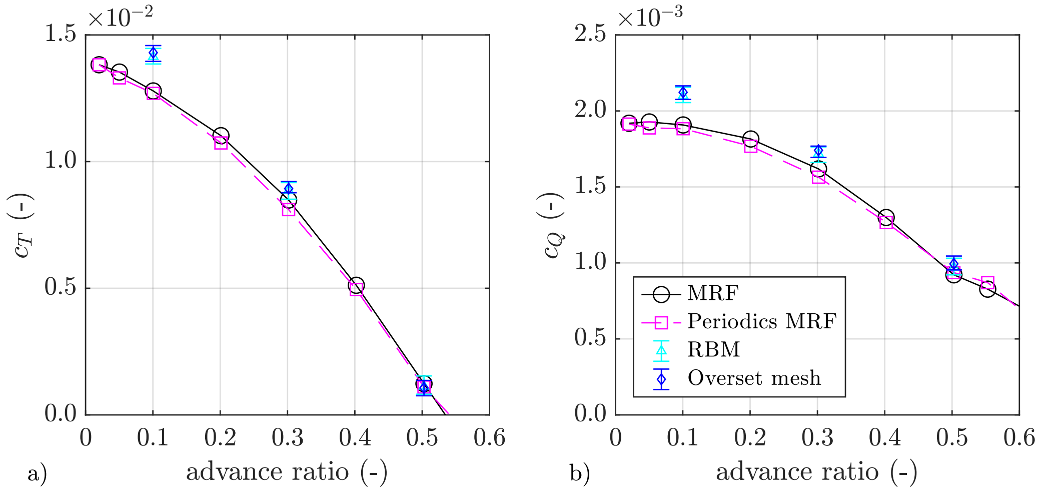

Figure 2.24: Performance predictions of the four-bladed reference propeller with different CFD RANS methods

The comparison of the different RANS models shows overall good agreement among the approaches. The MRF approach without periodic boundaries demonstrates its validity compared to the other simulation methods. It is at least three times faster than the overset mesh approach, making it the method of choice for the following comparisons.

2.4 Aerodynamic Validation of Performance Prediction Methodology

Finally the aerodynamic prediction methodology with the BEMT model is compared to results of the RANS prediction and aerodynamic data from the wind tunnel experiments. At first, the conducted wind tunnel experiments are described, before in a second step, the numerical results are compared to the experimental results.

2.4.1 Wind Tunnel Experiments

The wind tunnel experiments are conducted in the wind tunnel at FH Aachen University of Applied Sciences. The Eiffel-type wind tunnel has been aerodynamically analysed in conceptual studies to determine the operating limits of propellers and their impact on the wind tunnel [77]. These studies are crucial, as standard correction methods cannot be directly applied to this wind tunnel [16, 36, 55].

The facility is an open-circuit, free-jet, subsonic wind tunnel. The jet exhausts into a depression camber, with a measured circuit length of 4.1 m. The wind tunnel is powered by two fans located downstream of the test section, each with a power of 45 kW. This configuration allows for a maximum nozzle velocity of approximately 40 m/s. The polygonal nozzle has a total surface area of 2.2 m^2, with a maximum vertical extent of 1.4 m and a maximum horizontal extent of 2 m.

The studies in Ref. [77] conclude that the reference propeller can operate as a four-bladed propeller at a maximum rotational speed of 4500 rpm within the wind tunnel. This decision was based on maintaining a minimum core-jet to blade-tip distance of 10 cm, as evaluated using RANS simulations. As stated in Ref. [77], a propeller with a diameter of 80 cm can operate at 10.3 m/s, producing a thrust of 130 N. The tip clearance between the propeller and the core jet for the reference propeller is ensured at 16 cm at a wind speed of 10.3 m/s.

The propeller is mounted on a sting. A six-degrees of freedom (DoF) force balance is positioned at the tip of the sting, between the sting and the electric motor, which drives the propeller. The electric motor is a brushless outer-runner (Q-100-38-7 48V), controlled by the SPIN 200 Pro Opt electronic speed controller (ESC).

Fig. 2.25 presents an image of the experimental setup within the wind tunnel. Spacers are installed between the electric motor and the force balance to facilitate cooling. The six-DoF force balance (K6D80 500N/20Nm/MP11) features an accuracy class of 0.2% for a nominal force of 500 N and a nominal torque of 20 Nm. This results in error bands of 1 N in the forces and 0.04 Nm in the moments.

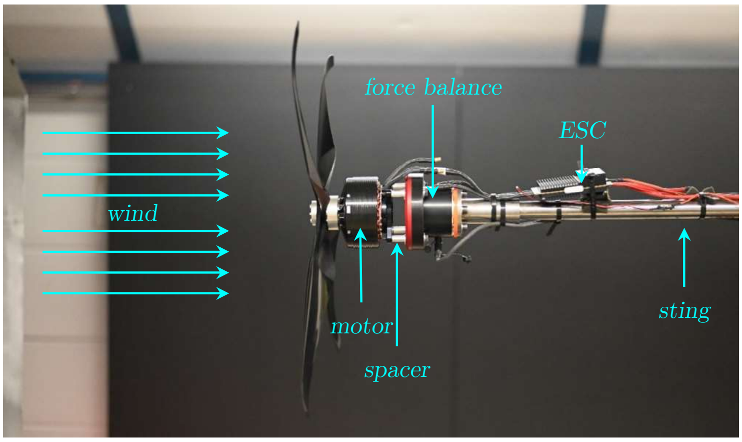

Figure 2.25: Picture of the experimental setup

The force balance operates with a sampling frequency of 12.5 kHz. The experimental data are processed using a low-pass and a band-pass filter to remove measurement noise originating from the motor, the electronic speed controller, and the wind tunnel.

To ensure high-quality data, the experiments are repeated three times under varying atmospheric conditions, with the setup disassembled and reassembled between runs to avoid systematic errors. The comparison of the different measurement series is presented in appendix C. This comparison demonstrates that the experimental data are consistent, with repeatability confirmed and error bars of negligible magnitude. The measurement accuracy of the force balance is also negligible. As a result, no error bars are included in the experimental results.

Since the wind tunnel lacks an air-conditioning system, the test results depend on the prevailing atmospheric conditions. The final experimental results are obtained under the following atmospheric conditions:

- Atmospheric temperature: $T = 299.0 \quad K$
- Atmospheric pressure: $p = 984.1 \quad hPa$
- Atmospheric density: $\rho = 1.148 \quad kg/m^3$

For a comparison of absolute thrust (N) and torque (Nm), the atmospheric conditions of the wind tunnel experiment must be considered. Alternatively, dimensionless parameters such as the thrust and torque coefficient as functions of the advance ratio can be compared. However, under hover conditions, where different rotational speeds are analysed, these dimensionless coefficients are not applicable.

Fig. 2.26 illustrates the thrust and torque of the two-, three-, and four-bladed propellers under wind-off conditions as functions of rotational speed. Wind-off conditions indicate that the wind tunnel is turned off, but the propeller remains positioned inside the wind tunnel and drives the airflow. Under these conditions, the highest resulting wind tunnel speed stays below 4 m/s. Diagram a) presents the thrust, while diagram b) displays the torque for the three propeller configurations. The advance ratio is assumed to be zero, even if the propellers operate inside the wind tunnel under wind-off conditions.

The rotational speed is varied from 1000 rpm to 3500 rpm for the four-bladed propeller and up to 4000 rpm for the two-bladed propeller. The difference in maximum rotational speeds arises from the power limitations of the electric motor and the ESC.

Diagram a) reveals that thrust increases with both the number of blades and the rotational speed. At 3500 rpm, the two-bladed propeller generates a thrust of 87 N, while the four-bladed propeller produces 132 N. Delivering 110 N of thrust, the three-bladed propeller lies between the two-bladed and four-bladed configurations, exceeding the former by 23 N and falling short of the latter by 22 N Over the full range of rotational speeds, the four-bladed propeller generates approximately 50% more thrust compared to the two-bladed propeller.

Diagram b) shows that torque increases with both rotational speed and blade number, following the trend of the thrust curves. However, torque is increased by approximately 90% from the two-bladed to the four-bladed configuration, while thrust increases by approximately 50%.

This increase is primarily due to the higher thrust. Greater thrust values lead to higher induced velocities, which, in turn, result in larger helix angles ϕ. With larger helix angles, the lift vectors of each 2D airfoils tilt more towards the plane of rotation, thereby increasing the torque generated by the lift. Even though c_l and c_d decrease because the higher induced velocity reduces the AoA, the tangential force increases.

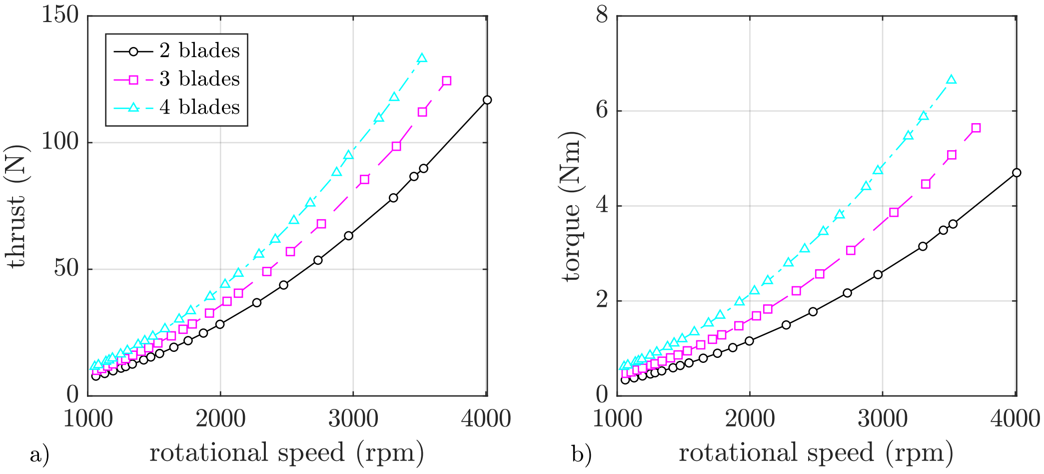

Figure 2.26: Measured performance of the 2, 3 and 4-bladed propeller in hover conditions

Fig. 2.27 illustrates the thrust and torque characteristics at different advance ratios. Diagram a) depicts c_T, while diagram b) shows c_Q. The experiments are conducted at the maximum achievable rotational speed for all propellers of 3500rpm. Due to the dimensionless representation, these results are valid across a range of rotational speeds, provided compressibility effects and Reynolds number changes remain small.

The experiments begin at the lowest feasible advance ratio within the wind tunnel. An advance ratio of zero cannot be achieved, as the propeller produces a self-induced flow under wind-off conditions within the wind tunnel. As the advance ratio increases, both c_T and c_Q decrease.

Diagram a) shows that all three propellers exhibit a zero-thrust crossing at $J = 0.55$. Thus, the number of blades does not affect the maximum achievable flight speed. The observed thrust difference of approximately 50% between the two- and four-bladed propellers under wind-off conditions, as well as the torque increase of about 90%, remains consistent at higher advance ratios.

Diagram b) reveals that the torque curve flattens with increasing advance ratio. At the zero-thrust condition, the c_Q value is 0.4×10^{-3} for the two-bladed propeller and 0.8×10^{-3} for the four-bladed propeller.

Extrapolation of the c_Q curve towards higher advance ratios predicts a zero crossing at $J = 0.7$. This zero-crossing is referred to as the windmilling condition, where the propeller operates without consuming power and is instead driven by the incoming airflow. However, under these conditions, the propeller generates a significant amount of negative thrust.

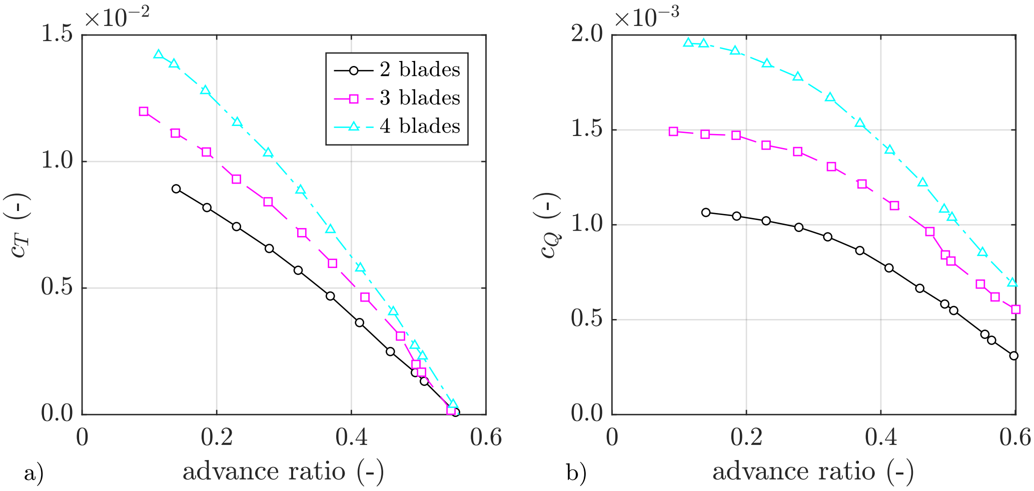

Figure 2.27: Measured performance of the reference propellers at different advance ratios

The comparison of thrust and torque indicates that doubling the blade number significantly reduces the thrust-to-torque ratio. However, the effect on the figure of merit (FoM) in hover conditions or the propulsive efficiency (η) cannot be directly derived. To address this, fig. 2.28 presents the hover efficiency as the FoM in diagram a) and the propulsive efficiency in diagram b).

Diagram a) shows that the FoM drops significantly at low rotational speeds. For the three- and four-bladed propellers, the FoM stabilises at a rotational speed of 1500 rpm. Following a steep increase from 1000 to 1500 rpm, the curve flattens but continues to rise gradually. The FoM of the three-bladed propeller is approximately 1% higher than that of the four-bladed propeller.

The two-bladed propeller exhibits distinct behaviour compared to the other propellers. Between 1000 and 1800 rpm, the FoM of the two-bladed propeller matches that of the four-bladed propeller. Beyond 1800 rpm, however, the FoM of the two-bladed propeller increases significantly more than the others. Up to 2800 rpm, the three-bladed propeller demonstrates the highest FoM, but above this rotational speed, the two-bladed propeller overtakes.

Diagram b) reveals that increasing the blade number decreases η. The peak efficiency of the two-bladed propeller is 8% higher than that of the four-bladed propeller. The three-bladed propeller's peak efficiency is 5% lower than the two-bladed propeller's. The absolute efficiency difference depends on the advance ratio and diminishes at both low and high advance ratios.

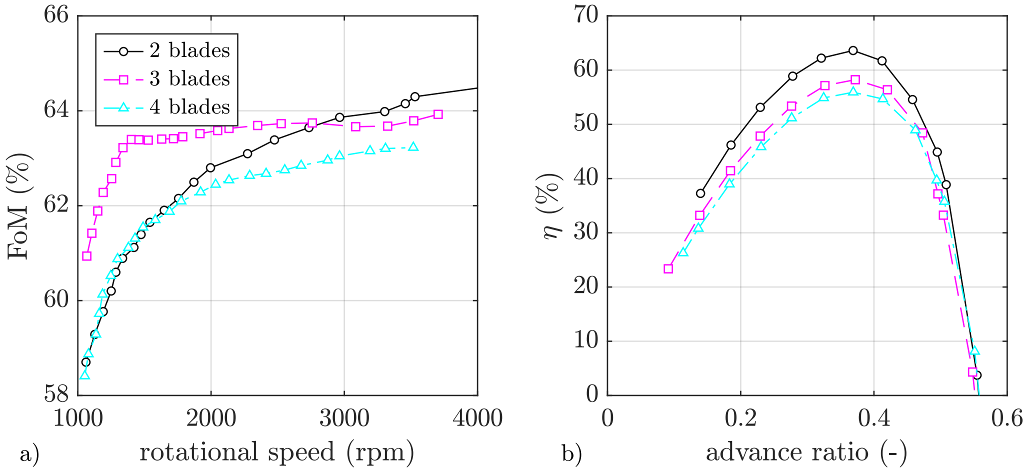

Figure 2.28: Measured static and propulsive efficiency of the reference propellers

The comparison of the efficiency measures reveals a different relationship compared to the thrust-to-torque ratio. While the thrust-to-torque ratio decreases by approximately 30% when moving from the two- to the four-bladed propeller, the efficiency measures show only a slight decrease.

However, these curves cannot be directly compared, as the design point is defined by both a thrust requirement and a flight speed requirement. As a result, the presented curves cannot be used to evaluate the propeller's performance at a specific operating point, where thrust and flight speed must align.

2.4.2 Comparison of Wind Tunnel Experiments and Performance Prediction

For the aerodynamic validation of the described procedure, the three propellers are evaluated using the reduced-order BEMT method. Additionally, the four-bladed propeller is analysed at various advance ratios to demonstrate its accuracy.

The performance predictions are carried out using the BEMT method with the following settings:

- Atmospheric conditions from wind tunnel experiments

- General momentum theory
- 3D stall model correction
- Without tip and hub loss correction method
- With sweep correction method

Hub and tip loss correction method is not used because of the forward swept geometry and therefore an increased tip loading.

Fig. 2.29 and 2.30 present the comparison of the two-, three-, and four-bladed propellers between wind tunnel experiments (WT) and BEMT simulations. Fig. 2.29 depicts the rotational speed variation under wind-off conditions, while fig. 2.30 illustrates the advance ratio sweep.

Diagram a) of fig. 2.29 compares the dimensional thrust, and diagram b) compares the dimensional torque. The lines without markers represent BEMT results computed at rotational speed intervals of 50 rpm, whereas the lines with markers correspond to the wind tunnel results, as shown in fig. 2.26.

Since the propeller operates inside the wind tunnel, the BEMT results are adjusted to account for the lowest possible advance ratios of the propellers by modifying the inflow velocity. The comparison in both figures demonstrates an excellent agreement between BEMT simulations and experimental results.

The thrust and torque predictions from the BEMT simulations are within 5% of the experimental data. In diagram a), the two-bladed propeller's thrust is slightly underpredicted, whereas the thrust of the four-bladed propeller is marginally overpredicted. In diagram b), the torque prediction aligns well for the three- and four-bladed configurations, but shows a slight discrepancy for the two-bladed configuration.

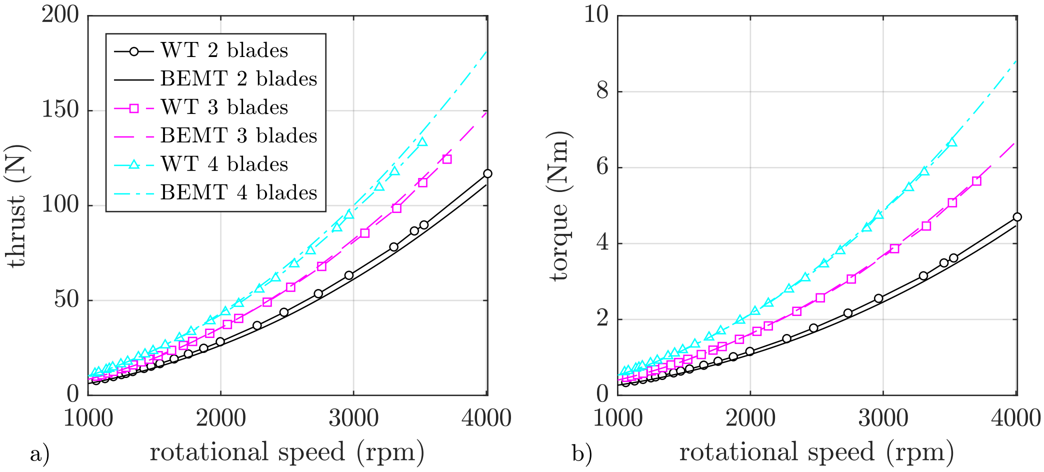

Figure 2.29: Performance comparison between the BEMT simulation and experimental data at static conditions

Fig. 2.30 presents the comparison of the predicted and experimental data over the advance ratio. The colour scheme from fig. 2.29 is applied to these diagrams, with the experimental data corresponding to fig. 2.27.

The comparison indicates that the relative error in thrust prediction is below 5%. However, the relative error in torque prediction increases to a maximum of 10%. The results show that torque tends to be underpredicted, while thrust is either overestimated or underpredicted, depending on the advance ratio.

The BEMT predictions exhibit straighter curves compared to the experimental data in both diagrams. This difference is particularly evident in the torque curves of diagram b), where the experimental data show significantly more curvature than the BEMT simulation results. Furthermore, the experimental torque measurements flatten after the zero-crossing of the thrust, a behaviour not captured by the BEMT simulations.

The analysis in 2.3.1.4 and 2.3.2.4 highlights that the BEMT results can vary significantly depending on the simulation approach. The highest thrust and torque predictions are obtained using the simple momentum theory (SMT) without corrections or stall modelling. In contrast, the lowest thrust and torque predictions result from the general momentum theory (GMT) with 3D stall modelling, as well as tip, hub, and sweep corrections. When most corrections are applied, the overall agreement between the simulation and experimental results becomes excellent.

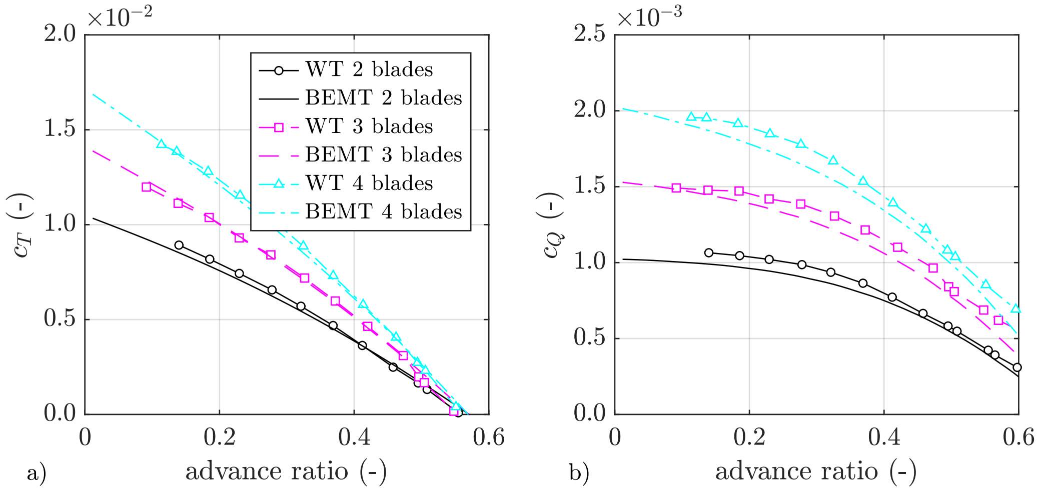

Figure 2.30: Performance comparison between BEMT simulation and experimental data at different advance ratios

The final step in the validation process involves comparing the BEMT results with the moving reference frame RANS (MRF RANS) simulations and experimental data. To minimise computational effort, this comparison is performed only for the four-bladed propeller.

As in fig. 2.30, an advance ratio sweep is analysed, with thrust predictions shown in diagram a) and torque predictions in diagram b). The black line represents the four-bladed wind tunnel results, the magenta dashed line represents the BEMT results, and the cyan dotted-dashed line represents the MRF RANS simulations, with each marker indicating a simulation result.

Diagram a) shows that the MRF RANS simulations' thrust prediction is significantly lower than the experimental and BEMT results. The relative error is approximately 10%. Compared to the BEMT simulation, the MRF RANS curve exhibits greater curvature, aligning better with the experimental data, even though the overall offset is noticeably larger.

In diagram b), the torque prediction error for the MRF RANS simulation is also about 10%, placing it within the same error band as the BEMT prediction. However, the trend in the RANS prediction matches the experimental data more closely than the BEMT prediction. Notably, the kink in the torque prediction at the thrust's zero crossing, observed in the experimental data, is captured in the RANS simulations. Since the thrust's zero crossing occurs at a lower advance ratio in the RANS prediction, the kink appears more pronounced.

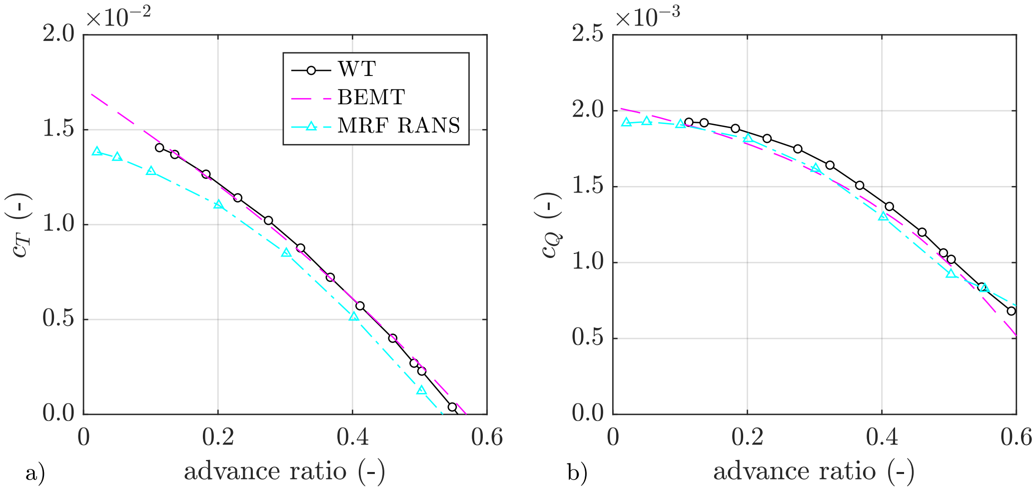

Figure 2.31: Performance comparison between BEMT prediction, MRF RANS prediction and the experiment at different advance ratios for the four-bladed propeller

With the comparison of the wind tunnel data against the BEMT and RANS simulations, the aerodynamic validation is complete. During the acoustic validation in section 3.3, additional geometries are subjected to aerodynamic analysis. This aerodynamic analysis consistently serves as the initial step in the aeroacoustic assessment.

Following the detailed investigation into the mode of action of the presented BEMT procedure, the first research question can be concluded.

RQ 1 - How applicable are reduced order aerodynamic simulation methods for electrically driven GA and AAM propellers in conceptual design?
An advanced general momentum BEMT solver, incorporating corrections for 3D stall characteristics based on 2D XFOIL predictions, a sweep correction model, as well as a root and tip loss corrections can predict the thrust and torque of a propeller under hover and forward flight conditions within 10% accuracy when compared to experimental data and CFD RANS simula-

tions of free-spinning propellers. The BEMT solver demonstrates this level of accuracy across multiple operating points and for two-, three-, and four-bladed propellers. Each operating point is simulated within a second, making the BEMT approach to the most suitable methods for the conceptual design and an MDO approach.

In this context, drag prediction is of less relevance for overall performance prediction, while accurate lift prediction is crucial. The application of the simple momentum theory leads to an overprediction of thrust and torque. Therefore, the general momentum theory should be used but it have to be derived for hover conditions instead of forward flight conditions. The application of root-and-tip loss correction depends on the propeller geometry and may not always be appropriate.

3 Propeller Acoustics

PROPELLER noise consists of tonal noise and broadband noise. During steady operations, broadband noise is primarily influenced by the boundary layer of the propeller, while tonal noise is mainly dominated by thickness and loading noise [131]. Broadband noise can be predicted using high-fidelity large-eddy simulations or advanced semi-analytical models [25, 99]. Details on broadband noise are provided in section 3.2. Tonal noise components can be estimated using reduced-order models [59].

Noise is the term for sound with negative connotation. Physical models employ various methods to predict the sound generated by the propeller, not its noise emissions. This sound must be converted into noise using psychoacoustic metrics, such as A-weighting or other psychoacoustic weightings. However, in general, propeller sound has a negative connotation, which is why it is referred to as propeller noise in this thesis.

Sound is a form of energy that travels through air or other media as waves, produced by fluctuations. The sound pressure level (SPL), commonly represented as L_p, is mathematically defined in eq. (3.1), where $\tilde{p}$ represents the sound pressure and p_0 denotes the reference sound pressure.

$$L_p = 20\log(\frac{\tilde{p}}{p_0}) = 10\log(\frac{\tilde{p}^2}{p_0^2}) \tag{3.1}$$

The doubling of sound pressure leads to an SPL increase of approximately 6 dB. Further explanations and the mathematical background are provided in appendix D.1.

The intensity of sound (L_I) is calculated using eq. (3.2), where o denotes the distance from the sound source to the observer. The sound power (L_W), expressed in eq. (3.3), is obtained by multiplying the sound intensity by the area A through which the sound propagates.

$$L_I = \frac{10^{(L_p/10)}}{4\pi o^2} \tag{3.2}$$

$$L_W = L_I \cdot A. \tag{3.3}$$

The Q-factor, which quantifies the change in sound power level, is defined in eq. (3.4). By substituting L_p into L_I and L_W, the relationship between the Q-factor and sound pressure is derived in eq. (3.4).

$$Q_S = 10 \cdot \log(\frac{L_{W,2}}{L_{W,1}}) = 10\log(\frac{\tilde{p}^2}{p_0^2}) \tag{3.4}$$

Eq. (3.4) shows that doubling the sound sources results in a Q-factor of 3 or a noise increase of 3 dB. Halving the sound sources results in a Q-factor of -3. However, the doubling factor of 3 is a physical quantity and is not related to human hearing. The present work does not focus on psychoacoustics. Nonetheless, human hearing must be considered in the optimisation of the propeller.

Most recent optimisation studies use no weighting [30, 31, 153] or the A-weighting [31, 66] as an acoustic metric for propeller noise calculation. None of these studies optimise the number of blades or the rotational speed of the propeller. As a result, no frequency shifts are expected, and frequency weighting is therefore not required.

Fig. 3.1 presents the weighting curves. All weighting functions have a zero-crossing at 1000 Hz because they are derived relative to this frequency. The weighting functions are based on empirical studies. The A-weighting shows a significant reduction in the low-frequency region, while the other weightings exhibit a less pronounced SPL reduction in this region.

Additionally, the A-weighting increases the SPL in the range between 1000 Hz and 6000 Hz. The B- and C-weightings reduce noise emissions in both low and high-frequency ranges. In the mid-frequency range, a plateau is present. The D-weighting applies noise penalties for frequencies around 5000 Hz. It was originally developed for aircraft noise but is no longer in use [131].

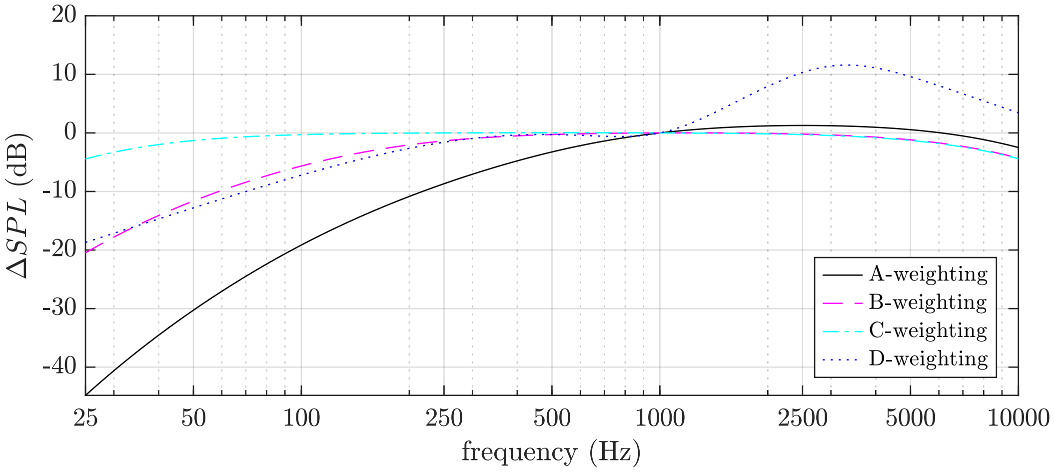

Figure 3.1: Acoustic weighting curves

When aerodynamic data are used to calculate the resulting pressure fluctuations in the air, the acoustic predictions are referred to as aeroacoustics. In the last century, many different aeroacoustic models have been developed to describe the noise emissions of propellers, fans, and jet engines. Gutin [69] developed the first reliable propeller noise prediction model in 1936. In the 1950s, significant progress in noise modelling was achieved through the acoustic wave analogy derived by Lighthill [100]. Many scientists applied this analogy to describe the noise emissions of moving surfaces such as propellers.

Ffowcs-Williams and Hawkings [45] developed the well-known FW-H equations. These equations describe noise radiation generated by arbitrary surface motions in a fluid with turbulent airflow. The FW-H equations require unsteady flow quantities as input, which are usually derived using URANS solvers. However, URANS simulations are time-consuming, particularly for rotating propellers. Simplifications have been developed by researchers such as Hanson [73] and Farassat [42].

Hanson simplified the FW-H equations for rotating propellers into a closed analytical form in the frequency domain. His formulation requires only section-wise distributed forces and velocities, typically calculated using a BEMT. Farassat's formulations use time-dependent surface pressures on the propeller as input, which are not typically provided by BEMT solvers. However, BEMT solvers can be coupled with Farassat's formulations by further simplifying the surface pressure.

Farassat's methods describe the SPL in the time domain, while Hanson's method operates in the frequency domain. The time-domain calculation allows the use of time-dependent aerodynamic input data. In contrast, frequency-domain calculations require steady results. Time-domain simulations are significantly more time-consuming than frequency-domain models. For time-domain calculations, the propeller revolution must be discretised with a resolution exceeding 520 steps per revolution. A discretisation study is presented in appendix D.3.

Both Hanson's and Farassat's models focus on calculating the tonal noise of the propeller. The rotational speed and the blade number (N_B) defines the harmonic frequency of the predicted tonal noise. Therefore, the blade passing frequency (BPF) is introduced in eq. (3.5)[1]. The tonal noise during steady operations is associated with the BPF and its higher harmonics. Other tonal frequencies can only be excited by unsteady aerodynamic effects.

$$BPF = f \cdot N_B \tag{3.5}$$

Next, the details of the relevant relations between velocities and geometry for noise predictions are described.

Fig. 3.2 depicts the orientation of the vectors and the coordinate system used for noise modelling in all subsequently presented methods. The observer position is shifted within the $x_{\text{propeller}} - z_{\text{propeller}}$ plane. The observer's location is described by the angle θ, which is measured between the rotational axis and the observer position.

The noise modelling based on the derivation of the FW-H equations relies on the movement of noise sources relative to the observer. Therefore, the approaches do not consider the movement of the air around the propeller. The depicted Mach numbers relate to the movement of the blade section rather than the air stream. The aerodynamic simulation provides the aerodynamic loading $\boldsymbol{F}_j$ of each blade section.

---

[1] The rotational speed is given as a frequency in Hz

The angle θ in fig. 3.2 is later used to describe the noise emissions around the propeller. It is therefore called the observer angle θ.

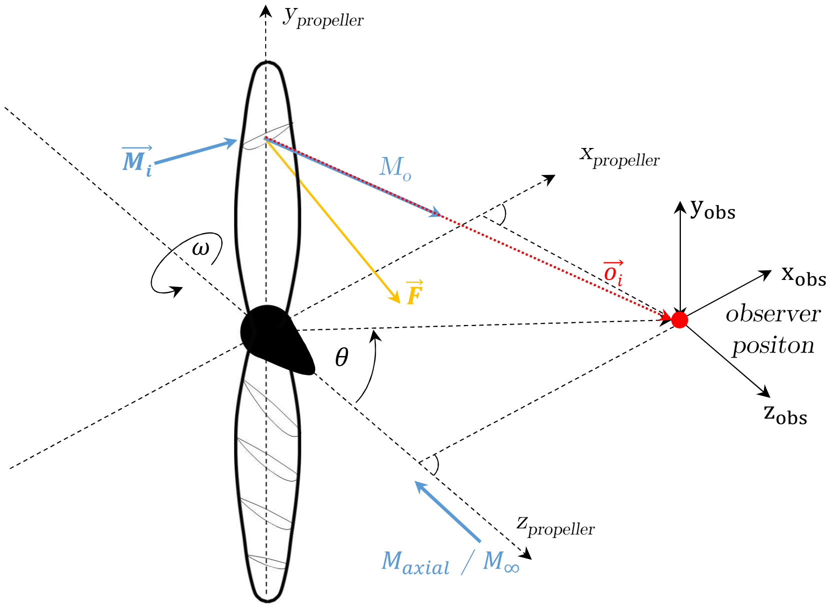

Figure 3.2: Relations of vector definitions and variables used in the acoustic models

Fig. 3.3 shows the principal noise directivity of different noise sources around the propeller. An observer moves at a constant distance from the propeller hub, following a semicircular path from upstream at 0° to downstream at 180°. The thrust vector points towards 0°. The noise directivity is displayed in polar coordinates, which are more illustrative than Cartesian coordinates. However, Cartesian coordinates provide greater precision for reading values compared to polar coordinates. Therefore, the following results are presented in Cartesian coordinates, while the results in fig. 3.3 are shown in polar coordinates.

Fig. 3.3 depicts the results for the four-bladed reference propeller operating at a rotational speed of 3500 rpm in hover conditions. The magnitude of the noise sources depends heavily on the operating conditions. Nevertheless, fig. 3.3 provides insights into the fundamental directivity behaviour of the noise sources.

The broadband noise exhibits a clear dipole characteristic around the propeller plane. Tonal thickness noise is typically modelled as a rotating line of monopoles, with the line rotating around the propeller axis. Tonal loading noise, on the other hand, is typically modelled as a rotating line of dipoles. The orientation of these dipoles depends on the surface normal and the loading vector $\vec{F}$ along the radius, as shown in fig. 3.2. As a result, the noise cancellation effect at 60° observer position in the tonal loading noise predictions varies with the operational state and propeller geometry.

Due to the symmetrical arrangement of the propeller blades around the propeller axis, tonal noise cancels out at the axis. This cancellation is known as positive interference. Positive interference occurs due to the phase shift between noise sources located on the propeller blades. Furthermore, this phenomenon restricts tonal noise models to observer positions near the propeller plane.

Broadband noise cannot vanish at the propeller axis, as surface fluctuations are stochastic. Broadband noise is typically modelled with a dipole characteristic, oriented 90° relative to the loading noise dipole. The dipole characteristics of the broadband noise model make it inappropriate for use in the plane of rotation.

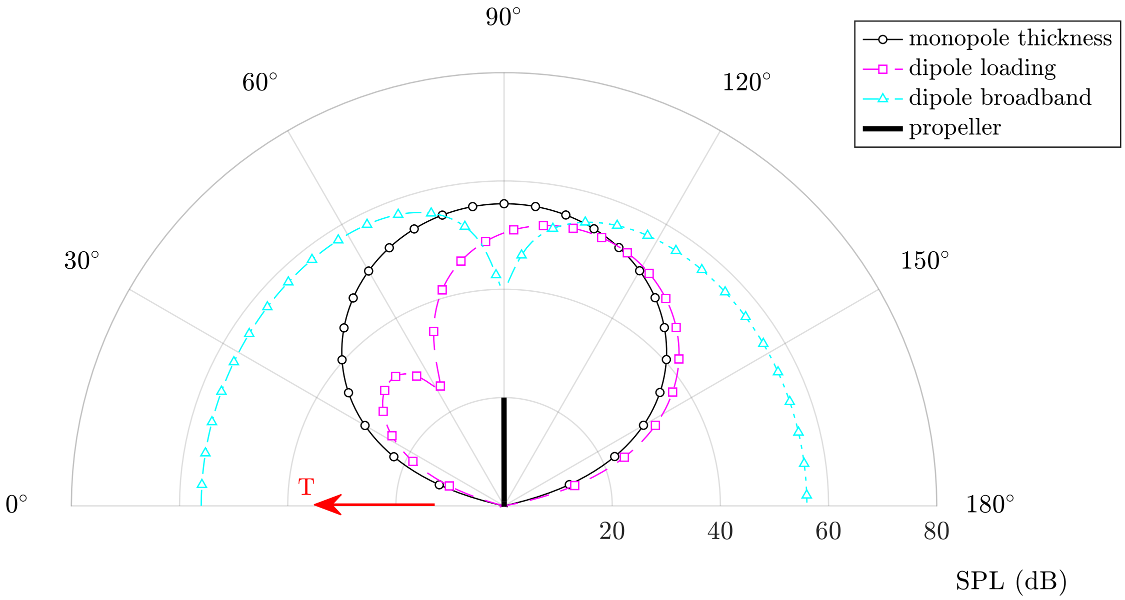

Figure 3.3: Pole characteristics of different noise sources for a four-bladed propeller in hover conditions

The following sections introduce three different tonal noise modelling approaches. First, section 3.1.1 describes a category one (Cat 1) model based on Gutin [69]. Second, section 3.1.2 outlines a category two (Cat 2) frequency-domain model developed by Hanson [73]. Third, section 3.1.3 presents another Cat 2 model in the time domain, derived from Farassat [42]. Fourth, different broadband noise modelling strategies are introduced.

Once all three models are described, section 3.3 validates Farassat's model, combined with the broadband model, using experimental data from the literature. Three independent studies with varying operational conditions and propellers are used for validation. Finally, the tonal noise models are assessed to determine whether the frequency-domain model or the Cat 1 model is suitable for predicting noise emissions within an optimisation routine. For this purpose, the models must demonstrate consistency in SPL prediction across different operational conditions, distances, and geometries.

3.1 Tonal Noise

As previously stated, tonal noise is typically modelled using sources located on the propeller blades. The strength of these sources depends on the aerodynamic excitation. However, the resulting sound pressure amplitudes are determined by the movement of the sources. This movement is purely a geometric relationship relative to the observer's position.

The Cat 1 model simplifies the aerodynamic excitation and reduces the noise emissions to a single noise source by empirical correlations. The Cat 2 models use the aerodynamic excitation to determine the strength of noise sources located along the blades and combine this with the movement of the sources. The following subsections describe these procedures in detail.

3.1.1 Gutin's Model

Gutin's model describes noise emissions as a single noise source located at the propeller hub. It is a Cat 1 model that employs empirical correlations to predict noise emissions. The sound pressure p of the harmonic order m primarily depends on the integrated thrust T and power consumption P. As Gutin's model operates in the frequency domain, the sound pressure is expressed using Fourier coefficients p_m instead of time-domain signals $\tilde{p}$. The geometry is defined by the propeller diameter D_P and the blade number N_B. The operating condition is characterised solely by the tip Mach number M_{tip}.

The observer's position is described by the observer-to-hub distance o_H and the angle θ, measured between the propeller axis and the vector pointing from the propeller hub to the observer. Using Bessel's functions (J_{mB}), the attenuation of higher harmonics due to noise cancellation effects is simulated. Gutin's model is expressed in eq. (3.6) and (3.7). All values must be input in SI units to calculate the sound pressure in pascals (Pa).

$$p_m = \frac{\pi m N_B M_{tip}}{o_H D_P \pi} \left[\frac{P}{981.18\ M_{tip}^2} - \frac{T}{4.448} \cos(\theta) \right] J_{mB}(x_G) \tag{3.6}$$

$$x_G = 0.8 \cdot M_{tip} \cdot m \cdot N_B \sin(\theta) \tag{3.7}$$

Gutin's model offers a simple way for fast noise calculations. However, it does not incorporate detailed information about the propeller geometry and is constrained by the use of Bessel's functions. These limitations restrict the model to a maximum of five propeller blades ($B < 5$), a maximum of six harmonics ($m < 6$), and blade tip Mach numbers within the range $0.3 < M_{tip} < 0.8$. Further details about this model can be found in Ref. [122]. Since this model does not account for blade geometry, it appears unsuitable for aeroacoustic optimisation, but this is examined in detail in section 3.4.

A better understanding of Gutin's model is achieved by evaluating Bessel's function, as shown in fig. 3.4. Fig. 3.4 depicts Bessel's function for different observer positions and arguments (x_G).

In this evaluation, the tip Mach number is set to 0.4, consistent with the reference case, which assumes a rotational speed of 3500 rpm. The propeller plane is located at 90°, with the left side representing the upstream region of the propeller and the right side representing the downstream region. The observer distance remains constant for all observer positions.

As Bessel's function is used to amplify the sound pressure, fig. 3.4 directly illustrates the characteristics of the sound pressure and, consequently, the noise emissions. However, Bessel's function is calculated only for each harmonic, as indicated by the white horizontal lines. A higher tip Mach number affects a greater number of harmonic lines. The colour plot is normalised to 1.

Fig. 3.4 shows a clear dipole characteristic, with a reduction in noise emissions towards the propeller axis. In the propeller plane, the noise emissions are highest, and the higher harmonics, in particular, decrease as they approach the propeller axis.

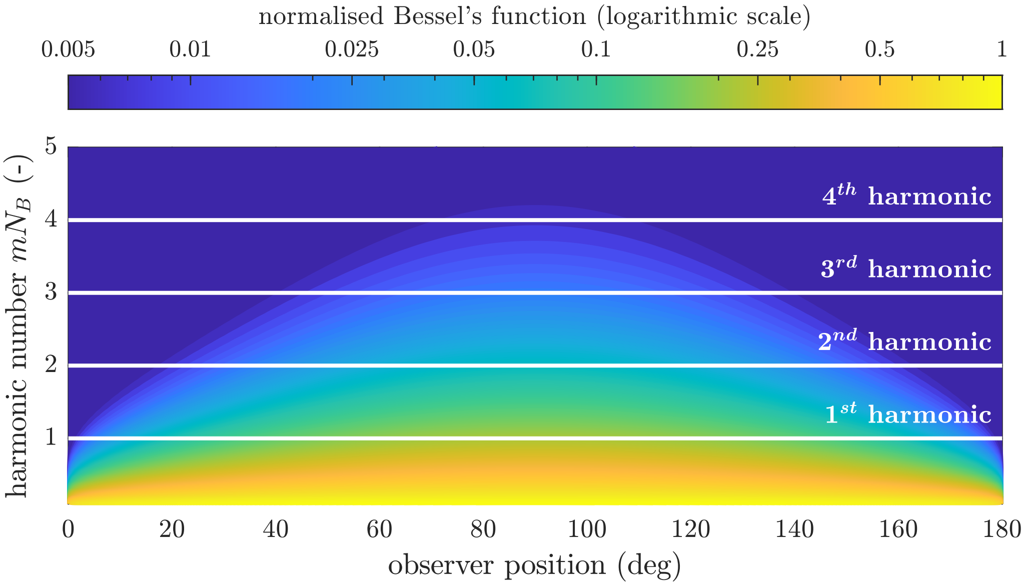

Figure 3.4: Normalised Bessel's function for a tip Mach number of 0.4

The model description reveals that neither the blade geometry nor the loading distribution are included as parameters. Only integrated performance parameters (thrust T, power P), global propeller parameters (blade count N_B, diameter D_P), and the rotational speed via the blade tip Mach number M_{tip} are used in the prediction. Therefore, the model is likely unsuitable for blade shape optimisation. The prediction accuracy of the tonal SPL is assessed in section 3.4.

3.1.2 Hanson's Model

Hanson's model is derived from the FW-H equation. It simplifies the description of motion by replacing the time-domain representation with a frequency-domain representation, taking advantage of the periodic nature of rotating motions. As a result, noise emissions are calculated in the frequency domain, similar to Gutin's model [73, 75]. Consequently, some parameters from Gutin's model are also present in Hanson's model. Hanson's model is classified as a Cat 2 model because it describes the physical behaviour of the blade and does not depend on empirical relations.

Hanson's model as stated in eq. (3.9) uses the introduced line sources to model noise emissions, which requires detailed blade parameters. The derivation of the model requires linearisation of the FW-H equations, enabling the decomposition of the equation into different noise sources. It describes the noise generated by the acting forces, lift l and drag d, as well as the displacement or thickness thi noise of each blade element. The lift and drag forces are replaced by their coefficients, c_l and c_d. The thickness noise is affected by the non-dimensional thickness of the airfoils t_b. By integrating along the non-dimensional propeller radius r_n, the resulting sound pressure in the frequency domain is calculated. The Fourier coefficients of the sound pressure for the three noise components (thi, l, and d) are summed according to eq. (3.8).

$$p_m = p_{m,thi} + p_{m,l} + p_{m,d} \tag{3.8}$$

Eq. (3.9) is derived from the far-field equations, as described in Ref. [76]. The far-field simplyfication reduces the computational effort. Far-field equations are used because the analysed observer distances are multiples of the propeller diameter. Further explaination are provided below.

$$\begin{bmatrix} p_{m,thi} \\ p_{m,l} \\ p_{m,d} \end{bmatrix} = Dop \cdot \frac{\rho_0 c_\infty^2 N_b \sin(\theta_{ret}) \exp[imN_b(\frac{\omega_{D_P} r}{c_\infty} - \frac{\pi}{2})]}{8\pi \frac{r_H}{D_P}} \cdot \int_{\text{hub}}^{\text{tip}} M_i^2 \exp[i(\Phi_0 - \Phi_S)] J_{mN_b}(x_G) \begin{bmatrix} -k_x^2 t_b \Psi_{thi}(k_x) \\ i k_y^2 \frac{c_l}{2} \Psi_l(k_x) \\ -i k_x^2 \frac{c_d}{2} \Psi_d(k_x) \end{bmatrix} dr_n \tag{3.9}$$

The index tip denotes the tip, while the index ret represents the retarded time or observer position. Due to the finite propagation speed of sound (the speed of sound (c_∞)), the visual position and the audible position do not coincide. This mismatch is accounted for by the retarded time or observer position, as stated in eq. (3.10).

$$\cos(\theta_{ret}) = \cos(\theta)\sqrt{1 - M_\infty^2 \sin^2(\theta)} + M_\infty \sin^2(\theta) \tag{3.10}$$

The local Mach number is indicated by the subscript i, representing the resulting speed of the element i normalised by the speed of sound in the surrounding environment. In addition to the local Mach number M_i, the tip Mach number M_{tip} and the flight Mach number M_∞ are also relevant for the calculation. The relationships are depicted in fig. 3.2.

Furthermore, the Doppler effect is considered as described in eq. (3.11). However, in a wind tunnel application without translational motion of the propeller, the Doppler effect is not relevant because the flight Mach number is zero.

$$Dop = \frac{1}{1 - M_{\infty}\cos(\theta_{ret})} \tag{3.11}$$

The retarded observer angle θ_{ret} can be determined using eq. (3.10). Similar to the Doppler effect, the retarded observer angle remains constant under test bench conditions.

Fig. 3.5 depicts the Doppler factor for various observer positions and Mach numbers. The factor equals one under hover conditions or in wind tunnel applications, indicating that noise emissions are not affected. The figure also shows the line where the Doppler factor is equal to one.

As the Mach number increases, this "1-line" shifts from the propeller plane downstream towards higher observer angles. At higher Mach numbers, the Doppler effect has a greater influence on noise emissions, meaning the Doppler factor deviates more significantly from one. The factor reaches its maximum upstream of the propeller and its minimum downstream of the propeller plane. Since the observer angle is measured from the propeller's perspective, smaller angles correspond to positions upstream of the propeller, whereas larger angles lie downstream. Therefore, fig. 3.5 shows that noise levels are highest when an aircraft is approaching the observer, fall as it passes overhead, and continue to decrease as it moves away.

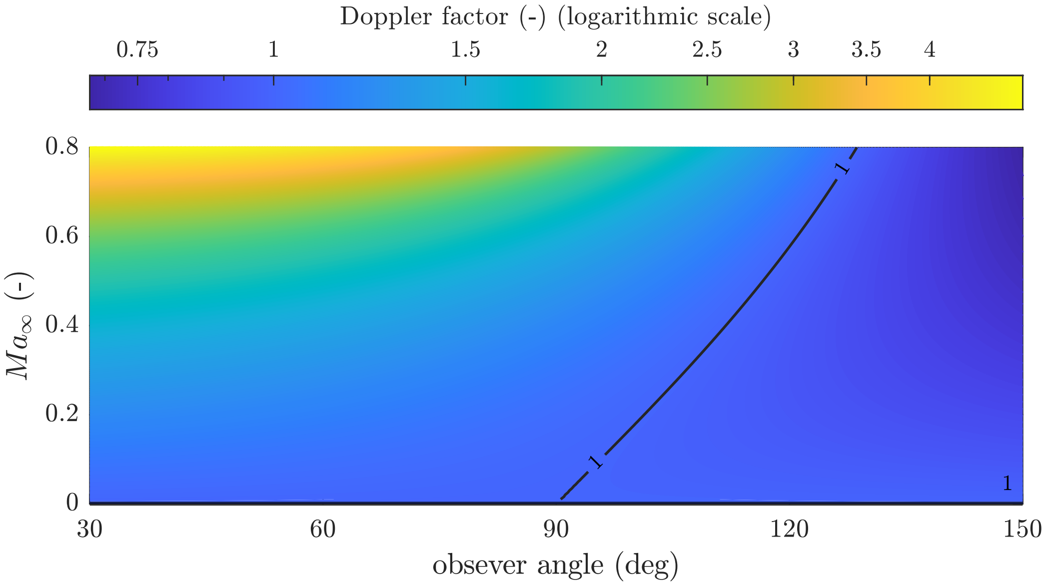

Figure 3.5: Contour plot of Doppler factor for different observer positions and Mach numbers

Hanson applies Bessel's function similarly to Gutin, but with a slightly modified argument as shown in eq. (3.12). Eq. (3.12) includes a Doppler correction and depends on the blade section, whereas Gutin's Bessel argument only depends on the hub motion, as described in eq. (3.7).

$$x_H = Dop \cdot r_n M_{tip} \cdot m \cdot N_B \sin(\theta_{ret}) \tag{3.12}$$

The acoustic wave numbers in the x- and y-directions are calculated using eq. (3.13). These wave numbers, k_x and k_y, describe how the blade-induced disturbance varies spatially. k_x represents wave propagation in the axial direction, while k_y represents wave propagation in the radial direction. The ratio of chord length to local diameter, $b_c = \frac{c}{2 \cdot r}$, influences the local wave numbers.

$$\begin{bmatrix} k_x \\ k_y \end{bmatrix} = Dop \cdot \frac{2mN_b}{M_i} \cdot b_c \begin{bmatrix} M_{tip} \\ \frac{1}{r_n}(M_i \cos(\theta_{ret}) - M_\infty) \end{bmatrix} \tag{3.13}$$

Propeller sweep and lean influence the phase shift of noise emissions from the propeller sections. This influence is accounted for by the phase alignment factors presented in eq. (3.14). The mid-chord alignment (MCA) represents the displacement of the radial station in the axial direction, while the force alignment (FA) corresponds to the tangential displacement of the airfoil section. These displacements are described as the local position of the mid-chord point relative to the propeller-fixed coordinate system.

$$\begin{bmatrix} \Phi_S \\ \Phi_0 \end{bmatrix} = Dop \cdot \frac{2mN_b}{M_i} \begin{bmatrix} M_{tip} \cdot \frac{MAC}{D_P} \\ \frac{1}{r_n} \cdot (M_i \cos(\theta_{ret}) - M_\infty) \cdot \frac{FA}{D_P} \end{bmatrix} \tag{3.14}$$

Eq. (3.15) considers the aeroacoustic non-compactness for the thickness noise and loading noise in the form of lift and drag. The shown parameters are approximations for the influence of the thickness, lift and drag distribution along the propeller chord as proposed by Hanson and derived in Ref. [76].

$$\begin{aligned} \Psi_{thi}(k_x) &= \begin{cases} \frac{2}{3}, & \text{for } k_x = 0, \\ \frac{8}{k_x^2}\left[\frac{2}{k_x}\sin(k_x/2) - \cos(k_x/2)\right], & \text{for } k_x \neq 0 \end{cases} \\ \Psi_{l,d}(k_x) &= \begin{cases} 1, & \text{for } k_x = 0, \\ \frac{2}{k_x}\sin(k_x/2), & \text{for } k_x \neq 0 \end{cases} \end{aligned} \tag{3.15}$$

The stated procedure incorporates detailed propeller geometry information, such as sweep and lean. This method does not require time-dependent aerodynamic solutions, which significantly reduces computational effort. However, it cannot be used when unsteady effects need to be analysed, as in transient simulations. The resulting pressure Fourier coefficients are transformed into a time-dependent signal using eq. (3.16), summed up, and analysed.

$$p(t_{\text{ret}}) = 2 \cdot \text{real}\left(\sum_{m=1}^{\infty} p_m e^{imN_b\omega_{Dop}t_{\text{ret}}}\right) \tag{3.16}$$

3.1.3 Farassat's Formulation

Farassat's formulation 1A (F1A) also results from the well-known FW-H equations [125]. Unlike Hanson's model, it is derived in the time domain. The subsequent formulations follow the compact form described in the ANOPP2 user manual [102] and [103][2]. Sound sources are positioned along the quarter-chord line and are summed up. The expressions are defined using the retarded time of emission at the source locations and must be transferred to the observer through time stretching. The derivation of the model requires acoustics linearisation, allowing the separation and superposition of different noise sources, as shown in (3.17) and done in Hanson's model. The sound pressures from thickness, p_{thi}, and loading, p_{lod}, are calculated separately and then added.

$$p(x,t) = p_{thi}(x,t) + p_{lod}(x,t) \tag{3.17}$$

Farassat's formulation is simplified using a shorthand notation, as shown in eq. (3.18), based on Lee's work [98]. This shorthand notation incorporates the distance to the observer, o, from each blade element and the projected Mach number, M_o, to describe the noise source's radiation[3]. Consequently, it is referred to as the radiation term. The first input of the radiation term, n, represents the exponent of the distance, while the second input, m, corresponds to the exponent of the so-called Doppler term, $(1 - M_o)$.

$$RF(n,m) = o^{-n}(1 - M_o)^{-m} = \frac{1}{o^n(1 - M_o)^m} \tag{3.18}$$

The Mach numbers are derived from the blade station's motion and are calculated using the time derivative of the observer vector. Here, M denotes the axial Mach number, $\boldsymbol{M_j}$ represents the Mach number as a vector at each blade station j, and M_o is the projection of $\boldsymbol{M_j}$ onto the normalised observer vector $\boldsymbol{\hat{o}_j}$, which extends from the blade element to the observer. The index j follows Einstein's summation convention. To enhance clarity, vectors are represented in boldface.

$$M_o = \boldsymbol{M_j} \cdot \boldsymbol{\hat{o}_j} \tag{3.19}$$

Eq. (3.18) resembles the Doppler factor described in eq. (3.11). The projected Mach number accounts for the angle between the observer and the motion of the source, similar to the $\cos(\theta)$ term in eq. (3.11). However, unlike Hanson's model, there is no straightforward relationship between axial flight speed and observer position because the actual motion of the noise source is considered.

The thickness noise is determined using eq. (3.20), requiring the cross-sectional area Θ (m^2), the section length K (m), and their time derivatives. The projected Mach number M_o is time-dependent as the angle between the resulting Mach number at the blade ($\boldsymbol{M_j}$) and the observer to blade section vector ($\boldsymbol{o_j}$) varies.

Furthermore, the emission terms in eq. (3.20) and (3.21) can be categorised into near-field (NF), far-field (FF), and, for thickness noise, also ultra-near-field (UNF) terms. This classification is based on the power coefficient (n) of the distance vector (o) in the radiation equation eq. (3.18).

---

[2] ANOPP2 is the second versions of NASA's Aircraft NOise Prediction Program, developed for the comprehensive analysis of aircraft noise

[3] The local Mach number is projected onto the observer vector (eq. (3.19)).

For the thickness term, the coefficients A_{FF} to F_{UNF} are determined using eq. (3.22), as described in [98]. In steady simulations, the time derivatives of Θ and K are zero. The terms are numerically integrated from hub to tip through summation.

$$\begin{aligned}\frac{4\pi}{\rho_0} p_{thi}(\boldsymbol{x},t) = & \sum_{\text{hub}}^{\text{tip}} \left[\left\{ \ddot{\Theta} K + 2\dot{\Theta}\dot{K} + \Theta\ddot{K} \right\} A_{FF} + \left\{ \dot{\Theta} K + \Theta \dot{K} \right\} B_{FF} + \Theta K C_{FF} \right]_{ret} \\ & \sum_{\text{hub}}^{\text{tip}} \left[\left\{ \dot{\Theta} K + \Theta \dot{K} \right\} D_{NF} + \Theta K E_{NF} \right]_{ret} + \\ & \sum_{\text{hub}}^{\text{tip}} \left[\Theta K F_{UNF} \right]_{ret}\end{aligned} \tag{3.20}$$

The loading sound pressure is determined using eq. (3.21), which requires the loading vector $\boldsymbol{F}_j$ (N/m) and the section length K. The coefficients $G_{FF,j}$ to $I_{NF,j}$ are calculated using eq. (3.22).

$$\begin{aligned}4\pi c_\infty\, p_{lod}(\boldsymbol{x},t) = & \sum_{\text{hub}}^{\text{tip}} \left[\left\{ \dot{\boldsymbol{F}}_j K + \boldsymbol{F}_j \dot{K} \right\} G_{FF,j} + \boldsymbol{F}_j K H_{FF,j} \right]_{ret} + \\ & \sum_{\text{hub}}^{\text{tip}} \left[\boldsymbol{F}_j K I_{NF,j} \right]_{ret}\end{aligned} \tag{3.21}$$

Eq. (3.22) shows the coefficients for the loading and thickness noise calculation. The coefficients isolate the Mach number and radiation components from the source strength terms (Θ, K, and $\boldsymbol{F}_j$).

$$A_{FF} = RF(1,3) \tag{3.22a}$$

$$B_{FF} = 2(\dot{M}_o) RF(1,4) \tag{3.22b}$$

$$C_{FF} = (\ddot{M}_o) RF(1,4) + 3(\dot{M}_o)^2 RF(1,5) \tag{3.22c}$$

$$D_{NF} = c_\infty (M_o + M_o^2 - 2M_\infty^2) RF(2,4) \tag{3.22d}$$

$$\begin{aligned}E_{NF} = & \; c_\infty (\dot{M}_o) RF(2,3) \\ + & \; c_\infty \left[(\dot{M}_o) - 3\boldsymbol{M}_j \dot{\boldsymbol{M}}_j \right] RF(2,4) \\ + & \; c_\infty (\dot{M}_o) \left[5(M_o - M_\infty^2) + (M_o^2 - M_\infty^2) \right] RF(2,5)\end{aligned} \tag{3.22e}$$

$$\begin{aligned}F_{UNF} = & \; c_\infty^2 (M_o^2 - M_\infty^2) RF(3,4) \\ + & \; c_\infty^2 \left[2(M_o - M_\infty^2)^2 + (M_o - M_\infty^2)(M_o^2 - M_\infty^2) \right] RF(3,5)\end{aligned} \tag{3.22f}$$

$$G_{FF,j} = RF(1,2) \hat{\boldsymbol{o}}_j \tag{3.22g}$$

$$H_{FF,j} = (\dot{M}_o) RF(1,3) \hat{\boldsymbol{o}}_j \tag{3.22h}$$

$$\begin{aligned}I_{NF,j} = & \; \hat{\boldsymbol{o}}_j RF(2,1) \\ + & \; (\hat{\boldsymbol{r}}_j - \boldsymbol{M}_j) RF(2,2) \\ + & \; (M_o - M_\infty^2) \hat{\boldsymbol{o}}_j RF(2,3)\end{aligned} \tag{3.22i}$$

Farassat's formulation capture only the tonal components of noise emissions. The model predicts no noise emissions at the propeller axis because the projected Mach number M_o (eq. (3.19)) becomes constant near the propeller axis. As a result, no pressure fluctuations are calculated for steady operations in this region, where broadband noise dominates the emissions.

Fig. 3.6 illustrates how the noise levels of the ultra-near-field, near-field, and far-field terms change with the distance. The y-axis represents the change in sound pressure level (SPL), normalised to a reference distance of 10 cm, while the x-axis shows the distance on a logarithmic scale. The ultra-near-field noise decreases by 18 dB when the distance is doubled. The near-field term decreases by 12 dB, and the far-field term decreases by 6 dB under the same condition. However, the initial SPL values at the propeller are determined by the source strength of each term. Therefore, a strict distinction between the field zones is not possible.

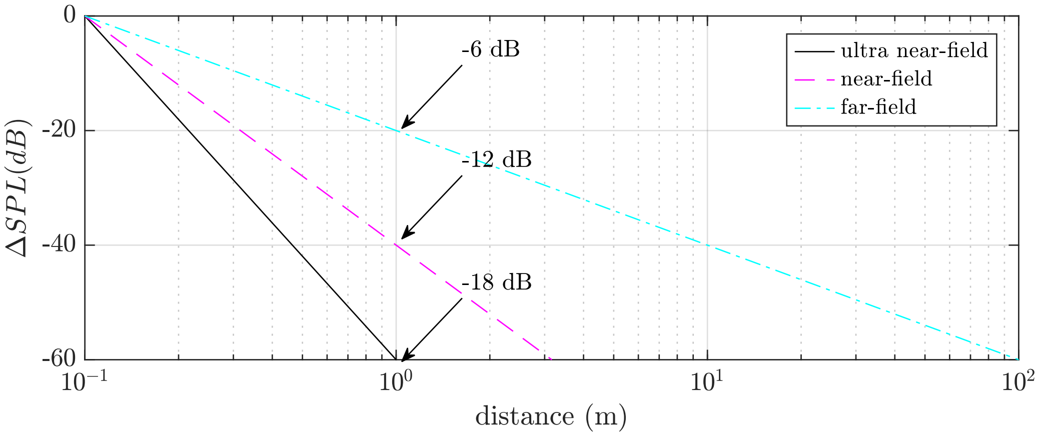

Figure 3.6: Comparison of noise reduction between ultra near-field, near-field, and far-field

As for the BEMT method, the model discretises the blade into spatial segments. Additionally, time is divided into finite steps. This requires an investigation of spatial independence, similar to the BEMT method in fig. 2.9, which is extended by a temporal discretisation.

Fig. 3.7 illustrates the required spatial and temporal discretisation. Diagram a) represents the spatial dependency, while diagram b) depicts the temporal dependency. The y-axis in both diagrams indicates the difference in SPL relative to the finest resolution, with the highest number of segments or time steps. The x-axis in diagram a) shows the number of spatial sections, whereas in diagram b), it displays the temporal discretisation in terms of time steps per revolution. An independent solution is achieved when the SPL deviation falls below 0.05 dB, as such noise changes are inaudible.

Diagram a) indicates that 37 sections are required for a spatially independent solution. While the BEMT method only requires 30 sections, the acoustic model demands at least 37 sections. Diagram b) reveals that a minimum of 540 time steps per revolution is necessary for a time-independent solution.

Further insights into the sound pressure's dependency on discretisation are provided in appendix D.3.

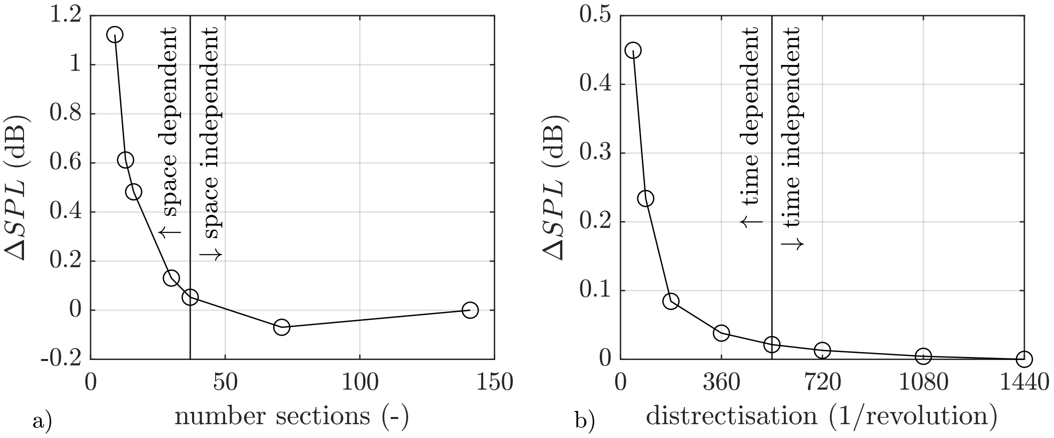

Figure 3.7: Temporal and spatial independence study of the F1A model

3.2 Broadband Noise

Broadband noise is generated by unsteadiness and turbulent structures in the fluid. These turbulent formations originate from various sources. They consist of vortices of different sizes, each exciting different frequencies based on its size and velocity. The characteristic scale for these frequencies is the Strouhal number. The Strouhal number is a dimensionless parameter that characterises vortex formations, with it's characteristic frequency, size ans velocity. Eq. (3.23) defines the Strouhal number in terms of the frequency f, the chord length c_r, and the inflow velocity v.

$$St = \frac{f c_r}{v} \tag{3.23}$$

Broadband noise can be self-induced or externally induced by the ingestion of turbulent structures. In particular, propeller and rotor applications in hover conditions can experience significant turbulent ingestion, primarily due to the advancing blade and blade-wake interactions. Self-induced broadband noise can be divided into five different sources [19]. The equations from eq. (3.24) to eq. (3.27) are provided in Ref. [19].

The enumeration highlights the main dependencies of the noise sources for each mechanism, excluding separation stall noise. Clearly, all noise sources depend, in addition to their specific state relations, on the Reynolds and Mach numbers. Moreover, a distinction must also be made between tripped and untripped boundary layers. Since the results presented in this thesis consider only fully tripped conditions, laminar vortex shedding noise is not relevant.

1. **Turbulent boundary layer - trailing-edge noise (TBLTE):** The interaction of the turbulent boundary layer with the trailing-edge.

$$TE = f(\alpha) \tag{3.24}$$

2. **Laminar boundary layer - vortex shedding noise (BLVS):** The laminar boundary creates bigger vortex formations compared to the turbulent boundary layer, which sheds from the trailing-edge.

$$BLVS = \begin{cases} f(\alpha) & \text{for laminar} \\ 20dB & \text{for turbulent} \neq 0 \end{cases} \tag{3.25}$$

3. **Trailing-edge bluntness - vortex shedding noise (BVS):** The vortex formations which develop behind a blunt body.

$$BVS = f(\alpha\text{,rel. TE thickness, TE angle}) \tag{3.26}$$

4. **Tip vortex formation noise (TV):** The turbulent structure which develop at the blade tip.

$$TV = f(\alpha_{tip}, AR) \tag{3.27}$$

5. **Separation stall noise (SSN):** The vortex formations which develop due to flow seperation. The SSN is covered by the TBLTE.

These noise sources can either be modelled or computed. High-fidelity large eddy simulations are the minimum requirement for accurately computing broadband noise [24]. However, such simulations are not feasible for optimisation studies. Therefore, a modelling approach is necessary.

When using a modelling approach, all five mechanisms must be included in the prediction methodology. In the past, semi-empirical methods have been primarily developed. These methods rely on empirical correlations to predict the noise generated by broadband noise mechanisms, but rely on the physical effects.

The fundamentals of broadband noise modelling were established in 1976 by Amiet, who proposed a model for trailing-edge noise (Amiet's model) based on a flat plate [3]. Over time, Amiet's model has been extended to include rotating airfoils [15, 89, 99, 138].

In 1989, Brooks, Pope, and Marcolini introduced a comprehensive model for four of the five broadband noise mechanisms, commonly referred to as the BPM model [19]. This model was developed through the analysis of a NACA0012 airfoil. The BPM model relies entirely on empirically estimated coefficients derived from the NACA0012 experiments.

The BPM model offers a significant advantage by being directly implementable into a reduced-order model, as all required boundary layer parameters are provided by the model. However, this advantage also presents a limitation, as the results are based solely on a single airfoil geometry. A detailed description of the BPM model can be found in Ref. [19].

Other models approximate complex broadband noise by fitting existing data from various measurements. Goody (Goody model) [57] developed an empirical correlation for surface pressure fluctuations, transforming them into a noise spectrum based on existing spectra. Another empirical wall-pressure spectral model was proposed by Prof. Seongkyu Lee in Ref. [97]. Lee derived a universal wall-pressure spectrum, as shown in eq. (3.28). He incorporated Goody's model and other approaches [26, 81, 85, 130] to fit the surface pressure spectrum coefficients into this equation.

$$\Phi(\omega)SS = \frac{a(\omega FS)^b}{[i(\omega FS)^c + d]^e + [(fR_T^g)(\omega FS)]^h} \tag{3.28}$$

The generic wall-pressure model requires a timescale R_T and scale factors for the spectrum (SS) and frequency (FS) to compute the pressure fluctuations. Eq. (3.29) defines the timescale ratio, which is calculated using the boundary layer thickness δ, the boundary layer edge velocity U_e, the kinematic viscosity ν, and the friction velocity $\sqrt{\tau_w/\rho}$.

$$R_T = \frac{\delta/U_e}{\nu/u_\tau^2} \tag{3.29}$$

The timescale ratio indicates that detailed information about the boundary layer is necessary to apply this model. Boundary layer parameters can be computed using tools like XFOIL or RANS simulations. However, these parameters are typically unavailable in reduced-order methods within an optimisation framework.

Ref. [25] compares state-of-the-art wall-pressure spectrum models with measurements. The comparison reveals significant discrepancies between the models and experimental data. It also highlights the need for improved models to predict wall-pressure fluctuations more accurately.

Recent developments in neural networks have introduced new models based on wind tunnel tests and simulations, such as the GL model proposed by Gill and Lee [53]. This model, however, is specifically derived for hover conditions. Using neural networks, the best-fitting coefficients of eq. (3.28) were determined. Gill's model redefines the scale factors with thrust- and solidity-based parameters, eliminating the need for detailed boundary layer information. Unlike traditional models, it avoids the use of the timescale ratio. Additionally, Gill modifies the equation's left-hand side to represent a 1/3-octave band SPL spectrum, directly incorporating the observer position. This adjustment enables straightforward implementation into optimisation frameworks. However, since the model is valid only for hover conditions, it cannot be applied to arbitrary flight missions. As a result, it is unsuitable for a comprehensive design environment.

As the BPM model is the only one that does not require calculated boundary layer properties, it is the most suitable model for the purposes of this thesis.

The influence of the BPM model on the OASPL prediction is illustrated in the fig. 3.8 and 3.9. The reference propeller is analysed under hover conditions with a rotational speed of 3500 rpm. This configuration results in a BPF of 233 Hz. The observer is located in a distance of 7 m. The tonal noise is predicted with the F1A model. The following analysis is valid only for the specified case, as the directivity and dominance of different noise sources vary with operational conditions, geometry, and observer position.

Fig. 3.8 presents the SPL prediction for an observer moving around the propeller from upstream (45°) to downstream (135°). The propeller plane corresponds to the 90° observer position.

The overall SPL (OASPL) is obtained by the linear superposition of tonal noise from the F1A model and broadband (BB) noise from the BPM model. Under the given conditions, the BB noise exhibits noise cancellation around the propeller plane at 90°. The BB noise shows a clear dipole characteristic centred around the propeller plane.

In contrast, the tonal noise displays a dipole characteristic centred around the axis of rotation, peaking at the propeller plane and minimising upstream and downstream of the propeller. As a result, BB noise dominates below 65° and above 120° observer positions, while tonal noise is dominant between these observer positions.

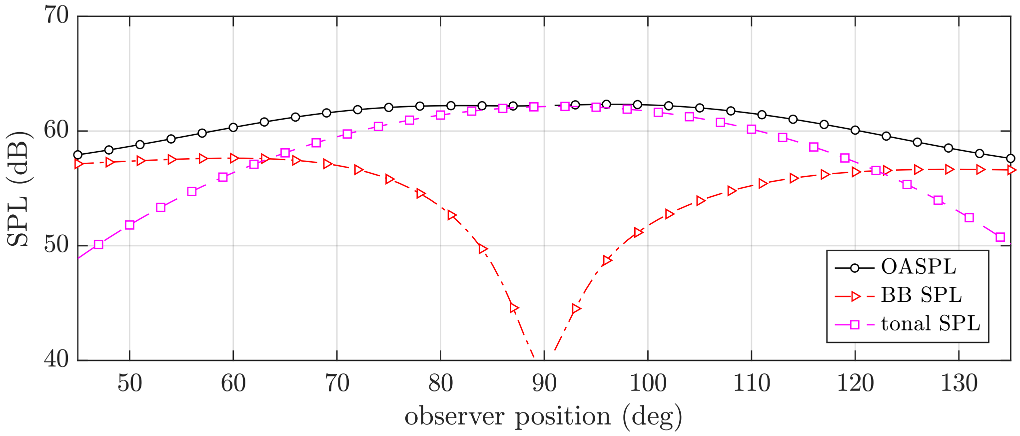

Figure 3.8: Directivity of broadband noise (BB) and tonal noise

Due to the change in the dominant noise source, different observer positions must be analysed to evaluate the BPM model. Fig. 3.9 presents the third-octave-band noise spectrum at three observer positions. Diagram a) represents the upstream position at 45°, diagram (b) the position at the propeller plane (90°), and diagram c) the downstream position at 135°. The frequency on the x-axis is normalised by the blade passing frequency (BPF).

The comparison reveals that the upstream and downstream positions are nearly mirrored. As a result, only diagrams a) and b) are discussed in detail.

Diagram a) shows three distinct noise peaks in the tonal noise at 0.5, 1, and 2 times the BPF. The second peak at 2 BPF is referred to as the first harmonic of the propeller. However, the peak at 1 BPF is dominant, being approximately 50 dB higher than the other harmonic peaks. The broadband noise displays a pronounced increase in the range from 4 to 256 BPF. In the range of 16 to 64 BPF, the amplitudes are comparable to those of the tonal noise. However, due to the broad range of elevated amplitudes, broadband noise becomes dominant.

At the propeller plane (diagram b), the tonal noise peak at 1 BPF increases by 15 dB, while the first harmonic at 2 BPF rises by 25 dB. Conversely, the broadband noise hump in the high-frequency range is reduced by 20 dB compared to the 45° position.

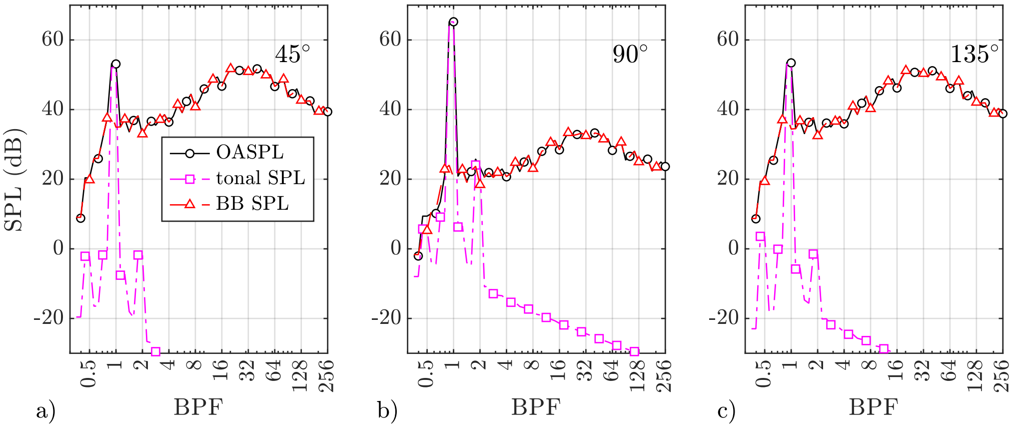

Figure 3.9: Frequency spectra of the reference propeller at three observer locations

Next, the broadband noise prediction of the BPM model is decomposed into its noise mechanisms to provide a more detailed analysis of the model's behaviour. Fig. 3.10 presents the results of the BPM model for the first observer position at 45°.

The broadband noise (BB) is the sum of all its components, visualised with red dashed lines and upwards-pointing triangles.

The tip vortex formation noise (TV) contributes to the high-frequency domain and is represented by diamonds. TV noise only affects the BB noise above a BPF of 200, equivalent to 40 kHz, making it inaudible to humans.

The turbulent boundary layer trailing-edge noise (TBLTE) dominates the BB prediction and is visualised in blue with right-pointing triangles. It exhibits a prominent hump in the region between a BPF of 3 and 256, where the TBLTE noise reaches a peak value of 52 dB. Outside this hump, the TBLTE noise remains at a consistently high level of 35 dB.

The boundary layer vortex shedding noise (BLVS) excites all frequencies evenly at 20 dB, as defined for a turbulent boundary layer. It is visualised with a violet line and left-pointing triangles.

In the ultra-low-frequency region, the blunt vortex shedding (BVS) mechanism is dominant, represented by an orange line with downward-pointing triangles. It increases the BB noise in the range between a BPF of 0.4 and 1.2.

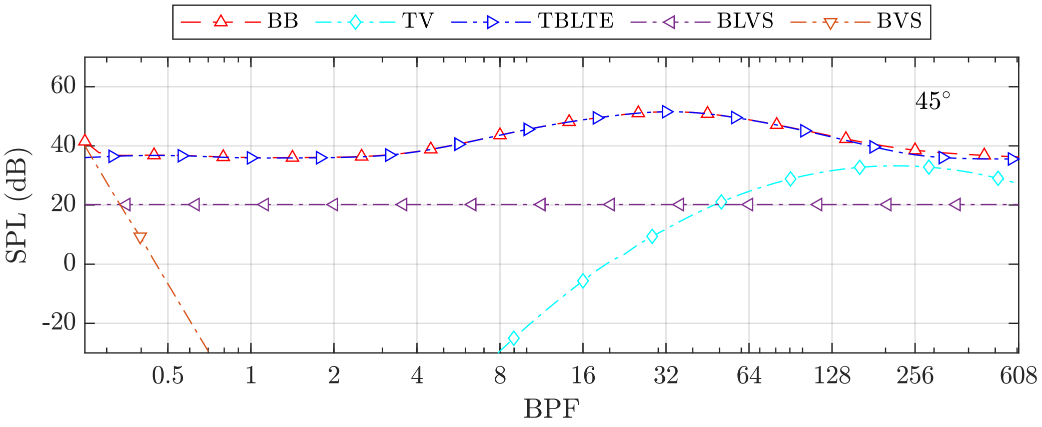

Figure 3.10: Frequency spectrum of the different broadband noise mechanisms (at 45°)

The aforementioned enumeration of noise sources highlights the dependencies of trailing-edge (TE) size, TE angle, and angle of attack (AoA) on broadband noise predictions.

Helix Carbon GmbH's propellers have a constant absolute TE thickness of 1 mm, regardless of the propeller design. From a manufacturing perspective, smaller TE thicknesses are not reliably producible. Additionally, the TE must provide sufficient stiffness and robustness to ensure proper handling of the blades on the aircraft.

This absolute TE thickness of 1 mm results in variable relative TE thicknesses, depending on the blade chord length. In contrast, NACA airfoils are inherently designed with relatively small TE sizes, typically featuring relative thicknesses below 1%.

The influence of relative TE thickness, TE angle, and AoA on broadband noise is assessed in fig. 3.11, 3.12, and 3.13.

Fig. 3.11 demonstrates the influence of varying relative TE thicknesses on blunt vortex shedding noise (BVS). The reference propeller was modified at the TE and analysed under the same conditions as in fig. 3.10. The TE thickness varies between 0.25% and 2%. In addition to the results presented in fig. 3.10, fig. 3.11 includes the results for the modified TE thicknesses, visualised in orange with different line styles. More solid lines correspond to smaller TE thicknesses.

The TE thickness impacts the magnitude of the BVS noise but not its slope. Smaller TE thicknesses result in higher BVS noise levels. In the current case, the BVS noise for TE sizes above 1% is masked by the TBLTE noise. Consequently, the TE size should be kept below 1%.

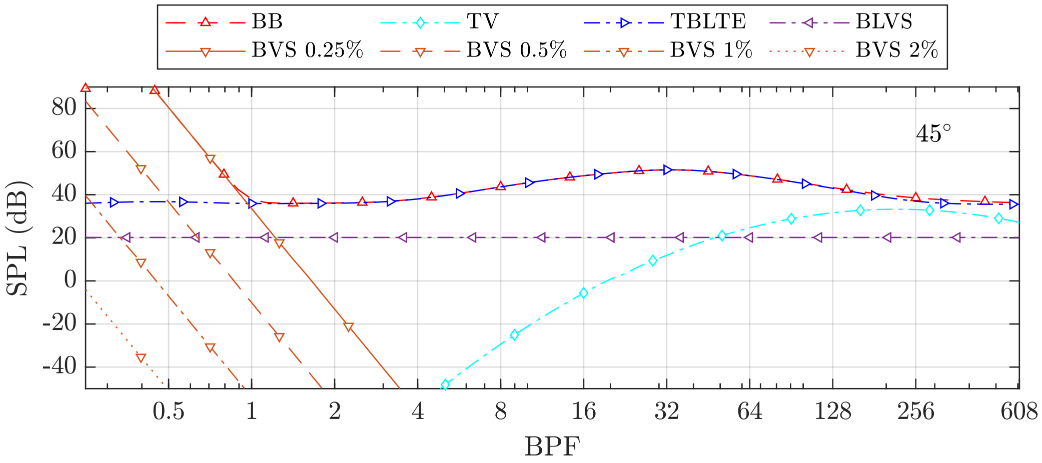

Figure 3.11: Influence of the trailing-edge thickness on the broadband noise spectrum (at 45°)

The BVS noise depends not only on the TE size but also on the TE angle, defined as the angle between the upper and lower surfaces of the airfoil. Fig. 3.12 illustrates the influence of the TE angle on BVS noise, complementing the analysis in fig. 3.11.

For this study, the TE angle of the reference propeller was modified by ±5°. The original TE is depicted by the solid orange line with downward-pointing triangles. The sharper TE, with a reduced TE angle, is shown by the orange dotted-dashed line, while the blunter TE is represented by a dashed line.

The comparison between the original propeller and those with adjusted TE angles indicates that sharper TE angles lead to higher BVS noise. However, compared to the influence of TE size in fig. 3.11, the BVS noise is less sensitive to variations in the TE angle.

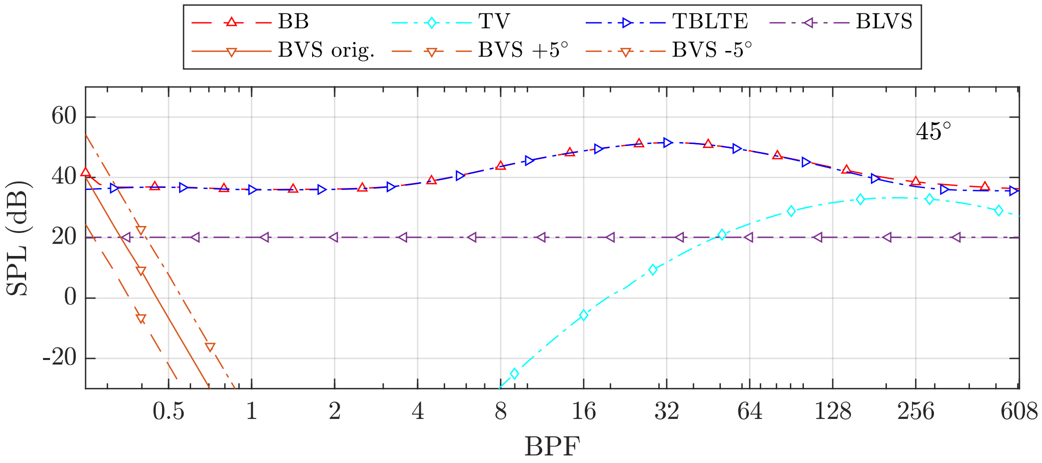

Figure 3.12: Influence of the trailing-edge angle on the broadband noise spectrum (at 45°)

The angle of attack (AoA) is the third key parameter for broadband noise, alongside the Reynolds number. Fig. 3.13 illustrates the effect of AoA on broadband noise. For this analysis, the AoA was artificially modified without considering aerodynamic effects, with adjustments of ±3°.

Diagram a) in fig. 3.13 depicts the AoA influence on tip vortex (TV) noise, while diagram b) shows its impact on turbulent boundary layer trailing-edge (TBLTE) noise. The blue dotted line represents the noise for the reference propeller.

Diagram a) shows that a lower AoA reduces TV noise, while a higher AoA increases it. However, even at an AoA of +3°, the maximum TV noise reaches only 36 dB at a BPF of 128. This value is relatively low and occurs at an extremely high frequency.

Diagram b) shows, that for TBLTE noise, two distinct effects are observed. A higher AoA results in a flattened TBLTE curve and increased overall noise levels. In contrast, a lower AoA causes oscillations and overshooting in the low BPF region.

At the predominant peak of the reference propeller at the 32nd BPF, the TBLTE noise is reduced with lower AoA. However, a second peak emerges at low BPF values between the 0.5th and 1st BPF as AoA decreases. The highest TBLTE noise is observed at -2°, while the -3° case shows a slightly lower level.

The observed frequency shifts suggest that, in cases of A-weighting, a lower AoA might be preferable to a higher AoA. This is because A-weighting attenuates low frequencies while amplifying higher ones. However, the suitability of this adjustment depends strongly on the propeller's current operating conditions.

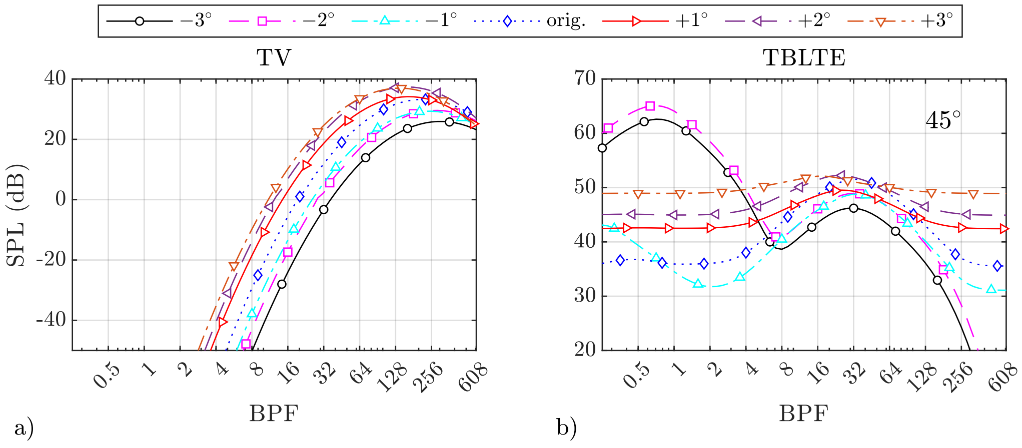

Figure 3.13: Influence of the angle of attack on the broadband noise spectrum (at 45°)

The validation of the broadband noise prediction is detailed in section 3.3.2 and 3.3.3, where the predicted results are compared with measurement data.

3.3 Aeroacoustic Validation Studies

First, Farassat's formulation 1A (F1A) is validated using data from the ideally twisted propeller provided by NASA's Urban Air Mobility Noise Working Group, Subgroup 1 (UNWG SG1) [148] (section 3.3.1). Second, the F1A model and the Brooks, Pope, and Marcolini (BPM) model are validated using another UNWG SG1 case, measured as a baseline for optimisation purposes [153]. Third, the F1A and BPM model are validated with a benchmark case provided by TU Delft 3.3.3.

The first reference case involves hover operations with varying pitch angles for a four-bladed propeller. The second test case includes hover and cruise conditions for a three-bladed propeller. Finally, the third test case examines operations with varying free-stream velocities for a two-bladed propeller. These validation cases encompass a wide range of operating conditions and geometries, which is essential for a robust validation.

3.3.1 NASA's Ideally Twisted Rotor

The validation case 1 compares the tonal noise prediction with the tonal noise extracted from measurements of the ideally twisted propeller. To extract tonal noise from the noise measurements, the SPL amplitudes of the blade passing frequencies (BPF) are identified from the noise spectrum. The resulting tonal noise emissions are recalculated through a logarithmic summation of the BPF noise amplitudes. The remaining noise spectrum, excluding the tonal amplitudes, represents the broadband noise spectrum, which is used to calculate the overall broadband noise.

The validation is conducted without considering structural effects, as no information on deformations are available. The microphones are positioned on an arc at a distance of 1.9 m from the propeller hub. The propeller is tested in hover conditions with various rotational speeds and three different pitch angles (3.9°, 6.9°, and 9.9°). Details about the testing procedure are provided in Ref. [124]. Ref. [124] also compares the measured data to noise predictions generated with NASA's ANOPP2.

Fig. 3.14 illustrates the experimental setup. Six microphones are used in the experiment: two are located upstream at 47° and 64°, one is in the propeller plane, and three are downstream at 108°, 125°, and 133°. The tests are conducted in an anechoic chamber.

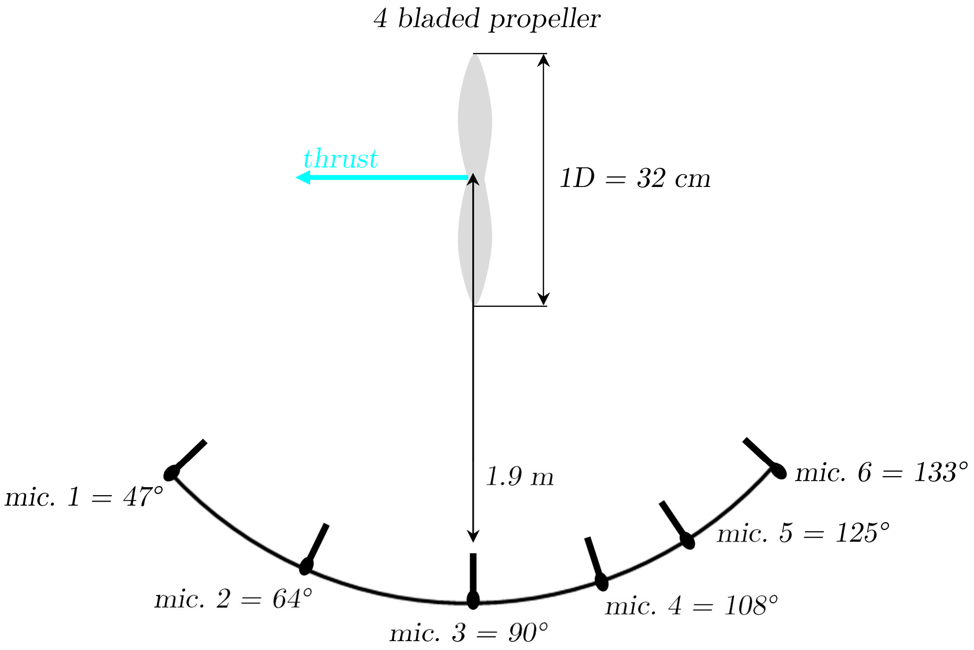

Figure 3.14: Experimentel setup of NASA's ideally twisted propeller validation case

All aeroacoustic validations must begin with the evaluation of the aerodynamic model. The left diagram in fig. 3.15 illustrates the propeller's thrust at three different pitch angles for varying rotational speeds. The BEMT method (sim.) is compared to performance measurements (exp.) from Ref. [124]. The BEMT simulations are conducted without the 3D stall model but include tip and hub loss correction as well as sweep correction. However, the sweep correction has no effect on the results, as the airfoils are perfectly staggered along the quarter chord line. The maximum thrust deviation between the experiment and BEMT simulation is 4% at 3957 rpm for the 6.9° pitch case.

The right diagram in fig. 3.15 compares the measured SPL with the predicted SPL at the design rotational speed of 5500 rpm. As noted by Pettingill et al. [124], the propeller's tonal noise is dominated by thickness noise. Thickness noise depends solely on the rotational speed and source position. The compact formulation in ANOPP2 does not depend on the pitch angle. Thus, increasing the thrust from 3.9° to 9.9° pitch does not affect the thickness noise for the three pitch angles. The errors between simulation and experiment align with those presented in Ref. [124]. The underprediction of the overall SPL is attributed to the observed recirculation in the anechoic chamber.

The predicted SPL shows slight variation across different pitch angles downstream of the propeller plane. The exact SPL deviations in the acoustic prediction are discussed in Ref. [98]. Overall, the results are consistent with the experimental data and simulation findings published in Ref. [124].

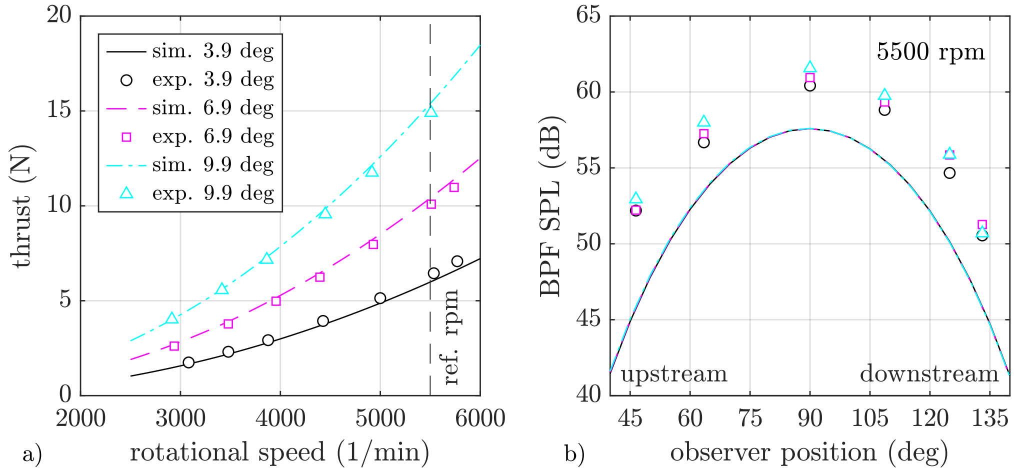

Figure 3.15: Aeroacoustics validation with experimental data of NASA's UNWG SG1

The tonal noise is decomposed in fig. 3.16. Diagram a) of fig. 3.16 shows the thickness noise, calculated using eq. (3.20), while diagram b) illustrates the loading noise, derived from eq. (3.21). A comparison between loading and thickness noise reveals that thickness noise is at least 10 dB higher at all observer positions. As a result, no significant difference in the total SPL across the three pitch angles is observed in fig. 3.15.

The thickness noise, depicted on the left, exhibits symmetric behaviour around the propeller plane at 90° because it behaves like a monopole noise source, without clear directivity. In contrast, the loading noise, shown on the right, has a peak shifted downstream to an observer position of approximately 100°. Loading noise behaves like a dipole source, resulting in asymmetric behaviour around the propeller plane. The maximum SPL of the loading noise increases by about 4 dB from 3.9° to 6.9° and again from 6.9° to 9.9°, while thrust increases by approximately 50% with each pitch increment.

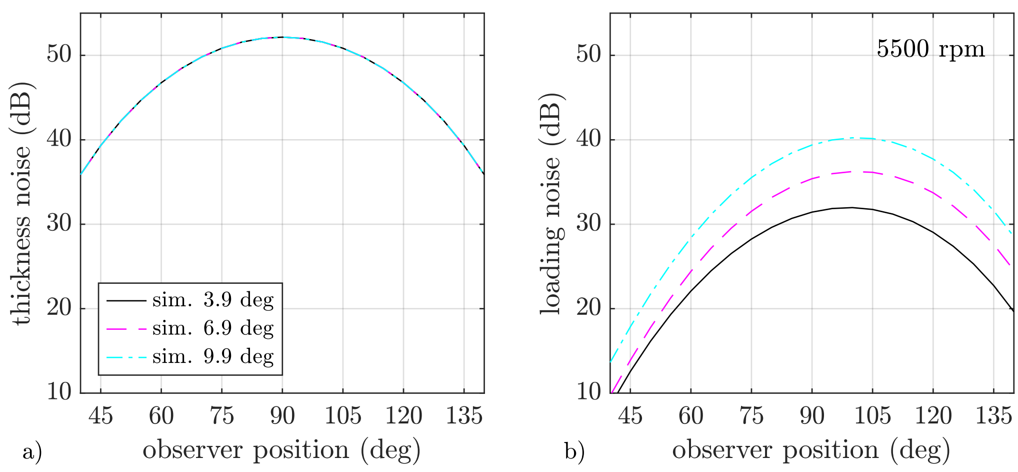

Figure 3.16: Thickness and loading noise of ideally twisted propeller

3.3.2 NASA's Proprotor Optimisation

The UNWG SG1 has published additional experimental data for validation purposes. In an extensive study, they designed and built four different propellers, testing them in an anechoic wind tunnel under hover and cruise conditions. The dataset includes broadband noise and tonal noise spectra measured at various observer positions. Fig. 3.17 illustrates the experimental setup.

The acoustic data are corrected to account for the wind tunnel's shear layer and to a constant observer distance. In hover conditions, where no wind tunnel shear layer exists, the shear layer correction is not applied. The shear layer correction results in a shift in the observer positions.

The validation is conducted using a helically twisted, three-bladed propeller with a diameter of 30.57 cm. The observer distance is 3.57 m.

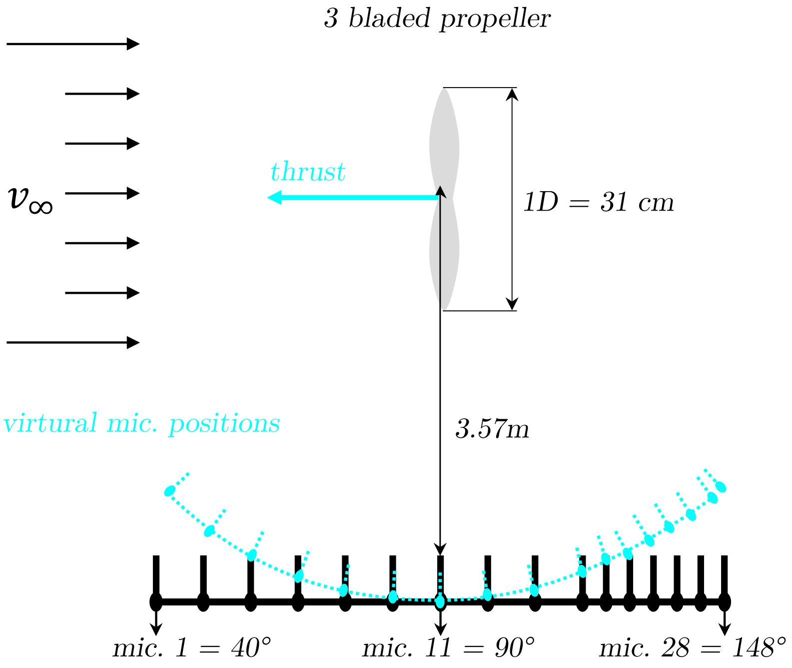

Figure 3.17: Experimentel setup of NASA's second validation case

Fig. 3.19 presents the thrust predictions for hover conditions (diagram a)) and various wind speeds (diagram b)), referred to as cruise conditions in the following. The aerodynamic simulations include no stall correction and PTL correction.

Additionally, the reference operational conditions for the acoustic simulations are highlighted. In hover conditions, rotational speeds of 4067 rpm and 6006 rpm are analysed. In cruise conditions, advance ratios of 0.23 and 0.54 are examined at a rotational speed of 7070 rpm.

The thrust comparison in diagram a) is dimensional, while in diagram b), it is non-dimensional. The comparison shows good agreement between predictions and measurements. The maximum relative error in thrust prediction for cruise and hover conditions is 3% compared to the experimental data.

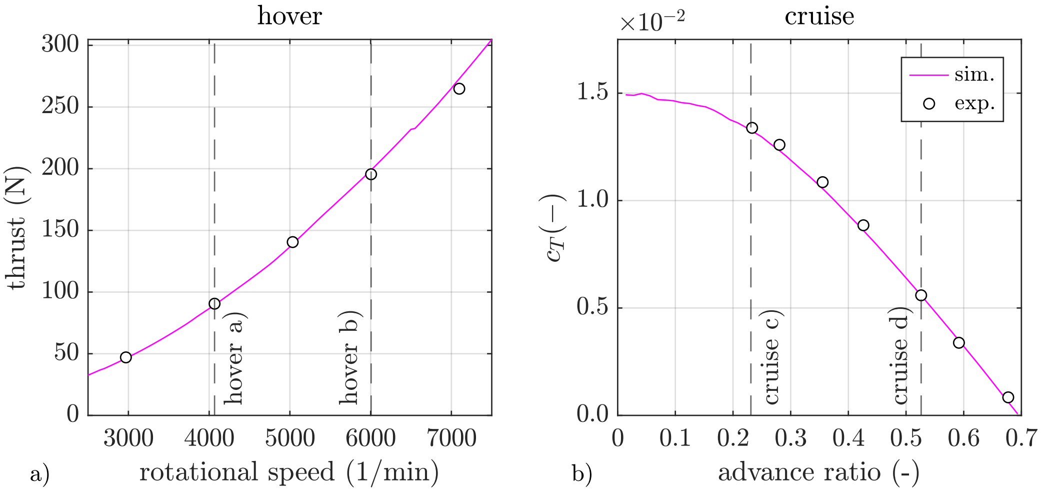

Figure 3.18: Comparison of thrust predictions for hover conditions and higher advance ratios

Fig. 3.19 presents the noise prediction results for the reference conditions shown in fig. 3.18. The upper diagrams represent hover conditions (a and b), while the lower diagrams illustrate cruise conditions (c and d). For consistency, the y-axis scale is identical across all operating points. The diagrams display the experimental tonal and broadband noise using markers only, while the simulation results for tonal and broadband noise are shown with markers and lines. Square markers represent broadband noise, whereas circular markers represent tonal noise.

The tonal noise prediction aligns within 7 dB across the entire observer position range for all four operating conditions, with overall trends matching in all cases.

In hover case a), the tonal noise is slightly underpredicted. The largest derivation between experiment and simulation is located at 125° with 6 dB.

In cases b) to d), the tonal noise measurements reveal plateau in the range from 120° to 135°, which is not captured by the simulation[4]. In hover case b), the tonal noise matches well except beyond the 120° observer position. In front of the 120° position, the error remains below 2 dB. In case c), the tonal noise prediction slightly exceeds the measurements, while in case d), the error increases further, reaching up to 7 dB.

The broadband noise prediction shows its cancellation effect at 90° in all four cases. This effect is discussed in fig. 3.8. Outside the cancellation region, the maximum deviation between experimental and simulation is also 7 dB. In diagrams a) and c), the broadband noise matches within a range of 2 dB. In hover case b), the broadband noise is slightly underpredicted by 6 dB, whereas in cruise case d), it is overpredicted by 7d dB. Nevertheless, the trend aligns well in all four cases.

---

[4] This plateau is also present in case (a), but it aligns with the peak, making it unidentifiable.

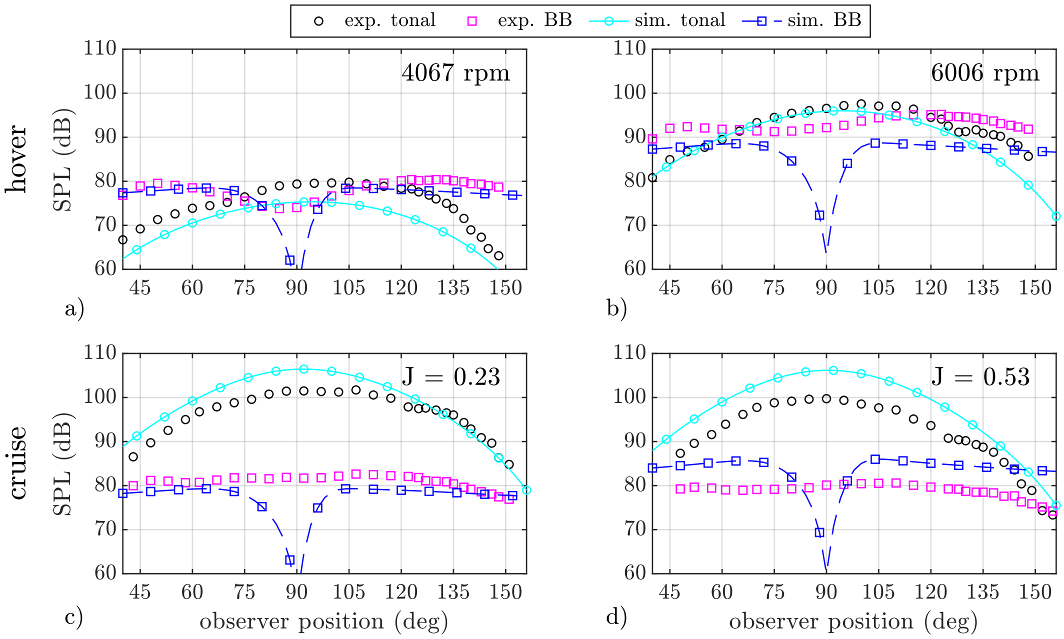

Figure 3.19: Comparison of tonal and broadband noise between simulation and measurement for four different condidtions

Tab.3.1 summarises the differences between the experimental measurements and the predictions for the four cases. It presents the maximum values of tonal and broadband noise. Furthermore, the absolute errors between the predictions and the experiments are presented for tonal and broadband noise in the Δ-columns. The errors are within 7 dB.

Table 3.1: Comparison of maximal SPL values for all four cases

Case	Max. tonal SPL (dB)			Max. broadband SPL (dB)		
	sim.	exp.	Δ	sim.	exp.	Δ
a)	75.3	79.8	-4.5	78.5	80.4	-1.9
b)	96.0	97.6	-1.6	88.7	95.2	-6.5
c)	106.4	101.7	+4.7	79.3	82.6	-3.3
d)	106.2	99.7	+6.5	86.0	80.6	+5.4

3.3.3 TU Delft's Benchmark Case

The third validation case is provided by TU Delft. A two-bladed propeller with a diameter of 30 cm is analysed in an anechoic wind tunnel at various rotational speeds and free-stream velocities. Noise emissions are measured using thirteen microphones mounted on a beam. The beam is aligned parallel to the free-stream and perpendicular to the propeller plane, causing the distance from the propeller hub to each microphone to vary. The experimental setup is described in Ref. [25] and illustrated in fig. 3.20. Additionally, fig. 3.20 highlights the microphone locations, which are analysed in detail in fig. 3.23.

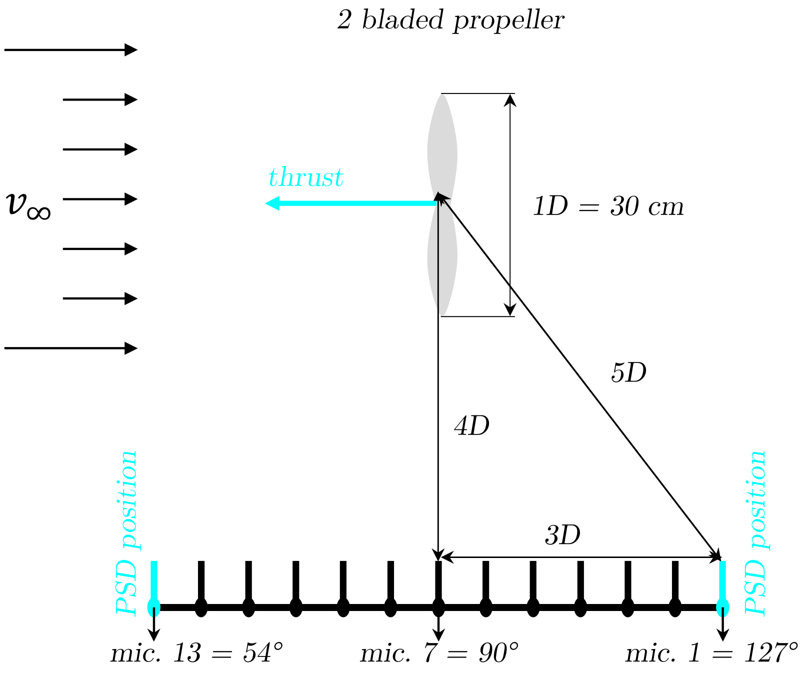

Figure 3.20: Experimentel setup of TU Delft's benchmark case

The TU Delft experimental data includes wind tunnel results for rotational speeds of 4000, 5000, and 6000 rpm. Fig. 3.21 compares the measurements with the simulation results. The simulations are conducted with 3D stall correction and without tip and hub loss correction. As observed in the NASA test case, the sweep correction model does not affect the simulation results.

The thrust prediction matches the experimental results within 5% in the low advance ratio region and within 10% at an advance ratio of 0.6. Above an advance ratio of 0.6, the relative error increases due to the shrinking denominator, although the absolute errors remain constant.

The diagram highlights four advance ratios where acoustic measurements are available. These different advance ratios can be interpreted as representing various flight states, ranging from hover to initial climb, secondary climb, and cruise conditions.

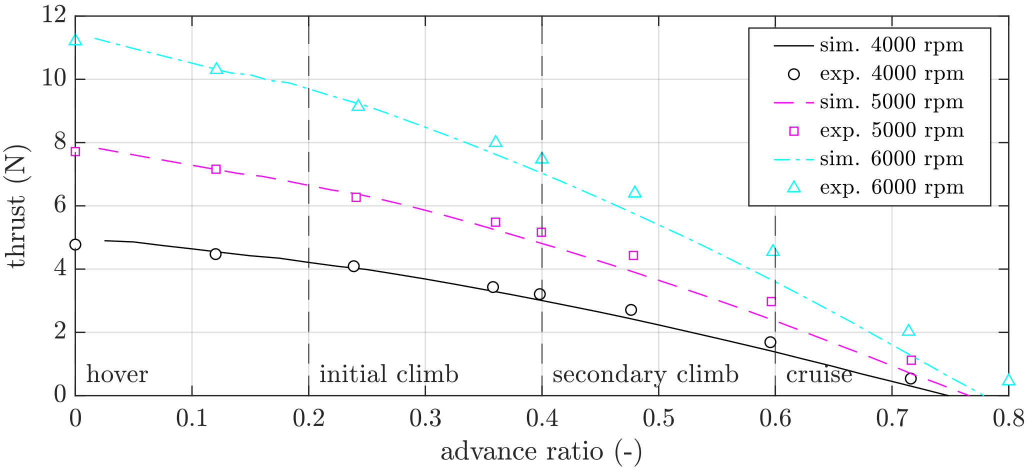

Figure 3.21: Thrust comparison between experiment and simulation for three rotational speeds

Fig. 3.22 compares the noise measurements with the simulation results. As in the previous case, the BPF noise is separated from the spectrum to validate the tonal noise prediction, and the y-axis scale is kept identical across all operating points for consistency. The experimental tonal SPL is represented by black circular markers, while the simulation results are shown with markers and lines. In fig. 3.22, the loading noise is depicted in blue, the thickness noise in cyan, and the total tonal noise, according to eq. (3.17), in magenta. Diagram a) shows the hover conditions at an advance ratio of 0, diagram b) the initial climb conditions ($J = 0.2$), diagram c) the secondary climb conditions ($J = 0.4$) and diagram d) the cruise conditions ($J = 0.6$).

The thickness noise depends only on the movement of the noise sources, which remains constant in the wind tunnel across all conditions. In contrast, the loading noise varies for different advance ratios due to changes in thrust. As the advance ratio increases, thrust decreases, leading to a corresponding reduction in loading noise.

The comparison of the tonal SPL between the simulation and experimental data shows excellent agreement in the region from 60° to 120° observer position. The maximum deviation is 2.5 dB at the 120° observer position for an advance ratio of 0.2. For an advance ratio of 0.6, the noise emissions are slightly underpredicted due to a thrust underprediction of 0.5 N compared to the experimental data.

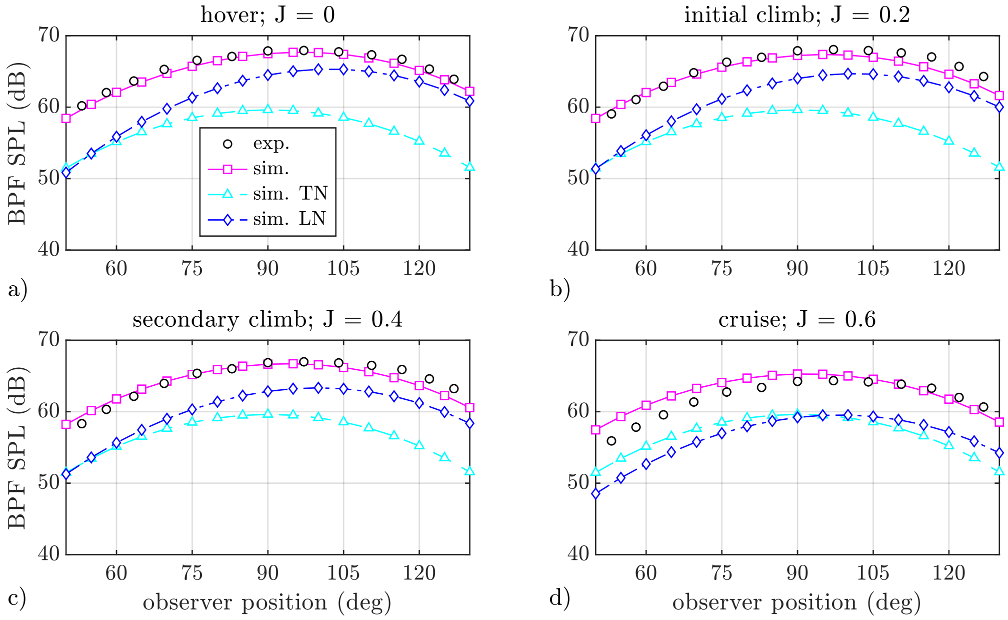

Figure 3.22: Comparison of the BPF SPL for different advance ratios, with information about loading (LN) and thickness (TN) noise

The TU Delft data includes not only tonal noise but also the power spectral density (PSD) for each microphone location and measurement point. Fig. 3.23 presents the PSD in third-octave bands for two different microphone locations and two different advance ratios.

The upper row displays the hover conditions (diagrams a) and b), while the lower row shows the secondary climb condition. The left diagrams represent the most forward microphone location (54°), and the right diagrams show the most rearward location (127°). Black lines indicate the experimental data, magenta lines represent the tonal noise prediction, and red lines correspond to the broadband noise prediction.

Due to the third-octave band representation, the tonal noise peaks are smeared across multiple frequencies. However, this accumulation of multiple frequencies is necessary for comparison with the BPM model. The x-axis frequency is normalised with the BPF, which is 167 Hz in this case.

The comparison demonstrates good agreement in amplitude at the BPF across all four diagrams. The second harmonic is masked by the broadband noise and is therefore not visible in the experimental data.

In hover conditions (diagrams a) and b)), the BPM model accurately predicts the frequency range from BPF's of 2 to 128. However, diagram b) shows a hump around the 10th BPF, which is not captured by the BPM model. Aside from this hump, the broadband noise is well represented by the model.

In the secondary climb condition, the BPM model underpredicts the broadband noise by 10 to 15 dB/Hz across most of the spectrum, except at higher frequencies. Despite this, the trend aligns well across the entire frequency range.

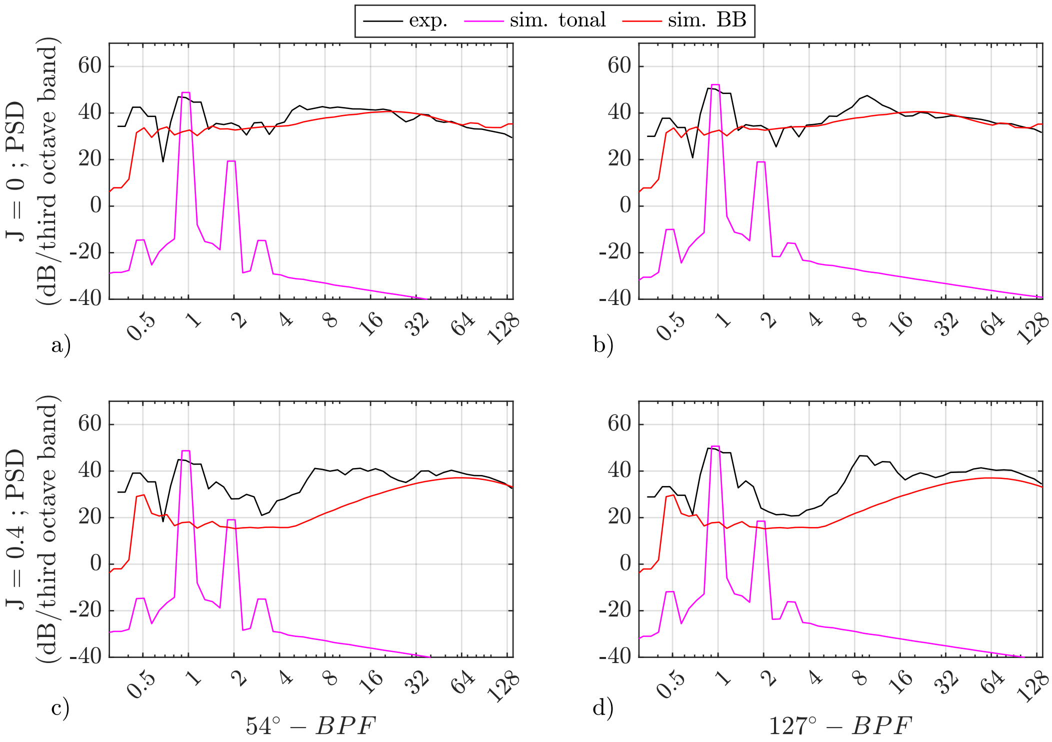

Figure 3.23: Comparison of third-octave-band PSD between measurements of TU Delft and prediction with the BPM model at 54° (left) and 127° (right)

The validation study demonstrates that the presented aeroacoustic prediction methodology is capable of accurately predicting the noise emissions of three different propellers with varying blade numbers and operational conditions. An accuracy of at least 7 dB is achieved in the region from 60° to 120° observer position.

The validation is conducted using independent datasets with different experimental setups. The only common feature across the three studies is the similar blade diameter, which is due to the availability of anechoic wind tunnels. Smaller diameters are more challenging to analyse than larger ones because of the reduced Reynolds numbers. Lower Reynolds numbers result in less stable XFOIL predictions and increase the relative boundary layer thickness, leading to more boundary-layer-induced broadband noise [19, 86, 147].

3.4 Assessment of Tonal Acoustic Models

The acoustic models must be self-contained and consistent to be applicable within an optimisation framework. Therefore, the three presented models are analysed to assess their ability to consistently predict the SPL under varying observer positions, wind speeds, blade numbers, and operational conditions. The validation demonstrates that Farassat's formulation 1A exhibits consistency across different distances, blade counts, and operational conditions. Consequently, this model is used as the reference for evaluating the other models.

The following subchapters present contour plots for the three models under various conditions, but only for the four-bladed propeller. Additional contour plots for both two- and four-bladed propellers, as well as further details regarding the comparisons, are provided in Appendix C.

The model comparisons are conducted in three distinct scenarios. The rotational speed in all scenarios is 3500 rpm. First, the observer distance is varied during static operations (advance ratio of zero) of the reference propeller. Second, the reference propeller is examined in a wind tunnel under different wind speeds. Third, a comparative analysis is performed for an overflight scenario. These comparisons are essential because, during an overflight, the observer's distance changes dynamically, and the Doppler effect introduces distinct noise patterns that differ significantly from those observed in wind tunnel measurements.

In the following analysis, only tonal noise is considered, eliminating the need to distinguish between overall SPL and BPF SPL. Therefore, SPL is used instead of BPF SPL to enhance readability and clarity.

3.4.1 Distance Variation

At first, the consistency of the models for different observer distances is analysed. Fig. 3.24 presents the SPL at various observer positions and distances as a contour plot for the four-bladed propeller. The observer moves around the propeller as in the first validation case (cf. section 3.3.1 and 3.20). The x-axis represents the observer position, and the y-axis represents the distance to the propeller hub.

Diagram a) shows the result for Gutin's model, diagram b) for Hanson's model, and diagram c) for the reference model based on Farassat's formulation 1A. Significant differences are evident between the predictions of the three models.

The F1A prediction in diagram c) shows its maximum at approximately 100° observer position, with a maximum SPL of 80 dB(A). Gutin's model (diagram a) exhibits severe noise cancellation at around 60° observer position. The highest SPL for Gutin's model occurs at approximately 110° observer position, but the maximum SPL is significantly lower compared to the F1A prediction.

Hanson's model (diagram b) closely resembles the prediction from F1A in terms of contour shape. However, the maximum SPL in Hanson's model is shifted towards higher observer positions. While the overall SPL is significantly lower than F1A, the general shape of the contour lines remains similar.

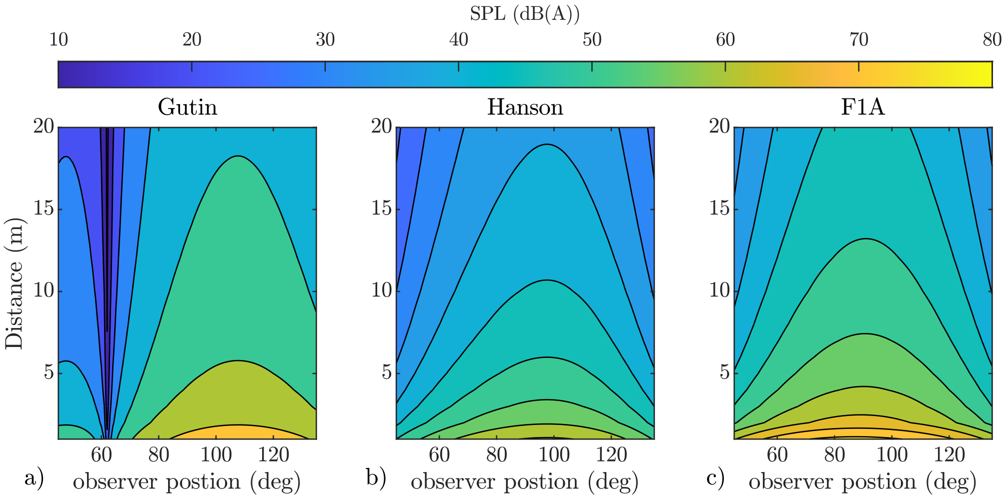

Figure 3.24: SPL predictions with the three tonal noise models for different distances and observer positions (4-bladed propeller)

Next, the comparison for different blade numbers at a constant distance is evaluated. Fig. 3.25 presents the SPL results at a distance of 10 m. Diagram a) of fig. 3.25 shows the result for the two-bladed, diagram b) for the three-bladed, and diagram c) for the four-bladed reference propeller. The y-axis represents the A-weighted SPL.

The trend of the noise prediction remains independent of the blade number. Gutin's model is affected by a cancellation region around 60° to 70° observer position. This cancellation region shifts towards lower observer positions as the blade number increases. Additionally, Gutin's model predicts the highest SPL values, whereas Hanson's model underpredicts the SPL by approximately 7 dB(A) compared to the F1A prediction. The trend predicted by Hanson's model aligns with the trend observed in the F1A prediction.

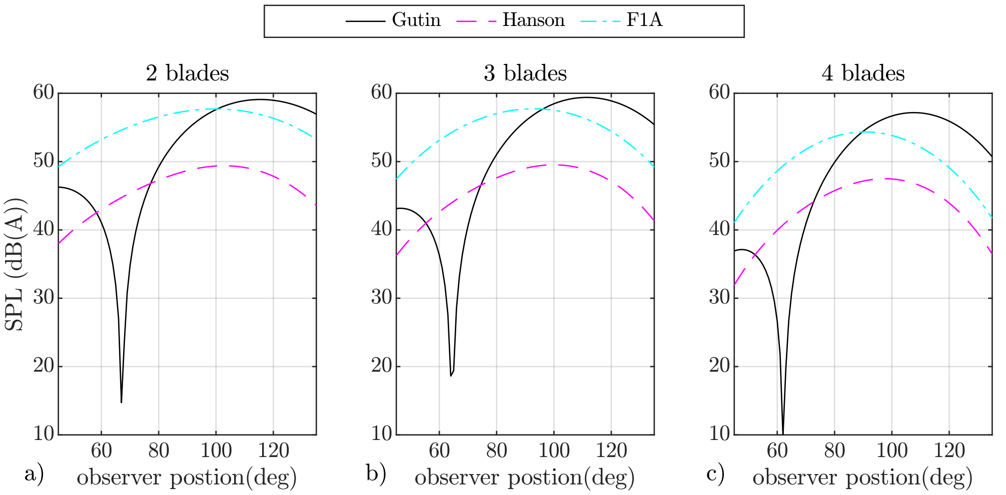

Figure 3.25: Comparison of the tonal noise models for different blade numbers at a distance of 10 diameters

The peak values and corresponding observer positions are presented in table 3.2 for all three blade numbers and models. A comparison of the maximum values shows that the SPL does not change from two to three blades but decreases from three to four blades. However, the location of the peak value shifts towards lower observer angles in all cases.

The last column of the table highlights the differences between the two-bladed and four-bladed propellers. The different models predict varying SPL reductions and observer position shifts between the two-bladed and four-bladed configurations. The results from Gutin's model are similar to those from the F1A prediction. However, Hanson's model exhibits significant discrepancies, indicating that this model is not capable of accurately predicting the influence of different blade numbers.

Table 3.2: Positions and peak values of the SPL prediction for different models and blade numbers

			2 Blades	**3 Blades**	**4 Blades**	**$\Delta 4-2$**
Gutin	**SPL**	dB(A)	59.1	59.4	57.2	2.9
	Pos.	deg	115	112	107	8
Hanson	**SPL**	dB(A)	49.4	49.5	47.5	1.9
	Pos.	deg	103	100	98	5
F1A	**SPL**	dB(A)	57.7	57.7	54.3	3.4
	Pos.	deg	100	93	91	9

After evaluating the dependency on the azimuthal observer position, the radial dependency for the three propellers is assessed. Fig. 3.26 illustrates the noise reduction with increasing normalised distance, following the representation of the evaluation of the distance law in fig. 3.6. The x-axis represents the distance, which is normalised by the propeller diameter and displayed on a logarithmic scale.

The analysis of the F1A curve reveals that beyond 3 diameters, the SPL decay is -6 dB(A) for a doubling of the distance, consistent with the behaviour of Gutin's and Hanson's models. In the near field of the propeller, the slope of the F1A model changes due to the near-field and ultra-near-field terms in the prediction. Hanson's model shows an offset of 7 dB(A) compared to the other curves. Gutin's and the F1A predictions align perfectly for the two-bladed propeller. However, as the number of blades increases, an offset occurs between Gutin's model and the F1A model.

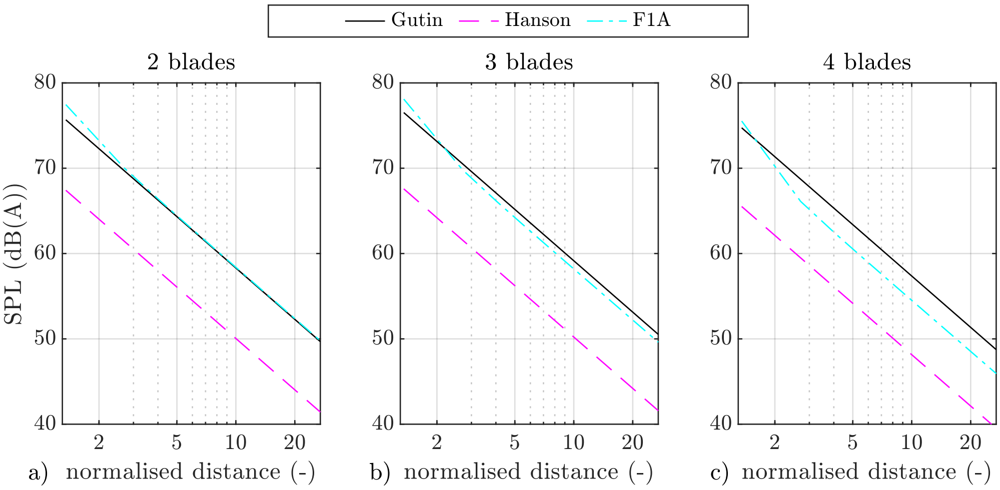

Figure 3.26: Comparison of the distance-dependent SPL prediction of the tonal noise models for different blade numbers at 110° observer position

The initial analysis of different observer positions and blade numbers reveals that Hanson's model does not predict the same SPL variation due to changes in blade number as the validated F1A formulation. Additionally, Hanson's model predicts SPL values that are 7 dB(A) lower compared to the F1A prediction. Gutin's model exhibits severe noise cancellation at observer positions between 60° and 70°. However, the peak values predicted by Gutin's model are similar to those of the F1A prediction. As the blade number increases, greater differences between the F1A prediction and Gutin's model become apparent.

3.4.2 Wind Speed Comparison

The second step of the assessment involves comparing the behaviour at different wind speeds. In this case, the propeller remains stationary (except for rotation), and the observer sweeps from upstream to downstream, as in the previous study. This assessment is similar to the second validation case (cf. section 3.3.1). The analyses are performed at a constant distance of 10 propeller diameters.

Fig. 3.27 shows the SPL predictions of the different models at varying advance ratios and observer positions. The y-axis represents the advance ratio. As in section 3.4.1, the second assessment begins with contour plots for the different models and the four-bladed reference propeller.

The F1A prediction (diagram c) shows no significant influence of advance ratio variation on noise emissions, as the emissions are dominated by thickness noise. Thickness noise is unaffected by changes in loading, which explains the absence of variation for different wind speeds.

In contrast, Gutin's and Hanson's models exhibit an influence of the advance ratio on noise emissions. Gutin's model shows a significant effect due to the absence of a term for thickness noise, as it is primarily driven by thrust and power consumption. Both thrust and power consumption decrease with increasing advance ratio, leading to a reduction in noise emissions.

Hanson's model, in theory, should account for thickness noise. In the current case, however, thickness noise is not dominant according to Hanson's model in the low advance ratio regime. Beyond an advance ratio of 0.4, thickness noise becomes dominant, which explains why no variation in noise emissions is observed above this value.

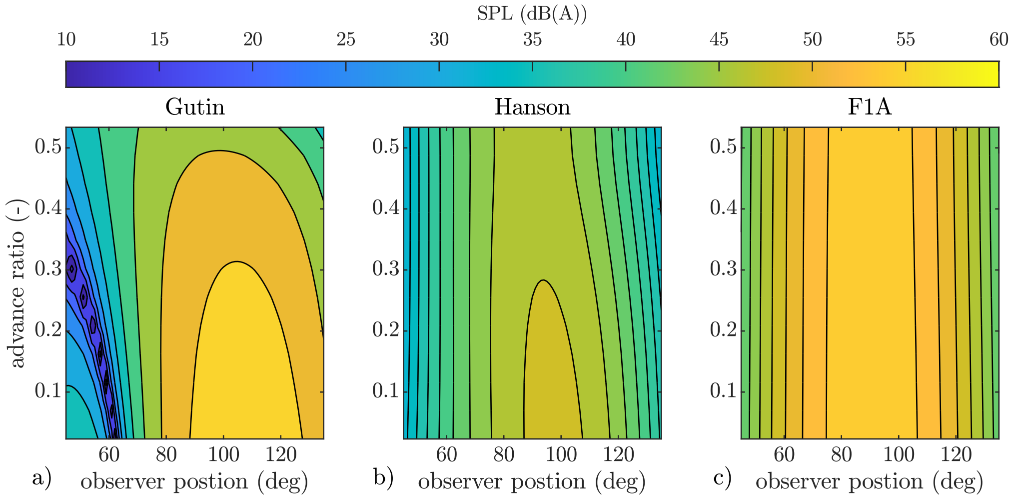

Figure 3.27: SPL prediction with the three tonal noise models for different advance ratios and observer positions (4-bladed propeller)

In the second step, the noise reduction with increasing advance ratio at an observer position of 110° is analysed for the two-, three-, and four-bladed propellers. Fig. 3.28 shows the comparison, with the advance ratio on the y-axis. As in the assessment of blade numbers in the previous study (cf. fig. 3.25 and 3.26), all three diagrams exhibit similar trends.

However, the F1A prediction reveals differences between the blade numbers. A reduction in the number of blades, while maintaining the blade geometry and operational conditions (rotational speed, pitch, and wind speed), leads to an increase in blade loading. Although the disk loading decreases, the blade loading increases. Consequently, tonal noise increases, and the two- and three-bladed propellers exhibit an advance ratio dependency.

Gutin's model is not suitable for this analysis due to the absence of a thickness noise prediction. It incorrectly predicts a noise reduction of approximately 10 dB(A).

Hanson's model shows a noise reduction for all three blade configurations. However, a plateau is observed in the advance ratio range from 0 to 0.2 for the two-bladed case, and a similar trend is seen for the three-bladed case. In this range, the blade thrust does not change significantly. As previously noted, in the high advance ratio regime, loading noise becomes dominant. This leads to a transition from loading noise dominance to thickness noise dominance.

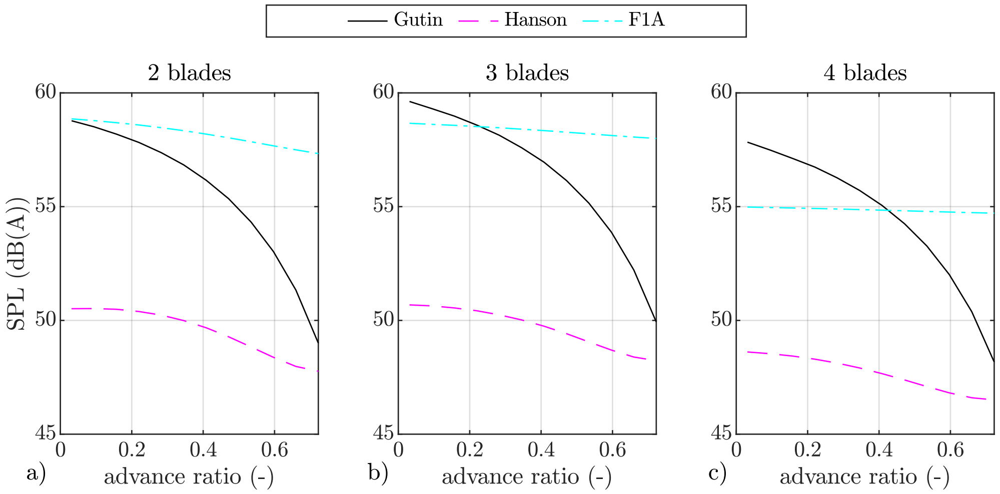

Figure 3.28: Comparison of the tonal noise models for different blade numbers and advance ratios at a distance of 10 diameters and 110° observer position

3.4.3 Overflight Comparison

The third step of the assessment consists of a constructed overflight scenario with a variable distance between the observer and the emitter. The propeller operates at an overflight height of 10 diameters. The overflight is performed at different flight speeds with a constant rotational speed of 3500 rpm. The pitch of the propeller remains unchanged, resulting in a reduction of thrust with increasing flight speed.

Since Gutin's and Hanson's model do not support transient manoeuvres with variable distances, each point in fig. 3.29 is calculated as a quasi-steady operational point.

Fig.3.29 illustrates the setup of the overflight comparison. At each circle the a quasi-steady operating point is assumed with the a certain flight speed but a constant observer position.

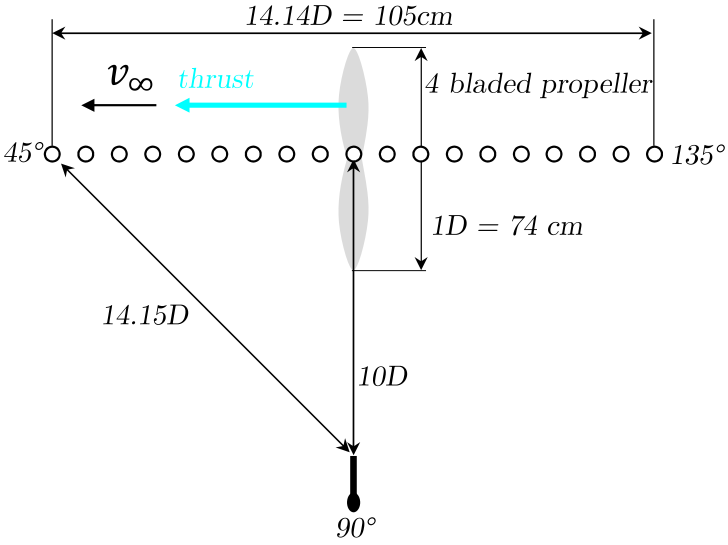

Figure 3.29: Experimental setup of the overflight scenario

The results presented are influenced by the Doppler effect, as described in eq. (3.11) and illustrated in fig. 3.5. Therefore, the noise emissions predicted by Gutin's and Hanson's model are expected to be higher for larger advance ratios and around the propeller plane compared to fig. 3.27. However, the reduction in loading with increasing advance ratio counteracts the increase caused by the Doppler effect.

Fig. 3.30 follows the same structure as fig. 3.27 but incorporates the Doppler effect. The behaviour of Gutin's model in fig. 3.30 remains consistent with that shown in fig. 3.27. Hanson's model and the F1A model, however, display curved contour lines compared to the previous results, as a consequence of the Doppler effect. Additionally, Hanson's model predicts an increased SPL for higher advance ratios around the propeller plane. This increase is not observed in the F1A prediction.

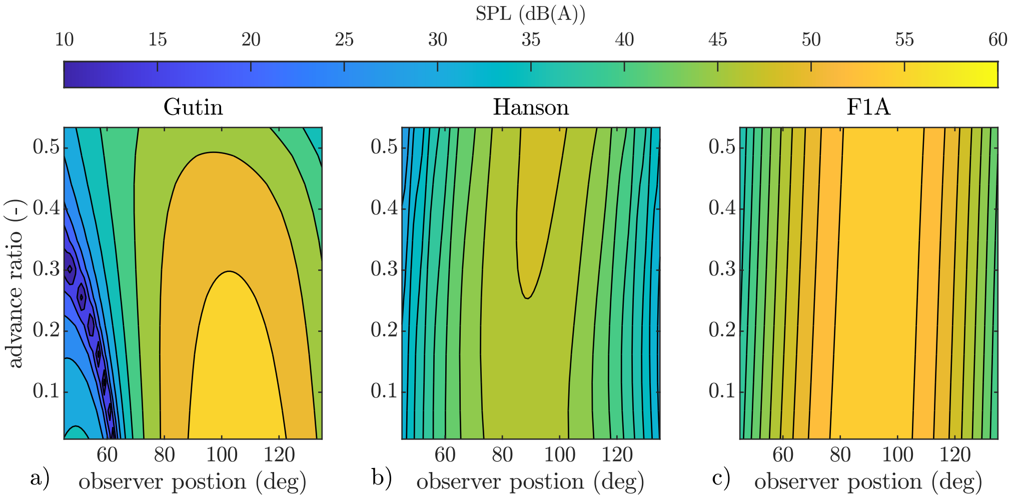

Figure 3.30: SPL predictions with the three tonal noise models for different advance ratios in the overflight scenario (4-bladed propeller)

The figures providing more details for different blade numbers or advance ratios do not offer significant additional insights. Therefore, this analysis is omitted from the main body but is available in appendix C.

The assessment of the three models with varying blade numbers, operational conditions, and observer positions reveals that Gutin's model and Hanson's model do not exhibit the same behaviour as the F1A model, which has been validated with experimental data. The following findings result from this assessment:

1. Gutin's model has noise cancellation at around 60° which is not present in the other models.
2. Gutin's model is sensitve to advance ratio changes leading to wrong behaviour for different flight speeds.
3. Hanson's model predicts about 7 dB(A) smaller SPL compared to the F1A model.
4. Hanson's model does not show the correct trend of variable blade number.
5. Hanson's model has a mismatch between loading and thickness noise compared to the F1A model.

The findings present critical issues to the application of Gutin's and Hanson's models in an optimisation routine. Both models exhibit inconsistencies, leading to incorrect behaviour when operational or geometrical conditions are altered. As a result, only the F1A model is employed in the subsequent optimisation framework.

Further comparisons between these models are not available in the literature. Although both models have been validated in standalone publications for single operating points, no direct comparisons have been conducted [43, 70, 72, 91, 104].

The analysis of tonal noise prediction, in comparison with the validation of Farassat's formulation 1A, partially addresses the second research question:
RQ 2 - Which aeroacoustic simulation method enables accurate prediction of noise from electrically driven GA and AAM propellers in conceptual design?
Only Farassat's formulation is capable of consistently predicting tonal noise emissions across a wide range of operating conditions. Therefore, Farassat's formulation must be applied for tonal noise emission prediction.

A temporal discretisation of 540 points per revolution with a spatial step size of 2.5% of the radius is required. Tonal noise can only be accurately assessed around the propeller plane, from observer positions approximately between 45° and 135°.

This assessment is not sufficient to fully answer the second research question. It remains uncertain whether broadband noise modelling is essential for analysing noise emissions of AAM vehicles. This aspect of the research question 2 is addressed in section 5.4.

4 Propeller Design Procedures

In general, propeller parameters can be divided into three main categories. First, the global parameters describe the propeller system.[1] Second, the blade shape parameters determine the aerodynamic and aeroacoustic performance of the system. Third, the details play an important role in aeroelasticity and manufacturing.[2] The combination of global and blade shape parameters defines the operational response of the propeller. A detailed blade shape optimisation cannot proceed before the global parameters are defined. Once the blade shape is determined, details such as the location of the quarter chord line, sweep and lean, or the tip and hub design become important. Tab. 4.1 tabulates the design parameters according to their categories.

Table 4.1: Overview about the blade design parameters

Global Parameter	**Blade Shape**	**Blade Details**
Diameter	Airfoil distribution	Sweep distribution
Blade number	Twist distribution	Lean distribution
Pitch system	Chord distribution	Hub design
Motor		Tip design

The propeller design and its parameters are subject to various aerodynamic and structural constraints in this thesis. First, constraints arise from the applied methodology. Second, the design must ensure stability and ground handling. Third, the designs must meet the manufacturer's requirements. They must be considered in the propeller optimisation process.

1. The blade tip Mach number must be smaller than 0.7 to avoid shock waves. Otherwise XFOIL cannot be used to generate the airfoil database.
2. The blade tip Mach number must be larger than 0.15 to improve XFOIL stability and maintain the underlying assumptions of BEMT.
3. The aspect ratio of the blade should be higher than 6 to maintain the underlying assumptions of BEMT.
4. The hub chord length should be smaller than 20% of the diameter for realistic and producible geometries.

---

[1] The pitch system and the motor are not directly parameters of the propeller geometry, but they have a significant influence on the overall design of the propeller, which is why they have to be listed in the global parameter section.

[2] It could be discussed if the airfoil distribution belongs in the blade shape parameter list or in the list of details. The performance influence of the airfoils is less relevant than the twist and chord distribution, but the airfoils have to be carefully chosen for a specific application.

5. The chord ratio between tip and hub (taper ratio) should be between 0.2 and 1 for realistic and producible geometries.
6. A minimum chord length must be maintained to provide sufficient space for the internal structure.
7. The relative thickness must be at least 10% at the root and at least 7% overall to ensure sufficient space for the internal structure.
8. The trailing edge thickness must be at least 1 mm to ensure stability and ground handling.

The aspect ratio equals the ratio of the propeller radius to the projected blade area. The definition is provided in eq. (4.1).

$$AR = \frac{R^2}{A_{Blade_{projceted}}} = \frac{R}{\bar{c}} \tag{4.1}$$

This chapter is divided into three subchapters. First, section 4.1 describes the aerodynamic design procedure for a single operating point according to the minimum induced loss (MIL) condition. An example uses the reference propeller parameters for a new design and shows the results of the MIL design. Second, the structural design of a propeller is briefly described, with extensive details available in Felix Möhren's dissertation. Third, section 4.3 introduces a novel multidisciplinary design strategy. This method was first presented by the author in Ref. [11]. In three steps, the design routine is outlined. First, the general optimisation process is explained. Second, the optimisation of the global parameter space is described. Finally, the blade shape optimisation is addressed. The optimisation of the blade details is not presented in this thesis because it is mainly driven by structural constraints discussed in Felix Möhren's thesis [112].

4.1 Aerodynamic Minimum Induced Loss Design

Based on potential theory, Betz [13] derived that the energy loss on a propeller is related to the kinetic energy of its wake. He demonstrated that, to minimise induced losses, the axial induced velocity must remain constant across the propeller plane, similar to wing aerodynamics. Betz first derived the theory for weakly loaded propellers in Ref. [13] and later extended it to highly loaded propellers in Ref. [12]. The result of Betz's MIL condition is that the circulation (eq. (2.39)) must be constant along the blade. The circulation for MIL is defined in eq. (4.2).

$$\Gamma = \frac{2\pi v_\infty w_a}{N_b \omega} G \tag{4.2}$$

G is the Goldstein function defined in eq. (4.3), which simplifies the relation by employing Prandtl's tip loss function stated in eq. (2.43) and a relation between the tangential and axial velocities given in eq. (4.4) [56]. Eq. (2.39) is applied to reconstruct the propeller geometry.

$$G = \frac{Fx^2}{x^2 + 1} \tag{4.3}$$

$$x = \frac{\omega r}{v_\infty} \tag{4.4}$$

Larabee [95] was the first to convert MIL into a computer program, although he did not consider the influence of airfoil drag. Adkins and Liebeck [1] addressed this simplification by publishing the first computation scheme for MIL design that also considers airfoil drag. Both Larabee and Adkins and Liebeck employed the concept of a constant circulation along the blade to calculate the blade geometry.

The following enumeration outlines the procedure of Adkins and Liebeck without detailing the solving algorithm. The procedure begins with an initial chord and twist distribution, arranged appropriately to accelerate the process, and an initial Γ. The initial Γ may be zero.

1. Determine the values of Prandtl's tip loss function and the helix angle Φ at each blade station.
2. Determine the product of resulting velocity w and chord length c at each blade station by the circulation equation (eq. (2.39)) and thereby the Reynolds number.
3. Determine the angle of attack for the optimal lift to drag ratio from the airfoil section data with the corresponding Reynolds number.
4. Add the optimal angle of attack to the helix angle to obtain the twist distribution.
5. Determine the induction factors according to eq. (2.32) and (2.33).
6. Calculate the resulting velocity w with the induction factors according eq. (2.38)
7. Compute the chord length from the product $w \cdot c$ from step 3. Recalculate the solidity σ
8. Determine the new Γ at an arbitrary section with eq. (4.2)
9. Determine the new thrust or power consumption depending on the requirement
10. Start over, if this new value for Γ is not sufficiently close to the old one (e.g., within 0.1%) at step 2 using the new Γ.

The circulation computation is adapted to consider thrust or power requirements [1, 95]. This procedure results in long chord lengths at the hub and high twist angles, as it strives to establish a constant Γ along the blade. Such propeller designs are challenging to manufacture, necessitating limitations. These limitations lead to discrepancies between the intended and actual propeller performance. Moreover, maintaining constant circulation along the blade prevents modifications of the blade at the hub. Consequently, a different design scheme has been developed. The novel procedure requires significantly more computational time compared to the method of Adkins and Liebeck. While Adkins and Liebeck's approach was developed for the computational power available in 1994, the new method leverages the power of 2020-era computers and requires only a fraction of a second to design the propeller on a standard computer.

The novel procedure calculates the optimal induced velocity using simple momentum theory (eq. (2.29)). The resulting optimal angle of attack distribution is used as a starting point. In an iterative scheme, the procedure computes the optimal propeller geometry by applying the MIL condition and the general momentum theory as described in section 2.3.1.1.

1. Apply BEMT to the new propeller geometry to calculate thrust and power consumption.

2. Apply a chord length correction by adjusting the entire chord length according to the relative error from the target values (relative thrust or power deviation).
3. Reapply BEMT to the adjusted propeller geometry.
4. Calculate the angle of attack distribution. Correct the local twist distribution to match the optimal angle of attack for the airfoils at the corresponding Reynolds numbers.
5. Reapply BEMT to the adjusted propeller geometry.
6. Equalise the induced velocities along the radius to achieve a homogeneous distribution by adjusting the chord length distribution.
7. Repeat the procedure from step one until the thrust or power requirements are met.

In each iteration, smoothing algorithms can be applied to achieve a continuous geometry. The geometry is constrained by outer limits as stated in the beginning of chapter 4.

The new procedure is applied on the operating conditions of the four-bladed reference propeller to demonstrate the benefits of the novel single point design approach. Therefore, the novel MIL design approach uses the geometric and operational properties of the reference propeller as input.

The reference propeller, operating at 3500 rpm in hover, produces 152 N of thrust with a torque of 6.53 Nm, equating to a power consumption of 2.39 kW. This performance corresponds to a Figure of Merit (FoM) of 0.762 and a thrust-to-power ratio (TtP) of 63.3 N/kW. Furthermore, the reference propeller has a maximum SPL at a distance of ten diameters of 72.2 dB. These values were calculated using BEMT theory in conjunction with general momentum theory, Prandtl tip and hub loss corrections, sweep corrections, 3D stall corrections, and Farassat's formulation 1A, along with the BPM broadband model for noise prediction.

Based on these performance metrics, the same thrust, rotational speed, number of blades, diameter and airspeed are used to evaluate the design procedure. The selected airfoils for the MIL design are NACA-44XX digit airfoils, with 16% thickness at the hub and 8% thickness at the tip.

Fig. 4.1 provides a geometric comparison between the new design and the reference propeller. Diagram a) shows the chord length distributions, diagram b) the twist distributions, and diagram c) the relative thickness distributions. In these diagrams, the solid black line represents the reference propeller, while the magenta dashed line corresponds to the MIL design.

The comparison shows that the MIL procedure results in larger chord lengths compared to the reference propeller. Furthermore, the twist distribution increases at the hub due to the MIL condition but the MIL twist distribution matches the reference propeller in the relevant region of the blade. Propeller manufacturers avoid this behaviour because it complicates the manufacturing process. Higher twist distributions require thicker production moulds, which are milled from aluminium. This increases costs, while the impact on aerodynamic efficiency is minimal.

The thickness distribution shown in diagram c) for the MIL design decreases linearly, while the thickness distribution of the reference propeller varies. The relative thickness reaches a maximum at a 15 cm radius, then decreases towards the tip, but increases again beyond 32 cm radius. This thickness distribution results from the swept planform of the geometry.

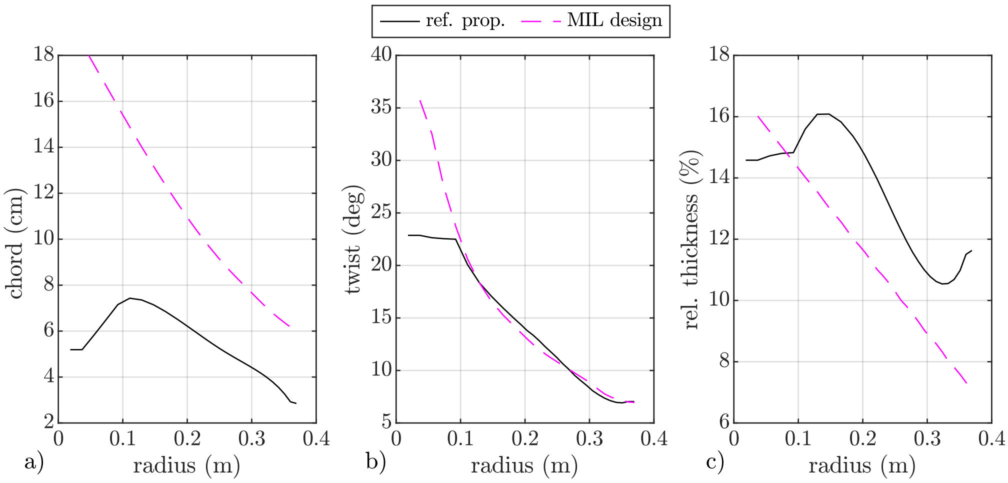

Figure 4.1: Comparison of the reference geometry and MIL geoemtry

Table 4.2 compares the aerodynamic and acoustic performance of the reference propeller with the newly designed propeller. Both propellers deliver the same thrust at the design point.

On the positive side, efficiency is significantly improved:

1. The thrust-to-power ratio increases by 3.5%.
2. The FoM rises by 2.7e-2.

However, the comparison also highlights drawbacks of a purely aerodynamic optimisation. Specifically, noise emissions increase by 2.6 dB, primarily due to a significant rise in thickness noise (cf. appendix E.1). Even if the relative thickness is reduced as shown in fig. 4.1, the absolut thickness increases due to the enlarged chord length.

Table 4.2: Performance and noise emission comparison between the reference and MIL design

		Reference	**MIL Design**
Thrust	(N)	152	152
Torque	(Nm)	6.53	6.32
Thrust/Power	(N/kW)	63.3	65.5
Figure of Merit	(-)	0.762	0.789
max. SPL	(dB)	72.2	74.8

Appendix E.1 provides further details comparing the reference propeller with the new design. The analysis reveals that, on one hand, the hover performance is significantly improved. On the other hand, the performance for higher advance ratios is worse because the propeller is designed to operate in hover. The maximum achievable advance ratio is reduced from 0.55 to 0.45.

The comparison highlights the need for a multidisciplinary design scheme to optimise noise emissions while maximising aerodynamic performance across an entire mission, rather than focusing solely on a single design point.

4.2 Structural Design Procedure

The structural layout of the propeller is closely related to the manufacturing process and the materials used. The MIL design often aims to minimise the chord length at the tip while exponentially increasing the chord length at the hub. Additionally, the twist at the hub is significantly increased, as the MIL procedure seeks to flatten the induced velocity distribution. To comply with the minimal and maximal producible chord lengths, both the tip and hub must be adjusted within the design scheme.

In collaboration with his co-worker Felix Möhren, the author demonstrates in Ref. [113] that, for certain applications, the structural layout can be optimised in a separate step using a pre-deflection analysis (PDA). The PDA generates the jig-shape of the propeller, which results in the desired flying shape under load conditions. This procedure adjusts the twist distribution to match the aerodynamic performance at the design point.

Secondly, aeroelastic tailoring, which modifies the material properties, can be applied to align the aeroelastic performance with the desired performance of the rigid propeller [114].

The PDA requires a structural model and initial structural parameters. An initial set of parameters is defined by a design engineer. In the first step, the structural layout of the propeller is designed to meet the static strength requirements under specific conditions with a safety factor of two.

The structural model uses one-dimensional piecewise straight finite beam elements with arbitrary orientation in space. The deformations are calculated according to moderate deflections theory. The preprocessor determines the cross-sectional stiffness data and the position of the shear center, tension center, and center of gravity with analytical formulations [54]. The theory is limited to thin-walled hollow cross-sections with general anisotropic material behaviour. Classical laminate theory determines the stiffness of anisotropic materials [139]. Orthogonal projection transfers the aerodynamic loads determined at the quarter-chord line onto the elastic axis. Further information about the modeling approach can be obtained from Ref. [117] and [115] and the dissertation of the co-worker Felix Möhren.

4.3 Multidiciplinary Aeroacosutic Optimisation

Different numerical optimisation schemes are used in the literature for propeller optimisation. The genetic algorithm (GA) can be parallelised and is capable of multi-objective design, which is required to find the Pareto front between noise emissions and energy consumption [64, 94]. Additionally, the GA does not require differentiation, which is not available for discrete values like the number of propellers or blades. Other gradient-free and gradient-based optimisation algorithms can be applied for propeller optimisation [51]. However, this thesis does not explore different optimisation algorithms. Instead, the fundamental procedure of analysing the parameter space using a stepwise approach is assessed. The procedure is presented in fig. 4.2.

MATLAB© offers various optimisation schemes, such as the GA, which are commonly used for propeller optimisation. The author developed an optimisation scheme that increases fidelity and calculation effort in three steps, as presented in fig. 4.2. In each step, the MDO calculates a Pareto front. The sweet spot of the Pareto front, defined in eq. (4.13), as the minimum distance to the utopia point to the Pareto front, defines the inputs for the next optimisation step.

At first, the global propeller parameters listed in table 4.1 are optimised in the global propeller parameter optimisation (GPPO). In this design stage, aircraft parameters are considered to find an appropriate propeller and reduce the parameter space for blade shape optimisation (BSO). The chord and twist distribution are optimised in the second step. In the final step, details of the blade are optimised under aeroacoustic and aeroelastic considerations (BDO).

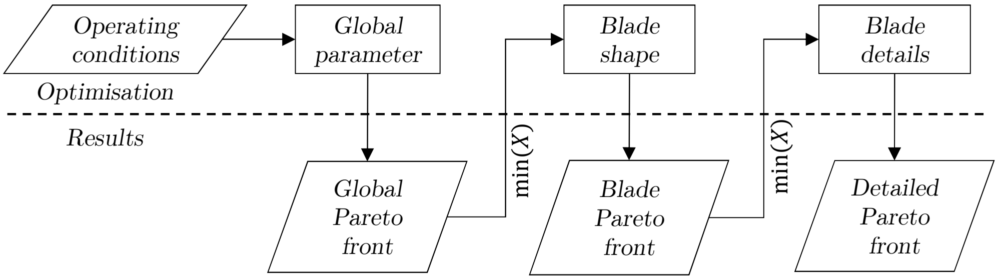

Figure 4.2: Propeller design strategy

Within the MDO approach, the aerodynamic is modelled using the derived BEMT approach; a general momentum theory, coupled with the 3D stall model, Prandtl's tip and root loss correction, and sweep correction. The tonal noise emissions are calculated using Farassat's formulation 1A. Furthermore, the influence of broadband noise and different acoustic weighting functions are assessed in section 5.2. The structural mechanics are modeled using a one-dimensional Timoshenko beam theory, as described in Ref. [116]. However, the structural optimisation is part of the dissertation of Felix Möhren.

4.3.1 General Optimisation Procedure

Within the MDO, four basic steps are performed:

1. A blade geometry is created.
2. A category one mass model is applied to predict the propeller and motor mass.
3. The aerodynamic performance of the geometry for the mission is calculated.
4. The aerodynamic performance is matched with a motor map to calculate the electric energy consumption.
5. The noise emissions are predicted.

At first, a propeller geometry is designed according to the design strategies (DS) described in paragraphs 4.3.2 and 4.3.3. The generated geometry is then preprocessed for aeroacoustic analysis.

Secondly, a *category one method*[3] predicts the propeller and motor mass. In hover conditions, where the propeller carries the entire weight of the aircraft, the propeller and motor mass significantly influence aircraft performance. In forward flight, where a wing lifts the aircraft, the propeller is used to overcome drag, which is why the influence of mass is less pronounced but still present. As the diameter (and number of blades) increases, the required torque also increases, leading to a rise in motor mass. Additionally, a variable-pitch system is significantly heavier than a fixed-pitch propeller.

The required thrust is adjusted by eq. (4.5), where the lift-to-drag ratio L/D influences the required thrust T_{Req}. The target thrust T_T represents the thrust required by the aircraft to complete its mission without accounting for the unknown mass of the propulsion system. The masses are multiplied by the gravitational acceleration g to determine the additional forces.

$$T_{\mathrm{Req}} = T_T + \frac{g \cdot (N_B \cdot m_B + m_H + m_M)}{(L/D)} \tag{4.5}$$

The propeller mass is calculated as the blade mass m_B multiplied by the number of blades N_B, plus the additional mass for the hub m_H. The blade mass can be estimated using an empirical relation, as defined in eq. (4.7)[4], and the activity factor AF [2]. The AF quantifies the blade surface area normalised by the diameter D and is calculated as an integral from the hub to the tip over the chord length c_r and the radius r.

$$AF = 10^5/D^5 \int_{\mathrm{hub}}^{\mathrm{Tip}} c_r \cdot r_r^3 \, dr \tag{4.6}$$

$$m_B = 2.2 \cdot 10^{-3} \cdot (D \cdot 3.28084)^{2.3} \cdot (0.456 \cdot AF) \cdot 0.453592 \cdot 0.85 \tag{4.7}$$

---

[3] A category one method is a purely empirical relationship that provides physical quantities based on top-level requirements.

[4] The diameter must be entered in metres in the empirical relation.

The hub mass m_H is estimated as a fraction of the total propeller mass. The hub of a variable-pitch propeller is approximately 60% of the propeller mass. In contrast, the hub of a fixed-pitch propeller is significantly lighter, making up only about 5% of the propeller mass [135].

$$m_{H,\text{variable-pitch}} = 0.6 \cdot N_B \cdot m_B \tag{4.8}$$

$$m_{H,\text{fixed-pitch}} = 0.05 \cdot N_B \cdot m_B \tag{4.9}$$

The motor mass m_M is estimated using an empirical relation, in which the mass depends on the maximum shaft power according to eq. (4.10). An optimistic empirical value of 5 kW/kg is used for this prediction [46]. The power density of electric motors varies widely, with values ranging from 0.09 kW/kg [120] to a potential maximum of 10 kW/kg in the future [150].

The shaft power can be estimated based on the ideal power consumption of the propeller. In hover conditions, the ideal power is calculated using the ideal Figure of Merit (FoM=1) (eq. (2.19)), while in flight conditions, it is determined using the ideal propulsive efficiency ($\eta = 1$) (eq. (2.18)). However, ideal efficiency cannot be achieved in practice. Therefore, an efficiency of 65% is assumed for the mass prediction.

$$m_M = \frac{\frac{P_{\text{ideal}}}{0.65\%}}{5kW/kg} \tag{4.10}$$

The maximum power consumption is determined by calculating the ideal power consumption at each operating point. The calculation of the FoM requires information about the propeller disk area A_p, the density ρ, and the thrust T. Similarly, the calculation of the propulsive efficiency depends on the flight velocity v_∞.

Since the disk area is unknown during the optimisation process in the GPPO stage, these calculations must be performed at each optimisation step. Higher-order electric motor models, which take into account the required torque and rotational speed of the propeller, are available [108, 121, 127]. However, these models require an iterative scheme involving torque, rotational speed, motor mass, and efficiency, which significantly increases computational effort.

If a torque approximation for a propeller is available, a mass fraction of 1 $\sim$10 Nm/kg can be assumed [123].

Thirdly, the geometry is analysed at all operating points to ensure it meets the mission requirements. During the mission analysis, the rotational speed is varied at each operating point to verify whether the target thrust at the design point can be achieved. The rotational speed is constrained by the predefined minimum and maximum allowable blade tip Mach numbers.

An iterative scheme with a second-order polynomial fit of the thrust curve is used to determine the rotational speed corresponding to the target thrust and power consumption. Calculating the target rotational speed based on the non-dimensional thrust and power coefficients is not feasible due to the influence of Mach and Reynolds numbers.

The mission analysis is used to determine the total energy consumption throughout the mission. The energy consumption of a mission is a well-suited measure of propeller efficiency, as it integrates multiple operating conditions with their respective durations.

Thus, the aerodynamic efficiency across various design points can be reduced to a single variable by summing the time-weighted power consumption of each operating point. Eq. (4.11) represents the summation of different operating points i, weighted by the duration of each operating point t. For a mission-independent comparison, the energy consumption is normalised by the total mission time τ.

$$W = \frac{1}{\tau} \sum_{i=1}^{n} P_i \cdot t_i \tag{4.11}$$

The calculation of energy consumption can be extended by incorporating a motor and pitch system model. For a blade pitch system, power consumption must be evaluated for different pitch angles. The optimal pitch angle for each operating point is determined by identifying the angle that minimises power consumption.

If a motor is considered, the propeller torque and rotational speed determine the motor's efficiency η_m at each operating point. The motor efficiency is then used to compute the electric power consumption, which is subsequently minimised. If a specific motor is available, its efficiency map can be utilised; otherwise, a generic motor efficiency map is required.

To address this, the authors developed a generic motor efficiency map, as shown in eq. (4.12), by scaling efficiency from the minimum to the maximum required rotational speed and torque, incorporating additional safety factors.

$$\eta_M = \frac{P_P}{P_{\text{in}}} \tag{4.12}$$

The generic motor map is generated after the mission analysis has been performed and the required ranges for rotational speed, torque, and shaft power are known.

The motor map is constrained to 120% of the maximum power consumption of the propeller. The motor efficiency map is created with a target motor efficiency η_m of 98% at 20% of the torque range and 20% of the rotational speed range.

At each operating point, the motor efficiency is interpolated from the map based on the required torque and rotational speed. Using the motor efficiency, the required electric power input of the motor P_{in} can be determined from the required power of the propeller P_P.

Fig. 4.3 presents the generic motor map, with its design point at approximately 40 Nm torque and a rotational speed of 1200 rpm. The upper-left corner is constrained by the maximum torque of the propeller. The upper-right region is limited by the maximum output power of the motor. The right boundary is defined by the motor's maximum rotational speed.

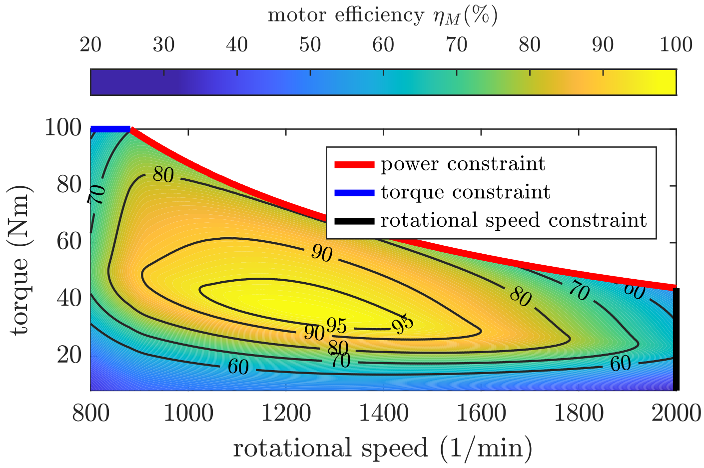

Figure 4.3: Example of a generic motor efficiency map

In the final step, noise emissions are analysed at a specified observer distance and operating point. Variations in maximum noise emission directivity, resulting from geometric changes and variations in rotational speed, are accounted for by performing an angular sweep from upstream to downstream at the defined observer distance. The highest SPL observed across these positions determines the maximum noise emissions.

A weighting function is required to balance energy consumption and noise emissions. The weighting function X is defined as the distance from an utopia point to the data set (eq. (4.13)). The utopia point is located at the minimum SPL and energy consumption on the Pareto front.

The SPL can be expressed in decibels (dB), A-weighted decibels (dB(A)), or D-weighted decibels (dB(D)). SPL and energy consumption are weighted to adjust the relative importance of energy consumption and noise emissions using the weighting exponents x_W and x_{SPL}. In the current study, values of $x_W = 1$ and $x_{SPL} = 1$ are chosen. These exponents have been determined heuristically.

The minimum value of the weighting function defines the sweet spot on the Pareto front.

$$X = \sqrt{\left(\left[\frac{W - \min(W)}{\min(W)}\right]^2\right)^{x_W} + \left(\left[\frac{SPL - \min(SPL)}{\min(SPL)}\right]^2\right)^{x_{SPL}}} \tag{4.13}$$

An additional noise balancing between different operating points is required if multiple operating points need to be acoustically considered. The acoustic balancing can be achieved using a logarithmic sum of the SPL over each operating point, as defined in eq. (4.14).

$$SPL_{\Sigma} = 10 \log \left(\sum_{i=1}^{n} 10^{\frac{SPL_i}{10}} \right) \tag{4.14}$$

The presented aerodynamic, acoustic, and structural models meet the requirements of an MDO by being both sufficiently accurate and computationally highly efficient. The aerodynamic and acoustic models are validated in section 2.4 and 3.3. The structural model is validated in the co-thesis of Felix Möhren. The above described methodology is summarised in a step-by-step procedure in appendix E.2.

4.3.2 Global Propeller Parameter Optimisation Procedure

The global propeller parameter optimisation (GPPO) determines the blade diameter, number of blades, and the most suitable pitch system (fixed or variable-pitch propeller) for the mission.

The geometry is designed using a simplified MIL approach for an arbitrary operating condition. The design variables therefore consist of the design thrust (T), the rotational speed, the flight speed (v_∞), the number of blades (N_B) and the diameter (D_P). From the derivation of the MIL condition, it is known that the axial-induced velocity (w_a) across the propeller plane should remain constant.

The induced velocity can be calculated using simple momentum theory, as given in eq. (2.29). The Prandtl tip loss factor F_{PTL} is applied to account for losses due to recirculation at the blade tip and vortices at the hub. This factor, originally derived by Betz in Ref. [13], modifies the induced velocity according to eq. (4.15).

$$w_{a,PTL} = w_a \cdot F_{PTL} \tag{4.15}$$

The chord distribution c_r must be calculated according to eq. (4.16) to match the thrust requirement of the design point. However, in a standard MIL approach, the chord distribution must be iteratively calculated during the propeller design process. This iteration is avoided by varying linear chord distributions to compute the propeller's thrust. The thrust calculation can be performed as a matrix multiplication, which is significantly faster than an iterative procedure.

The linear chord distributions are defined by the chord length at the hub and the taper ratio. The distribution that results in the lowest deviation from the design thrust is selected for the new geometry.

$$\frac{T}{N_B} = \int_{\text{hub}}^{\text{Tip}} \frac{\rho}{2} w^2 c_{l_{\text{opt}}} c_r \cos(\phi)\, dr \tag{4.16}$$

For the calculation of the resulting velocity w, a combination of eq. (2.20) and (2.38) is applied, neglecting tangential induced velocities, as in the simple momentum theory (SMT) described in eq. (2.29).

$$w = \sqrt{u^2 + (v_\infty^2 + w_{a,PTL}^2)} \tag{4.17}$$

The twist distribution θ is determined based on the helix angle ϕ (eq. (4.18)) and the optimal angle of attack α_{opt} of the airfoils (eq. (4.19)).

$$\tan(\phi) = \frac{v_\infty + w_{a,PTL}}{u} \tag{4.18}$$

$$\theta = \phi + \alpha_{\mathrm{opt}} \tag{4.19}$$

Within the design strategy for GPPO, the geometry can be determined without iterations. This is an enormous advantage for an optimisation scheme. The design strategy requires five optimisation parameters.

The primary advantage of the design strategy with MIL is its minimal computation time, as it does not require an iterative approach. Furthermore, the geometry is derived based on aerodynamic assumptions. However, its main limitation is that propeller geometries are constrained to a linear chord length distribution. Consequently, the design strategy is only suitable for defining global propeller parameters, such as the number of blades and the diameter, as well as assessing the pitch system.

4.3.3 Blade Shape Optimisation Procedure

The design strategy for blade shape optimisation (BSO) is based on the class shape transformation (CST) description [93][92]. The CST method represents the geometry using a set of polynomials for the twist, chord length, lean, sweep, and airfoil sections. The required polynomial order depends on the geometric complexity.

The CST description enables geometry modifications through simple adjustments of the spline parameters, making it well-suited for optimisation. One key advantage of the CST approach is that it ensures smooth blade geometries without discontinuities.

The diameter, number of blades, maximum and minimum root twist and chord, as well as the taper ratio, are preselected by the GPPO. While the blade diameter and number of blades are fixed by the GPPO, the design space for twist and chord is only constrained to a smaller range. As a result, the overall parameter space is significantly reduced.

The CST approach does not incorporate any aerodynamic considerations in the propeller design. An arbitrary blade geometry is generated by adjusting the CST parameters and then evaluated in the mission analysis.

A fifth-order polynomial defines the chord and twist distribution. As a result, twelve parameters must be evaluated in the BSO, consisting of two sets of six parameters to describe the polynomials.

The CST geometry is initialised using the sweet spot propeller from the GPPO. After initialisation, the blade shape can vary arbitrarily between the tip and the hub, while the overall design space constrains the hub and tip variables.

The advantage of BSO is that the blade can have arbitrary twist and chord distributions. Since propeller generation is merely a function evaluation, it is significantly faster than the MIL design in the GPPO.

However, the flexibility of allowing arbitrary blade shapes also presents a major drawback. Many generated geometries may not have the required blade forms to produce sufficient thrust. As a result, a significantly higher number of function evaluations is necessary. Following geometric constraints are applied to stabilise the geometry design process.

1. The twist distribution must constantly decrease from hub to tip.
2. The maximum and minimum chord length are constraint by the diameter and root chord length.
3. The chord length distribution is checked for minima and maxima along the blade. Only one local minimum or maximum is allowed along the blade to avoid oscillating geometries.

The presented procedures are assessed for a generic flight mission in the next chapter.

5 Design Studies

The previous chapters provided the necessary information about the aerodynamic and aeroacoustic models, as well as the optimisation strategies. These optimisation strategies are evaluated in this chapter.

The propeller design is conducted for an exemplary generic mission of a tilt-propeller or tilt-wing aircraft. The mission, presented in table 5.1, consists of a hovering phase of six minutes, a transition phase of twelve minutes, and a cruise phase of 48 minutes. Each operating point is treated as quasi-steady, without acceleration. Depending on the mission phase, different thrust requirements at varying flight speeds are prescribed. Additionally, the lift-to-drag (L/D) ratio is specified to determine the additional thrust required to lift the mass of the motor and propeller.

Table 5.1 provides the ideal power and ideal energy consumption for each operating point, calculated using either the ideal propulsive efficiency or the ideal Figure of Merit. The ideal hover power consumption depends on the propeller diameter, which is why a range of ideal energy consumption values must be provided. The diameter range is set between 1.5 m and 4 m. The ideal power is used to calculate the motor design power with the safety factor of 65% (cf. eq. (4.10)).

The comparison of the ideal energy consumption reveals that energy consumption is primarily driven by cruise conditions. Therefore, aerodynamic performance must be optimised for cruise, while noise emissions should be minimised in hover. The optimisation must balance overall energy consumption and noise emissions.

The lowest theoretical energy consumption is 8.87 kWs/s, obtained by summing the ideal energy consumption across all operating points. Noise emissions are evaluated at an observer-to-propeller hub distance of 10 m.

Table 5.1: Generic mission parameters

Design Point	**Thrust** (N)	**Velocity** (m/s)	**Duration** (min)	**L/D** (-)	**Ideal power** (kW)	**Motor design power** (kW)	**Ideal energy** (kWs/s)
Hover	1200	1	6	1	7.5 - 20.0	11.5 - 30.7	0.68 - 1.82
Transition	600	15	12	5	9	13.9	1.64
Cruise	300	30	48	10	9	13.9	6.55

In addition to the mission requirements, geometric constraints are needed. The geometry is constrained according to table 5.2. The root chord length and sweep are normalized with the propeller diameter. The sweep is defined as a tangential tip displacement. As in the previous section a NACA4416 airfoil is used at the hub and a NACA4408 airfoil at the tip. The relative thickness is reduced linearly, and the blade-tip Mach number (M_{tip}) is constrained to between 0.25 and 0.7.

Table 5.2: Geometric design space

Constraints		**Min**	**Max**
Blades	(-)	2	9
Diameter	(m)	1.5	4
Taper ratio	(%)	20	100
Root chord length	(%)	5	30
Root twist	(deg)	15	75
Tip twist	(deg)	0	40

First, section 5.1 presents the single-point design analysis for the reference mission. The influence of the number of blades, diameter, and design M_{tip} on aerodynamic and aeroacoustic performance is examined. In the first design study, the MIL procedure, as described in section 4.1, is applied for single-point optimisation in both cruise and hover. The assessment reveals overall trends and the need for a multi-dimensional approach.

Second, section 5.2 presents the multi-dimensional optimisation (MDO) as described in section 4.3. Section 5.2 examines the influence of acoustic weighting, the additional mass of the propeller and motor, and the motor efficiency map on the aeroacoustic results. In addition, the improvement of the blade shape optimisation using the CST approach, compared to global propeller parameter optimisation, is presented.

Third, section 5.3 shows the assessment of the optimised geometry in detail and provides the validation of the MDO approach with high fidelity CFD RANS simulations.

Finally, section 5.4 presents the lessons learned from the assessment of the optimisation approach.

5.1 Parameter Study for the Aeroacoustic Assessment of Geometric Parameters

In this section, the MIL approach is applied to design a propeller for cruise and hover conditions. In cruise, the propellers must generate a thrust of 300 N at a flight speed of 30 m/s, whereas in hover, the propeller provides 1200 N, as shown in table 5.1. The geometries are generated with varying blade numbers, diameters, and design rotational speeds. After the design process, acoustic emissions are evaluated for different observer positions at a fixed distance of 10 m.

Minor deviations from the target thrust may occur after the MIL design. If the required and target thrust do not match, the propeller is trimmed to achieve the required thrust within an accuracy of ±0.5%. Trimming is performed by adjusting the pitch after the MIL design.

The influence of the parameters on aerodynamic performance and noise emissions is analysed in three steps. First, the effect of the blade number on propeller performance and noise emissions in cruise and hover is examined. Second, the influence of diameter and M_{tip} is assessed for hover conditions, followed by the same analysis for cruise conditions in the third step. In each subsection, the impact of the parameters on aerodynamic performance is evaluated first, followed by the acoustic assessment.

The figures in the following subsections show A-weighted sound pressure levels for broadband and tonal noise. The SPL shown represent the maximum levels of the components, regardless of the position of the observer and at a constant distance. Due to the different directivity of tonal and broadband noise, the SPL values are not taken from the same observer position. Additional information of the parameter variation and results are presented in appendix F.1.

5.1.1 Assessment of the Blade Number

Initially, the influence of the blade number as a design variable on aerodynamic performance and noise emissions is assessed. The blade number varies from two to nine, as stated in table 5.2.

Therefore, the diameter and the design M_{tip} remain constant in this subsection. The diameter is set to 2 m, and the design M_{tip} is fixed at 0.3. This combination of design M_{tip} and diameter results in a rotational speed of 975 rpm.

As the blade number increases, the blade loading decreases, leading to small tip chords. A preliminary assessment indicates that higher tip speeds than 0.3 are not feasible because the chord length decreases with increasing design M_{tip}, resulting in excessively short tip chords for configurations with many blades. Consequently, the design M_{tip} is set to 0.3.

The preliminary assessment further reveals that the two-bladed hover propeller is constrained by the maximum allowable chord length of 30% radius. Therefore, the propeller must be pitched by +4.5° during the trimming process to meet the thrust requirement. The pitch corrections required for the other geometries remain below ±1° throughout the trimming process.

Since the +4.5° pitch adjustment affects the results, the two-bladed hover propeller is excluded from the main results and presented separately in the figures of section 5.1.1. At the upper end of the design space, under cruise conditions with eight and nine blades, the pitch is reduced to meet the target thrust. However, this negative pitching is less pronounced. The pitch angles are presented in appendix F.1 and F.1.

Fig. 5.1 shows geometric information of the designed propeller. However, presenting the twist and chord distributions for all geometries is impractical; therefore, global propeller and blade parameters are shown instead. Diagram a) shows the chord length at 75% of the radius, as this parameter is limited by the design procedure. Second, the mean solidity (cf. eq. (2.31)) of the propeller as a measure for the total blade area, in diagram b) is shown. Third, the blade aspect ratio (cf. eq. (4.1)) as a measure for the tip losses and the aerodynamic efficiency of the blade, in diagram c) is shown.

A high aspect ratios results from slender blades. As in fixed-wing aerodynamics, a high aspect ratio results in lower blade tip losses. The solidity combines the number of blades with the projected surface of the blade relative to the disk area. The hover and cruise geometry for the five bladed propeller, indicated by the vertical dashed line in fig. 5.1, are presented in 5.2. The hover results are visualised in the black lines, and the cruise results in the magenta lines.

Diagram a) visualises that, in the case of the hover geometry, the upper bound of the chord length is reached. In contrast, the chord length at 75% does not change in the cruise case for blade numbers above six. In general, the chord length decreases parabolically with an increasing number of blades. Doubling the blade number results in a chord length reduction of more than 50%, as the induced velocities and, consequently, the thrust generated by the propeller strongly depend on the solidity. This demonstrates that there is no linear relationship between chord length, blade number, and produced thrust, which remains fixed in the current study.

Therefore, diagram b) illustrates the blade solidity. It shows that, for hover designs, the solidity increases significantly with the number of blades, whereas it slightly decreases for cruise designs.

Additionally, diagram c) illustrates that the aspect ratio increases with the number of blades. The increase in aspect ratio is more pronounced in cruise designs than in hover designs. The high aspect ratios indicate that the blades experience low loading. For blade numbers above seven in cruise designs, no further increase occurs, as the lower bound of the chord length, determined by structural constraints, is reached.

A comparison of hover and cruise geometries in the diagrams reveals that cruise geometries are significantly more slender than hover geometries.

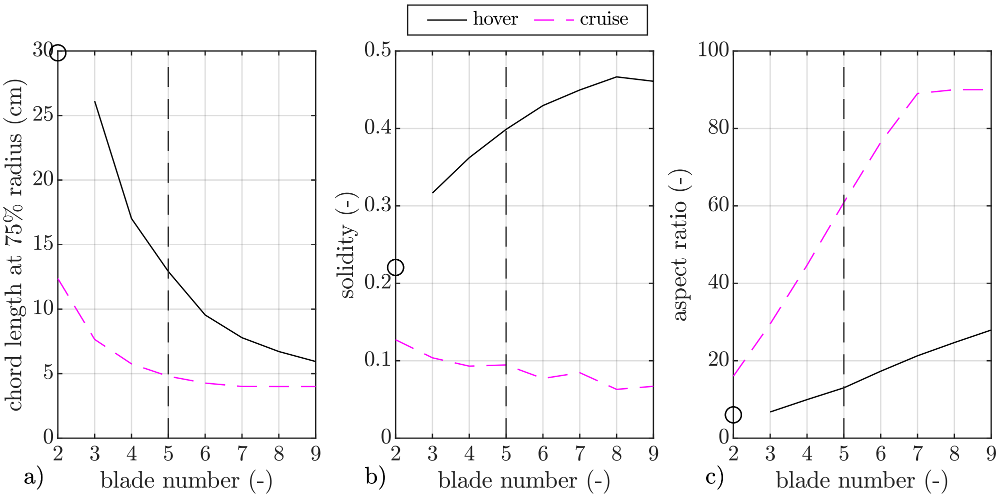

Figure 5.1: Geometric properties as function of the blade number for given thrust, rotational speed, and diameter requirements

Fig. 5.2 presents the differences between the hover and cruise propeller geometries, exemplified by the five-bladed propeller. The figure aims to provide a visual understanding of the generated geometries.

Diagram a) shows the top view of a blade with an equidistant axis spacing. The hover geometry is represented in black, while the cruise geometry is shown in magenta. Diagram b) illustrates the chord and twist distributions. The chord distribution, represented in black, corresponds to the left axis, whereas the twist distribution, shown in magenta, corresponds to the right axis.

The comparison in diagram a) shows that the cruise geometry has a significantly more slender blade than the hover geometry. The top view of the geometries appears to have lower chord lengths at the root. However, this reduction in the top view results from the twist of the geometry. Diagram b) reveals that both the chord and twist distributions increase towards the hub, even though diagram a) does not explicitly show this trend. The comparison of the twist distribution in diagram b) indicates that, under hover conditions, approximately 10° more twist is required than in cruise conditions.

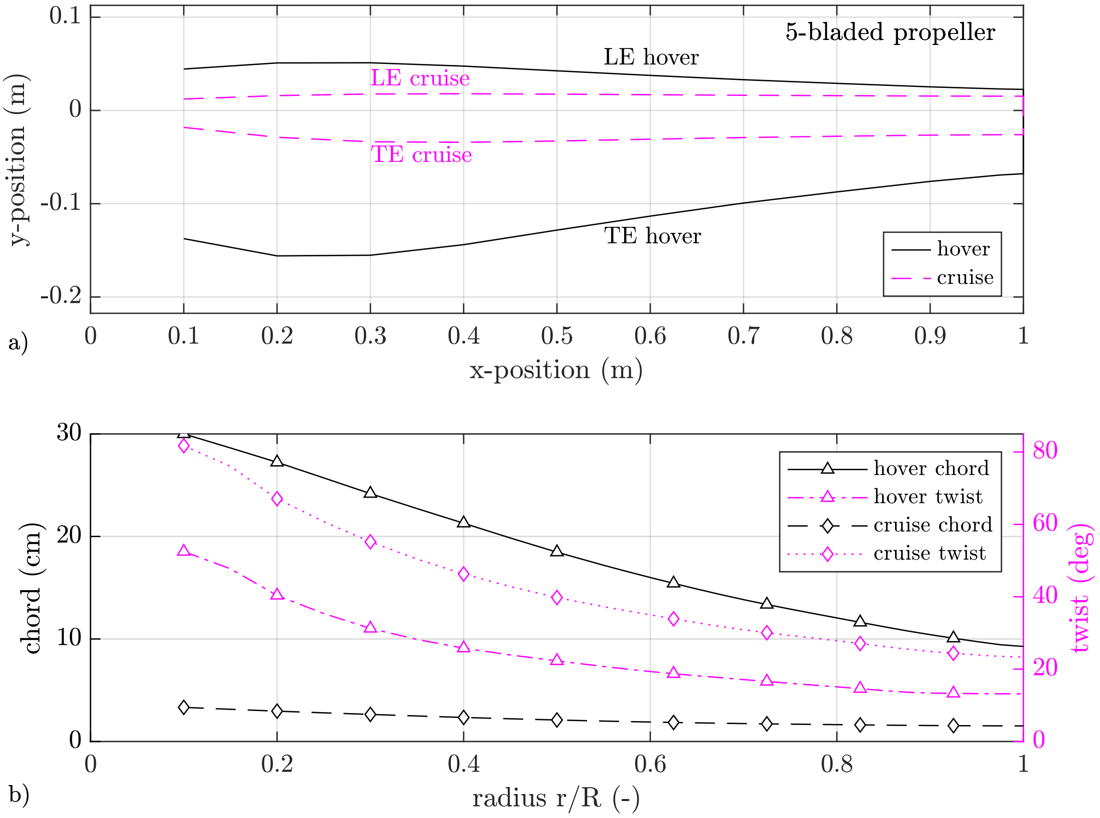

Figure 5.2: Top view and geometric properties of the five-bladed hover and cruise propeller

Fig. 5.3 presents the aerodynamic performance. Diagram a) illustrates the hover performance in terms of the Figure of Merit (FoM) and the thrust-to-power ratio (TtP) for different blade numbers. The FoM is shown on the left y-axis with a black solid line, while the TtP is displayed on the right y-axis with a magenta dashed line. Both values serve as measures of aerodynamic performance.

The FoM is dimensionless but depends on the disc loading and therefore disc area, which is why it cannot be used for comparisons involving different diameters. In the initial assessment, the disc area remains fixed. However, in section 5.1.2 and 5.1.3, the diameter is varied, making the TtP a relevant additional performance index. While the FoM represents a dimensionless parameter for hover efficiency, the TtP is dimensional. A higher TtP value indicates that more thrust is generated per unit of power.

Diagram b) replaces the FoM with the propulsive efficiency η, which is plotted on the left y-axis as a solid black line, while the TtP is shown on the right y-axis as a magenta dashed line, both as functions of the blade number. Since η is the product of TtP and flight speed, which remains fixed in this study, TtP and η align perfectly.

Diagram a) shows that FoM and TtP reach their maximum for the five-bladed propeller in hover. This is why the corresponding geometry is presented in fig. 5.2. The two-bladed propeller has an FoM approximately 0.02 lower than that of the three-bladed propeller. The TtP decreases from the five-bladed to the two-bladed propeller by about 1 N/kW. This reduction results from the increased pitch, which leads to lower lift-to-drag ratios of the 2D airfoils. From the five- to the nine-bladed propeller, the TtP decreases by 0.75 N/kW.

Similar but less pronounced changes can be observed under cruise conditions in diagram b). The maximum efficiency is reached with the three-bladed propeller. As the number of blades increases, propeller efficiency decreases by 2.5% and the thrust-to-power ratio (TtP) drops by 0.8 N/kW. However, the difference between the two- and three-bladed propellers is negligible under cruise conditions.

In conclusion, under hover conditions, the five-bladed propeller exhibits the highest efficiency, whereas under cruise conditions, the three-bladed propeller is the most efficient. Furthermore, the blade aspect ratio cannot be directly used as a measure of propeller efficiency when comparing different blade variations.

Under the given geometric and operational constraints the two-bladed hover propeller is overloaded. This overloading occurs due to an increased pitch, which leads to unfavourable airfoil polar conditions and higher losses. For configurations with fewer blades, a strong tip vortex dominates the losses. As the blade number increases, the strength of the tip vortex decreases because the blade loading is reduced and the aspect ratio increases. Beyond the optimal blade number, friction and pressure drag increase with the number of blades, resulting in a linear decline in aerodynamic performance.

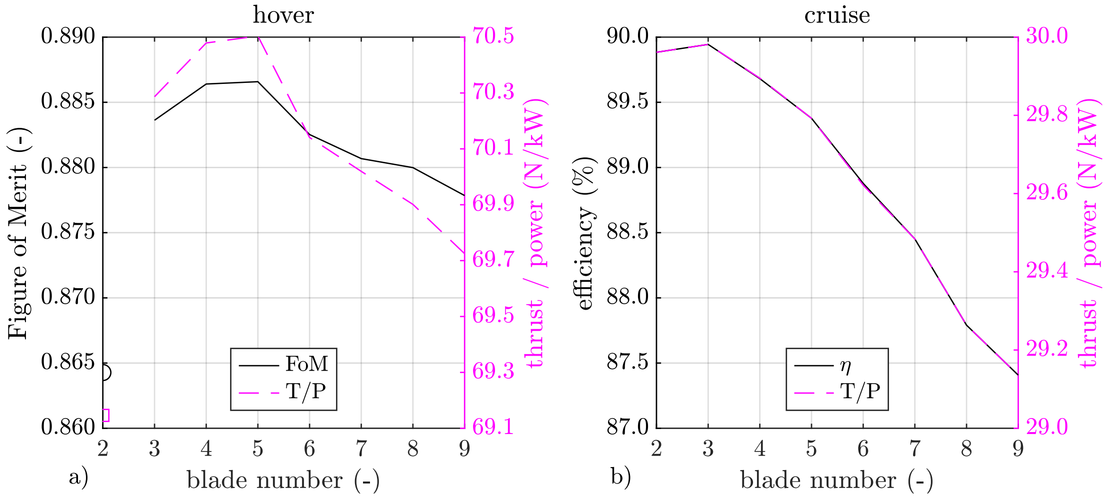

Figure 5.3: Dependency of the blade number on the aerodynamic performance in hover and cruise

Fig. 5.4 presents the A-weighted acoustic results, divided into loading, thickness, and broadband noise components. Changing the blade number at a fixed rotational speed results in a shift in the blade passing frequency (BPF), which is why A-weighting is applied.

The left diagram (diagram a) illustrates the noise emissions in hover conditions (for the hover designs) as a function of the blade number, while the right diagram (diagram b) presents the results of the cruise designs for cruise conditions. Broadband noise is represented by black solid lines, loading noise by magenta dashed lines, and thickness noise by cyan dash-dotted lines.

Diagram a) reveals that hover noise emissions are primarily driven by broadband noise. While loading and thickness noise decrease with an increasing blade number, broadband noise increases up to five blades. Beyond five blades, broadband noise decreases again and then remains constant from six to nine blades. However, even in the two-bladed configuration, loading noise is 20 dB(A) lower than broadband noise, and thickness noise is approximately 40 dB(A) lower than loading noise.

The significant reduction in loading and thickness noise is caused by the exponential decrease in blade loading and blade volume as the number of blades increases, as shown in fig. F.2. The peak in loading noise for the seven-bladed propeller results from blade interactions. Even blade numbers exhibit stronger noise cancellations between the blades than odd blade numbers.

The broadband noise is highest in the five-bladed configuration. However, a clear explanation for this phenomenon cannot be provided. The analysis of the relative TE thickness in fig. 3.11 shows that thinner TE thicknesses result in higher noise emissions in the low-frequency range. Since the TE thickness is fixed at 1 mm for manufacturing reasons, the relative thickness increases with the number of blades as the blades become more slender (cf. fig. F.1). As a result, blunt vortex shedding decreases with an increasing number of blades[1].

The Reynolds number is influenced by the chord length of the airfoils. In hover conditions, the Reynolds number varies by a factor of five between the two-bladed and the nine-bladed configurations, as shown in the chord length diagram in fig. 5.1 (diagram a)). The effective AoA along the blade is not constant due to the trimming process and the variation in the optimal AoA with the Reynolds number. This variation affects both tip vortex noise and turbulent boundary layer – trailing-edge noise. At the 75% span section, the AoA varies by 2°, as shown in fig. F.1 (cf. diagram b)).

All of these interactions may counteract or amplify each other, making it impossible to provide a definitive explanation for the broadband noise increase at five blades.

Diagram b) of fig. 5.4 presents the results for cruise conditions. In general, the trends in broadband, loading, and thickness noise align with the observations from hover conditions. The peak in loading noise at the seven-bladed propeller remains present.

---

[1] Figure 3.11 shows the trend of reduced BVS noise for increasing relative TE thicknesses.

However, the maximum broadband noise has shifted towards the six-bladed propeller. If the six-bladed propeller is excluded, broadband noise decreases slightly with increasing number of blades. From two to nine blades, broadband noise is reduced by 6 dB(A).

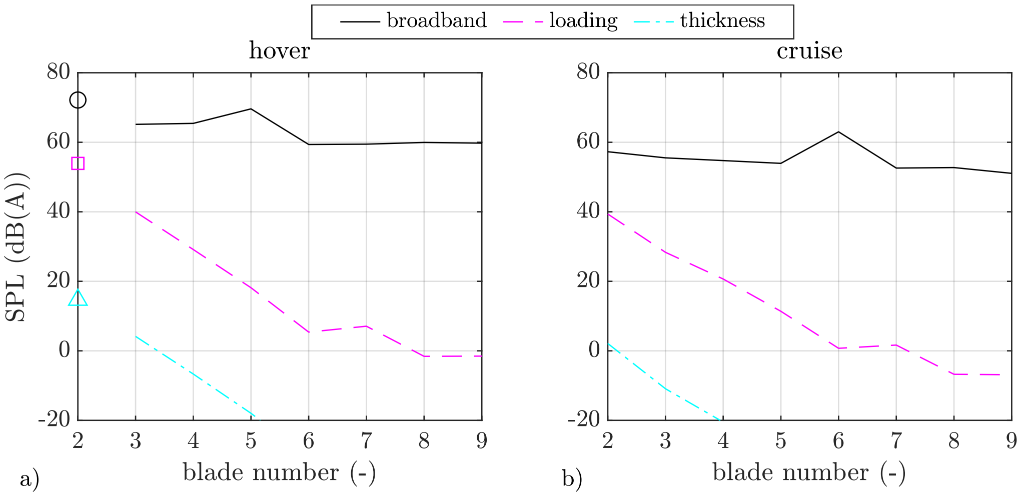

Figure 5.4: Dependency of the blade number on the noise emissions in hover and cruise

5.1.2 Assessment of Diameter and Blade Tip Mach in Hover Conditions

While section 5.1.1 examines the influence of different blade numbers on aerodynamic and acoustic results, section 5.1.2 investigates the effects of diameter and blade tip Mach number M_{tip} under hover conditions. Both parameters are varied within the MIL design for a constant blade number of two in hover conditions. This subsection begins with an analysis of the aerodynamic results and continues with the acoustic results.

Fig. 5.5 presents the aerodynamic performance of different geometries designed for hover conditions. Diagram a) displays the torque of the designs, diagram b) shows the TtP, and diagram c) illustrates the FoM. The lower corner at low M_{tip} and small diameters remains unfilled because no geometries were found that could provide the required thrust.

Since two parameters are varied, a colormap is used to represent the aerodynamic properties. The same type of representation is applied to the acoustic results in fig. 5.7 and the geometric results in fig. 5.6.

Diagram a) shows that torque decreases quadratically with M_{tip}, as indicated by the increasing spacing between the iso-lines, which are placed equidistantly in 25 Nm steps. At low M_{tip}, the iso-lines are horizontal, whereas at higher M_{tip}, they increase with diameter.

Torque itself does not provide information about aerodynamic efficiency. However, it is included because the required torque is a crucial parameter for motor design.

Diagram b) presents the dimensional TtP. For small diameters, the TtP is approximately independent of M_{tip}, whereas for larger diameters, higher M_{tip} values result in higher TtP. The highest TtP ratio is observed for large diameters and low M_{tip}.

Diagram c) presents the dimensionless FoM. The highest FoM is not located at any edge or corner of the diagram but appears in a band, which is found at high M_{tip} for small diameters and shifts towards lower M_{tip} as the diameter increases. The lowest FoM occurs at high rotational M_{tip} and large diameters.

According to eq. (2.19), the FoM should be highest for high disc loadings resulting in small diameter for constant thrust. However, if the propeller is overloaded at low rotational speeds, the FoM decreases due to higher tip vortex losses, which increase power consumption. The overloading can be observed in fig. 5.6, where the pitch adjustments from the trimming process are visualised.

The comparison of TtP and FoM reveals that they do not share the same optimum, as shown in the variation of the blade number in fig. 5.3. TtP reaches its maximum at a diameter of 4 m and the lowest M_{tip}, whereas FoM tends towards low disc loadings. Therefore, in an optimisation study of a hover propeller where diameter, blade number, and M_{tip} are unknown, TtP must be optimised.

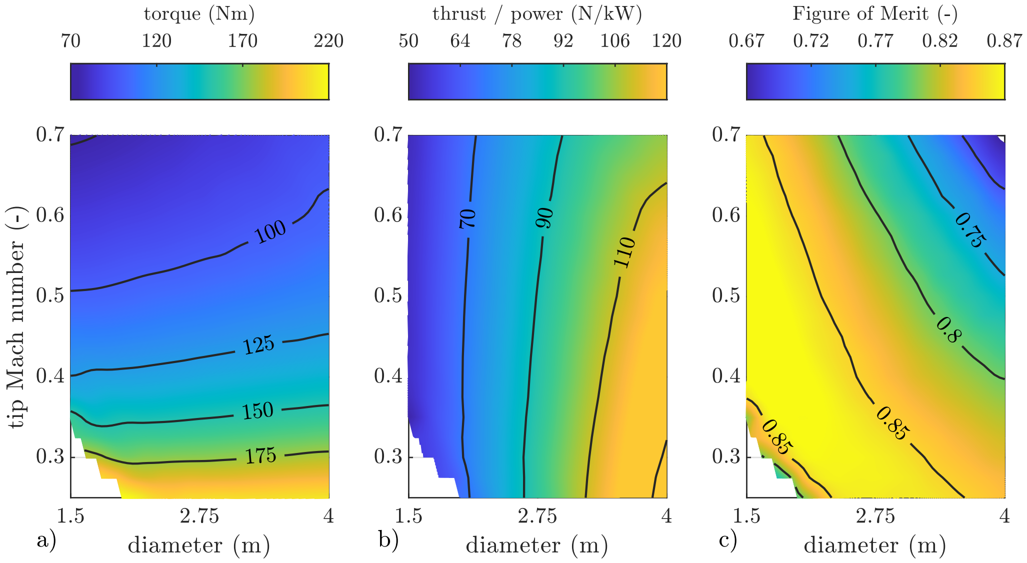

Figure 5.5: Aerodynamic hover performance for two-bladed propellers with variable design diameter and M_{tip}

Fig. 5.6 provides additional insights into the designed geometry as well as the aerodynamic and acoustic assessment. Diagram a) presents the aspect ratio of the blades, diagram b) shows the pitch adjustments from the trimming process, diagram c) illustrates the relative TE thickness at 75% of the radius, and diagram d) depicts the effective AoA at 75% of the radius.

The aspect ratio increases parabolically with both the design M_{tip} and the diameter. The lowest aspect ratio is 6, while the highest reaches 95. In section 5.1.1, additional details on the blade geometry (chord length, solidity, and blade volume) are provided. However, these parameters do not offer additional information beyond what is already captured by the aspect ratio as long as the blade number remains unchanged.

Diagram b) shows that within the trimming process, only the lower-left corner of the design space requires significant blade pitch adjustments. In the upper-left corner, a slight negative pitch of -1.5° is required.

The relative TE thickness, shown in diagram c), increases with the design M_{tip}. Additionally, it decreases from smaller diameters towards larger diameters. At the lowest M_{tip}, the TE thickness is 0.3%, whereas at the highest M_{tip}, it reaches 3.2%. Notably, the iso-line of 0.3% exhibits a kink and does not follow the trend of the other iso-lines.

Finally, diagram d) reveals that the effective AoA remains approximately constant across the majority of the design space, indicating a successful MIL approach.

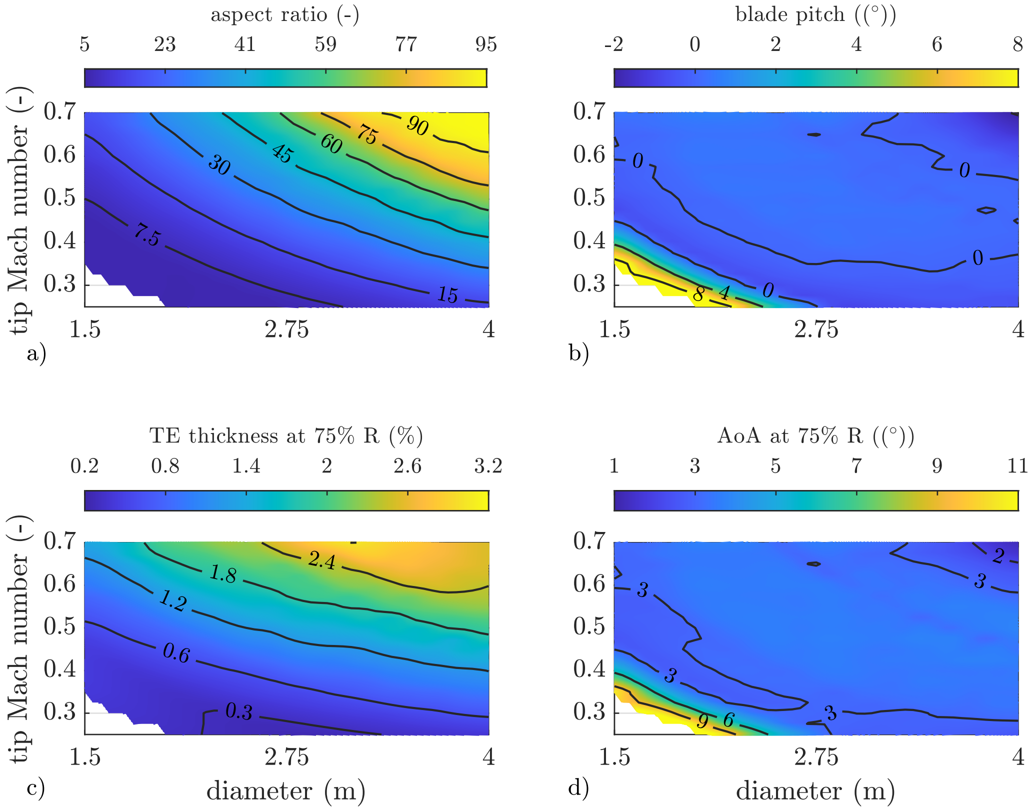

Figure 5.6: Representation of the designed hover geometries

Fig. 5.7 shows the A-weighted SPL for tonal noise (diagram a), and broadband noise (diagram b). The loading and thickness noise is combined to the tonal noise and not further diveded, as the previous study shows, that the trends align between loading and thickness noise and the thickness noise is of less relevance. Both diagrams have the same colour limits, with equidistant iso-lines in 5 dB(A) steps. The maximal SPL values of each component is shown independently of the observer position. The broadband noise has it's maximum at around 65°-75° observer position, while the tonal SPL has it's maximum at around 110°-120° observer position.

Diagram a) shows, that the tonal noise increases towards higher M_{tip} and lower diameters. The highest tonal SPL is 85 dB(A) for the M_{tip} of 0.7 and the diameter of 1.5 m, while the lowest tonal SPL is reached at the opposite corner with 45 dB(A). The trimming process increases the tonal noise at the left lower corner due to higher pitch angles and therefore higher blade loadings. The overall trend of the iso-lines shows an increases from smaller to larger diameters and a higher density of iso-lines towards higher M_{tip}.

Diagram b) shows, the broadband noise. The highest broadband noise is found for the largest diameter and highest M_{tip}. A second band of high SPL about 75 dB(A) reaches over from the M_{tip} of 0.5 to 0.4 with increasing diameter. Within this band, local maxima with SPLs of approximately 80 dB(A) are visible.

The trimming process increases the effective AoA and therefore the broadband noise in the left lower corner. A plateau of constant broadband noise is visible above an M_{tip} of approximately 0.55 and below a diameter of 3.5 m. The SPL in this plateau is 70 dB(A).

The overall trend suggests a decrease in broadband SPL with increasing diameter. However, the behaviour is not uniform, as distinct bands of increased noise levels appear throughout the parameter space. These bands indicate regions where broadband noise does not follow a strictly monotonic trend but instead fluctuates due to complex acoustic interactions. Such variations suggest that multiple competing effects, such as blade loading and tip vortex interactions, influence the noise generation.

The region with SPL levels below 65 dB(A) at the lower M_{tip} limit corresponds to the iso-line of TE thickness in diagram c) of fig. 5.6. The escalating SPL in the upper-left corner, at high M_{tip} and large diameters, aligns with the reduction in AoA in diagram d) to values below 2°. Similarly, the band of high SPL, extending from an M_{tip} of 0.5 at 1.5 m to 0.4 at 2.75 m, coincides with the reduced AoA region in diagram d). These correlations indicate a relationship between TE thickness and the AoA but are insufficient to directly link the acoustic noise sources to the operational conditions or geometry. Reynolds number effects, which correlate with the aspect ratio for a given diameter, cannot be observed.

The comparison of tonal noise with broadband noise shows that broadband noise is dominant at low M_{tip}, as well as for large diameters. In contrast, for small diameters and high M_{tip}, tonal noise becomes the dominant noise source.

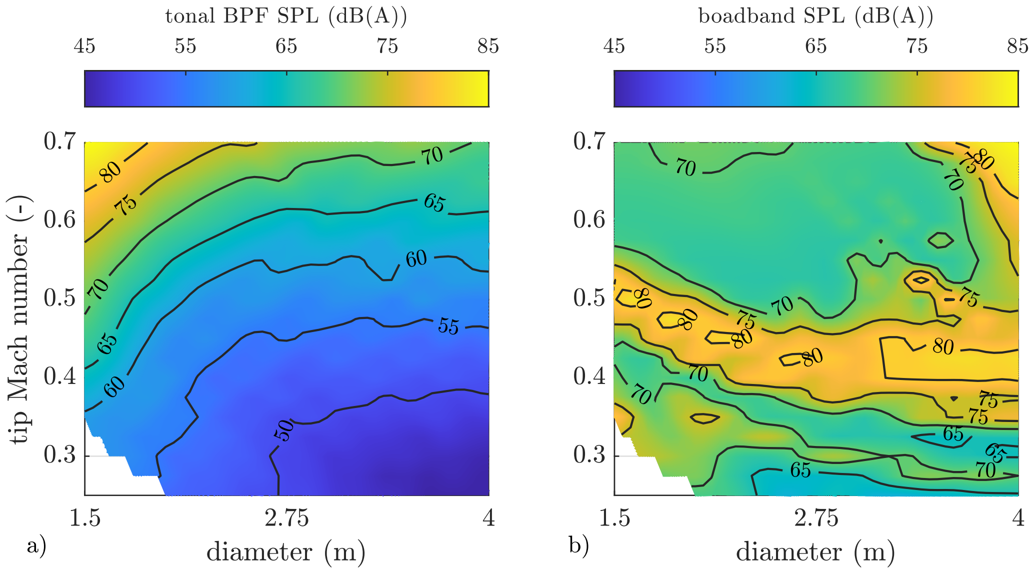

Figure 5.7: Acoustic emissions in hover of two-bladed propellers with variable design diameter and M_{tip}

The results differ from the findings of Ref. [60], where thickness and broadband noise are compared for a given geometry at constant thrust loading. The key difference between the results of fig. 5.7 and those of Ref. [60] lies in the geometry input. In the current study, the geometry is optimised using the MIL procedure for each rotational speed, whereas in Ref. [60], it is kept constant. As a result, thickness and loading noise do not diverge in the same manner towards higher rotational speeds as observed in Ref. [60].

Furthermore, the comparison indicates a strong coupling between TE thickness and AoA with broadband noise.

Finally, fig. 5.8 presents a comparison of the hover design space in terms of aerodynamic efficiency and overall noise emissions. Diagram a) depicts the previously shown TtP, while diagram b) illustrates the overall SPL (OASPL), representing the summation of tonal and broadband noise.

The OASPL reveals that, depending on the configuration, either tonal noise or broadband noise is dominant. However, for an efficient propeller, only large diameters and low M_{tip} values are relevant. In this region, the OASPL is primarily driven by broadband noise, which is why broadband noise must be optimised for an efficient and quiet propeller.

In the best case—achieved with a 4 m propeller at an M_{tip} of 0.25—a TtP of 133 kN/kW at an OASPL of 65 dB(A) can be reached.

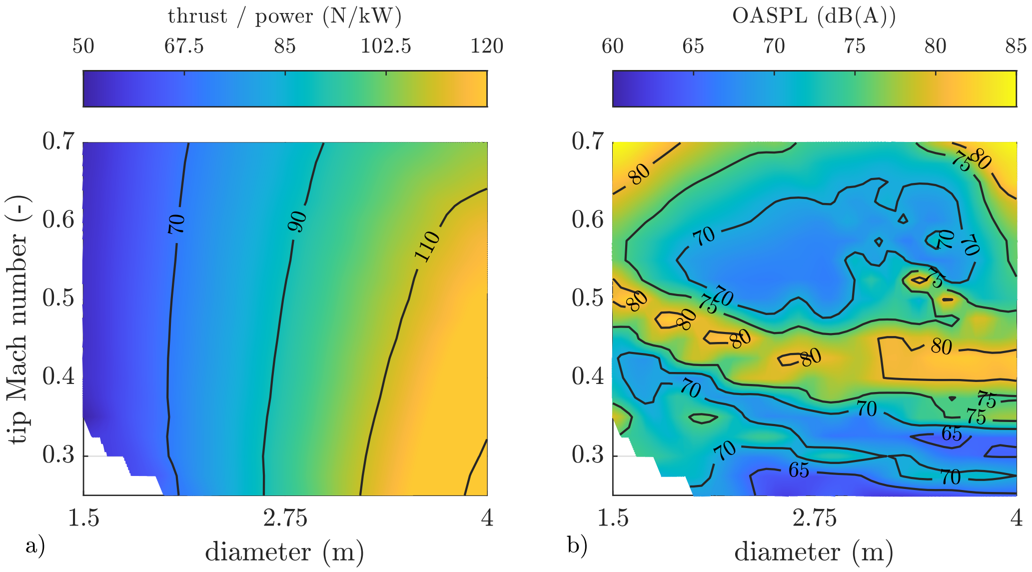

Figure 5.8: Comparison of the aerodynamic performance and noise emissions in hover of two-bladed propellers with variable design diameter and M_{tip}

5.1.3 Assessment of Diameter and Blade Tip Mach in Cruise Conditions

Lastly, in section 5.1, the influence of design diameter and M_{tip} on cruise performance and noise emissions are assessed. The evaluation of the cruise design follows the same processing steps as in section 5.1.2.

Under hover conditions, propellers with small diameters and low M_{tip} values are overloaded. In contrast, under cruise conditions, propellers with large diameters and high M_{tip} values are underloaded. As a result, the upper-right corner remains empty in the following diagrams.

Fig. 5.9 presents the aerodynamic performance in cruise conditions. Diagram a) shows the torque of the designs, diagram b) illustrates the thrust-to-power ratio (TtP), and diagram c) depicts the efficiency. As previously explained, TtP and propulsive efficiency are interchangeable, but both metrics are relevant for categorising the design.

In the hover case, torque primarily depends on M_{tip}. However, under cruise conditions, a strong dependency on diameter is also evident. Torque increases as M_{tip} decreases and towards larger diameters. A comparison between fig. 5.9 and 5.5 reveals that maximum torque is reduced by 30 Nm from hover (220 Nm) to cruise conditions (190 Nm).

TtP in diagram b) is shown to compare the development of TtP from hover to cruise conditions. In hover, TtP ranges from 50 to 120 N/kW, whereas in cruise conditions, it ranges from 28 to 32 N/kW. As a result, greater power savings can be achieved in hover, while only marginal efficiency improvements are possible in cruise.

However, in the exemplary eVTOL tilt-wing or tilt propeller mission, the hover phase is significantly shorter than the cruise phase, meaning that more energy could be saved during cruise. These opposing trends must be balanced within an optimisation framework.

Diagram c) reveals that the highest propulsive efficiency is achieved with the largest diameter and the lowest M_{tip}. In the current study, efficiencies of up to 95% are achieved.

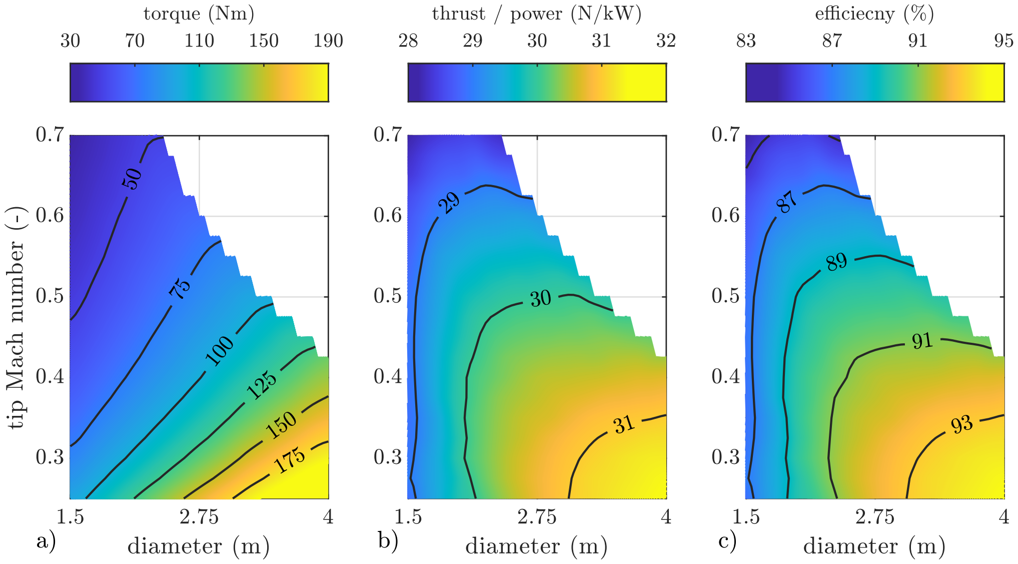

Figure 5.9: Aerodynamic cruise performance for two-bladed propellers with variable design diameter and M_{tip}

Fig. 5.10 provides additional insights into the designed geometry, analogous to the assessment in section 5.1.1.

As observed in section 5.1.1, the aspect ratio increases parabolically with both the design M_{tip} and the diameter, ranging from 5 to 95. Similarly, the relative TE thickness in diagram c) follows the trend of increasing with M_{tip} while decreasing with diameter. At the lowest M_{tip}, the TE thickness is 0.4%, whereas at the highest M_{tip}, it reaches 5.4%.

Diagram b) shows that the boundary to the underloaded region exhibits highly negative pitch angles. Furthermore, the lower-left corner of the design space requires slight positive pitch adjustments.

Finally, diagram d) reveals variations in the effective AoA, with trends comparable to those discussed in section 5.1.1. Across the majority of the design space, the effective AoA at 75% of the radius remains around 4°.

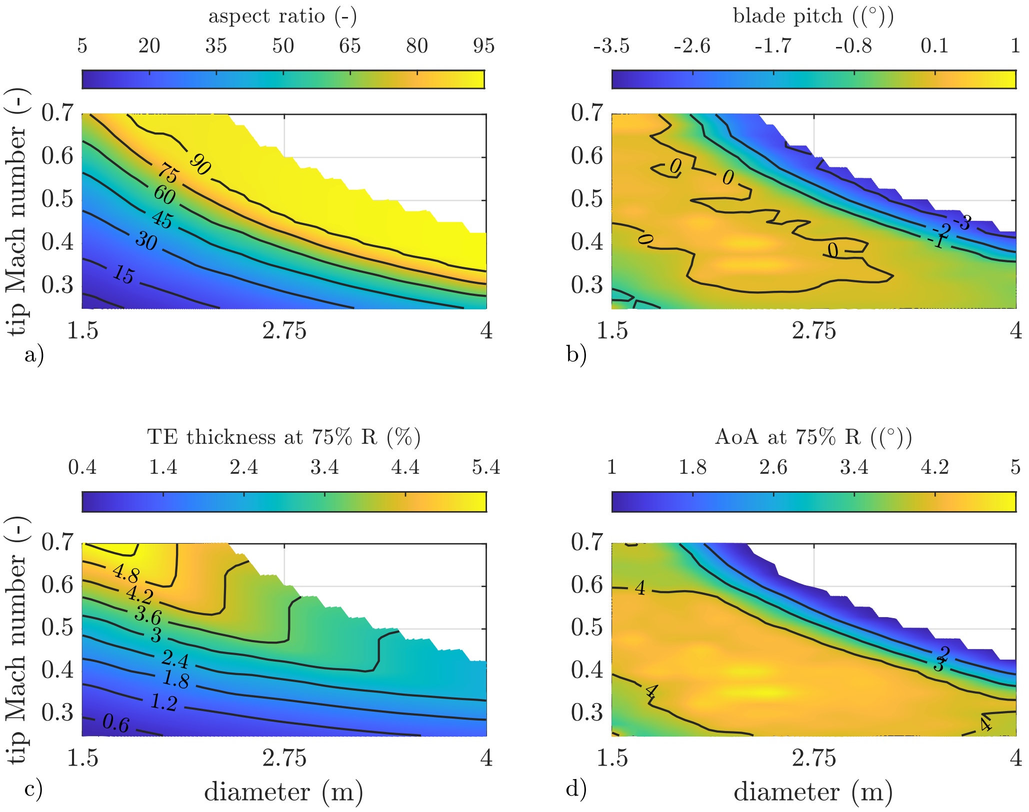

Figure 5.10: Representation of the designed cruise geometries

The assessment of noise emissions from the MIL-designed propeller under cruise conditions is presented in fig. 5.11. The tonal noise, shown in diagram a), increases with M_{tip} and is highest for small diameters. This behaviour aligns with the trend observed in hover conditions.

The broadband noise map in diagram b) appears significantly less disturbed compared to hover conditions. Broadband noise is highest at low M_{tip} and near the boundary of the underloaded region. Outside these boundaries, a stable region with a slight SPL increase towards higher M_{tip} can be observed. The lowest broadband SPL is found at approximately 3 m and a design M_{tip} of 0.325.

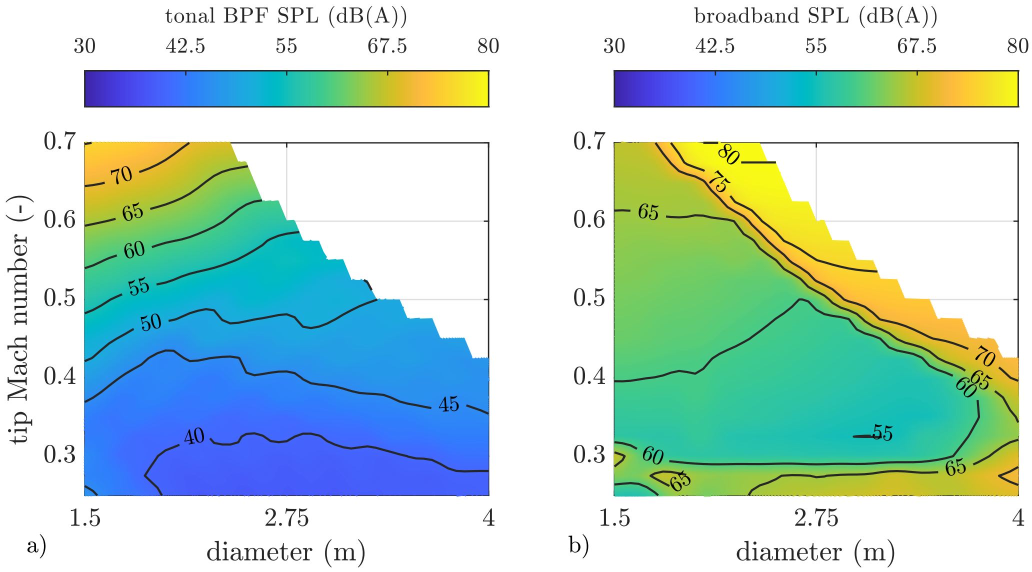

Figure 5.11: Acoustic emissions in cruise of two-bladed propellers with variable design diameter and M_{tip}

As in section 5.1.2, section 5.1.3 concludes with the presentation of aerodynamic efficiency and overall noise emissions of the cruise design space in fig. 5.12.

The aerodynamic efficiency is highest at a diameter of 4 m and the lowest possible M_{tip}.

The OASPL distribution reveals that it is primarily influenced by broadband noise, except in the upper-left region. The lowest OASPL is found in the region between a design M_{tip} of 0.3 and 0.4, where values of 55 dB(A) are observed.

Unlike in hover conditions, a compromise between aerodynamic efficiency and noise emissions must be found.

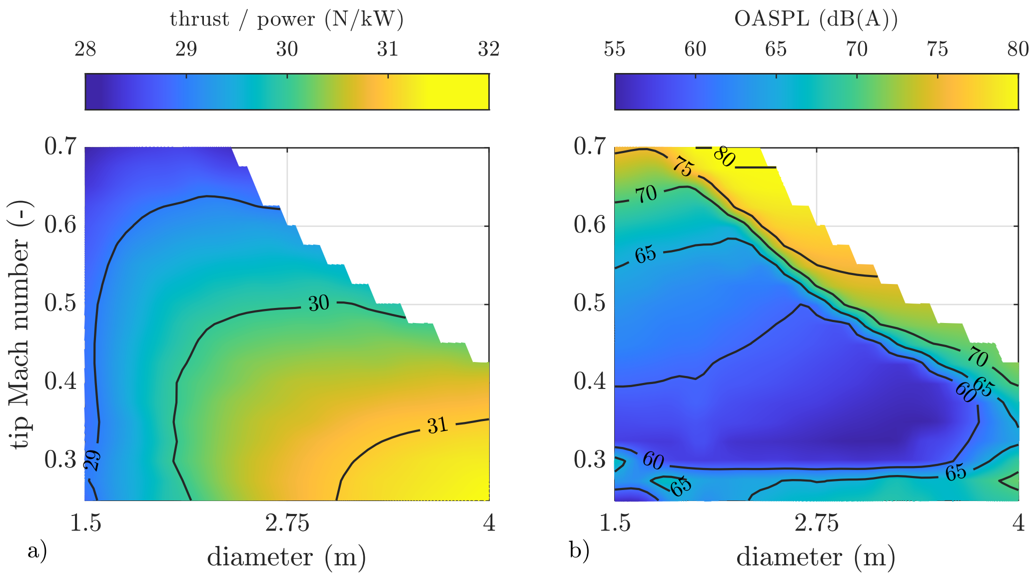

Figure 5.12: Comparison of the aerodynamic performance and noise emissions in cruise of a two-bladed propeller with variable design diameter and M_{tip}

5.1.4 Single Point Optimisation Observations

The presented singular optimisation studies, assessing the impact of diameter, blade number, and M_{tip} on the aerodynamic and acoustic performance of the propeller, clearly highlight the need for a multi-disciplinary and multi-operational optimisation strategy. The conflicting geometric requirements of cruise and hover must be balanced through MDO. Furthermore, broadband and tonal noise can also be optimised to achieve a suitable trade-off.

Under the given constraints, the following findings can be summarised:

1. In hover and cruise, different blade numbers achieve the highest aerodynamic efficiency.
2. The blade number variation reveals that the seven-bladed propeller exhibits increased tonal noise due to the cancellation effects of even blade numbers. However, in installed configurations, e.g., in front of a wing, prime blade numbers are beneficial as they interact less with the harmonic excitation of the surrounding structure.
3. The Figure of Merit is not an appropriate measure in an optimisation study when the diameter or the design M_{tip} is varied.
4. All analysed geometries are dominated by broadband noise in regions of high aerodynamic efficiency. Therefore, the propeller could sustain increased loading without significant acoustic drawbacks.

However, the systematic evaluation of the geometric parameters within the MIL-designed propeller and their aeroacoustic effects reveals that the broadband noise model exhibits complex interactions. These interactions cannot be fully explained solely by evaluating the geometry.

More detailed analyses are required to identify all relevant effects influencing the broadband noise model.

5.2 Multidisciplinary Optimisation Results

As discussed in section 5.1, an MDO approach is required to find the optimal balance between multiple operating points and various physical requirements, such as noise emissions and aerodynamic performance. Therefore, the procedure described in section 4.3 is applied to the reference mission. The assessment of the proposed approach is conducted in three steps.

First, the GPPO is performed with different additional models to evaluate their influence on overall performance. Second, the BSO is executed to determine the optimal propeller. Third, the optimised propeller is analysed in detail and validated using RANS CFD simulations.

The geometric constraints listed in table 5.2 are applied during the GPPO stage to identify the optimal geometry for the reference mission, as outlined in table 5.1. Additionally, operational conditions are limited to M_{tip} values between 0.25 and 0.7.

As commonly seen in tilt propeller and tilt-wing applications, variable-pitch systems help mitigate the conflict between hover and cruise conditions. Therefore, the advantages of a variable-pitch system over a fixed-pitch propeller are assessed, considering differences in system mass and motor efficiency. The propeller pitch can be adjusted between –6° and 6°. The evaluation of the pitch system is carried out during the GPPO stage in section 5.2.1.4 to 5.2.1.6.

5.2.1 Assessment of the Global Propeller Parameter Optimisation

The evaluation follows a stepwise approach, progressively incorporating additional factors into the optimisation process:

1. **Baseline Optimisation:** A purely aerodynamic and acoustic optimisation is conducted, excluding broadband noise and acoustic weighting.
2. **Broadband Noise Influence:** The effect of broadband noise on the optimisation results is assessed.
3. **Acoustic Weighting Influence:** The impact of different acoustic weighting functions are analysed.
4. **Blade Pitch System Influence:** The influence of a variable blade pitch system is examined, while motor efficiency and mass remain unchanged.
5. **Mass Penalty Influence:** The additional effects of propeller and motor mass are incorporated.
6. **Motor Efficiency Influence:** Motor efficiency and system mass are included in the final evaluation.

This structured approach allows for a systematic investigation of the various factors influencing propeller design while highlighting the dependencies between modelling complexity and optimisation outcomes. Table 5.3 provides a comprehensive overview of the models applied in the following six studies.

Table 5.3: Overview of applied models in the following optimisation studies

Study	**Broadband Noise**	**Acoustic Weighing**	**Pitch System**	**Mass Penalty**	**Motor Efficiency**
1	✗	✗	✗	✗	✗
2	✓	✗	✗	✗	✗
3	✓	✓	✗	✗	✗
4	✓	✓	✓	✗	✗
5	✓	✓	✓	✓	✗
6	✓	✓	✓	✓	✓

The GPPO stage is performed with a maximum of 300 generations. The population size of each generation is set to 20 times the number of variables, which is five according to section 4.3.2. Therefore, up to 30,000 propeller geometries can be designed and evaluated by the GPPO.

However, if the Pareto front remains unchanged for 20 generations, the GPPO is terminated early, reducing computational time. The generation and population size factors are determined heuristically and conservatively to prevent convergence toward local instead of global minima. Appendix. F.2 provides details on each optimisation study.

The MDO process concludes between 127 and 295 generations, resulting in 1,763 to 3,893 geometries that meet the thrust requirements. However, only 13 to 53 geometries from the enormous number of propellers contribute to the Pareto front.

The exact energy consumption and noise emission values are summarised at the end of the assessment in section 5.2.1.7, as intermediate quantitative results are of minor interest. Since the results are evaluated qualitatively, no detailed SPL or energy values are provided throughout the process. Only the final geometry of the sixth optimisation step is further processed in the BSO.

5.2.1.1 Baseline Optimisation

The optimisation assessment begins with a purely aeroacoustic optimisation of a fixed-pitch propeller. Noise emissions are simulated using the F1A model without considering broadband noise.

Fig. 5.13 presents the optimisation results for all generations. Each circle represents a possible propeller geometry that meets the mission requirements. Alongside the optimisation results, fig. 5.13 shows the Pareto front, the set of optimal solutions, and the sweet spot, the best compromise between noise emissions and energy consumption. Both the Pareto front and the sweet spot are highlighted in black. The x-axis represents the unweighted SPL (dB), while the y-axis shows the normalised energy consumption, as defined in eq. (4.11).

Diagram a) of fig. 5.13 colours the circles according to the blade number, while diagram b) uses the diameter for colour coding. Both diagrams present the same results but provide significant insights into the optimisation process.

The GPPO is intended to determine the blade number and diameter for the reference mission, which is why these parameters are highlighted and labelled within the figure. The sweet spot of the optimisation, considering only tonal noise, results in a six-bladed propeller with a diameter of 3.9 m.

Diagram a) reveals that a lower blade number results in reduced energy consumption, while tonal noise emissions increase. The results clearly distinguish between blade numbers ranging from two to five. However, for larger blade numbers, the data points overlap, making them less distinguishable.

These findings confirm general aerodynamic knowledge of propellers and align with the noise trends observed in section 5.1.1. However, the aerodynamic results in section 5.1.1 suggest that three-, four-, or five-bladed propellers perform optimally. This comparison highlights that manual propeller design may lead to suboptimal configurations, even when analysing only a single operating point.

Diagram b) shows that larger diameters result in lower tonal noise and reduced energy consumption. Both observations are well-known principles in tonal noise optimisation, confirming the physical robustness of the optimisation process. An increased blade number and larger diameters reduce blade loading, thereby decreasing loading noise. Since M_{tip} decreases with increasing blade number and diameter, the impact of thickness noise is mitigated.

The Pareto front shows a compromise between noise emission and energy consumption for each number of blades, which leads to a staircase-like shape of the front. This staircase-like shape can be found in most of the following results, as the diameter is optimised for each number of blades.

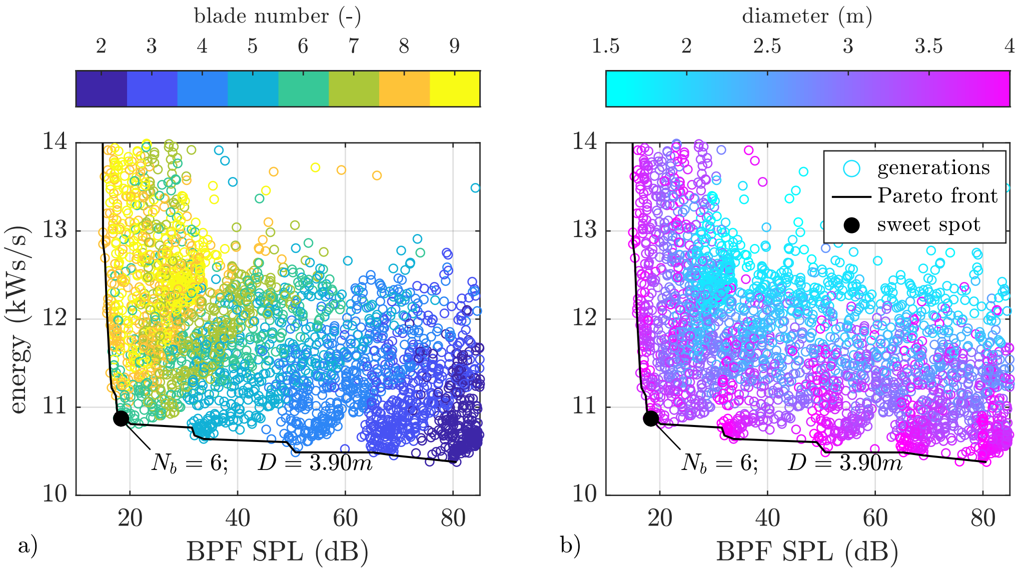

Figure 5.13: Influence of blade number and diameter on energy consumption and noise emissions with the consideration of tonal noise (Study 1)

The resulting geometries of the Pareto front are presented in fig. 5.14. As described in section 4.3, the GPPO stage is constrained to linear chord distributions.

Diagrams a) and c) in fig. 5.14 present the same chord distributions, with different line colours indicating noise emissions in diagram a) and energy consumption in diagram b). Diagrams c) and d) follow the same approach for twist distributions. The black dashed line represents the geometry of the sweet spot.

The diagrams reveal that the diameters of the Pareto front range between 3.5 m and 4 m. When comparing chord and twist distributions, it may appear that fewer chord distributions are visualised than twist distributions. However, some chord distributions overlap exactly, making them indistinguishable in the diagram.

Diagram a) shows that larger chord lengths result in higher noise emissions, whereas smaller chord lengths lead to lower noise emissions. A similar trend in terms of energy consumption in diagram c) cannot be observed.

Diagram b) indicates that lower twist distributions result in reduced noise emissions, while diagram d) shows that lower twist distributions increase energy consumption.

Consequently, the sweet spot geometry represents a compromise positioned between the extreme cases of twist and chord distributions.

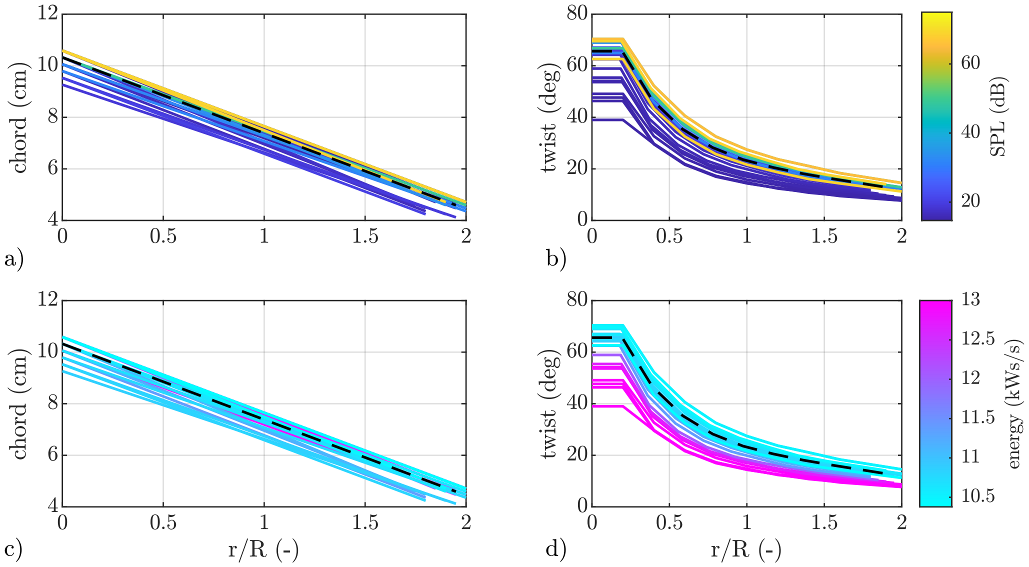

Figure 5.14: Resulting propeller geometries along the Pareto front of the baseline optimisation

However, section 5.1 shows, the contrary trends between tonal and broadband noise, why the broadband noise is considered next.

5.2.1.2 Influence of Broadband Noise

Fig. 5.15 presents the optimisation results considering broadband noise. The same representation as in fig. 5.13 is applied to the aeroacoustic optimisation with broadband noise.

Due to the influence of broadband noise, the geometry of the sweet spot shifts from a six-bladed propeller to a nine-bladed propeller, while the diameter decreases from 3.9 m to 2.9 m. In general, the slope of the Pareto front increases compared to fig. 5.13. The Pareto front of the baseline analysis exhibits an L-shape, whereas the Pareto front with broadband noise consideration follows a parabolic shape.

While in the baseline optimisation (cf. fig. 5.13) the blade numbers are clearly separated, the inclusion of broadband noise blurs the boundaries between different blade numbers. The Pareto front predominantly consists of eight- and nine-bladed propellers around the sweet spot. However, two- and three-bladed propellers appear in the region of minimum energy consumption.

A comparison of diagram b) in fig. 5.13 and 5.15 indicates that the distinct diameter trend observed in fig. 5.13 does not hold when broadband noise is considered. Smaller diameters appear to reduce noise emissions, whereas larger diameters lead to lower energy consumption.

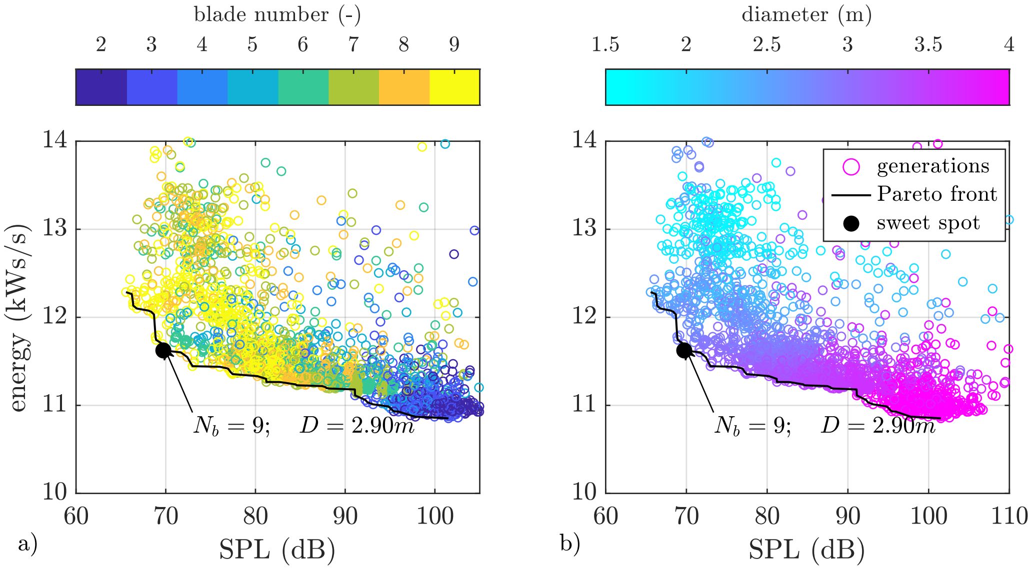

Figure 5.15: Influence of blade number and diameter on energy consumption and noise emissions with the consideration of tonal and broaband noise (Study 2)

The comparison between the baseline optimisation and the optimisation including broadband noise highlights the necessity of considering broadband noise in the optimisation process.

5.2.1.3 Influence of the Acoustic Weighting

Next, the influence of acoustic weighting on propeller optimisation is assessed. The noise emissions are weighted using A- and D-weighting, as these are the most common weighting functions in aviation.

Fig. 5.16 illustrates the influence of acoustic weighting on the blade number, while fig. 5.17 presents its effect on the diameter. Diagram a) shows the unweighted results, diagram b) the A-weighted results, and diagram c) the D-weighted results. The y-axis remains consistent across all three diagrams, whereas the x-axis is adjusted. The unweighted results in diagram a) are the same as those in fig. 5.15.

Initially, the lowest energy consumption remains similar across all three cases, with variations occurring only in noise emissions and, consequently, in the sweet spot parameters. The lowest energy consumption is achieved with two- or three-bladed configurations in all three cases. The unweighted optimisation results in a nine-bladed propeller with a diameter of 2.8 m, while the A-weighting favours four blades and 4 m, and the D-weighting leads to eight blades and a diameter of 3.1 m.

The comparison shows that A-weighting tends towards fewer blades. This results from the weighting advantages given to frequencies below 1000 Hz. In contrast, the benefits of low frequencies in D-weighting are less pronounced, leading to higher blade counts. However, even with D-weighting, the clear dominance of the nine-bladed propeller observed in diagram a) is not evident. Instead, seven- and eight-bladed configurations dominate the region around the sweet spot.

While the unweighted and D-weighted Pareto fronts follow a parabolic shape, the Pareto front of the A-weighted optimisation exhibits an L-shape.

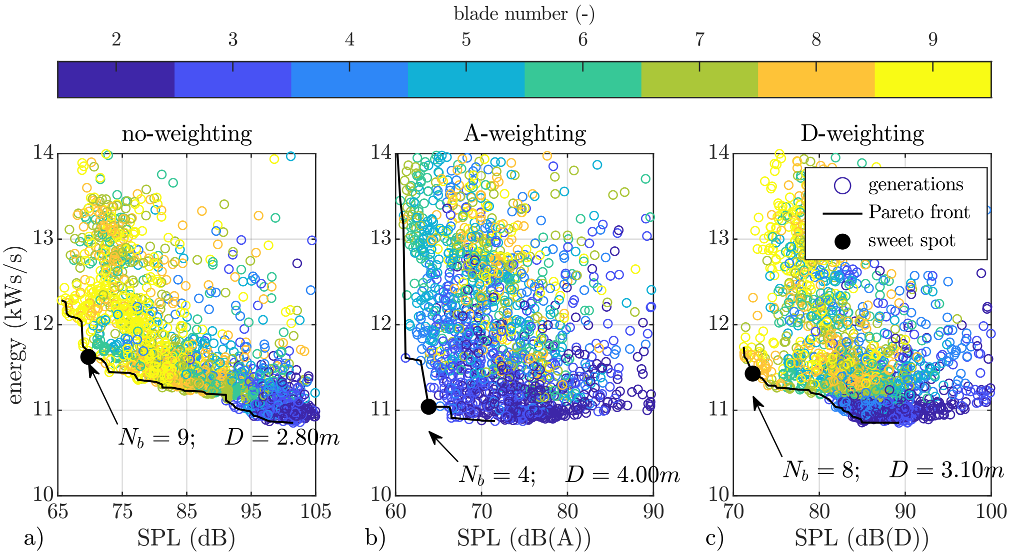

Figure 5.16: Influence of different acoustic weighing on blade number optimisation (Study 3)

Fig. 5.17 illustrates the influence of acoustic weighting on diameter selection.

In the unweighted results, a smooth transition can be observed from smaller diameters in the region of low noise emissions towards larger diameters in the region of low energy consumption. A similar trend is present in the D-weighted optimisation, although larger diameters increasingly dominate the Pareto front. In the case of A-weighting, larger diameters fully dominate the Pareto front.

The optimisation with D-weighting and A-weighting results in larger diameters compared to the unweighted sweet spot geometry. The diameter of the D-weighted sweet spot increases by 0.3 m, while the diameter of the A-weighted propeller increases by 1.2 m.

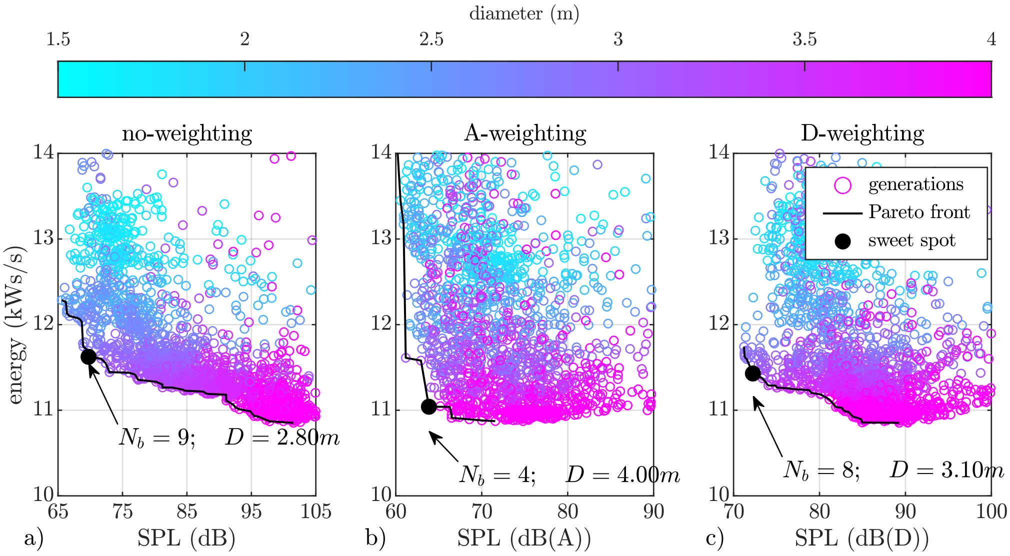

Figure 5.17: Influence of different acoustic weighing on diameter optimisation (Study 3)

The weighting not only influences tonal noise but also affects the low-frequency region of broadband noise, which is primarily driven by blunt vortex shedding (BVS) noise, as shown in fig. 3.11. BVS noise mainly depends on the relative TE thickness, which is influenced by the the propeller's chord length, as the absolute TE thickness is fixed at 1 mm.

Fig. 5.18 presents the resulting geometries for the sweet spots. Diagram a) illustrates the chord distribution along the radius, while diagram b) shows the twist distribution. The unweighted results are represented by black solid lines, the A-weighted results by dashed magenta lines, and the D-weighted results by cyan dash-dotted lines.

Diagram a) shows that the A-weighted propeller has a significantly higher chord length compared to the other geometries, which correlates with the reduced blade number. Since the A-weighted propeller has less blades, a higher blade aspect ratio is required. The unweighted and D-weighted blade numbers are similar, resulting in nearly identical chord distributions.

Design rotational speed, free-stream velocity, and thrust primarily determine the twist distribution. Therefore, diagram b) reveals that the unweighted and D-weighted sweet spot propellers are designed for similar conditions, following the stated procedure. The A-weighted propeller exhibits higher twist and chord values, requiring operation at higher rotational speeds.

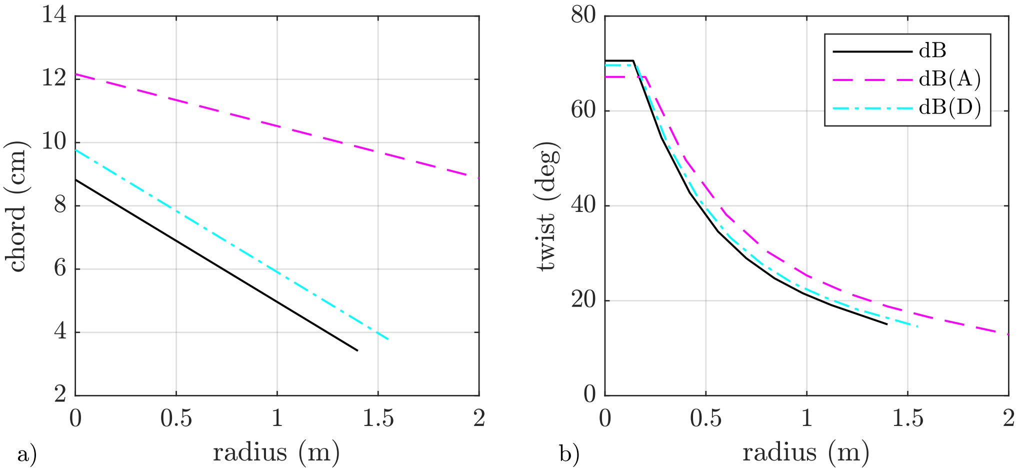

Figure 5.18: Comparison of the sweet spot propeller geometries between different acoustic weightings (Study 3)

The following optimisation studies are conducted using the A-weighted results, as the previous assessment demonstrates that considering weighting is crucial for diameter and blade number. A-weighting is more commonly used than D-weighting.

5.2.1.4 Influence of the Blade Pitch System

Next, the assessment of the pitch system is conducted. In this analysis, fixed-pitch propellers are compared to variable-pitch propellers. The variable-pitch propellers can be adjusted in flight within a range of -6° to +6°. Both propeller types are also variable-speed propellers, as they are intended for operation with electric motors.

Fig. 5.19 illustrates the selection process of the blade number for both propeller types. Diagram a) presents the results for the fixed-pitch propeller, while diagram b) shows the results for the variable-pitch propeller. The y-axis is shifted from the range of 10–14 kWs/s in previous figures to 9–14 kWs/s in fig. 5.19 and 5.20. This shift may create the impression that the fixed-pitch propeller requires more energy than in previous results. However, the optimisation results remain consistent with those shown in diagram b) of fig. 5.16 and 5.17. For consistency, the convention of presenting fixed-pitch results on the left and variable-pitch results on the right is maintained in the following optimisation results.

The comparison reveals that the variable-pitch propeller requires less energy than the fixed-pitch propeller. The variable-pitch propeller also favours a four-bladed configuration, though its diameter is slightly reduced to 3.6 m.

The dominance of the two-bladed propeller in diagram a) is less pronounced in diagram b). The lower boundary of the variable-pitch Pareto front is not exclusively composed of two-bladed propellers. Instead, a smooth transition along the Pareto front from two to eight blades, corresponding to lower noise levels, is observed.

Additionally, the density of results near the Pareto front in diagram b) is significantly higher than in diagram a). The MDO process for the variable-pitch case concludes 30 generations earlier than for the fixed-pitch case (cf. appendix F.2) and identifies 92 additional geometries that meet the mission requirements. Thus, the variable-pitch MDO demonstrates better convergence than the fixed-pitch MDO.

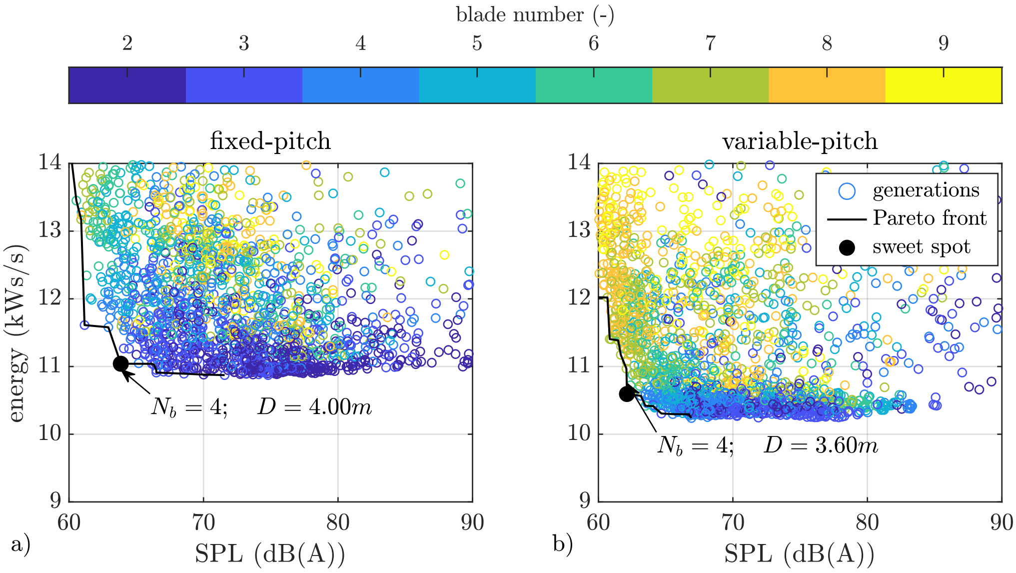

Figure 5.19: Influence of fixed- or variable-pitch propellers on the optimisation of the blade number (Study 4)

Fig. 5.20 compares the diameters between fixed- and variable-pitch propellers. The results in diagram a) have already been analysed in the discussion of fig. 5.17.

In diagram b), a smooth transition from a 4 m propeller to smaller diameters along the Pareto front is visible. A comparison of fig. 5.19 and 5.20 shows a clear correlation between propeller diameter and blade number. Fewer blades result in larger diameters, while a higher blade count leads to smaller diameters.

This finding suggests that, in all cases, the propeller operates at the lowest possible rotational speed settings, as reducing rotational speed minimises power consumption. This conclusion is supported by the fact that produced thrust primarily depends on diameter, blade number, and rotational speed at a specific design point. Larger diameters, higher blade counts, and increased rotational speeds all contribute to higher thrust. If diameter and blade number exhibit an inverse correlation, the rotational speed must be maintained at a certain level to balance the thrust production.

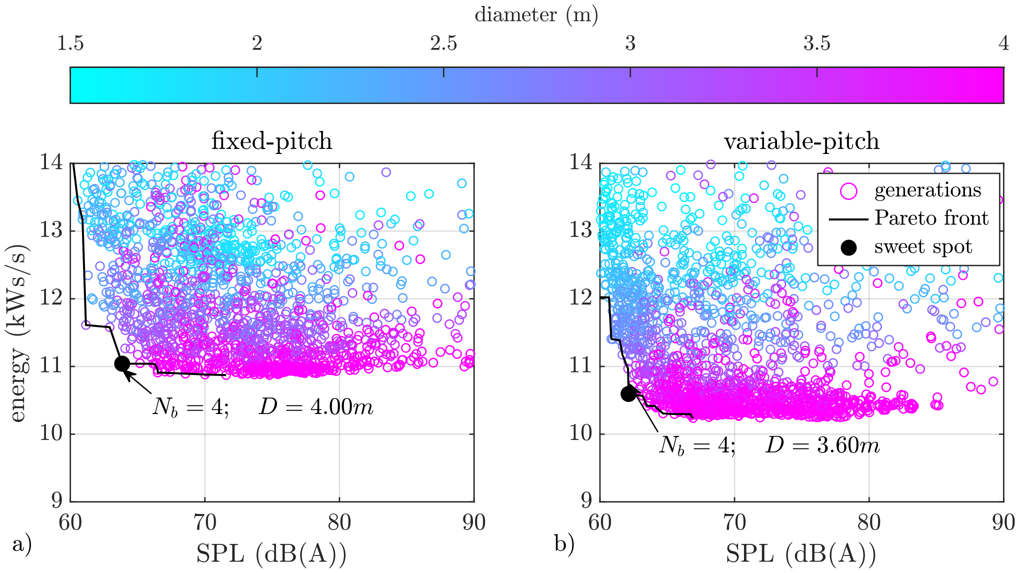

Figure 5.20: Influence of fixed- or variable-pitch propellers on the optimisation of the diameter (Study 4)

Fig. 5.21 presents the geometries of the sweet spot propellers. Diagram a) illustrates the chord length, while diagram b) shows the twist distribution for the fixed- and variable-pitch propellers. The fixed-pitch propeller is represented by a solid black line, whereas the variable-pitch propeller is shown as a magenta dashed line.

The variable-pitch propeller has a higher taper ratio and a larger root chord length compared to the fixed-pitch propeller. A comparison of the twist distribution reveals that both propellers are designed for the same operating point, as previously discussed in the analysis of fig. 5.18.

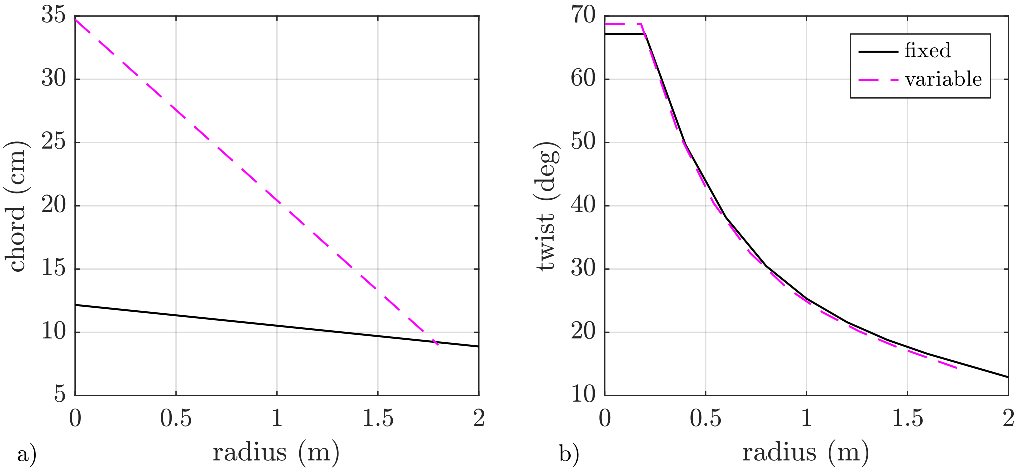

Figure 5.21: Comparison of the sweet spot propeller geometries between fixed- and variable-pitch propellers (Study 4)

5.2.1.5 Influence of Mass Penalty

Next, the pitch system is assessed with consideration of the influence of propeller and motor mass, analogous to the previous assessment. The y-axis is again shifted to the range of 10–14 kWs/s.

First, a comparison of section 5.2.1.4 and 5.2.1.5 shows that the additional mass significantly increases the required energy. The energy consumption of the fixed-pitch propeller is more affected compared to the variable-pitch propeller. The fixed-pitch propeller experiences an increase of approximately 1 kWs/s, while the variable-pitch propeller energy consumption increases by only 0.5 kWs/s in the sweet spot.

Second, the mass penalty significantly reduces the diameter, from 4 m to 3 m in the fixed-pitch case and from 3.6 m to 3.3 m in the variable-pitch case. Additionally, the blade number of the variable-pitch propeller changes from a four-bladed to a five-bladed configuration.

Diagram a) of fig. 5.22 shows that with an increasing blade number, the energy consumption rises significantly. The clear trend is not observed when the mass penalty is excluded. The fixed-pitch diagram can be divided into three distinct regions. The two-bladed and three-bladed propellers form clearly separated regions. Above the three-bladed configurations, all higher blade numbers are mixed without a clear trend, which forms the third region. This mixing results from the additional mass of each blade, leading to increased thrust requirements. The increased thrust demand with higher blade numbers limits the operational range of the fixed-pitch propeller, making fewer blades more advantageous.

Diagram b) shows a distinct region for two-bladed propellers. The remaining geometries are scattered across the entire Pareto front, with four-, five-, and six-bladed propellers dominating the distribution. The significantly increased propeller hub mass, compared to the fixed-pitch case, leads to enhanced mixing.

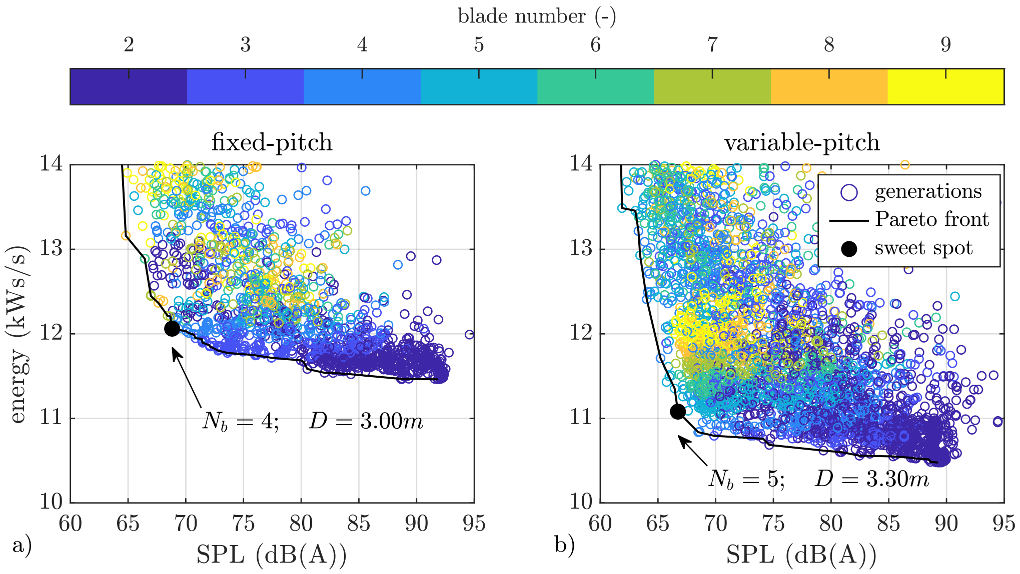

Figure 5.22: Influence of mass consideration on blade number optimisation (Study 5)

Fig. 5.23 presents the diameter assessment. While the blade number is scattered across the optimisation results in both cases, a clear trend is observed for the diameter. Fig. 5.23 shows a smooth transition from larger diameters at the lower energy consumption bound to smaller diameters at the lower noise emissions bound.

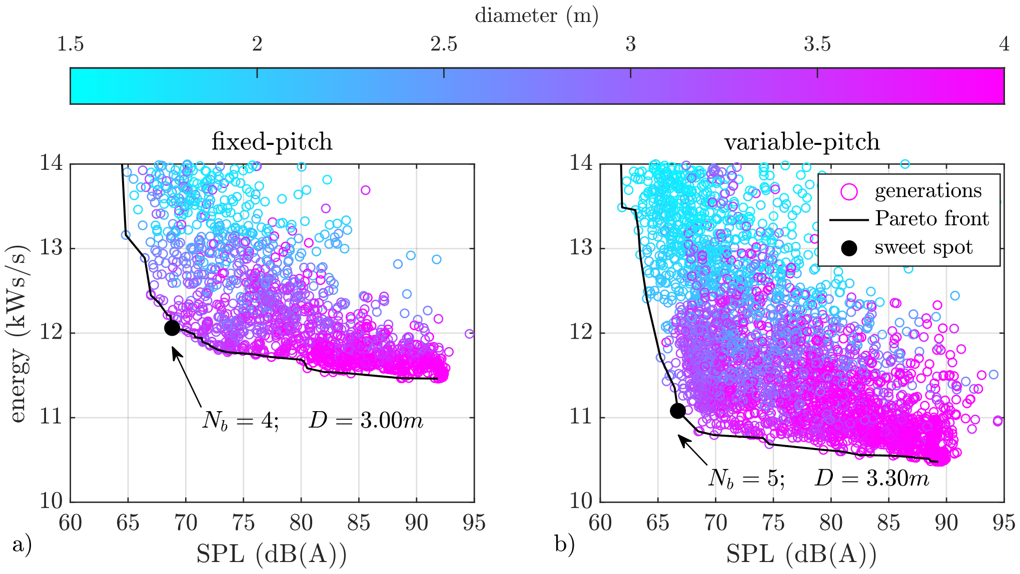

Figure 5.23: Influence of mass consideration on diameter optimisation (Study 5)

Further details about the sweet spot geometries do not provide additional insights, which is why they are not shown for the results of section 5.2.1.3. However, for the sake of completeness, they can be found in appendix F.2 in fig. F.3.

As in section 5.2.1.4, the variable-pitch optimisation shows better convergence than the fixed-pitch optimisation, requiring approximately 93 fewer generations and identifying more than twice as many matching geometries.

5.2.1.6 Influence of Motor Efficiency Penalty

Finally, the influence of motor efficiency is assessed, incorporating all previously described correction methods.

Fig. 5.24 and 5.25 show a significant increase in energy consumption due to motor losses. As a result, the y-axis is extended up to 20 kWs/s. Energy consumption increases by approximately 3 kWs/s for the fixed-pitch propeller and by about 2 kWs/s for the variable-pitch propeller compared to the assessment without motor considerations. Additionally, the blade number and diameter of the sweet spot geometry change in both cases. The fixed-pitch propeller's sweet spot geometry now has five instead of four blades, with an increased diameter of 3.4 m instead of 3 m. For the variable-pitch propeller, the blade number changes from five to eight, while the diameter decreases by 0.1 m.

Diagram a) of fig. 5.24 shows that blade number continuously increases with energy consumption while reducing noise emissions. The motor model prevents the blade number results from being scattered across the diagram, resulting in a clear transition in the fixed-pitch case. The variable-pitch results, shown in diagram b), exhibit a small transition region where the sweet spot is located. However, the diagram is primarily dominated by two- and nine-bladed propellers.

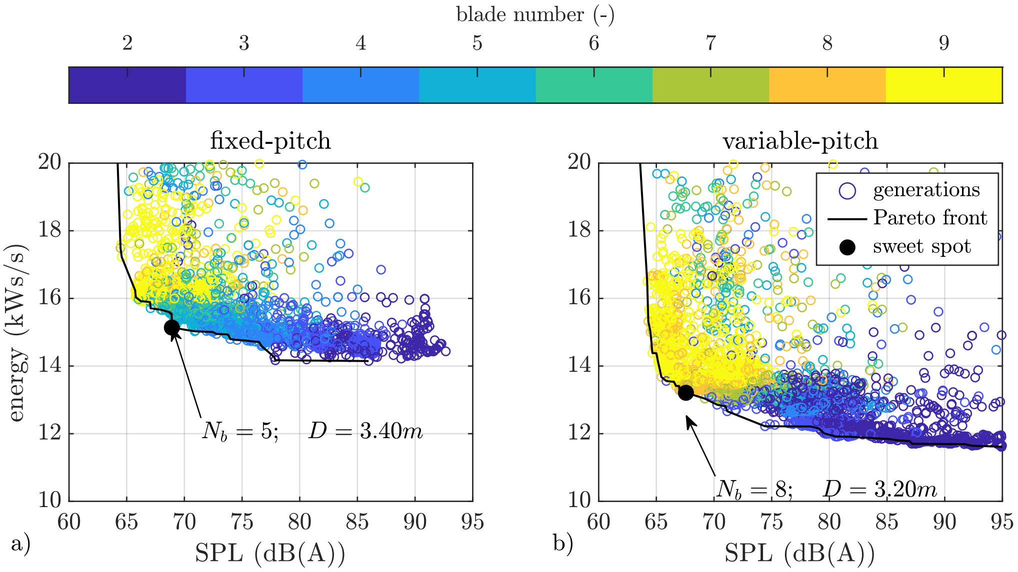

Figure 5.24: Influence of mass and motor consideration on blade number optimisation (Study 6)

Fig. 5.25 is dominated by diameters ranging from 2.5 m to 4 m. At the upper energy consumption bound, some smaller diameters appear, but the majority of the Pareto front is composed of larger propellers.

The fixed-pitch case exhibits a smooth transition from larger to smaller propellers along the Pareto front, whereas the variable-pitch Pareto front is primarily dominated by propellers with diameters between 2.5 m and 3.5 m. The diameter does not directly correlate with the blade number, as the transitions between fewer and more blades, as well as smaller and larger diameters, observed in fig. 5.24 and 5.25, differ.

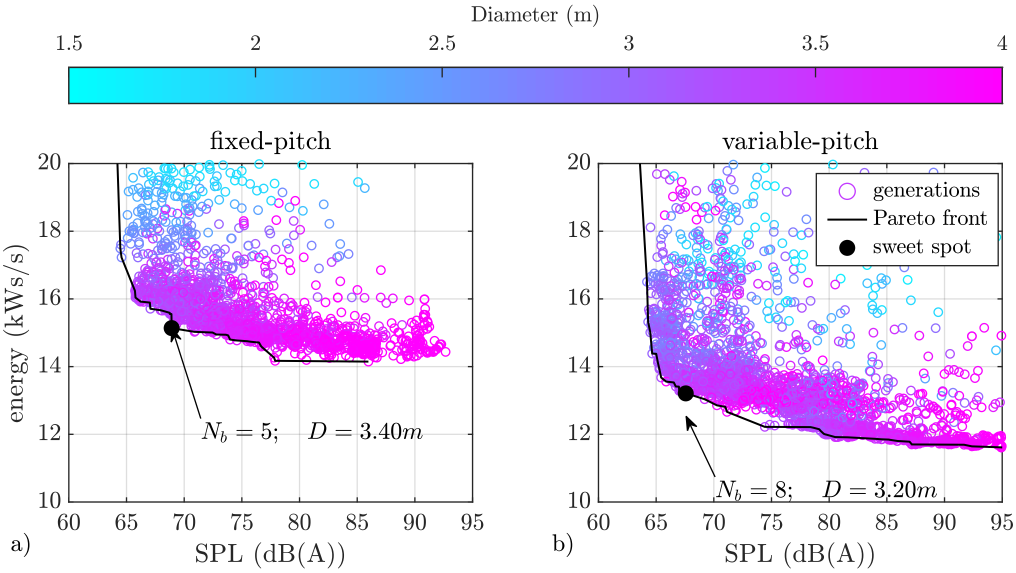

Figure 5.25: Influence of mass and motor consideration on diameter optimisation (Study 6)

Unlike in previous cases, the fixed-pitch propeller exhibits better convergence. The fixed-pitch Pareto front is fully developed after 146 generations, with an average of 15.7 propellers found per generation, whereas the variable-pitch Pareto front requires 295 generations, yielding only 12.1 propellers per generation.

As in section 5.2.1.6, the assessment of the sweet spot geometry does not provide additional insights. Therefore, for the sake of completeness, these geometries are presented in appendix F.2.

Only the consideration of all models together provides a valid overview of the benefits of the pitch system. For this reason, no quantitative values for SPL and energy were presented in the previous assessments. This gap is addressed in section 5.2.1.7.

5.2.1.7 Summary of MDO Assessment

Table 5.4 summarises the results of the assessment study. These results are valid only for the defined reference mission, and further work is required to verify their general applicability by assessing different missions.

The first study focuses solely on tonal noise. In study 2, broadband noise is introduced, leading to an increase in blade number from six to nine. While the blade diameter decreases, energy consumption increases. Due to the inclusion of broadband noise, the SPL rises to 69.7 dB.

Study 3 demonstrates the influence of A- and D-weighting on the optimisation process. Acoustic weighting significantly affects the sweet spot of the Pareto front, altering the resulting geometry. With A-weighting, the blade number decreases from nine to four, while the diameter increases from 2.9 m to 4.0 m. Since the diameter is limited to 4.0 m, it could be that the optimal diameter is even larger, but this limitation is not relevant in the following studies, which show that smaller diameters are optimal. The larger blades and lower blade count improve energy consumption by approximately 0.6 kWs/s. With D-weighting, the blade number decreases to eight, and the diameter increases by 0.2 m, reducing energy consumption by approximately 0.2 kWs/s. Due to the weighting effects, noise emissions change significantly and cannot be directly compared. All subsequent results are assessed with A-weighted SPL.

Study 4 compares fixed-pitch and variable-pitch propellers. The energy consumption decreases by approximately 0.4 kWs/s, and noise emissions are reduced by 1.8 dB(A) due to the pitch system.

Study 5 introduces the mass penalty due to the propeller and motor into the optimisation. The blade number undergoes minor changes, but the diameter decreases. For the fixed-pitch propeller, the diameter is reduced by 1 m, while for the variable-pitch propeller, it decreases by 0.3 m. The energy consumption increases due to the mass penalty by approximately 1 kWs/s for the fixed-pitch propeller and 0.5 kWs/s for the variable-pitch propeller. Additionally, noise emissions increase by 5.1 dB(A) for the fixed-pitch propeller and 4.6 dB(A) for the variable-pitch propeller.

Finally, Study 6 incorporates motor efficiency models. The motor efficiency map further influences the sweet spot geometry, increasing the blade number to five and eight. The diameter of the fixed-pitch propeller increases to 3.4 m, while the diameter of the variable-pitch propeller decreases to 3.2 m. Energy consumption increases due to motor losses, with the fixed-pitch propeller requiring approximately 3.0 kWs/s more and the variable-pitch propeller requiring an additional 2.1 kWs/s. The influence on noise emissions is minor, with an increase of 0.1 dB(A) for the fixed-pitch propeller and 0.9 dB(A) for the variable-pitch propeller. Considering the electric motor efficiency map is crucial for optimisation and equally important when applying optimisation to combustion engines [67].

The propeller without a motor efficiency map requires approximately 80% less energy for the fixed-pitch propeller and 84% less energy for the variable-pitch propeller compared to the results with motor efficiency map. However, this difference strongly depends on the mission.

Table 5.4: Summary of optimisation results

Study	**Name**		**Blade Number**	**Diameter** (m)	**Energy** (kWs/s)	**SPL** (dB)
1	Baseline Optimisation		6	3.9	10.87	18.4
2	Broadband Noise		9	2.9	11.62	69.7
3	Acoustic Weighting	(A / D)	4 / 8	4.0 / 3.1	11.04 / 11.43	63.9*/ 72.2†
4	Pitch System	(F / V)	4 / 4	4.0 / 3.6	11.04 / 10.59	63.9*/ 62.1*
5	Mass Penalty	(F / V)	4 / 5	3.0 / 3.3	12.06 / 11.08	68.8*/ 66.7*
6	Motor Efficiency	(F / V)	5 / 8	3.4 / 3.2	15.14 / 13.21	68.9*/ 67.6*

* A-weighted SPL
† D-weighted SPL

The comparison between study 4, which is a purely aeroacoustic optimisation, and study 6 reveals drastic differences across all parameters. Study 4 predicts an efficiency increase of approximately 4% for the variable-pitch propeller compared to the fixed-pitch propeller, whereas study 6 results in an efficiency gain of approximately 13%. The noise reduction benefit of the variable-pitch propeller over the fixed-pitch propeller remains similar, ranging from 1.3 dB(A) to 1.6 dB(A). In conclusion, even when considering the additional mass, the variable-pitch propeller remains significantly more efficient and slightly quieter. However, these are preliminary results from the GPPO.

The findings of this study emphasise the importance of considering system mass and motor efficiency during the conceptual design stage to achieve appropriate propeller sizing.

5.2.2 Assessment of the Blade Shape Optimisation

After the GPPO defines the blade number, diameter, and a reference geometry, the BSO is conducted. The parameter space for root and tip twist, as well as chord, is reduced to match the GPPO parameters within a 30% margin.

Fig. 5.26 presents the Pareto fronts of the GPPO and BSO for the fixed-pitch propeller in diagram a) and the variable-pitch propeller in diagram b). The black solid lines represent the GPPO results, while the magenta dashed lines indicate the BSO results.

A comparison of the Pareto fronts reveals that the BSO improves both energy consumption and noise emissions. The improvements are more pronounced in the fixed-pitch case compared to the variable-pitch case. The detailed numerical results are provided in table 5.5.

The BSO runs for a maximum of 600 additional generations. A higher number of generations is required compared to the 300 generations of the GPPO due to the larger number of design variables. The GPPO optimises five variables, whereas the BSO must optimise twelve.

The fixed-pitch BSO converges after 534 generations, identifying 13,250 propellers that meet the mission requirements. The variable-pitch BSO converges after 277 generations, finding 4,369 valid propellers. However, the Pareto front of the fixed-pitch optimisation consists of 20 propellers, while the Pareto front of the variable-pitch BSO contains 45 propellers.

In conclusion, the variable-pitch BSO converges significantly faster, likely due to the smaller improvement margin. However, as the author conducted multiple optimisation runs from different starting points, the identified sweet spot is definitively a global optimum.

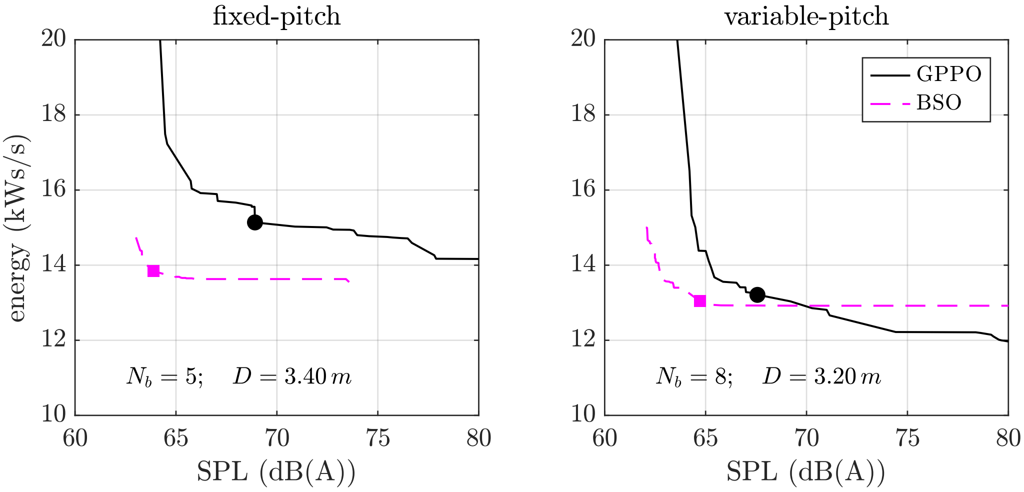

Figure 5.26: Pareto fronts of the BSO and GPPO for the fixed- and variable-pitch propellers

Second, the geometries of the fixed-pitch Pareto front are visualised in fig. 5.27. The variable-pitch geometries follows in fig. 5.28. The already used representation of the chord and twist distribution from fig. 5.14 is applied on the results of the BSO.

Fig. 5.27 shows that the chord distribution varies between 10 cm and 14 cm at the root and around 4 cm at the tip. Diagrams a) and c) reveal that smaller chord distributions result in higher noise emissions but lower energy consumption, especially when the outer region of the blades has a smaller chord length.

The twist distribution shows, that two different root twist distributions are possible. First, more parabolic distributions with increasing twist towards the root are observed. Second, more linear distributions that flatten at the tip are found. The sweet spot geometry uses the parabolic increase at the tip. Diagram b) and d) show, that smaller tip twists results in lower noise emissions but larger energy consumptions.

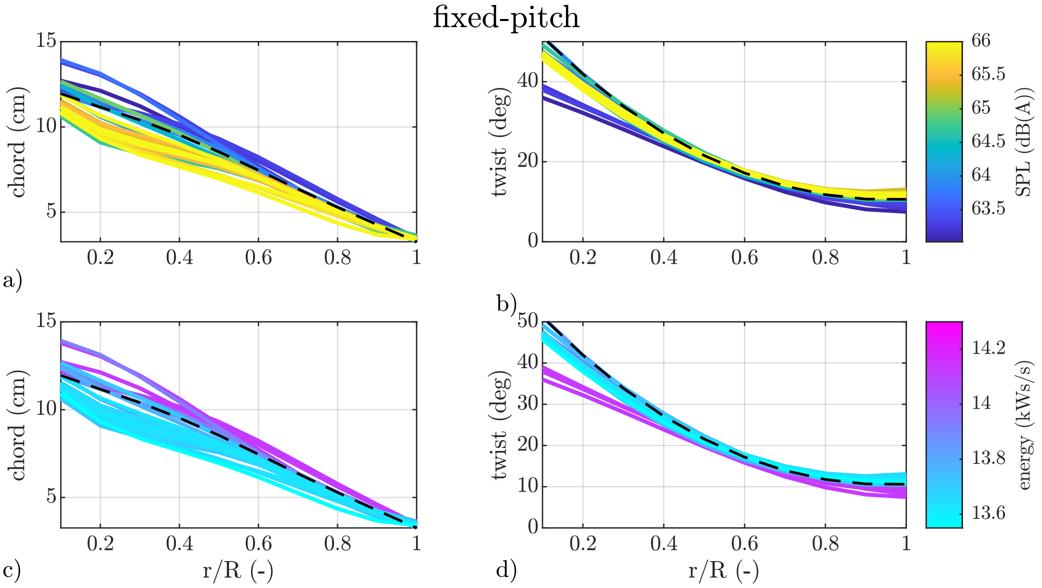

Figure 5.27: Fixed-pitch propeller geometries of BSO

The assessment of the variable-pitch propellers along the Pareto front reveals the same behaviour as that observed in the fixed-pitch propeller. However, the chord distribution changes in the variable-pitch optimisation. The optimisation identifies geometries with significantly increased chord distributions in the middle section of the blade. Similar geometries are also found in the literature for noise-optimised propellers [31, 68, 153].

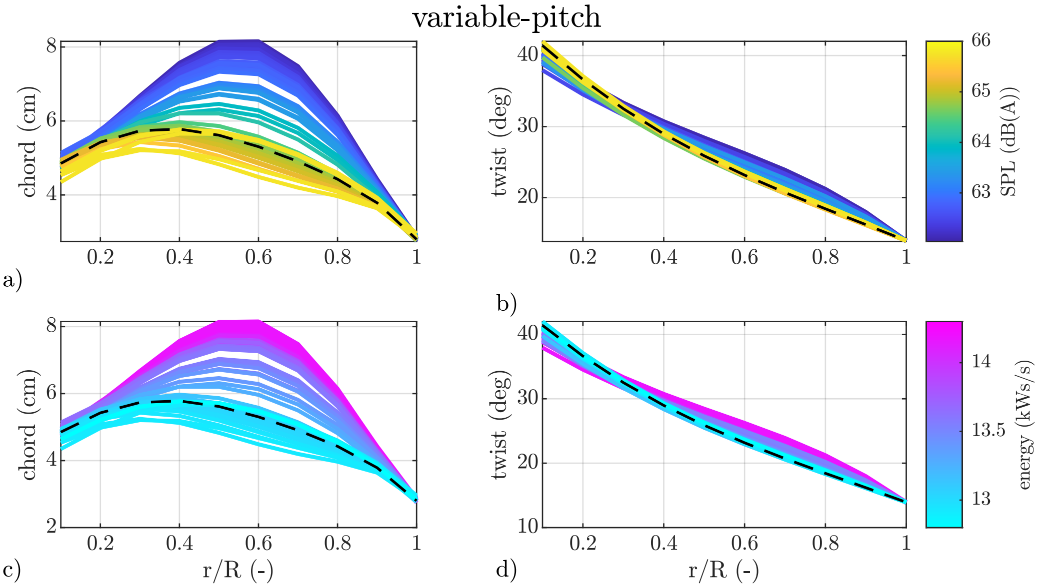

Figure 5.28: Variable-pitch propeller geometries of BSO

The geometric comparisons between energy consumption and noise emissions clearly illustrate the balance between both parameters, highlighting the necessary compromise.

Finally, the assessment of the MDO procedures concludes with a comparison of the improvements achieved by the BSO compared to the GPPO. Table 5.5 presents the improvements in energy consumption and noise emissions. The fixed-pitch propeller benefits more from the BSO than the variable-pitch propeller. Energy consumption is reduced by 1.3 kWs/s and noise emissions by 5.0 dB(A) for the fixed-pitch propeller, whereas for the variable-pitch propeller, energy consumption decreases by 0.17 kWs/s and noise emissions by 2.9 dB(A).

Overall, the fixed-pitch propeller exhibits lower noise emissions but higher energy consumption compared to the variable-pitch propeller. The energy consumption of the fixed-pitch propeller is 6.1% higher, while its noise emissions are 0.8 dB(A) lower compared to the variable-pitch propeller.

Table 5.5: Blade shape optimisation results

	Energy (kWs/s)		SPL (dB(A))	
	fixed	vari.	fixed	vari.
GPPO	15.14	13.21	68.9	67.6
BSO	13.84	13.04	63.9	64.7
Difference	-1.30	-0.17	-5.0	-2.9

As a result the benefits of the variable-pitch propeller over the fixed-pitch propeller are significantly reduced compared to the GPPO. Therefore, the benefits of the variable-pitch propeller must be weighed against the increased complexity of the pitch system by a design engineer.

5.3 Detailed Analysis of Optimised Propellers

The results of the BSO must be evaluated to show, how the geometries perform in detail. Therefore, the resulting geometries are analysed in detail with the presented procedures.

At first, the additional masses of the propeller and motor are relevant. The five-bladed fixed-pitch propeller has a mass of 12.0 kg, while the eight-bladed variable-pitch propeller has a mass of 22.5 kg.

The ideal power consumption in transition and cruise does not depend on the diameter or the blade number, which is why it is equivalent for both propellers. The ideal power consumption is 9 kW for both flight phases. In hover, the fixed-pitch propeller has an ideal power consumption of 8.8 kW with the diameter of 3.4 m and the variable pitch propeller of 9.4 kW with 3.2 m.

The motor efficiency for the motor mass prediction is assumed to be 65% of the maximum ideal power consumption. The motor design power for the fixed-pitch propeller is determined by the transition or cruise condition and is 13.8 kW. For the variable-pitch propeller, the highest power consumption occurs in hover, leading to a design power consumption of 14.4 kW.

Therefore, the motor mass of the fixed-pitch propeller is 2.8 kg, and for the variable-pitch propeller, it is 2.9 kg. As an example, the HPD16 brushless electric motor from the manufacturer Geiger Engineering GmbH has a mass of 4.7 kg at a maximum continuous power of 16 kW [50]. However, this motor has been in operation for about 10 years, and newer motor designs result in higher power densities. The motor in the fixed-pitch case accounts for 19% of the propulsion system mass, while in the variable-pitch case, it accounts for 11% of the system mass.

With the in table 5.1 given lift-to-drag ratios the new required thrust in the operating point for the fixed- and variable-pitch propeller is calculated and presetend in table 5.6.

Table 5.6: Adjustment of the thrust requirements for each mission point

	Thrust (N)	**L/D** (-)	**Propeller mass** (kg)		**Motor mass** (kg)		**New thrust** (N)	
			fixed	vari.	fixed	vari.	fixed	vari.
Hover	1200	1	12.0	22.5	2.8	2.9	1345	1449
Transition	600	5	12.0	22.5	2.8	2.9	629	650
Cruise	300	10	12.0	22.5	2.8	2.9	315	325

The resulting propeller geometries from the BSO are analysed at the three design points to determine the rotational speed that meets the thrust requirements. In the case of the variable-pitch propeller, both the optimal rotational speed and the corresponding blade pitch angle must be determined.

Fig. 5.29 presents the thrust and electric power consumption for the three operating conditions. The electric power consumption is calculated according to eq. (5.1). The propeller torque and rotational speed are matched with the motor map to determine the motor efficiency. The match between the operating points and the motor map is presented in fig. 5.31.

$$P_{electric} = \frac{P_{Propeller}}{\eta_{Motor}} \tag{5.1}$$

Diagram a) of fig. 5.29 presents the thrust as a function of rotational speed, while diagram b) illustrates the electric power consumption. The hover performance is represented by the black solid line, the transition phase at a flight speed of 15 m/s by the magenta dashed line, and the cruise phase by the cyan dash-dotted line. Additionally, the diagram indicates the operating points for hover (hover point (HP)), transition (transition point (TP)), and cruise (cruise point (CP)).

The rotational speed is constrained by the tip Mach number limits. The lowest allowable tip Mach number is set to 0.25, corresponding to a rotational speed of 480 rpm. The highest allowable tip Mach number is 0.7, equivalent to a rotational speed of 1350 rpm for the fixed-pitch propeller.

Furthermore, the possible rotational speeds are constrained by the electric motor. The motor must deliver sufficient torque at a given rotational speed, but torque is limited by the maximum output power. In general, the propeller torque decreases with increasing flight speed, at a constant rotational speed. Consequently, higher rotational speeds can be achieved at higher flight speeds as the power consumption decreases. The propeller performance curves are thus limited by the motor's capabilities. Therefore, the y-axis of fig. 5.29 is limited to a rational speed of 900 rpm corresponding to blade tip Mach number of 0.47.

The rotational speed of the operating points is determined by the thrust requirements, which in turn define the electric power consumption. The quantitative values for all design points are provided in table 5.7. The rotational speed in the transition condition is lower than in hover conditions, while the cruise condition requires the highest rotational speed.

The electric power consumption for hover and transition conditions is similar over the entire rotational speed range. However, since the rotational speed of the transition point is significantly lower, the corresponding electric power consumption is also reduced. The two curves do not perfectly align, as they diverge at lower rotational speeds. This discrepancy results from different torque requirements and, consequently, varying motor efficiencies.

The electric power curve for the cruise condition exhibits a distinct kink at lower rotational speeds. The kink in the cruise curve is caused by the motor efficiency map (cf. diagram a) of fig. 5.31). When the speed is reduced, the torque decreases significantly, which leads to a higher efficiency of the motor, which causes the kink in the curve. The electric power required in the cruise operating point lies between the power demands of the hover and transition phases.

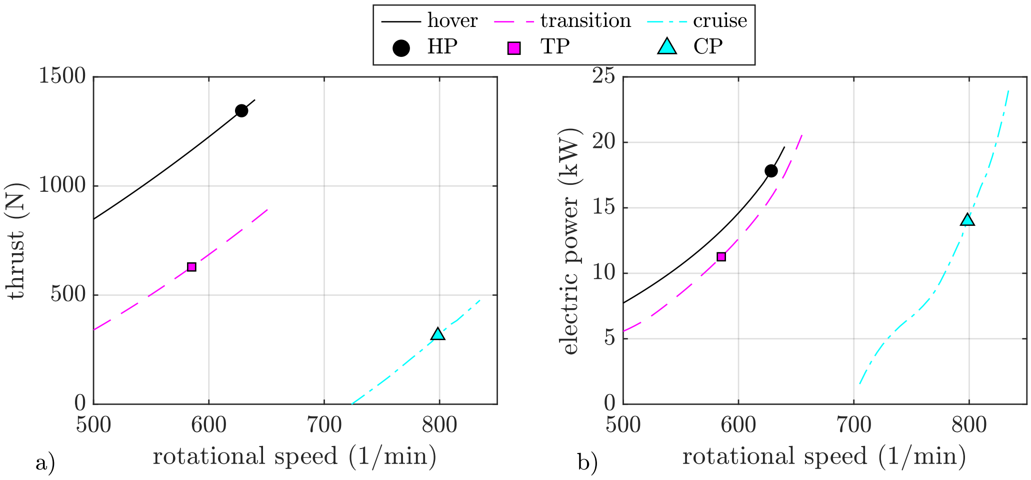

Figure 5.29: Aerodynamic performance of the optimised fixed-pitch propeller

Fig. 5.30 presents the equivalent analysis for the variable-pitch propeller. However, since pitch introduces an additional degree of freedom, a separate plot is created for each operating point. The upper row of fig. 5.30 displays thrust as a function of rotational speed, while the lower row illustrates electric power consumption. Blade pitch is discretised in 0.25° increments, with the colour bar representing the pitch domain from -6° to 6°.

As different pitch settings can achieve the target thrust for each operating point, a continuous range of valid operating points exists, forming the hover line (HL), transition line (TL), and cruise line (CL). The optimal operating point is determined by the lowest electric energy consumption.

In general, increasing pitch results in higher thrust, allowing for lower rotational speeds, while torque increases with blade pitch.

Diagrams a) and d) present the hover results. The pitch sweep shows that as pitch increases from -6° to -2°, the required rotational speed decreases. However, above -2°, thrust suddenly drops. Beyond 0° blade pitch, thrust slightly decreases at a constant rotational speed. This behaviour is caused by flow separation at the blade. The slight decrease in thrust beyond 0° blade pitch results from the effects of the 3D stall model.

The optimal blade pitch in hover is found at -6°, in the transition phase at -1.25°, and in cruise conditions at 6°. At the same time, in hover conditions, the highest possible rotational speed is found to be optimal, whereas in cruise, the lowest possible rotational speed is preferred. This behaviour is explained by the performance of the cruise point, which must be optimised, as indicated in table 5.1.

A larger pitch range could potentially improve performance further. However, since the pitch range is an input parameter in the optimisation, modifying the range affects the sweet spot geometry and the overall optimisation process. Therefore, the pitch range is not adjusted at this stage of the analysis.

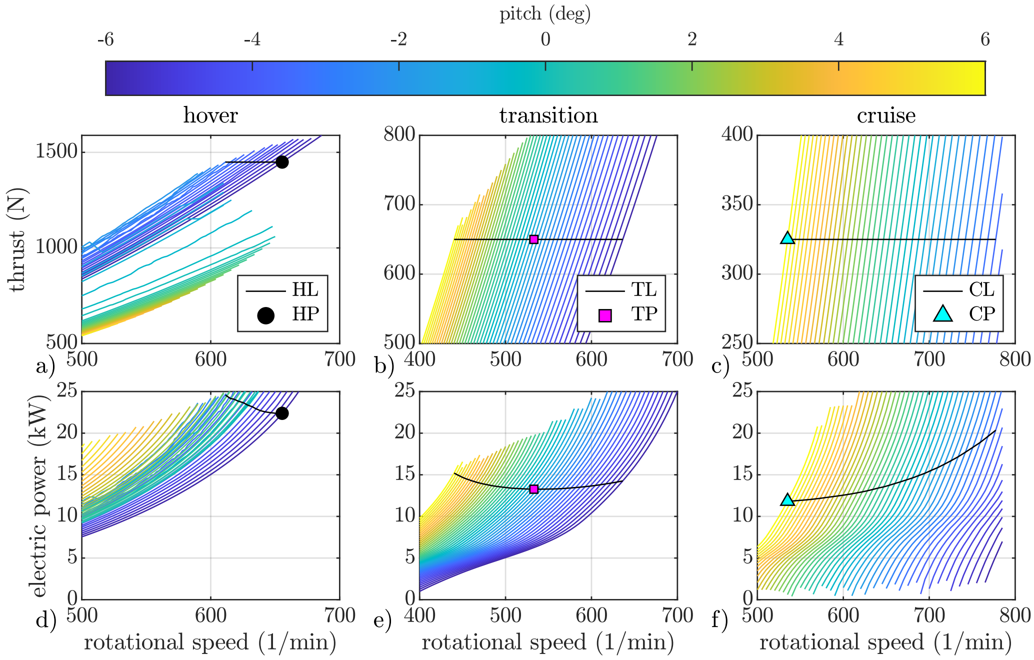

Figure 5.30: Aerodynamic performance of the optimised variable-pitch propeller

Fig. 5.31 illustrates the correlation between aerodynamic performance and the motor map for both propellers. Since the operational limits differ between the fixed- and variable-pitch propellers, distinct motor maps are required. These maps are developed based on the aerodynamic solutions. As a result, the x- and y-axes in both diagrams vary. Diagram a) presents the fixed-pitch results, while diagram b) displays the variable-pitch results.

For the fixed-pitch propeller, torque is highest in hover conditions. The transition point is located near the design point of the motor map. The cruise point exhibits the lowest motor efficiency, corresponding to the lowest torque.

In diagram b), not only the optimal operating points but also the possible operational lines are presented. The variable-pitch system enables the operating points to be positioned at the highest motor efficiency.

Despite these differences, the overall placement of the hover point, transition point, and cruise point within the motor efficiency map is consistent between the fixed- and variable-pitch propellers.

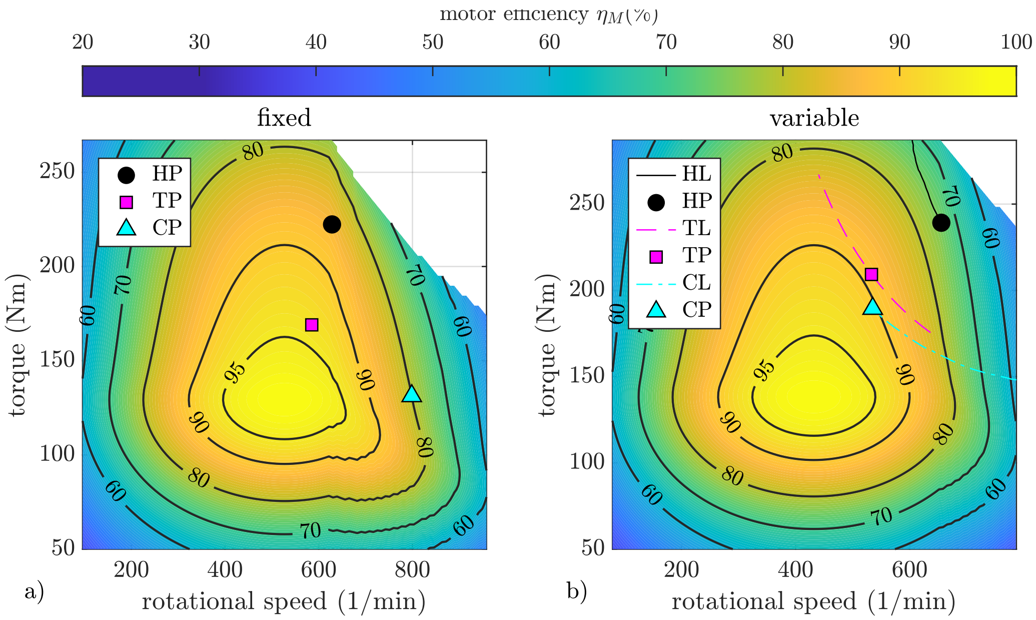

Figure 5.31: Combination of motor efficiency map and propeller performance in hover, transition, and cruise

The aerodynamic results are summarised in table 5.7. First, the rotational speed is presented, followed by the propeller torque obtained from the BEMT analysis. Next, the motor efficiencies at the optimal operating points are listed, and finally, the corresponding electric power consumption is provided.

These parameters are used to recalculate the energy consumption for the mission. The fixed-pitch propeller requires 13.84 kWs/s, while the variable-pitch propeller consumes 13.04 kWs/s. These values match the results from table 5.5.

A comparison of the electrical power consumption reveals that the fixed-pitch propeller requires less energy in hover and transition but consumes more energy in the cruise phase compared to the variable-pitch propeller. Despite this, the variable-pitch propeller is overall more efficient, as the cruise phase has the greatest influence on total energy consumption. This improvement is achieved through a lower rotational speed and higher motor efficiency at the cruise operating point for the variable-pitch propeller compared to the fixed-pitch propeller.

Table 5.7: Detailed representation of the optimised propeller performance

	Rotational speed (1/min)		**Propeller torque** (Nm)		**Shaft power** (kW)		**Motor efficiency** (%)		**Electric power** (kW)	
	fixed	vari.	fixed	vari.	fixed	vari.	fixed	vari.	fixed	vari.
Hover	628	655	222	239	14.6	16.4	82	73	17.8	22.4
Transition	585	533	169	209	10.4	11.7	92	88	11.3	13.3
Cruise	798	535	131	189	11.0	10.6	79	90	14.0	11.8

The shaft-power column of table 5.7 shows the drawbacks of the motor-mass prediction within a predictor step. In the fixed-pitch case for a propeller with a diameter of 3.4 m, the maximal ideal power consumption is 9 kW; applying the safety factor of 0.65% yields a design shaft power of 13.8 kW (cf. eq. (4.10)), yet the simulation requires 14.6 kW. In the variable-pitch case (diameter 3.2 m), the maximal ideal shaft power is 9.4 kW. Applying the 0.65% safety margin results in a design shaft power of 14.4 kW, whereas the simulation requires 16.4 kW. This underprediction could be avoided by using a more conservative safety factor (e.g. 0.55% instead of 0.65%).

The aerodynamic performance of the optimised propellers are validated using CFD RANS simulations. Since the propellers are significantly larger and have more blades than those analysed previously, the moving reference frame approach with periodic interfaces is applied. The fixed-pitch propeller requires approximately 180 million cells, while the variable-pitch propeller requires 150 million cells. The required mesh independence study and further details are provided in appendix F.3.

The optimised propellers are analysed with their corresponding pitch settings at the three operating points. The comparison is presented in table 5.8. The relative deviations between the BEMT predictions and the CFD RANS predictions for thrust and torque, calculated according to eq. (5.2), are provided.

$$\Delta = \frac{BEMT - CFD}{CFD} \tag{5.2}$$

The highest relative error is 9.5% in the thrust prediction and 5.2% in the torque prediction. However, as the thrust of the CFD simulations is not trimmed to the target thrust by pitch variation, the error in the torque must be related to the error in thrust prediction.

In the hover condition, the RANS prediction slightly under-predicts the required thrust, indicating that more flow separation occurs than predicted by the BEMT simulation. The flow separation results in higher torque values. In the transition phase, thrust is also slightly underpredicted, while torque is over-predicted. In cruise conditions, both thrust and torque are overpredicted. This matches the findings of the wind tunnel assessment in section 2.4.2.

Table 5.8: Validation of the aerodynamic performance of the optimised propeller

	Thrust difference (%)		**Torque difference** (%)	
	fixed	vari.	fixed	vari.
Hover	-8.9	-9.5	+2.3	+3.5
Transition	-2.3	-3.3	+4.3	+5.2
Cruise	+5.5	+6.3	+2.4	+4.7

In the final step, the noise emissions of the fixed- and variable-pitch propellers in hover conditions are analysed at a distance of 10 m. Fig. 5.32 presents the A-weighted noise levels at different observer positions around the propeller. Diagram a) illustrates the tonal noise, while diagram b) displays the broadband noise. The fixed-pitch results are represented by black solid lines, whereas the variable-pitch results are shown as dashed magenta lines. Additionally, the vertical line at the 110° observer position marks the location where the spectral data in fig. 5.33 are presented.

A comparison between diagrams a) and b) indicates that broadband noise dominates the overall noise emissions. Diagram a) reveals that the tonal noise of the fixed-pitch propeller is significantly higher than that of the variable-pitch propeller. However, the A-weighted tonal noise, with a maximum BPF SPL of 10 dB(A), is negligible compared to broadband noise emissions.

Diagram b) shows that the broadband noise of the variable-pitch propeller is higher than that of the fixed-pitch propeller. The maximum broadband noise level for the fixed-pitch propeller is 63.9 dB(A) at 117.5°, while for the variable-pitch propeller, it reaches 64.7 dB(A) at 115°. These results align with the findings presented in table 5.5.

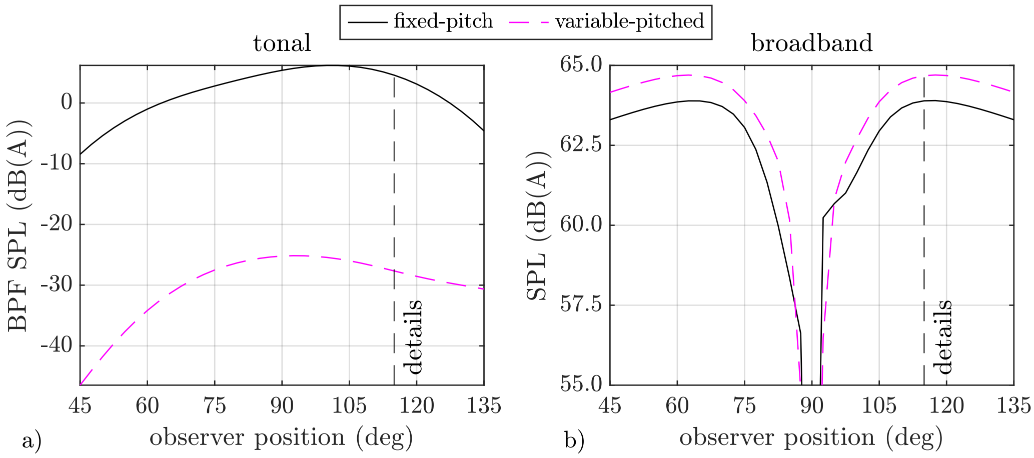

Figure 5.32: Comparison of tonal and broadand noise emissions in hover

Finally, fig. 5.33 presents the A-weighted third-octave-band spectrum of the fixed- and variable-pitch propellers at the 110° observer position. The figure follows the same structure as fig. 5.32.

Diagram a) reveals that only the first harmonic of the propeller is relevant for tonal noise. Diagram b) shows that trailing-edge noise is negligible for the overall broadband noise, as its significance is reduced by the A-weighting. At the higher end of the spectrum, corresponding to a BPF range of 128 to 256, tip vortex noise can be identified. However, A-weighting also reduces the relevance of this noise component.

Only the mid-frequency range, which is dominated by turbulent boundary layer – trailing-edge noise, significantly contributes to the overall broadband noise. This noise source is primarily influenced by the angle of attack.

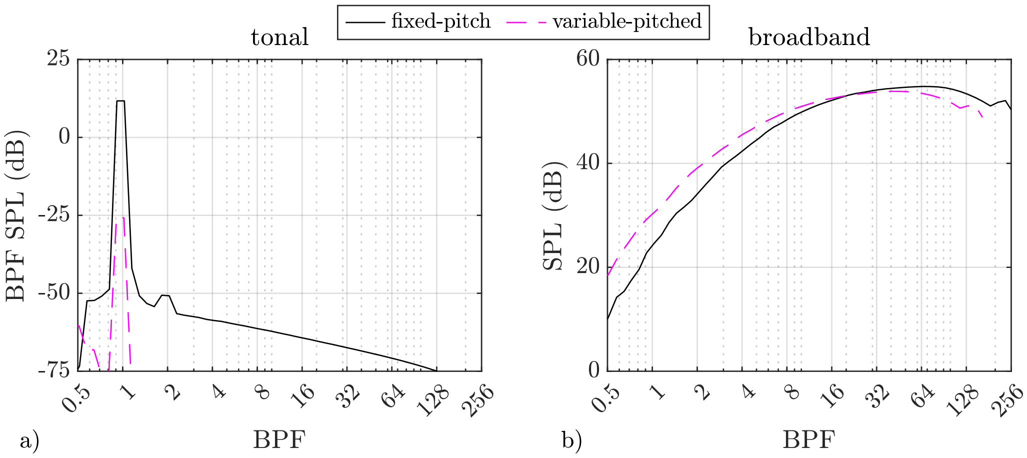

Figure 5.33: Spectrum of the fixed- and variable pitch propeller at 110° observer position

The comparison of broadband noise and tonal noise hightlights the importance of the broadband noise modelling in an MDO.

5.4 Design Guidelines

This section summarises the lessons learned in the propeller design. First, the limitations of the approach are presented before the lessons learned are derived.

The developed MDO approach has some limitations. The approach relies on the derived models, which are validated but still contain some inaccuracies. Thrust and torque are predicted within 10% accuracy, as shown in section 2.4.2 and 3.3. However, in most operating points, the thrust prediction accuracy is much higher. Therefore, final trimming with higher-fidelity simulation frameworks is required. The noise emissions are predicted within an accuracy of 7 dB, as shown in section 3.3.

The motor mass model is implemented only within a prediction step. The mass is calculated based on an ideal power consumption prediction. Multiple models exist that use torque and rotational speed to predict the motor mass. However, a more sophisticated model leads to an iterative scheme between the motor model and aerodynamic performance prediction, which should be avoided in a conceptual design and global propeller parameter optimisation. In the current study, the motor mass is less important, as the propeller mass is significantly higher.

The motor efficiency map is based on a generic approach but is crucial for the design. A motor model that provides more realistic motor maps might be incorporated into the MDO approach.

The analysed operating states are stationary operating conditions without harmonic excitation due to cross-flow conditions. The analysis of such flow states requires a fully coupled aerodynamic and structural mechanic solver, which is avoided in the conceptual design. However, in the detailed design, such analyses are required.

Under the given assumptions and for the given reference mission, the following findings are made.

1. Acoustic weighting is required if the blade number and rotational speed are varied in the optimisation process.
2. The propeller and motor mass significantly influences the optimisation.
3. The motor efficiency map significantly influences the optimisation.
4. For the given reference mission, the variable pitch propeller is 6.1% more efficient but has 0.8 dB(A) higher noise emissions.
5. The benefits of the variable pitch propeller are much smaller than observed after the GPPO. Therefore, a careful trade-off between complexity and aerodynamic efficiency must be made.
6. A larger pitch range than the 12° used in the optimisation might further improve the variable pitch results.

These findings lead to the complete answering of the second research question.

RQ 2 - Which aeroacoustic simulation method enables accurate prediction of noise from electrically driven GA and AAM propellers in conceptual design?

In the current study, the broadband model dominates noise emissions at small blade tip Mach numbers, which is why it must be modelled. This might be different if highly loaded general aviation aircraft propeller are analysed instead of propeller in hover conditions. Furthermore, acoustic weighting must be applied to find the global optimum. In conclusion, Farassat's formulation 1A in combination with at least the BPM model and acoustic weighting is required to optimise propeller noise. The thesis showed that Hanson's model, as it is presented, should not be used for a parametric assessment, as the trend does not align with the model of Farassat, which is validated in section 3.3.

Additionally, some more general conclusions about propeller design can be drawn for engineers who are starting to search for a propeller.

1. The energy consumption of each operating point should be analysed before starting the optimisation process. This assessment helps to identify the most crucial operating point and may help to reduce the parameter space.
2. The thickness distribution should continuously decrease towards the tip, with large thicknesses at the root of about 15% for structural integrity. Similar constraints are required for the chord distribution.
3. The largest possible diameters with the lowest possible blade numbers and the lowest possible rotational speed are the most efficient. However, this does not result in the quietest propeller.
4. More blades reduce the noise emissions but increase the energy consumption.
5. The blade mass should be considered when designing for vertical take-off and landing configurations.
6. A careful assessment of the pitch system is required, as the benefits might be less than expected.

With these findings, the third research question can be answered.

RQ 3 - How can electrically driven propellers be designed with aerodynamic, aeroacoustic, and aeroelastic considerations for a complete flight mission during conceptual design?
The results of the parameter study in section 5.1 and the MDO assessment in section 5.2 show that a numerical optimisation approach is required to find the optimal blade form, blade number, and diameter. A systematic assessment of the parameter space is not sufficient. Therefore, a multidisciplinary optimisation scheme with the following models must be used to find the optimal geometry. The models derived within this thesis are sufficiently accurate, reliable, and robust for the conceptual design of the propeller.

1. A BEMT theory for the prediction of the aerodynamic performance.
2. A 3D stall model to calculate off-design performance.
3. A tip- and root-loss model to improve the aerodynamic performance prediction.
4. Farassat's formulation 1A for the tonal noise prediction.
5. A broadband noise model, e.g., the Brooks, Pope, and Marcolini model.
6. An acoustic weighting function to correct the noise emissions if variable speeds or blade numbers are analysed.
7. A mass model to correct the required thrust to lift the aircraft.
8. A motor efficiency map to calculate the required energy consumption of the motor.
9. A structural design scheme based on the jig shape approach. Structural constraints limit the chord and thickness distribution.

In further work, the MDO approach can be extended with the modelling of the inverter and battery for a complete assessment of the propulsion system. However, this optimisation requires additional parameters, such as the battery discharge rate, the voltage and electric current of the inverter and motor, and further geometric constraints of the electric motor.

Furthermore, the mission assessment can be extended by the analysis of multiple propellers. Thereby, not only the optimal number of blades and diameter but also the optimal aircraft configuration can be searched.

In the case of a vertical take-off and landing vehicle, where the propellers lift the aircraft, they are used for steering by abrupt changes in rotational speed. For these manoeuvres, the moment of inertia of the propellers should be as low as possible. Therefore, a third constraint for the optimisation might be the moment of inertia of the propeller. This third constraint can be incorporated into the MDO by implementing a structural design against maximal bending loads at the root in a third step after calculating the noise emissions.

The broadband noise model relies on empirical correlations and has an accuracy of only 7 dB. Despite this limitation, it has demonstrated consistency and validity across multiple operating conditions and test cases. It therefore represents the most practical option for integration into the optimisation framework when high-resolution boundary-layer data are unavailable. Nonetheless, its predictions should be validated against experimental measurements or high-fidelity simulations wherever feasible. Future efforts should therefore prioritise the development and incorporation of more accurate broadband noise models, which are already under active investigation.

6 Conclusions and Outlook

This thesis focuses on the analysis and optimisation of electrically driven propellers for advanced air mobility (AAM) applications, addressing key challenges in aerodynamic and aeroacoustic design. The study concentrates on three primary propeller categories: GA propellers, lift propellers, and tilt propellers, as they are most affected by electrification. Unlike turboprops and open-fans, which are typically analysed using high-fidelity simulations, and rotors, which operate at constant rotational speeds, these propeller types benefit significantly from the variable-speed capabilities of electric motors. Similarly, low-Reynolds-number drone propellers are subject to fewer performance constraints, reducing the necessity for highly accurate predictive methodologies.

A key challenge in the electrification of air mobility is the lack of experience manufacturers have in the design of electrically driven propellers. This gap is even more pronounced in the context of AAM, as there is currently no extensive knowledge about the design of propellers for such applications. This thesis addresses the gap by providing a reduced-order model for the design of this type of propeller. Accordingly, it formulates and addresses three central research questions (RQ) concerning the required modelling effort.

RQ 1 - How applicable are reduced order aerodynamic simulation methods for electrically driven propellers in conceptual design?
The conceptual design requires a reduced-order model. Since the model is implemented within an optimisation routine, only the blade element momentum theory (BEMT) is considered, as it is significantly faster than, for example, the lifting line theory. Induced velocities are described using the general momentum approach. Axial and tangential induced velocities are derived for hover conditions. The 2D airfoil data are computed using XFOIL. These data are extended to the post-stall region by means of a 3D stall model. Stall modelling is essential, as parts of the propeller may operate in deep-stall conditions during a flight mission. The classical tip and root loss correction according to Prandtl is applied to account for 3D effects. Additionally, a novel sweep correction model is included to improve prediction accuracy for highly swept propellers.

The model is validated using multiple experimental datasets, both obtained by the author and extracted from literature, as well as through CFD RANS simulations. The advanced BEMT model predicts thrust and torque under hover and forward flight conditions, and for multiple propeller geometries with an accuracy of 10%. Each operating point is simulated within a second on a standard desktop computer, making the method well-suited for conceptual design and integration into an MDO approach. This level of accuracy is only achieved if the blade is discretised into at least 30 sections. However, depending on the models applied, predicted thrust and torque can deviate by up to 10% when using no corrections and the simple momentum theory. Performance prediction deviates by a further 15% when the 3D stall model is replaced with a post-stall model that neglects 3D effects. It is also shown that drag prediction is less critical for overall performance estimation, whereas accurate lift prediction is essential.

The comparison of four blade-resolving CFD RANS simulation approaches for performance prediction shows deviations of up to 10% between them. Time-resolved unsteady RANS simulations, which require at least four times the computational effort, improve thrust and torque prediction—particularly under hover conditions. The comparison between the steady moving reference frame CFD RANS simulation and experimental data shows an accuracy of 10%. Due to the high computational cost of unsteady simulations, they are less commonly used for propeller performance prediction. Instead, the moving reference frame approach is typically employed for CFD RANS propeller analysis.

After addressing the question of aerodynamic simulation effort, the thesis continues with the question of acoustic simulation effort. The acoustic method must be compatible with the aerodynamic method, as both are intended to be integrated into an optimisation framework.

RQ 2 - Which aeroacoustic simulation method enables accurate prediction of noise from electrically driven GA and AAM propellers in conceptual design?
To answer the second research question, three different tonal noise models according to Gutin, Hanson, and Farassat are analysed in detail. Only Farassat's formulation is capable of consistently predicting tonal noise emissions across a wide range of operating conditions. It is validated against experimental data from the literature and remains within an error margin of 7 dB across three different propeller geometries and various operational conditions. A temporal discretisation of 540 points per revolution with 36 blade sections is required. Hanson's model does not align with Farassat's predictions when analysing different propellers in various operational regimes. Therefore, Hanson's model is not reliable and should not be used in a design routine.

However, while tonal noise dominates in general aviation and helicopter applications, it is only one contributor in the AAM. In addition to tonal noise, broadband noise must also be analysed. To account for broadband noise, the Brooks, Pope, and Marcolini (BPM) model is introduced. Validation shows that broadband noise can be predicted with the BPM model within an error margin of 7 dB.

Electrification allows for reduced propeller rotational speeds, as electric motors provide higher torque at lower speeds compared to combustion engines. This enables significantly lower tip Mach numbers. At low tip Mach numbers, broadband noise dominates overall noise emissions, while tonal noise becomes less significant. This effect becomes more pronounced when acoustic weighting is applied, as low frequencies are damped by the weighting.

A BEMT method using Farassat's Formulation 1A, combined with the BPM model and acoustic A-weighting, is required to optimise propeller noise. These models are integrated into a multidisciplinary optimisation (MDO) framework to answer the third research question.

RQ 3 - How can electrically driven propellers be designed with aerodynamic, aeroacoustic, and aeroelastic considerations for a complete flight mission during conceptual design?
The third research question is assessed in two steps. First, a singular aerodynamic design according to the minimum induced loss conditions for hover and cruise is performed. The aerodynamically designed propellers are then analysed acoustically. As completely different blade shapes are optimal for hover and cruise, a method is required that balances aerodynamic performance and noise emissions over an entire flight mission.

An MDO approach is applied to optimise both energy consumption for a flight mission and noise emissions during hover. A serial approach is used: blade number and diameter are optimised first, followed by the blade shape. It is shown that considering the motor efficiency map, motor mass, and propeller mass is crucial to identifying the optimal diameter and blade number for a given mission. Additionally, a comparison between a fixed-pitch propeller and a variable-pitch propeller is presented. The blade shape optimisation reveals that the fixed-pitch propeller produces 0.8 dB(A) less noise in hover conditions, but the variable-pitch propeller is 6.1% more efficient over the complete flight mission. However, the increased complexity of the variable-pitch system must be weighed against its operational efficiency.

The answers to the three research questions provide guidance for the application of aerodynamic and acoustic analysis and design procedures. This thesis establishes a robust framework for the conceptual design of propellers. On the one hand, the design procedure can be applied in conceptual aircraft design to determine the optimal propeller diameter, which directly influences the configuration in AAM. Furthermore, the optimisation framework supports decision-making regarding whether a pitch system is required. On the other hand, propeller manufacturers can use the framework to optimise the blade shape in detail for specific requirements.

Several aspects require further investigation and refinement to enhance the accuracy and applicability of the approach.

In terms of aerodynamics, the current performance prediction methodology could be improved by incorporating a more sophisticated stall model. The existing approach relies on empirical corrections and simplified assumptions, which may not fully capture complex three-dimensional flow phenomena, particularly under off-design conditions. A more advanced stall model would allow for improved accuracy in predicting aerodynamic performance across a wider range of operating states.

Regarding aeroacoustics, the broadband noise model currently used in the optimisation framework is based on empirical correlations. Future work should focus on integrating a more advanced broadband noise model that accounts for boundary-layer effects with higher fidelity. This would enable a more precise evaluation of noise emissions, particularly in AAM applications, where broadband noise might dominate.

The MDO can also be extended to further enhance the design process. An improved motor model, incorporating more detailed efficiency maps and loss mechanisms, would increase the reliability of power consumption predictions. Additionally, integrating an electric inverter and battery model into the optimisation would allow for a more comprehensive assessment of the entire propulsion system, capturing key interactions between the battery, inverter, and motor. A detailed design approach with iterative coupling between the motor and propeller design would further refine system-level performance, ensuring that both components are optimally matched.

Finally, for hover propellers, moment of inertia plays a crucial role in flight control. Future work should include an additional optimisation constraint to minimise the moment of inertia, improving the dynamic response of the propeller for vertical take-off and landing applications.

These extensions will contribute to a more accurate and holistic design framework, ensuring that electrically driven propellers meet the demanding requirements of next-generation AAM solutions.

Bibliography

[1] Adkins, C. N.; Liebeck, R. H.: Design of optimum propellers. Journal of Propulsion and Power, Vol. 10, No. 5, pp. 676–682, 1994. doi: https://doi.org/10.2514/3.23779

[2] Amatt, W.; Bates, W. E.; Borst, H. V.: Summary of Propeller Design Procedures and Data. Volume II. Structural Analysis and Blade Design: AD-774-836. USAAMRDL Technical Report 73-34B, 1973.

[3] Amiet, R. K.: Noise due to turbulent flow past a trailing edge. In: Journal of Sound and Vibration. 47, pp. 387–393. doi: https://doi.org/10.1016/0022-460X(76)90948-2

[4] Babetto, L.; König, R.; Fassnacht, J.; Stumpf, E.: Study on public acceptance of eVTOLs: safety and noise. In: DLRK 2023. Stuttgart, Deutschland, 2023.

[5] Barnes, J. P.: Hybrid Blade Element and Lifting Line for Propeller or Propfan Performance. In: AIAA AVIATION 2017 Forum. Denver, CO, p. 484, 2017. doi: https://doi.org/10.2514/6.2017-3570

[6] Bauersfeld, L.; Scaramuzza, D.: Range, Endurance, and Optimal Speed Estimates for Multicopters. In: IEEE Robot. Autom. Lett. (IEEE Robotics and Automation Letters). 7, pp. 2953–2960. doi: https://doi.org/10.1109/LRA.2022.3145063

[7] Bergmann, O.; Götten, F.; Braun, C.; Janser, F.: Comparison and evaluation of blade element methods against RANS simulations and test data. In: CEAS Aeronautical Journal. 13, pp. 535–557, 2022. doi: https://doi.org/10.1007/s13272-022-00579-1

[8] Bergmann, O.; Möhren, F.; Braun, C.; Janser, F.: Aerodynamic Design of Swept Propeller with BEMT. In: DLRK 2022. Dresden, Germany, 2022.

[9] Bergmann, O.; Möhren, F.; Braun, C.; Janser, F.: Aerodynamic Analysis of Swept Propeller with BET and RANS. In: DLRK 2021. Bremen, Germany, 2021.

[10] Bergmann, O.; Möhren, F.; Braun, C.; Janser, F.: On the influence of elasticity on swept propeller noise. In: AIAA SciTech 2023 Forum. National Harbor, MD & Online, 2023. doi: https://doi.org/10.2514/6.2023-0210

[11] Bergmann, O.; Möhren, F.; Frey, D.; Janser, F.; Braun, C.: Assessment of Aeroacoustic Optimisation Schemes for a Tilt-Propeller Application in Hover and Cruise. In: 49th European Rotorcraft Forum. Bückeburg, Germany, 2023.

[12] Betz, A.; Helmbold, H. B.: Zur Theorie stark belasteter Schraubenpropeller. In: Ingenieur-Archiv. 3, pp. 1–23.

[13] Betz, A.; Prandtl, L.: Vier Abhandlungen zur Hydrodynamik und Aerodynamik, Göttingen: Universitätsverlag Göttingen, ISBN 978-3-941875-75-3, 1919.

[14] Billman, L. C.; Gruska, C. J.; Ladden, R. M.; Leishman, D. K.; Turnberg, J. E.: Large scale prop-fan structural design study. Volume 2: Preliminary design of SR-7. NASA CR 174993, 1988.

[15] Blandeau, V. P.; Joseph, P. F.: Validity of Amiet's Model for Propeller Trailing-Edge Noise. In: AIAA Journal. 49, pp. 1057–1066. doi: https://doi.org/10.2514/1.J050765

[16] Blocks, P. J. W.: Operational evaluation of a proppeller test stand in the quiet flow facility at Langley Research Center. In: NASA Technical Memorandum. 84523.

[17] Bohorquez, F.; Pines, D.; Samuel, P. D.: Small Rotor Design Optimization Using Blade Element Momentum Theory and Hover Tests. Journal of Aircraft, Vol. 47, No. 1, pp. 268–283, 2010. doi: https://doi.org/10.2514/1.45301

[18] Borst, H. V.: Summary of Propeller Design Procedures and Data, Volume I - Aerodynamic Design and Installation: AD-774-831. USAAMRDL Technical Report 73-34A, 1973.

[19] Brooks, T. F.; Pope, D. S.; Marcolini, M. A.: Airfoil Self-Noise and Prediction. In: NASA Reference Publication. 1218.

[20] Burger, C.; Hartfield, R.: Design, Testing and Optimization of a Constant Torque Propeller. In: Applied Aerodynamics Conference. Miami, FL, 2007.

[21] Busemann, A.: Aerodynamischer Aufrieb bei Überschallgeschwindigkeiten. In: Conference Proceedings. Roma, pp. 315–347, 1935.

[22] Carreno Ruiz, M.; D'Ambrosio, D.: Aerodynamic optimization of quadrotor blades operating in the martian atmosphere. In: AIAA SciTech 2022 Forum. American Institute of Aeronautics and Astronautics (AIAA), 2022. doi: https://doi.org/10.2514/6.2022-0743

[23] Carroll, J.; Marcum, D.: Comparison of a Blade Element Momentum Model to 3D CFD Simulations for Small Scale Propellers. SAE International Journal of Aerospace, No. 6(2), pp. 721–726, 2013. doi: https://doi.org/10.4271/2013-01-2270

[24] Casalino, D.; Barbarino, M.: Stochastic Method for Airfoil Self-Noise Computation in Frequency Domain. In: AIAA Journal. 49, pp. 2453–2469. doi: https://doi.org/10.2514/1.J050773

[25] Casalino, D.; Grande, E.; Romani, G.; Ragni, D.; Avallone, F.: Definition of a benchmark for low Reynolds number propeller aeroacoustics. Aerospace Science and Technology, Vol. 113, p. 106707, 2021. doi: https://doi.org/10.1016/j.ast.2021.106707

[26] Catlett, M. R.; Anderson, J. M.; Forest, J. B.; Stewart, D. O.: Empirical Modeling of Pressure Spectra in Adverse Pressure Gradient Turbulent Boundary Layers. In: AIAA Journal. 54, pp. 569–587. doi: https://doi.org/10.2514/1.J054375

[27] Celi, R.; Friedmann, P. P.: Structural optimization with aeroelastic constraints of rotor bladeswith straight and swept tips. AIAA Journal, Vol. 28, No. 5, pp. 928–936, 1990. doi: https://doi.org/10.2514/3.25141

[28] Chiew. Jonathan J.; Aftosmis, M. J.: Efficient Simulation of Multi-rotor Configurations with Low Reynolds Number Propellers. In: AIAA AVIATION 2018 Forum. Atlanta, GA, pp. 594–609, 2018. doi: https://doi.org/10.2514/6.2018-4119

[29] Chin, J.; Aretskin-Hariton, E.; Ingraham, D.; Hall, D.; Schnulo, S. L.; Gray, J.; Hendricks, E. S.: Battery Evaluation Profiles for X-57 and Future Urban Electric Aircraft. In: AIAA Propulsion and Energy 2020 Forum. Reston, Virginia: American Institute of Aeronautics and Astronautics (AIAA), ISBN 978-1-62410-602-6, 2020. doi: https://doi.org/10.2514/6.2020-3567

[30] Chirico, G.; Barakos, G. N.; Bown, N. W.: Numerical aeroacoustic analysis of propeller designs. The Aeronautical Journal, Vol. 122, No. 1248, pp. 283–315, 2017. doi: https://doi.org/10.1017/aer.2017.123

[31] Clarke, M. A.; Botero, E.: Aeroacoustic Optimization of VTOL Rotor Blades. In: AIAA SciTech 2023 Forum. National Harbor, MD & Online, 2023. doi: https://doi.org/10.2514/6.2023-0209

[32] Dinyavari, M. A. H.; Friedmann, P. P.: Application of time-domain unsteady aerodynamics to rotary-wing aeroelasticity. In: AIAA Journal. 24, pp. 1424–1432. doi: https://doi.org/10.2514/3.9459

[33] Drela, M.: XFOIL: An Analysis and Design System for Low Reynolds Number Airfoils. Low Reynolds Number Aerodynamics. Lecture Notes in Engineering, Vol. 54, pp. 1–12, 1989. doi: https://doi.org/10.1007/978-3-642-84010-4

[34] Drobietz, R. Neuwerth, G.; Jacob, D.: Noise Reduction Potential of Swept Propeller Blades. In: Proceedings of CEAS Forum on Aeroacoustics of Rotors and Propellers. 31: Rome, Italy, pp. 65–77, 1999.

[35] Duffy, M.; Sevier Abigail; Hupp, R.; Perdomo Enrique; Wakayama Sean: Propulsion Scaling Methods in the Era of Electric Flight. AIAA/IEEE Electric Aircraft Technologies Symposium, Vol. 2018, 2018. doi: https://doi.org/10.2514/6.2018-4978

[36] Durand, W. F.: Experimental research on air propellers: In Three Parts. In: NASA Technical Memorandum. 14.

[37] Engineering Science Data Unit: Approximate Parametric Method for Propeller Thrust Estimation: ESDU 83001, November 1, 1983.

[38] Eppler, R.; Somers, D. M.: A Computer Program for the Design and Analysis of Low-Speed Airfoils. In: NASA Technical Memorandum. 80210.

[39] Eppler, R.; Somers, D. M.: Supplement to: A computer propgram for the Design and Analysis of Low-Speed Airfoils. In: NASA Technical Memorandum. 81862.

[40] Falissard, F.; Boisard, R.; Gaveriaux, R.; Delattre, G.; Gardarein, P.; Chelius, A.; Canard-Caruana, S.; Mauffrey, Y.: Influence of Blade Deformations on Open-Rotor Low-Speed and High-Speed Aerodynamics and Aeroacoustics. Journal of Aircraft, Vol. 55, No. 6, pp. 2267–2281, 2018. doi: https://doi.org/10.2514/1.C034676

[41] Falk Götten: Exploration and Development of New Drag Prediction Models for UAVs. RMIT University, PhD thesis, April 2021.

[42] Farassat, F.: Linear Acoustic Formulas for Calculation of Rotating Blade Noise. In: AIAA Journal. 19, pp. 1122–1130. doi: https://doi.org/10.2514/3.60051

[43] Farassat, F.; Succi, G. P.: A Review of Propeller discrete frequency noise predition technology with emphasis on two current methods for time domain calculations. In: Journal of Sound and Vibration. 71, pp. 399–419.

[44] Federal Aviation Administration: Next Generation Air Transportation System (NextGen), https://www.faa.gov/nextgen, 14.01.2025.

[45] Ffowcs Williams, J. E.; Hawkings, D. L.: Sound Generation by Turbulence and Surfaces in Arbitrary Motion. Philosophical Transactions of the Royal Society of London. Series A, Mathematical and Physical Sciences, Vol. 264, No. 1151 (May 8, 1969), pp. 321-342, 1969.

[46] Finger, D. F.: Methodology for Multidisciplinary Aircraft Design under Consideration of Hybrid-Electric Propulsion Technology. RMIT University, PhD thesis, 2020.

[47] Flightpath 2050: Europe's Vision for Aviation: Report of the High-Level Group on Aviation Research. Policy / European Commission, Luxembourg: Publ. Off. of the Europ. Union, ISBN 978-92-79-19724-6, 2011.

[48] Froude, R. E.: On the Part Played in Propulsion by Differences of Fluid Pressure. Trans. Inst. Naval Architects, Vol. 30, p. 390, 1889.

[49] Froude W.: On the elementary relation between pitch, slip, and propulsive efficiency, Paris, 1920.

[50] Geiger Engineering: HPD Motor Product Series, https://www.geigerengineering.de/avionik/produkte, 2020.

[51] Geng, X.; Liu, P.; Hu, T.; Qu, Q.; Dai, J.; Lyu, C.; Ge, Y.; Akkermans, R. A.: Multi-fidelity optimization of a quiet propeller based on deep deterministic policy gradient and transfer learning. In: Aerospace Science and Technology. 137. doi: https://doi.org/10.1016/j.ast.2023.108288

[52] Gennaretti, M.; Rubeis, B. de; Poggi, C.; Bernardini, G.: Acoustic analysis of a rotor in forward flight with deformable blades through a boundary integral formulation. In: AIAA AVIATION 2023 Forum. San Diego, CA, 2023. doi: https://doi.org/10.2514/6.2023-3216

[53] Gill, H.; Lee, S.: Development of New Empirical Rotor Broadband Noise Prediction Models for Urban Air Mobility Applications. In: AIAA SciTech 2024 Forum. Orlando, FL, 2024. doi: https://doi.org/10.2514/6.2024-2473

[54] Gladwell, G. M. L.; Bauchau, O. A.; Craig, J. I.: Structural Analysis. Solid mechanics and its applications, Dordrecht: Springer Netherlands, 2009.

[55] Glauert, H.; H; Lock, C. N. H.: On the Advantages of an Open Jet Type of Wind Tunnel for Airscrew Tests, 10333, 1926.

[56] Goldstein, S.: On the Vortex Theory of Screw Propellers. In: Göttinger Nachrichten. 123, pp. 193–213.

[57] Goody, M.: Empirical Spectral Model of Surface Pressure Fluctuations. In: 42, pp. 1788–1794. doi: https://doi.org/10.2514/1.9433

[58] Götten, F.; Finger, F.; Havermann, M.; Braun, C.; Marino, M.; Bil, C.: A Highly Automated Method for simulating Airfoil Characteristics at Low Reynolds Number using a RANS - Transition Approach. In: DLRK 2019. Darmstadt and Germany, 2019. doi: https://doi.org/10.25967/490026

[59] Grande, E.; Romani, G.; Ragni, D.; Avallone, F.; Casalino, D.: Aeroacoustic Investigation of a Propeller Operating at Low Reynolds Numbers. AIAA Journal, pp. 1–12, 2021. doi: https://doi.org/10.2514/1.j060611

[60] Greenwood, E.; Brentner, K. S.; Rau, R. F.; Ted Gan, Z. F.: Challenges and opportunities for low noise electric aircraft. International Journal of Aeroacoustics, Vol. 21, No. 5-7, pp. 315–381, 2022. doi: https://doi.org/10.1177/1475472X221107377

[61] Gur, O.: Airfoil Importance for Propeller Optimized Design. In: Proceedings of the 56th 3AF International Conference on Applied Aerodynamics for Lower Environmental Impact. Toulouse, France, 2022.

[62] Gur, O.: Engine–Propeller Matching. In: Propeller Design. 6: Reston: American Institute of Aeronautics and Astronautics (AIAA), pp. 121–140, ISBN 9781624107146, 2024. doi: https://doi.org/10.2514/5.9781624107146.0121.0140

[63] Gur, O., ed.: Propeller Design, Reston: American Institute of Aeronautics and Astronautics (AIAA), ISBN 9781624107146, 2024.

[64] Gur, O.; Lazar, G.: Prop-Rotor Design for an Electric Tilt-Rotor Vehicle. In: Future Vertical Lift Aircraft Design Conference. San Francisco, CA, 2012.

[65] Gur, O.; Rosen, A.: Comparison between blade-element models of propellers. The Aeronautical Journal, Vol. 112, No. 1138, pp. 689–704, 2008. doi: https://doi.org/10.13140/RG.2.1.3854.5129

[66] Gur, O.; Rosen, A.: Multidisciplinary Design Optimization of a Quiet Propeller. In: 14th AIAA/CEAS Aeroacoustics Conference. 14: Vancouver, British Columbia, Canada, p. 193, 2008. doi: https://doi.org/10.2514/6.2008-3073

[67] Gur, O.; Rosen, A.: Optimization of Propeller Based Propulsion System. Journal of Aircraft, Vol. 46, No. 4, pp. 95–106, 2009. doi: https://doi.org/10.2514/1.36055

[68] Gur, O.; Silver, J.; Dítě, R.; Sundhar, R.: Hover-Propeller Full Design Cycle - Performance and Acoustic. PhD thesis, 2022.

[69] Gutin, L.: On the Sound field of a rotating propeller. Physikalische Zeitschrift der Sowjetunion, No. Band 9, Heft 1, 1936.

[70] Hambrey, J.; Kotwicz Herniczek, M. T.; Feszty, D.; Meslioui, S.-A.; Park, J.: Comparison of Three Popular Methods for the Prediction of High Speed Propeller Noise. In: AIAA AVIATION 2017 Forum. Denver, CO, p. 1, 2017. doi: https://doi.org/10.2514/6.2017-4181

[71] Hamilton Standard: Generalized Method of Propeller Performance Estimation 1961-1963, https://hdl.handle.net/2144/10454, 1963.

[72] Hanson, D. B.: Direct frequency domain calculation of open rotor noise. In: AIAA Journal. 30, pp. 2334–2337. doi: https://doi.org/10.2514/3.11223

[73] Hanson, D. B.: Helicoidal Surface Theory for Harmonic Noise of Propellers in the Far Field. In: AIAA Journal. 18, pp. 1213–1220. doi: https://doi.org/10.2514/3.50873

[74] Hanson, D. B.: Theory for Broadband Noise of Rotor and Stator Cascades With Inhomogeneous Inflow Turbulence Including Eeffects of Lean and Sweep. In: NASA Contractor Report. 2001-210762.

[75] Hanson, D. B.: Compressible Helicoidal Surface Theory for Propeller Aerodynamics and Noise. In: AIAA Journal. 21, pp. 881–889. doi: https://doi.org/10.2514/3.60132

[76] Hanson, D. B.: Influence of Propeller Design Parameters on Far-Field Harmonic Noise in Forward Flight. In: AIAA Journal. 18, pp. 1313–1319. doi: https://doi.org/10.2514/3.50887

[77] Heinritz, Y.; Bergmann, O.; Möhren, F.; Janser, F.: Numerical Evaluation of a Wind Tunnel Design for Propeller Testing. In: DLRK 2021. Bremen, Germany, 2021.

[78] Hennes, C. C.; Brentner, K. S.: The Effect of Blade Deformation on Rotorcraft Acoustics. In: Journal of the American Helicopter Society, Vertical Flight Society. doi: https://doi.org/10.4050/JAHS.53.398

[79] Hepperle, M.: Electric Flight – Potential and Limitations, STO-MP-AVT-209, 2009.

[80] Hu, H.; Jordan, L. A.; Baeder, J. D.: Computational simulation and analysis of double-swept blade in BVI noise reduction. Advances in Engineering Software, Vol. 36, No. 2, pp. 67–76, 2005. doi: https://doi.org/10.1016/j.advengsoft.2004.08.002

[81] Hu, N.; Herr, M.: Characteristics of Wall Pressure Fluctuations for a Flat Plate Turbulent Boundary Layer with Pressure Gradients. In: 22nd AIAA/CEAS Aeroacoustics Conference. Lyon, France, 2016. doi: https://doi.org/10.2514/6.2016-2749

[82] Iousef, S.; Montazeri, H.; Blocken, B.; van Wesemael, P.: Wall-resolved versus wall-modeled LES of the flow field and surface forced convective heat transfer for a low-rise building. In: Building and Environment. 244. doi: https://doi.org/10.1016/j.buildenv.2023.110678

[83] Issawi, C.: The 1973 Oil Crisis and After. Journal of Post Keynesian Economics, Vol. 1, No. 2, pp. 3–26, 1978. doi: https://doi.org/10.1080/01603477.1978.11489099

[84] Jeanneret, B.; Des Guille Buttes, A.; Keromnes, A.; Pélissier, S.; Le Moyne, L.: Optimal Control for Cleaner Hybrid Vehicles: A Backward Approach. Applied Sciences, Vol. 12, No. 2, p. 578, 2022. doi: https://doi.org/10.3390/app12020578

[85] Kamruzzaman, M.; Bekiropoulos, D.; Lutz, T.; Würz, W.; Krämer, E.: A Semi-Empirical Surface Pressure Spectrum Model for Airfoil Trailing-Edge Noise Prediction. In: International Journal of Aeroacosutics. 14, pp. 833–882. doi: https://doi.org/10.1260/1475-472X.14.5-6.83

[86] Kang, D. H.; Lee, S.: On the Effect of Boundary-layer Tripping for Trailing-edge Noise Predictions. In: AIAA SciTech 2023 Forum. National Harbor, MD & Online, 2023. doi: https://doi.org/10.2514/6.2023-0972

[87] Kaya, M. N.; Köse, F.; Uzol, O.; Ingham, D.; Ma, L.; Pourkashanian, M.: Aerodynamic Optimization of a Swept Horizontal Axis Wind Turbine Blade. Journal of Energy Resources Technology, Vol. 143, No. 9, 2021. doi: https://doi.org/10.1115/1.4051469

[88] Keck, R.-E.: A numerical investigation of nacelle anemometry for a HAWT using actuator disc and line models in CFX. In: Renewable Energy. 48, pp. 72–84. doi: https://doi.org/10.1016/j.renene.2012.04.004

[89] Kim, Y. N.; George, A. R.: Trailing-Edge Noise from Hovering Rotors. In: AIAA Journal. 20, pp. 1167–1174. doi: https://doi.org/10.2514/3.51176

[90] Kosmatka, J. B.; Friedmann, P. P.: Structural dynamic modeling of advanced composite propellers by the finite element method. In: 28th Structures, Structural Dynamics and Materials Conference. Monterey, CA, p. 740, 1987. doi: https://doi.org/10.2514/6.1987-740

[91] Kotwicz Herniczek, M. T.; Feszty, D.; Meslioui, S.-A.; Park, J.: Applicability of Early Acoustic Theory for Modern Propeller Design. In: AIAA AVIATION 2017 Forum. Denver, CO, 2017. doi: https://doi.org/10.2514/6.2017-3865

[92] Kulfan, B. M.: Recent extensions and applications of the 'CST' universal parametric geometry representation method. The Aeronautical Journal, Vol. 114, 2010. doi: https://doi.org/10.2514/6.2007-7709

[93] Kulfan, B. M.: Universal Parametric Geometry Representation Method. In: Journal of Aircraft: devoted to aeronautical science and technology, American Institute of Aeronautics and Astronautics. doi: https://doi.org/10.2514/1.29958

[94] Kvurt, A.; Ruf, D.; Hertzman, O.; Stalnov, O.; Ben-Gida, H.: getPROP - A MATLAB Suite for Low-Signature Propeller Design, Analysis, and Optimization. In: AIAA SciTech 2023 Forum. National Harbor, MD & Online, 2023. doi: https://doi.org/10.2514/6.2023-0026

[95] Larrabee, E. E.: Design of Propellers for Motorsoarers: The Science and Technology of Low Speed and Motorless Flight, Pt. 1, 1979.

[96] Lee, H.; Sengupta, B.; Araghizadeh, M. S.; Myong, R. S.: Review of vortex methods for rotor aerodynamics and wake dynamics. Advances in Aerodynamics, Vol. 4, No. 1, 2022. doi: https://doi.org/10.1186/s42774-022-00111-3

[97] Lee, S.: Empirical Wall-Pressure Spectral Modeling for Zero and Adverse Pressure Gradient Flows. In: AIAA Journal. 56, pp. 1818–1829. doi: https://doi.org/10.2514/1.J056528

[98] Lee, S.; Brentner, K.; Farassat, F.: Analytic Formulation and Numerical Implementation of an Acoustic Pressure Gradient Prediction. Journal of Sound and Vibration, No. 319, 2009. doi: https://doi.org/10.2514/6.2007-3710

[99] Li, S.; Lee, S.: Prediction of Rotorcraft Broadband Trailing-Edge Noise and Parameter Sensitivity Study. In: Journal of the American Helicopter Society. 65, pp. 1–14. doi: https://doi.org/10.4050/JAHS.65.042006

[100] Lighthill, M. J.: On sound generated aerodynamically I. General theory. Proceedings of the Royal Society of London. Series A. Mathematical and Physical Sciences, No. 1107, pp. 564–587, 1952. doi: https://doi.org/10.1098/rspa.1952.0060

[101] Long, Q.; Ma, J.; Jiang, F.; Webster, C. J.: Demand analysis in urban air mobility: A literature review. Journal of Air Transport Management, Vol. 112, p. 102436, 2023. doi: https://doi.org/10.1016/j.jairtraman.2023.102436

[102] Lopes, L. V.: ANOPP2's Farassat Formulations Internal Functional Modules (AFFIFMs) Reference Manual. In: NASA Technical Memorandum. 20210021111.

[103] Lopes, L. V.: Compact Assumption Applied to the Monopole Term of Farassat's Formulation. In: AIAA AVIATION 2015 Forum. 54: Dallas, Texas, pp. 1649–1663, 2015. doi: https://doi.org/10.2514/6.2015-2673

[104] M. H. Dunn; A. F. Tinetti; D. M. Nark: Open Rotor Noise Prediction Using the time Domain Formulations of Farassat. International Journal of Aeroacoustics, Vol. 14, No. 1-2, pp. 51–86, 2015. doi: https://doi.org/10.1260/1475-472X.14.1-2.51

[105] Marden, J. H.: Scaling of maximum net force output by motors used for locomotion. The Journal of experimental biology, Vol. 208, No. Pt 9, pp. 1653–1664, 2005. doi: https://doi.org/10.1242/jeb.01483

[106] Marinus, B. G.: Comparative Study of the Effects of Sweep and Humps on High-Speed Propeller Blades. In: 18th AIAA/CEAS Aeroacoustic Conferecne. 2219: Colorado Springs, CO, 2012. doi: https://doi.org/10.2514/1.J052833

[107] McCrink M. H.; Gregory, J. W.: Blade Element Momentum Modeling of Low-Reynolds Electric Propulsion Systems. Journal of Aircraft, Vol. 54, No. 1, pp. 163–176, 2017. doi: https://doi.org/10.2514/1.C033622

[108] McDonald, R. A.: Electric Propulsion Modeling for Conceptual Aircraft Design. In: AIAA SciTech 2014 Forum. National Harbor, MD, 2014.

[109] Menter, F. R.: Two-equation eddy-viscosity turbulence models for engineering applications. AIAA Journal, Vol. 32, No. 8, pp. 1598–1605, 1994. doi: https://doi.org/10.2514/3.12149

[110] Menter, F. R.; Smirnov, P. E.; Liu, T. A.; Avancha, R.: A One-Equation Local Correlation-Based Transition Model. In: Flow Turbulence Combust. 95:583–619.

[111] Mohamad, A. A.: Lattice Boltzmann Method: Fundamentals and Engineering Applications with Computer Codes, London: Springer London, 2019.

[112] Möhren, F.: Structural Modelling and Design Strategies for Lifting Propellers. RWTH Aachen University, PhD thesis, 2025.

[113] Möhren, F.; Bergmann, O.; Janser, F.; Braun, C.: On the suitability of the Jig-Shape approach for structural design of propellers. International Forum on Aeroelasticity and Structural Dynamics, No. 4, pp. 2094–2109, 2022.

[114] Möhren, F.; Bergmann, O.; Janser, F.; Braun, C.: An Enhanced Jig-Shape Approach to Lifting Propeller Design. AIAA SciTech 2024 Forum, 2024. doi: https://doi.org/10.2514/6.2024-1706

[115] Möhren, F.; Bergmann, O.; Janser, F.; Braun, C.: Assessment of structural mechanical effects related to torsional deformations of propellers. CEAS Aeronautical Journal, 2024. doi: https://doi.org/10.1007/s13272-024-00737-7

[116] Möhren, F.; Bergmann, O.; Janser, F.; Braun, C.: On the Influence of Elasticity on Propeller Performance: A Parametric Study. Deutscher Luft- und Raumfahrtkongress 2021, 2021.

[117] Möhren, F.; Bergmann, O.; Janser, F.; Braun, C.: On the influence of elasticity on propeller performance: a parametric study. CEAS Aeronautical Journal, Vol. 14, No. 2, pp. 311–323, 2023. doi: https://doi.org/10.1007/s13272-023-00649-y

[118] Montgomerie, B.: Methods for Root Effects, Tip Effects and Extending the Angle of Attack Range to ±180°: FOI-R 1305 Sed, 2004.

[119] Nierling, J.; Leutz, R.; Radowski, H.; Zhao, J.; Romac, B.: The Economics of Vertical Mobility: A guide for investors, players, and lawmakers to scceed in urban air mobility, 2021.

[120] Noth, A.: Design of Solar Powered Airplanes for Continuous Flight. ETH Zürich, PhD thesis, 2008.

[121] Odvárla, E.; Mebarik, A.; Gerada, D.; Brown, N.; Ondrusek, C.: Electric Motor-Generator for a Hybrid Electric Vehicle. In: Engineering MECHANICS. 16, pp. 131–139.

[122] Parry, A. B.; Crighton, D. G.: Asymptotic theory of propeller noise - Part I - Subsonic single-rotation propeller. In: AIAA Journal. 27, pp. 1184–1190. doi: https://doi.org/10.2514/3.10244

[123] Pelz, P. F.; Leise, P.; Meck, M.: Sustainable aircraft design — A review on optimization methods for electric propulsion with derived optimal number of propulsors. Progress in Aerospace Sciences, Vol. 123, p. 100714, 2021. doi: https://doi.org/10.1016/j.paerosci.2021.100714

[124] Pettingill, N. A.; Zawodny, N. S.; Thurman, C.; Lopes, L. V.: Acoustic and Performance Characteristics of an Ideally Twisted Rotor in Hover. AIAA SciTech 2021 Forum, 2021. doi: https://doi.org/10.2514/6.2021-1928

[125] Prieur, J.; Rahier, G.: Comparison of Ffowcs Williams-Hawkings and Kirchhoff rotor noise calculations. In: 4th AIAA/CEAS Aeroacoustics Conference, 1998. doi: https://doi.org/10.2514/6.1998-2376

[126] R. Hallaz; C. Colageli; J. Cuenca; L. De Ryck: Impact of electric propulsion on aircraft noise - all-electric light aircrafts case study. AIAA/IEEE Electric Aircraft Technologies Symposium, Vol. 2018, 2018. doi: https://doi.org/10.2514/6.2018-4982

[127] Ragot, P.; Markovic, M.; Perriard, Y.: Optimization of Electric Motor for a Solar Airplane Application. In: International Conference on Electric Machines and Drives. Miami, FL, pp. 1487–1493, 2009. doi: https://doi.org/10.1109/IEMDC.2005.195917

[128] Rankine, W.: On the Mechanical Principles of the Action of Propellers. Transactions of the Institution of Naval Architects, Vol. 6, 1865.

[129] Risse, K.: Preliminary Overall Aircraft Deisgn With Hybrid Laminar Flow Control. RWTH Aachen, PhD thesis, 2016.

[130] Rozenberg, Y.; Robert, G.; Moreau, S.: Wall-Pressure Spectral Model Including the Adverse Pressure Gradient Effects. In: 50, pp. 2168–2179. doi: https://doi.org/10.2514/1.J051500

[131] Ruijgrok G. J. J.: Elements of aviation acoustics, Delft and Netherlands, ISBN 90-6275-899-1, 1993.

[132] Ruiz, M. C.: CFD Simulation of Propellers: Best Practices Analysis. Politecnico di Torino, PhD thesis, 01.03.2019.

[133] S. Gaggero; C. M. Rizzo; G. Tani; M. Viviani: EFD and CFD Design and Analysis of a Propeller in Decelerating Duct: Hindawi Publishing Corporation International Journal of Rotating Machinery. In: International Journal ofRotating Machinery. 2012, pp. 1–15. doi: https://doi.org/10.1155/2012/823831

[134] Sakthivel, T.; Venkatesan, C.: Rotorcraft control response using linearised and non-linear flight dynamic models with different inflow models. The Aeronautical Journal, Vol. 121, pp. 553–575, 2017. doi: https://doi.org/10.1017/aer.2017.8

[135] Sand, E.; Elliott, D. A.; Borst, H. V.: Summary of Propeller Design Procedures and Data, Volume III - Hub, Actuator, and Control Design: AD-776-998. USAAMRDL Technical Report 73-34C, 1973.

[136] Sandberg, R. D.: Compressible-Flow DNS with Application to Airfoil Noise. Flow, Turbulence and Combustion, Vol. 95, No. 2-3, pp. 211–229, 2015. doi: https://doi.org/10.1007/s10494-015-9617-1

[137] Schlichting, H.: Grenzschicht-Theorie, Berlin, Heidelberg: Springer-Verlag Berlin Heidelberg, ISBN 3-540-23004-1, 2006.

[138] Schlinker, R.; Amiet, R. K.: Helicopter rotor trailing edge noise. In: NASA Contractor Report. 3470. doi: https://doi.org/10.2514/6.1981-2001

[139] Schürmann, H.: Konstruieren mit Faser-Kunststoff-Verbunden, Springer-Verlag Berlin Heidelberg, ISBN 978-3-540-72189-5, 2007.

[140] Schwarze, R.: CFD-Modellierung: Grundlagen und Anwendungen bei Strömungsprozessen. SpringerLink Bücher, Berlin and Heidelberg: Springer, ISBN 9783642243783, 2013.

[141] Shelley, M. J.: A study of singularity formation in vortex-sheet motion by a spectrally accurate vortex method. In: Journal of Fluid Mechanics. 244, pp. 493–526. doi: https://doi.org/10.1017/S0022112092003161

[142] Sodja, J.; Breuker, R.; Nozak, D.; Drazumeric, R.; Marzocca P.: High- and Low-Fidelity Investigations of Flexible Propeller Blades. 52nd Aerospace Sciences Meeting, p. 236, 2014. doi: https://doi.org/10.2514/6.2014-0410

[143] Sodja, J.; Drazumeric, R.; Kosel, T.; Marzocca, P.: Design of Flexible Propellers with Optimized Load-Distribution Characteristics. Journal of Aircraft, Vol. 51, No. 1, pp. 117–128, 2014. doi: https://doi.org/10.2514/1.C032131

[144] Spalart, P. R.: Strategies for turbulence modelling and simulations. In: International Journal of Heat. 21, pp. 252–263.

[145] Spera, D. A.: Models of Lift and Drag Coefficients of Stalled and Unstalled Airfoils in Wind Turbines and Wind Tunnels. In: NASA Contractor Report. 2008-215434.

[146] Succi, G. P.: Design of Quiet Efficient Propellers. In: SAE Technical Paper. 790584.

[147] Thurman, C.; Boyd, D. D.; Simmons, B. M.: Comparison of Prediction Modeling Methodologies for Aeroacoustic Characterization of Hovering sUAS Rotors. In: AIAA SciTech 2023 Forum. National Harbor, MD & Online, 2023. doi: https://doi.org/10.2514/6.2023-0027

[148] Thurman, C. S.; Zawodny, N. S.; Pettingill, N. A.; Lopes, L. V.: Physics-informed Broadband Noise Source Identification and Prediction of an Ideally Twisted Rotor. AIAA Scitech 2020 Forum, 2020. doi: https://doi.org/10.2514/6.2021-1925.vid

[149] Traub, L. W.: Range and Endurance Estimates for Battery-Powered Aircraft. Journal of Aircraft, Vol. 48, No. 2, pp. 703–707, 2011. doi: https://doi.org/10.2514/1.C031027

[150] Warwick, G.: Siemens Takes Lead Among Emerging Electric Propulsion OEMs, https://aviationweek.com/air-transport/aircraft-propulsion/siemens-takes-lead-among-emerging-electric-propulsion-oems, 02.04.2018.

[151] Watamura, T.; Nagasaka, T.; Kikuchi, Y.; Miyamoto, T.: Flying a Micro-Drone by Dynamic Charging for Vertical Direction Using Optical Wireless Power Transmission. In: energies. 18, pp. 351–371. doi: https://doi.org/10.3390/en18020351

[152] YAMAMOTO, O.; AUGUST, R.: Structural and Aerodynamic Analysis of a Large-Scale Advanced Propeller Blade. Journal of Propulsion and Power, Vol. 8, No. 2, pp. 367–373, 1992. DOI: https://doi.org/10.2514/3.23487

[153] ZAWODNY, N. S.; PETTINGILL, N. A.; LOPES, L. V.; INGRAHAM, D. J.: Experimental Validation of an Acoustically and Aerodynamically Optimized UAM Proprotor Part 1: Test Setup and Results. In: NASA Technical Memorandum. 20220015637.

A Derivation of general momentum theory

Analysing the aerodynamic forces on a propeller blade involves understanding the relationship between the velocities and the forces generated. In this section the general momentum theory is derived in detail, because it's missing in the standard literature. As the derivation is done for a 2D section, the radial dimension dr is skipped in the derivation.

The thrust T' (eq. (A.1)) and the torque Q' (eq. (A.2)) on an angular section of the propeller blade can be described by the following equations:

$$T' = \frac{\rho}{2} w^2 c (c_l \cos(\Phi) - c_d \sin(\Phi)) N_B \tag{A.1}$$

$$Q' = \frac{\rho}{2} w^2 c (c_l \sin(\Phi) + c_d \cos(\Phi)) N_B r \tag{A.2}$$

The axial and tangential velocities (v_a and v_t) are reformulated with the induction factors instead of the shown summation of absolute velocities in eq. (2.36) and eq. (2.37).

$$v_a = v_\infty (1 + a_a) \tag{A.3}$$

$$v_t = \omega r (1 - a_t) \tag{A.4}$$

Therefore, the relative velocities changes to eq. (A.5).

$$w^2 = (\omega r (1 - a_t))^2 + (v_\infty (1 + a_a))^2 \tag{A.5}$$

With the new induced velocities, the helix angle could be reformulated.

$$\tan(\Phi) = \frac{v_\infty}{\omega r} \frac{(1 + a_a)}{(1 - a_t)} \tag{A.6}$$

The tangential induced velocity is expressed as function of the axial induced velocity and the helix angle.

$$\omega r (1 - a_t) = \frac{v_\infty (1 + a_a)}{\tan(\Phi)} \tag{A.7}$$

Applying trigonometric functions, with the identities $1 + \tan^2(\Phi) = \frac{1}{\cos^2(\Phi)}$ and $\tan(\Phi) = \frac{\sin(\Phi)}{\cos(\Phi)}$, simplifies the resulting velocity formulation eq. (A.5) to (A.8).

$$w^2 = (v_\infty (1 + a_a))^2 \left(\frac{1}{\tan^2(\Phi)} + 1 \right) \tag{A.8a}$$

$$w^2 = (v_\infty (1 + a_a))^2 \left(\frac{1 + \tan^2(\Phi)}{\tan^2(\Phi)} \right) \tag{A.8b}$$

$$w^2 = (v_\infty (1 + a_a))^2 \left(\frac{1}{\cos^2(\Phi) \tan^2(\Phi)} \right) \tag{A.8c}$$

$$w^2 = \frac{(v_\infty (1 + a_a))^2}{\sin^2(\Phi)} \tag{A.8d}$$

The sectional thrust formulation eq. (A.1) is reformulated to eq. (A.9) by inserting the velocities.

$$T' = \frac{\rho}{2}\frac{(v_\infty(1+a_a))^2}{\sin^2(\Phi)}c(c_l\cos(\Phi) - c_d\sin(\Phi))N_B \tag{A.9}$$

By application of the simple momentum theory on the strip, the sectional thrust can be calculated with eq. (A.10a), which is reformulated with the use of the axial induction factor (eq. (A.3)) to eq. (A.10b)

$$T' = 2\rho \cdot 2\pi r \cdot v(v - v_\infty) \tag{A.10a}$$

$$T' = 4\rho\pi r \cdot v_\infty^2 a_a(1+a_a) \tag{A.10b}$$

Equalizing eq. (A.9) and eq. (A.10b), inserting the solidity (eq. (2.30)) and resolving it to the induction factors leads to eq. (A.11).

$$a_a = (1+a_a)\cdot\left(\frac{\sigma(c_l\cos(\Phi) - c_d\sin(\Phi))}{4\sin^2(\Phi)}\right) \tag{A.11}$$

The analogue procedure is applied for the derivation of the tangential induction factor. However, instead of the axial momentum theory the angular momentum theory have to be applied.

$$\dot{L_{ex}} - \dot{L_{int}} = \sum M = Q \tag{A.12}$$

Therefore, the angular momentum equation (eq. (A.12)) can be reformulated, for the area $4\pi r\cdot dr$ (with $dr = 1$). The negative sign is dropped to maintain the sing convention of the torque calculation.

$$\dot{L'_{int}} = \dot{m}\cdot r\cdot u = \rho 4\pi r v_\infty \cdot r\cdot \omega r \tag{A.13a}$$

$$\dot{L'_{ex}} = \dot{m}\cdot r\cdot u = \rho 4\pi r v_\infty \cdot r\cdot \omega r(1-a_t) \tag{A.13b}$$

$$Q' = -\rho 4\pi r v_\infty \cdot r\cdot \omega r\cdot a_t \tag{A.13c}$$

Eq. A.13 shows, that the torque is acting against the rotation due to the sign of the equation. Eq. A.13 is equated with eq. (A.2). However, in eq. (A.2), the velocity formulation of w^2 is reformulated with the result of eq. (A.15).

The velocity formulation eq. (A.5) is reformulated to replace the axial velocity formulation done in eq. (A.7).

$$v_\infty(1+a_a) = \omega r(1-a_t)\tan(\Phi) \tag{A.14}$$

$$w^2 = (\omega r(1-a_t))^2 + (\omega r(1-a_t)\tan(\Phi))^2 \tag{A.15a}$$

$$w^2 = (\omega r(1-a_t))^2(1+\tan(\Phi)^2) \tag{A.15b}$$

$$w^2 = \frac{(\omega r(1-a_t))^2}{\cos(\Phi)^2} \tag{A.15c}$$

Thereby, the sectional torque equation eq. (A.2) can be reformulated with eq. (A.15) to eq. (A.16).

$$Q' = \frac{\rho}{2}\frac{(\omega r(1-a_t))^2}{\cos(\Phi)^2}c(c_l\sin(\Phi)+c_d\cos(\Phi))N_B r \tag{A.16}$$

leading to following eq. (A.17)

$$a_t = (1-a_t)^2\frac{\sigma\cdot[c_l\sin(\phi)+c_d\cos(\phi)]}{4\cos^2(\phi)}\cdot\frac{v_\infty}{u} \tag{A.17}$$

In case, that the velocity w^2 is replaced by eq. (A.8) the sectional torque results in eq. (A.18).

$$Q' = \frac{\rho}{2}\frac{(v_\infty(1+a_a))^2}{\sin(\Phi)^2}c(c_l\sin(\Phi)+c_d\cos(\Phi))N_B r \tag{A.18}$$

Thereby the tangential induction factor results in eq. (A.19) instead of A.17. However, both equation could be translated into each other.

$$a_t = (1+a_a)^2\frac{\sigma\cdot[c_l\sin(\phi)+c_d\cos(\phi)]}{4\sin^2(\phi)}\cdot\frac{u}{v_\infty} \tag{A.19}$$

However, eq. (A.17) and eq. (A.19) are only valid for moderately loaded propeller. The equation is not valid for hover conditions, because the incoming velocity is not v_∞. Instead the axial induced velocity have to be inserted in eq. (A.13).

$$L'_{int} = \dot{m}\cdot r\cdot u = \rho 4\pi r v_\infty(1+a_a)\cdot r\cdot\omega r \tag{A.20a}$$

$$L'_{ex} = \dot{m}\cdot r\cdot u = \rho 4\pi r v_\infty(1+a_a)\cdot r\cdot\omega r(1-a_t) \tag{A.20b}$$

$$Q' = -\rho 4\pi r v_\infty(1+a_a)\cdot r\cdot\omega r\cdot a_t \tag{A.20c}$$

The sectional torque coefficient could pe expressed as function of the axial induction factor (eq. (A.16)) or the tangential induction factor (eq. (A.18)). Equalising equation eq. (A.20) and eq. (A.16) results in eq. (A.21) for the tangential induced velocities, which is used for the calculation in this thesis.

$$a_t = (1+a_a)\frac{\sigma\cdot[c_l\sin(\phi)+c_d\cos(\phi)]}{4\sin^2(\phi)}\cdot\frac{v_\infty}{u} \tag{A.21}$$

Equalising equation eq. (A.20) and eq. (A.18) results in eq. (A.22).

$$\begin{aligned} a_t &= \frac{1-a_t}{1+a_a}\quad\frac{\sigma\cdot[c_l\sin(\phi)+c_d\cos(\phi)]}{4\cos^2(\phi)}\cdot\frac{u}{v_\infty} \\ &= \qquad\qquad\frac{\sigma\cdot[c_l\sin(\phi)+c_d\cos(\phi)]}{4\cos^2(\phi)}\cdot\frac{1}{\tan\phi} \end{aligned} \tag{A.22}$$

Fig. A.1 presents a comparison of performance predictions using the four derived equations for angular induced velocity: eq. (A.17), A.19, A.21, and A.22[1]. Diagram a) depicts the thrust predictions, while diagram b) illustrates the torque predictions.

With the hover equation, thrust and torque increase at shallow advance ratios, whereas with the cruise equations, thrust and torque decrease as the advance ratio approaches hover. This phenomena is causend by the reduction of mass flow within the cruise formulation. Furthermore, fig. A.1 demonstrates, that the different formulations for hover and for cruise results in the same predictions. The prediction is numerically stabilised by applying artificial damping, detecting extrema, and limiting the helix angle to a maximum of 90°.

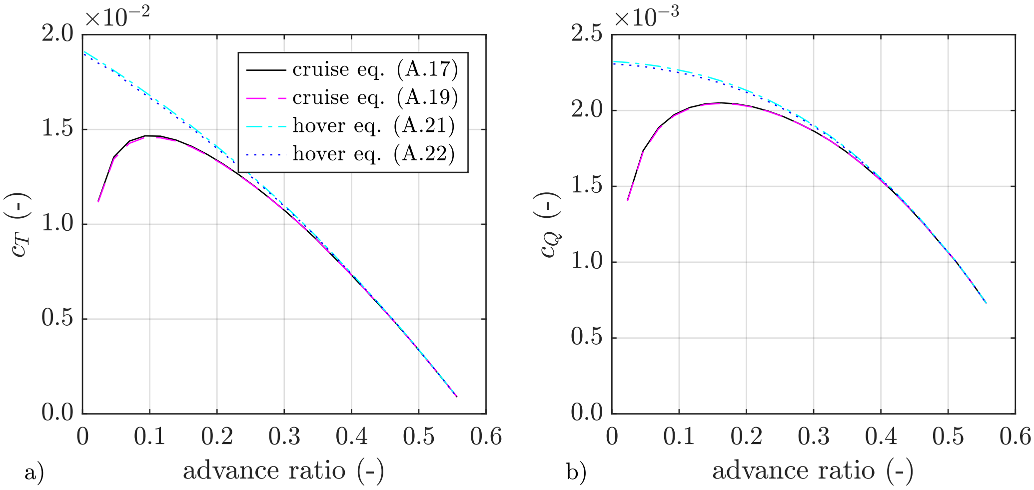

Figure A.1: Comparison of aerodynamic performance with different equations for the tangential induction factor

---

[1] The simulations are performed without any correction model and with 2D XFOIL data and 30 sections

B Physical Background of Applied RANS Simulations

Appendix B provides further details about the simulation approach. Fig. B.1 illustrates the mesh of the moving reference frame simulation approach. The base size of the shown meshes is $0.55 \cdot \text{Diameter}$. The mesh density is controlled by three offset functions, which generate a smooth transition from the coarser mesh to the finer mesh at the surface. The blue mesh domain represents the propeller-attached mesh, while the brown mesh represents the static mesh. The blue mesh is used for modelling blade motion.

The left diagrams in fig. B.1 show a side view normal to the propeller plane, while the right diagrams provide a front view of the propeller plane. The upper left diagram depicts the mesh for the moving reference frame approach (MRF). The highlighted boundary is cylindrical and separates the moving frame from the static frame. The upper right diagram illustrates the periodic moving reference frame (MRF) approach, including its interfaces. The periodic MRF domain size is the same as in the standard MRF simulation.

The lower left diagram depicts the mesh for the RBM simulation. Here, the moving frame is significantly shorter compared to the MRF approach to accelerate the simulation. Wake information are transported across the boundaries into the static region, allowing the rotating domain to be smaller. The smaller the rotating domain, the faster the simulation, as less volume requires transformation.

The fourth diagram illustrates the overset mesh approach, which features the smallest rotating volume. The rotating domain is defined by the second offset mesh shown in the upper left diagram.

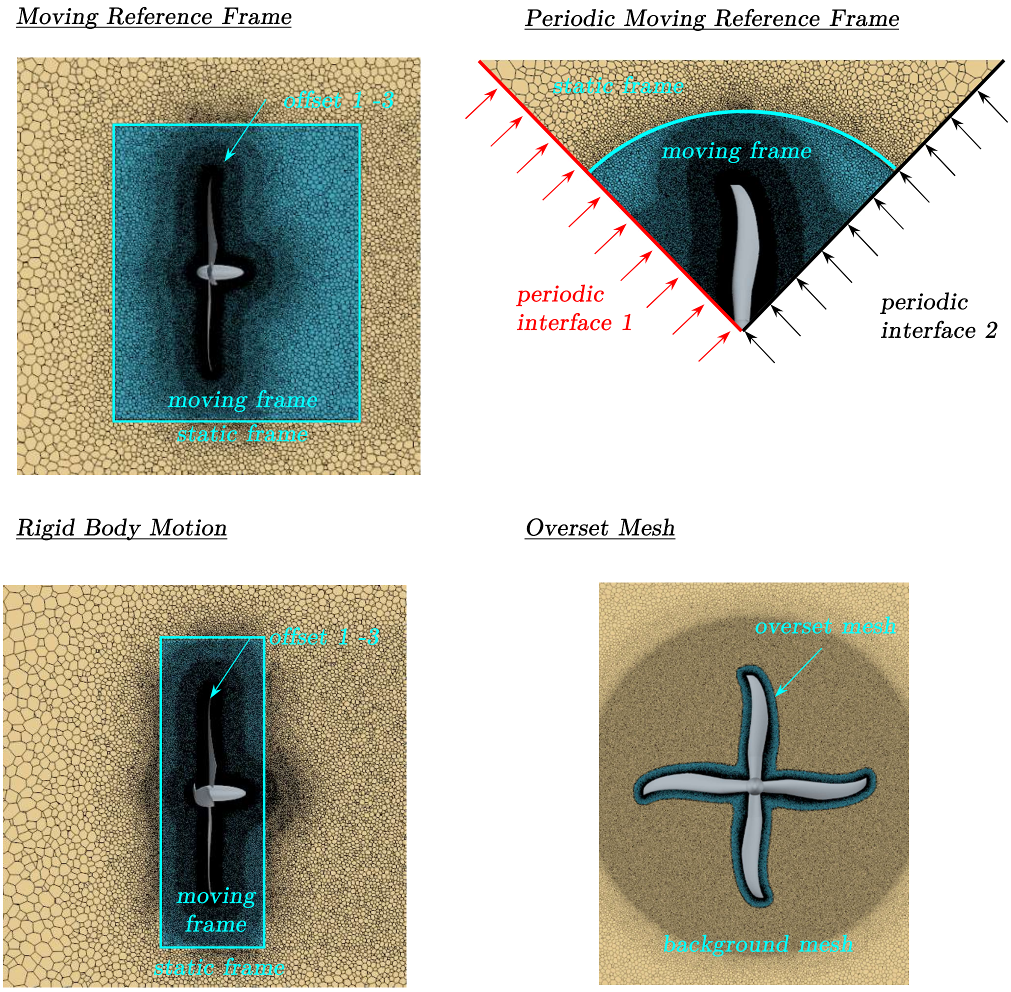

Figure B.1: Mesh comparison for different simulation approaches

Further details about the mesh resolution are provided in B.2 and B.3. Fig. B.2 offers a closer view of the mesh resolution at the blade tip. The mesh density is increased around the leading-edge, tip, and trailing-edge. A high mesh density is particularly necessary at the thin leading-edge to accurately resolve the geometry.

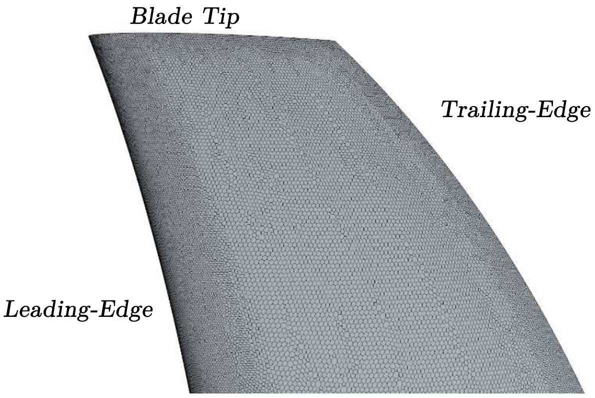

Figure B.2: Surface mesh at the propeller tip

Fig. B.3 shows the pressure distribution at a blade section located at 75% of the radius. The displayed pressure distribution bases on the reference conditions presented in table 2.1 simulated with the MRF approach. The boundary layer parameters are constant along the blade. They are defined according to the flow conditions of the 75% section shown in fig. B.3. The prism-layer thickness is reduced at the leading and trailing-edges to maintain appropriate cell aspect ratios within the prism layer. The number of prism layers is also reduced at the trailing-edge due to stability issues.

Furthermore, fig. B.3 illustrates the transition from the fine mesh near the blade surface to the coarser mesh in the surrounding vicinity. The highest mesh density is observed at the leading-edge.

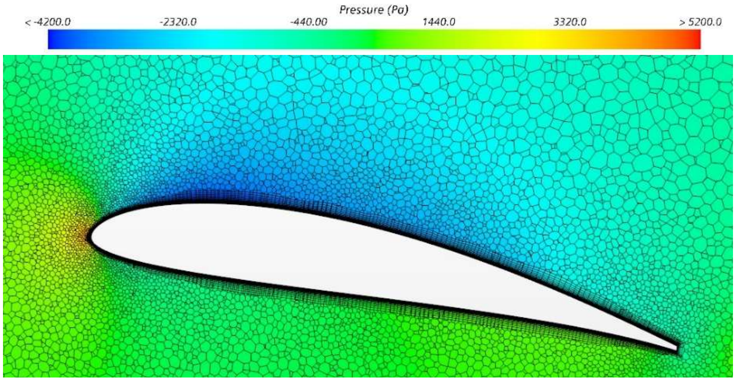

Figure B.3: Mesh visualisation at the 75% radial propeller section

Fig. B.4 presents the mesh independence study for all four simulation approaches Diagram a) illustrates the thrust dependency on the number of cells (in millions), while diagram b) depicts the torque dependency. A comparison of diagram a) and diagram b) reveals that torque prediction requires more cells than thrust prediction to achieve mesh independence. This behaviour is consistent with the 2D RANS simulations, where drag converges more slowly than lift (cf. fig. 2.16).

The MRF simulation without periodic interfaces achieves mesh independence beyond 60 million cells. The periodic MRF simulation requires 49 million cells, while the RBM simulation converges at 52 million cells. The overset mesh simulation achieves mesh independence with the smallest cell count, at 39 million cells.

As a result, the periodic approach provides no significant advantage over the full MRF simulation in terms of cell count. Moreover, the periodic interfaces introduce additional computational overhead, slowing down the simulation. Consequently, the periodic and non-periodic approaches require similar computational time.

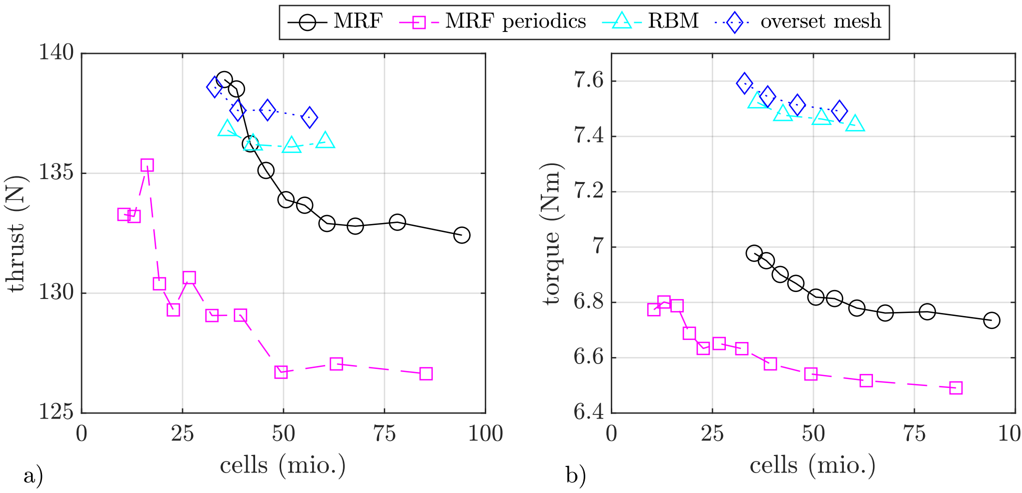

Figure B.4: Mesh independence study for the different simulation approaches

Fig. B.5 compares the vorticity in the propeller plane across four simulation approaches: the moving reference frame (MRF) approach without periodic interfaces, the MRF approach with periodic interfaces, the rigid body motion (RBM) approach, and the overset mesh approach.

This figure serves as a continuation of fig. 2.23, where a quarter of the MRF, RBM, and overset mesh simulations are extracted and compared. The physical details of these simulations are provided in section 2.3.3.

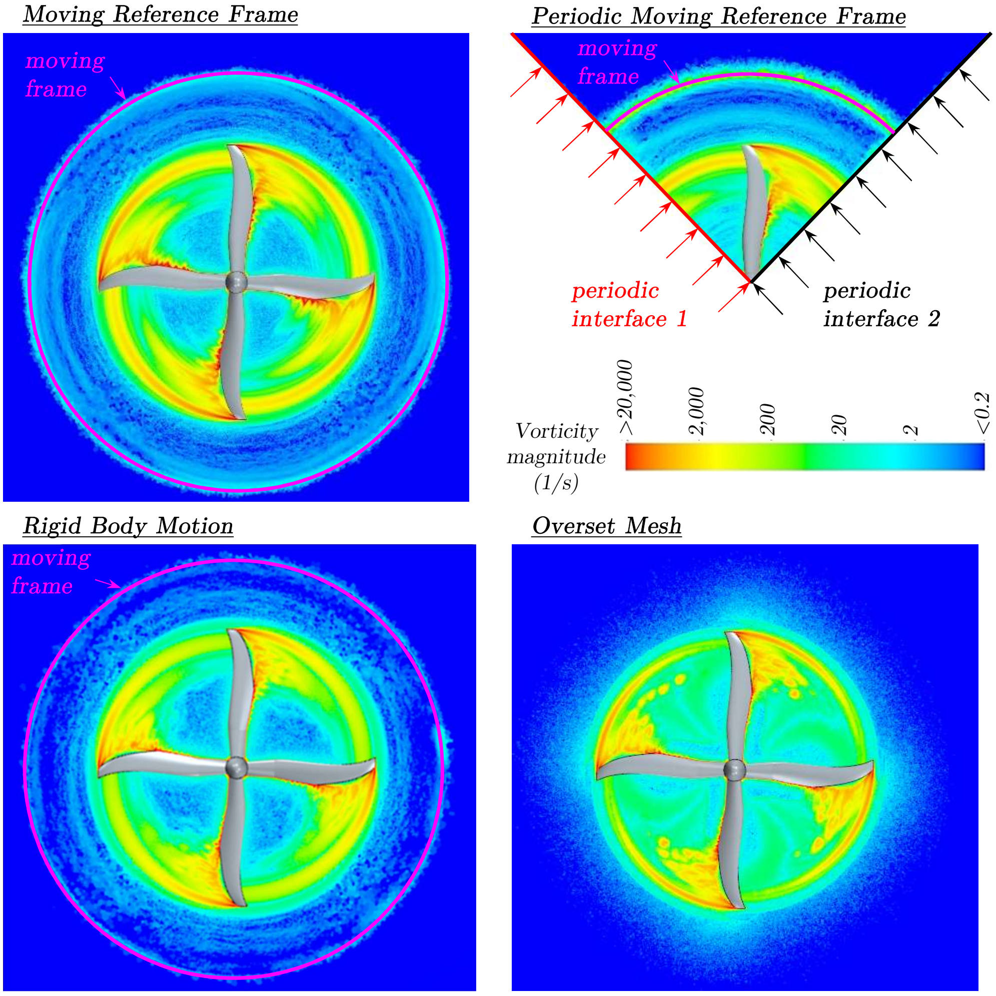

Figure B.5: Comparison of the vorticity in the propeller plane for the different simulation approaches

C Comparison of Different Series of Measurements

The following two figures (C.1 and C.2) illustrate the deviation between different series of measurements conducted under varying atmospheric conditions. Between these measurement series, the test bench is disassembled and reassembled to eliminate systematic errors.

Multiple measurement series are carried out to verify that parameters such as the settings of the electronic speed controller, the sampling frequency of the force balance, the sampling duration, and other operational parameters are valid.

Fig. C.1 presents the results without any correction for density changes. Despite this, the agreement between the curves demonstrates the repeatability and reliability of the measurement data.

Fig. C.2 depicts non-dimensional parameters, which exhibit perfect alignment between the different series.

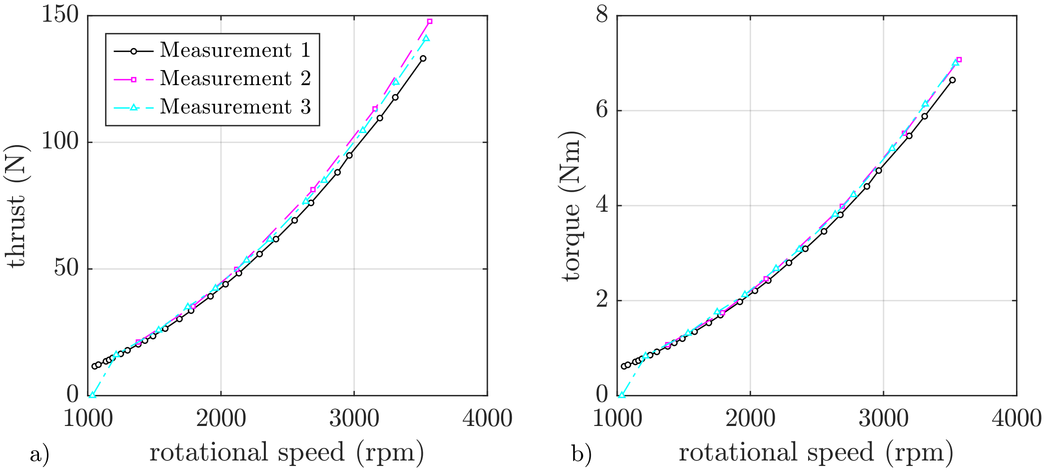

Figure C.1: Performance measurement of the four-bladed propeller in hover for three different series of measurement

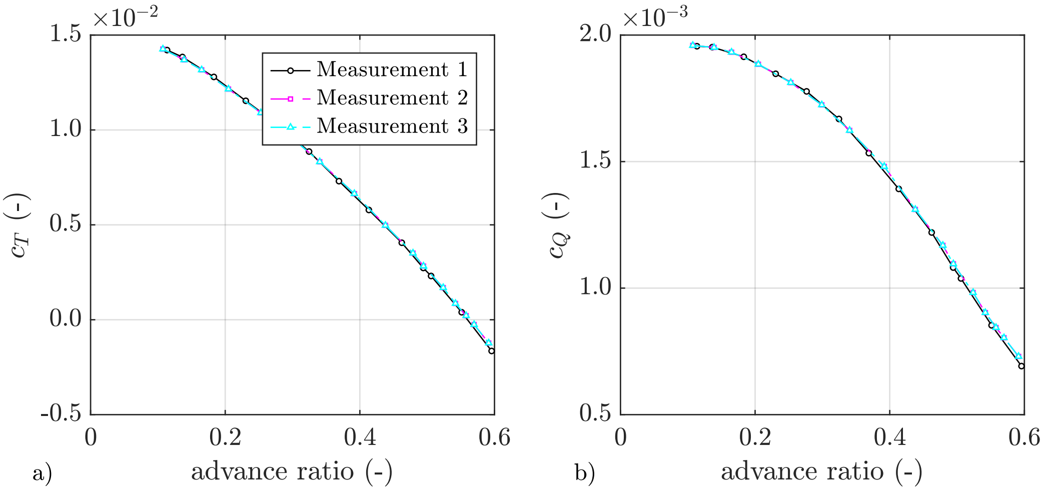

Figure C.2: Performance measurement of the four-bladed propeller at different advance ratios for three different series of measurements

The propeller axis is mounted horizontal. However, the most wind tunnels has some kind of non-symmetric inflow. To check the flow conditions an AoA sweep is performed.

Fig. C.3 shows the AoA dependency of the two-, three-, and four-bladed propeller. Diagram a) shows the thrust coefficient over the angle of attack of the horizontal axis and diagram b) shows the torque coefficient.

The trend between diagram a) and b) does not match. While in diagram a) the AoA for minimal thrust depends on the blade number, the minimal torque is reached at 0° for all blades. The thrust curve of the two-bladed propeller reaches a first minimum at +1° and increases towards -2° but then decreases again. The thrust curve of the three-bladed propeller reaches it's minimum at -4°, and of the four-bladed propeller at -2°.

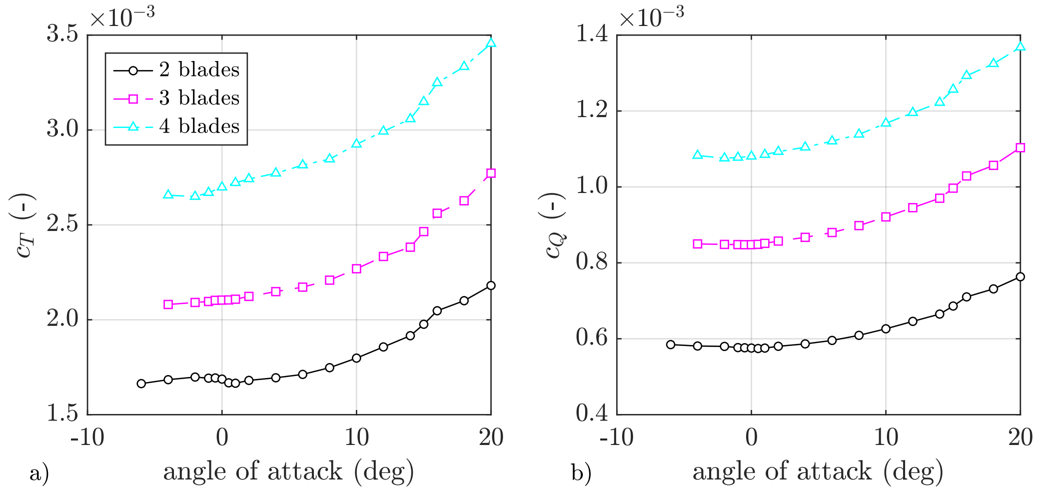

Figure C.3: Angle of attack dependency of thrust and torque for the two-, three-, and four-bladed propeller at the advance ratio of 0.5

Because fig. C.3 does not exhibit a clear trend, the non-dimensional forces and moments around all three axes are presented in fig. C.4. The coefficients are calculated according to eq. (2.15) and eq. (2.16), with forces and moments replaced to correspond to the respective axis. The axes of the force balance are defined such that the z-axis points in the thrust direction. These values are shown in fig. C.3. The y-axis represents the axis of rotation, while the x-axis, following the right-hand rule, points towards the ground in this wind tunnel setup.

The first row of fig. C.4 presents the x- and y-force coefficients in diagrams a) and b), respectively. The second row shows the x- and y-moment coefficients in diagrams c) and d) for all three blade configurations.

In all four diagrams, the zero-crossing occurs approximately at 0° AoA, indicating an axisymmetric inflow. As a result, all measurements are conducted with the propeller axis at 0° AoA.

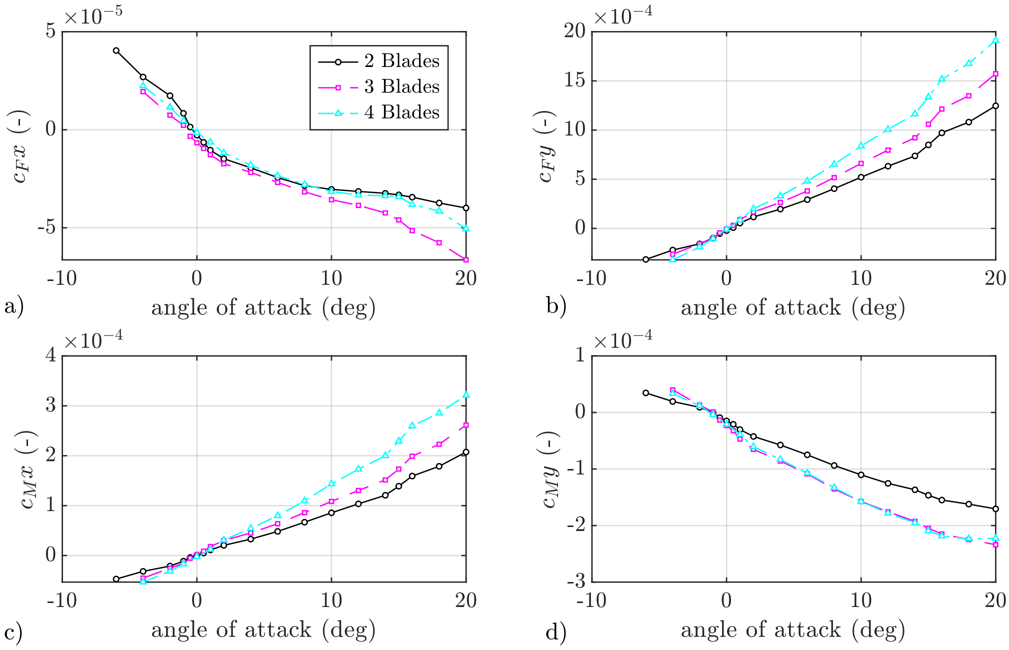

Figure C.4: Angle of attack dependency of in plane forces and moments for the two-, three-, and four-bladed propeller at the advance ratio of 0.5

D Additional Information about Acoustic Models

Appendix D is organised into four sections. First, key mathematical transformations are presented. Second, the potential of sweep for noise reduction is briefly described. Third, the acoustic mesh and the time-independence study are discussed.. Finally, the missing figures for the assessment of the different acoustic models are provided.

D.1 Mathematical Operations for Noise Calculations

Eq. D.1 shows the transformation from SPL to sound pressure and vis versa.

$$L_p = 10\log_{10}(\frac{\tilde{p}^2}{p_0^2}) \Leftrightarrow \tilde{p}^2 = p_0^2 \cdot 10^{\frac{Lp}{10}} \tag{D.1}$$

To maintain the logarithmic behaviour of the SPL, $\tilde{p}$ have to be summed. After summation of $\tilde{p}$, the new $\tilde{p}$ have to be transformed back into the SPL according to eq. (D.2).

$$L_{p\sum} = 10\log_{10}(\sum_i 10^{\frac{L_{p_i}}{10}}) \tag{D.2}$$

The equation shows, that summing two noise sources results in an increase of approx. 3dB.

If two noise sources should be subtracted, eq. (D.3) shows the logarithmic rule applied on noise calculations .

$$\Delta L_p = 10\log_{10}(L_{p,2}) - 10\log_{10}(L_{p,2}) = 10\log_{10}(\frac{L_{p,2}}{L_{p,1}}) \tag{D.3}$$

The transformation from the frequency domain into the time domain can be performed in different ways. In cases where a single-sided amplitude spectrum ($\hat{p} = func(f)$) of the acoustic results is available, the time-domain solution can be calculated. The amplitude spectrum can be generated using a fast Fourier transform (FFT) from any time-domain signal.

$$p_t = \sum_i (\hat{p} \cdot sin(2\pi \cdot f_i \cdot t + \psi)) \tag{D.4}$$

As a first assumption, the approximation stated in eq. (D.5) can be applied, based on the premise that the noise signal is sinusoidal.

$$\hat{p} = \tilde{p} \cdot \sqrt{2} \tag{D.5}$$

D.2 The Potential of Sweep for Noise Reduction

The potential noise reduction achievable through sweep is reported in [34, 73]. However, this potential can only be utilised for higher frequencies.

Sweep leverages constructive interference between noise sources to reduce noise emissions. These noise sources are located on the propeller blade. Perfect constructive interference requires a phase shift of 180°. A phase shift can be achieved through a spatial displacement between the noise sources.

The wavelength λ of a noise source on the propeller blade can be calculated using eq. (D.6). As an example, eq. (D.6) calculates the wavelength for a blade passing frequency (BPF) of 100 Hz. The resulting wavelength is 3.4 m, which means that a spatial displacement of 1.7 m is required to achieve a phase shift of 180°. This displacement cannot be reached by sweep. Therefore, sweep is only effective at higher BPF frequencies, which could be achieved with more blades or faster spinning propeller.

$$\lambda = c_0/f = c_0/BPF = \frac{340\frac{m}{s}}{100Hz} = 3.4m \tag{D.6}$$

Sweep cannot be applied for the reduction of broadband noise, because broadband noise is a stochastic phenomena.

D.3 Mesh and Time Independence Study of the Farassat's Model

The tonal SPL sensitivity to temporal and spatial discretisation is already discussed in section 3.1.3. However, the influence on the sound pressure is not presented in section 3.1.3.

Fig. D.1 illustrates the temporal discretisation study. Diagram a) shows the resulting sound pressure over time, while diagram b) displays the difference between the finest and the coarser simulations. The temporal discretisation is expressed as steps per revolution, where a higher number of steps corresponds to a smaller time step. This representation is independent of the rotational speed.

Diagram a) shows no distinguishable differences in the time history above 90 steps per revolution. However, diagram b) reveals differences up to 540 steps per revolution. These findings align with the SPL independency discussed in fig. 3.7.

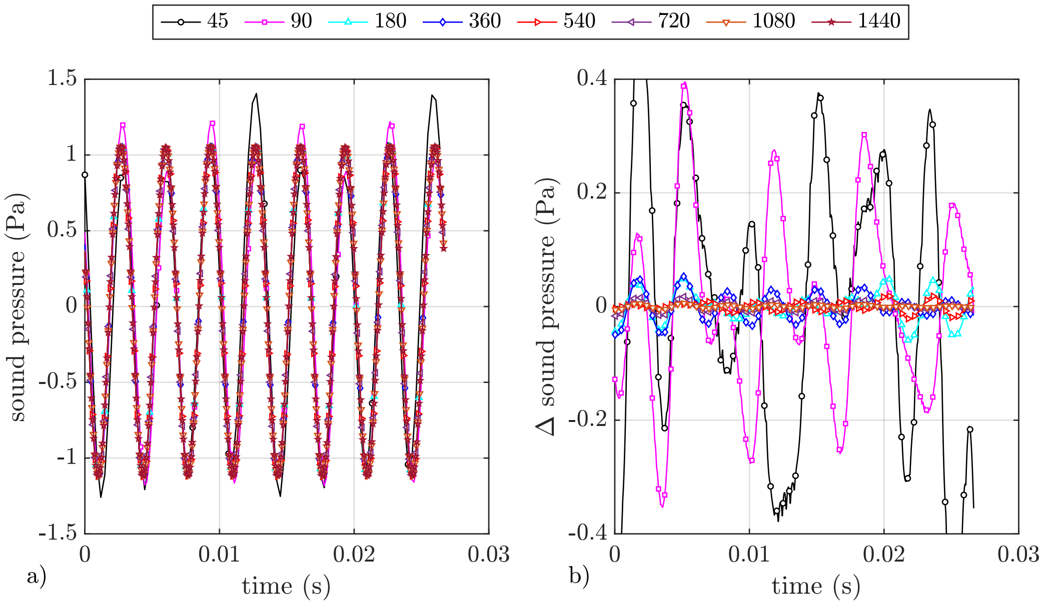

Figure D.1: Influence of spatial discretisation on the sound pressure

Fig. D.2 presents the spatial independence study, with the sound pressure shown in diagram a) and the differences shown in diagram b). The spatial discretisation is described in terms of radial steps, ranging from a step size of 10% of the radius (resulting in 5 sections) to a step size of 0.5% (resulting in 200 sections).[1]

As in fig. D.1, diagram a) shows no significant differences in the time history across the various spatial discretisations. However, diagram b) reveals that a step size of at least 2.5% should be used to ensure a mesh-independent solution.

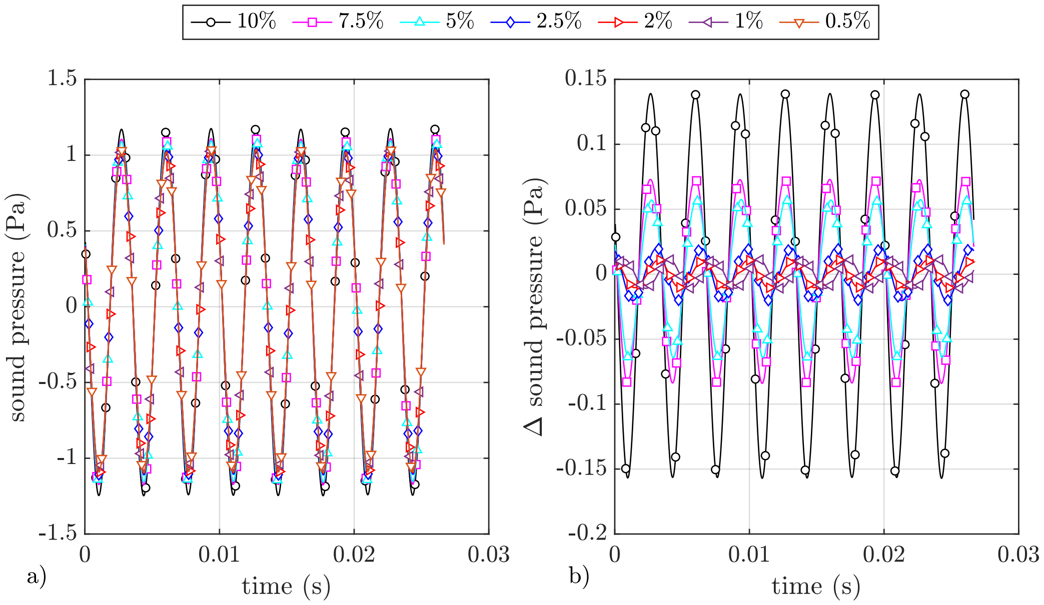

Figure D.2: Influence of temporal discretisation on the sound pressure

---

[1] The propeller root, which ranges from 0% to 0.15% of the radius, is not modelled using the BEMT and the F1A approach.

D.4 Supplementary Diagrams of the Assessment of acoustic models

Finally, supplementary diagrams that are not included in section 3.4 are provided. For each subsection of section 3.4, a separate subchapter is included.

D.4.1 Distance Variation

First, the supplementary figures for the distance variation at fixed pitch and advance ratio are assessed to illustrate the observer position dependency. Fig. D.3 and fig. D.4 present the contour plots for different distances for the two- and three-bladed propellers.

A comparison of the figures reveals that the trends between the two- and three-bladed propellers match perfectly. However, the SPL amplitudes differ slightly between the two configurations. In the two-bladed propeller case shown in D.3, the F1A plot contains a small zone of 80 dB(A), which is not present in the three-bladed case.

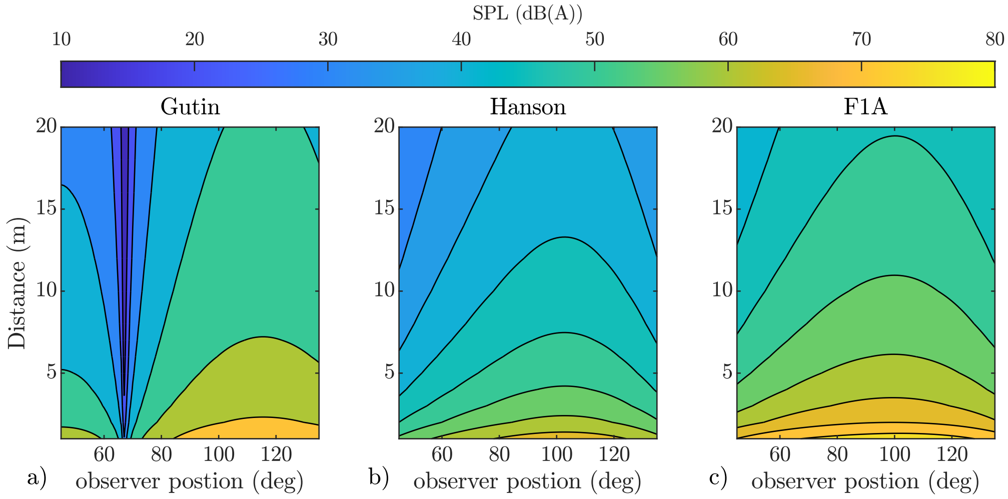

Figure D.3: Acoustic Assessment: Distance variation in case of a two-bladed propeller

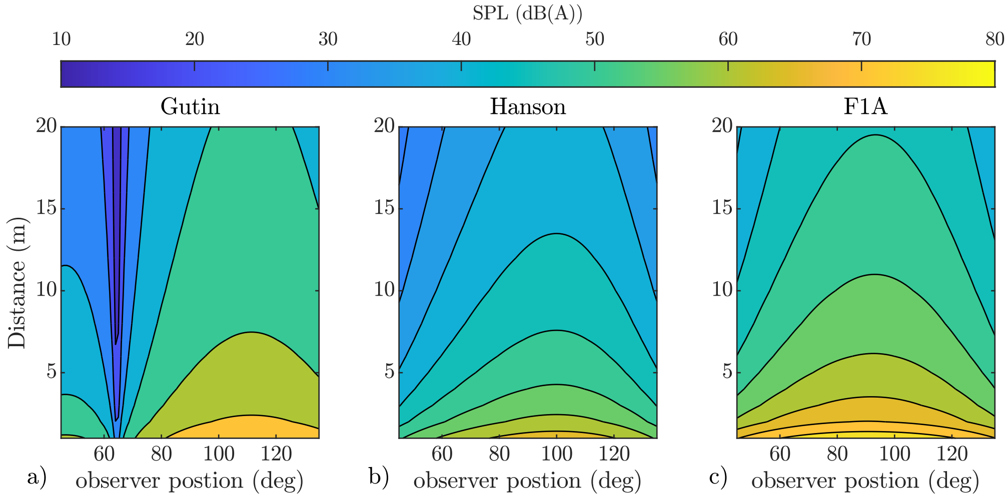

Figure D.4: Acoustic Assessment: Distance variation in case of a three-bladed propeller

D.4.2 Wind Tunnel Comparison

Second, supplementary figures for different wind speeds at constant pitch are provided. As in the previous case, fig. D.5 and fig. D.6 exhibit similar trends between the two- and three-bladed propellers, with slightly differing amplitudes.

The two-bladed propeller in fig. D.5 demonstrates a larger noise reduction due to increased advance ratios compared to the three-bladed propeller in fig. D.6.

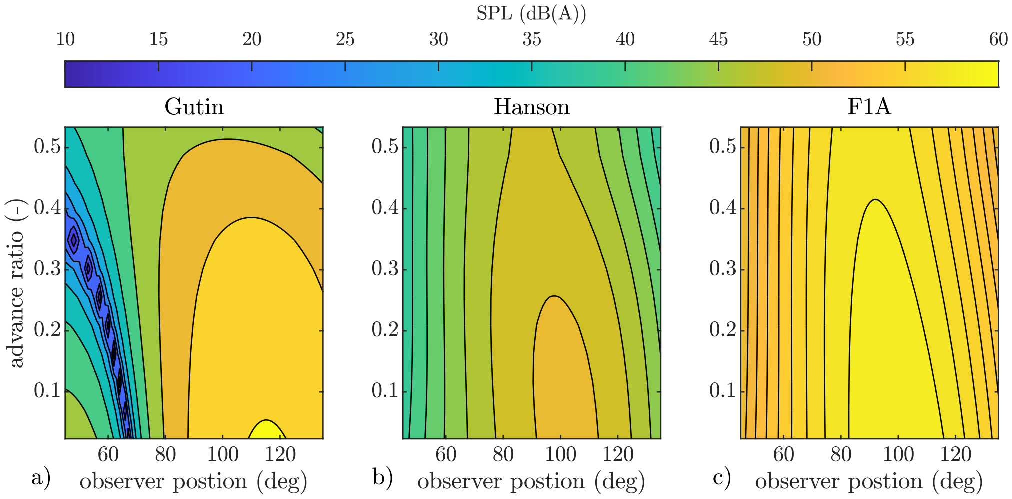

Figure D.5: Acoustic Assessment: Axial speed variation in case of a two-bladed propeller

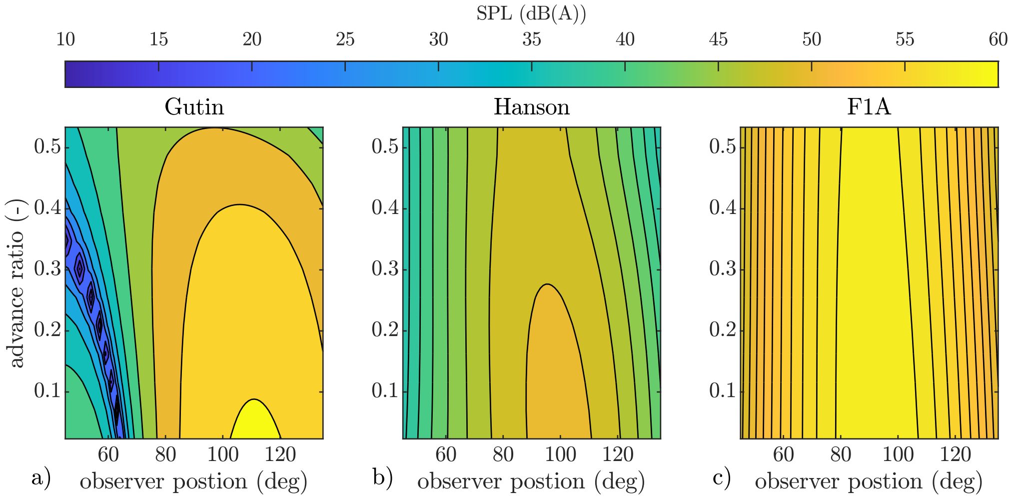

Figure D.6: Acoustic Assessment: Axial speed variation in case of a three-bladed propeller

For the sake of completeness, the observer sweep at an advance ratio of 0.5 is shown, as performed in the analysis of the first case in fig. 3.25.

The comparison between the two-bladed (diagram a) and three-bladed (diagram b) propeller reveals that their noise emissions are approximately the same. However, the noise emissions of the four-bladed propeller are reduced by 5 dB.

A closer examination of D.7 shows that the two-bladed propeller produces slightly lower noise emissions than the three-bladed propeller.

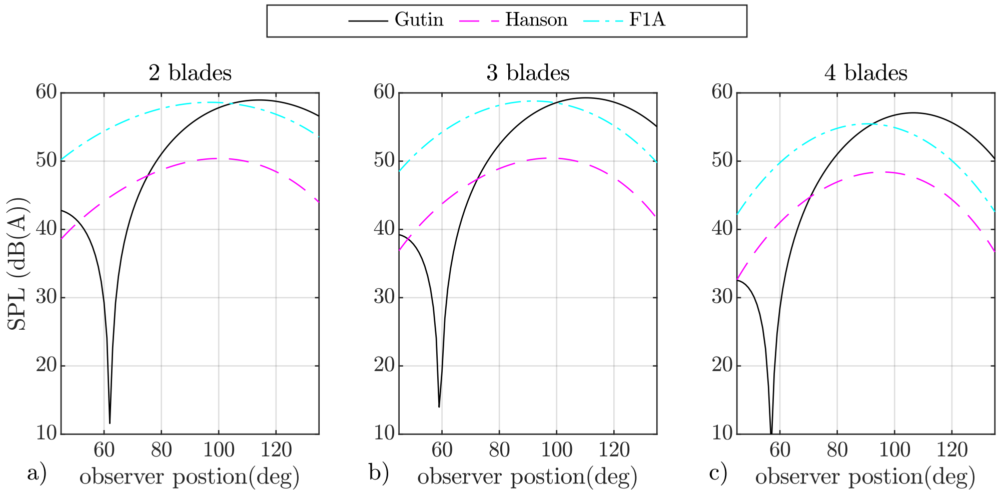

Figure D.7: Comparison of the tonal noise models for different blade numbers at an advance ratio of 0.5

D.4.3 Overflight Comparison

Finnaly the supplementary figures for the overflight comparison with consideration of the Doppler effect is presented. As in the previous cases, the contour plots in fig. D.8 and fig. D.9 reveals that the trends matches and the noise of the three-bladed propeller in fig. D.9 is slightly higher than of the two-bladed propeller in fig. D.8.

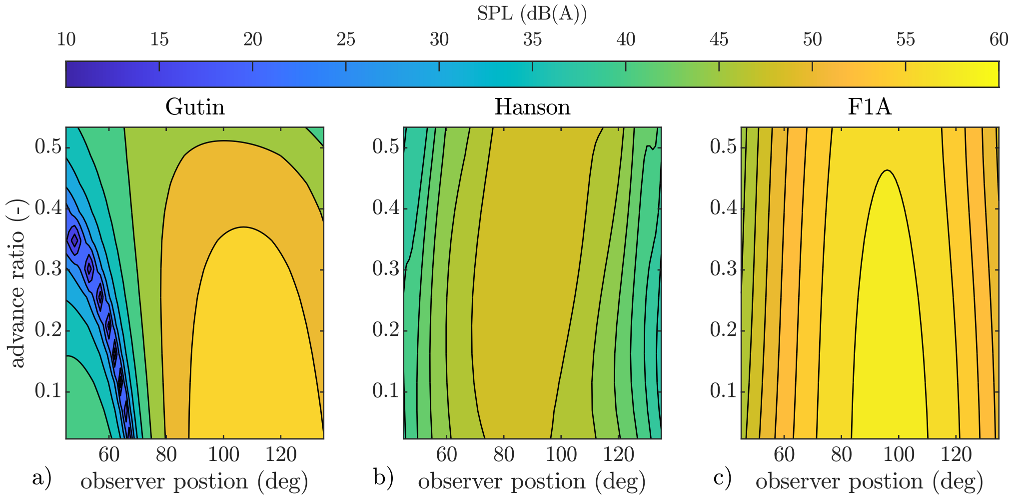

Figure D.8: Acoustic Assessment: Overflight with different advance ratios for variable observer position for a two-bladed propeller

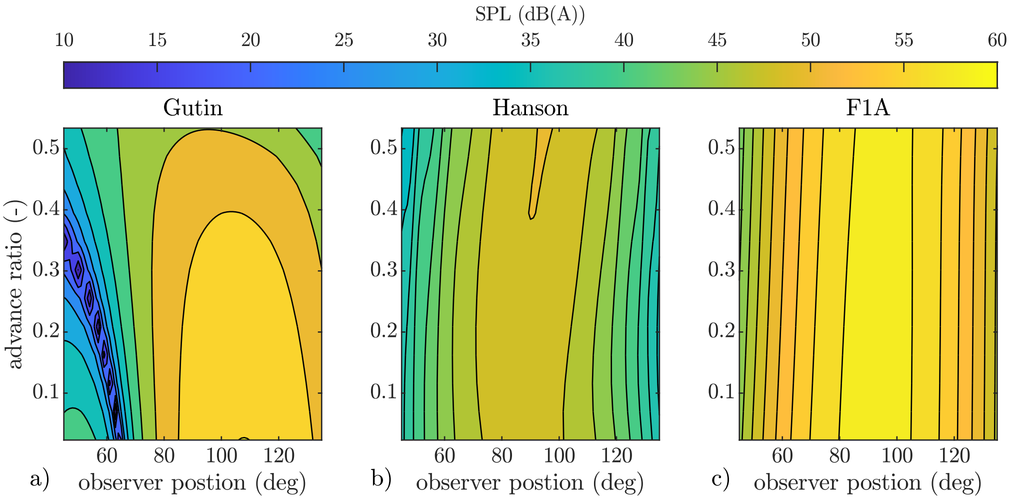

Figure D.9: Acoustic Assessment: Overflight with different advance ratios for variable observer position for a three-bladed propeller

Fig. D.10 parallels fig. 3.29 and includes Doppler effects. The comparison in fig. D.10 shows that the two- and three-bladed propellers emit similar noise levels. The four-bladed propeller emits less noise. Gutin's model predicts a noise reduction with increasing advance ratio for all cases. Hanson's model predicts an increase in noise emissions. The F1A model predicts a reduction for the two-bladed case, a constant SPL for the three-bladed case, and a slight increase in the four-bladed case. Hanson's and Gutin's models do not show the trend of the validated F1A prediction methodology.

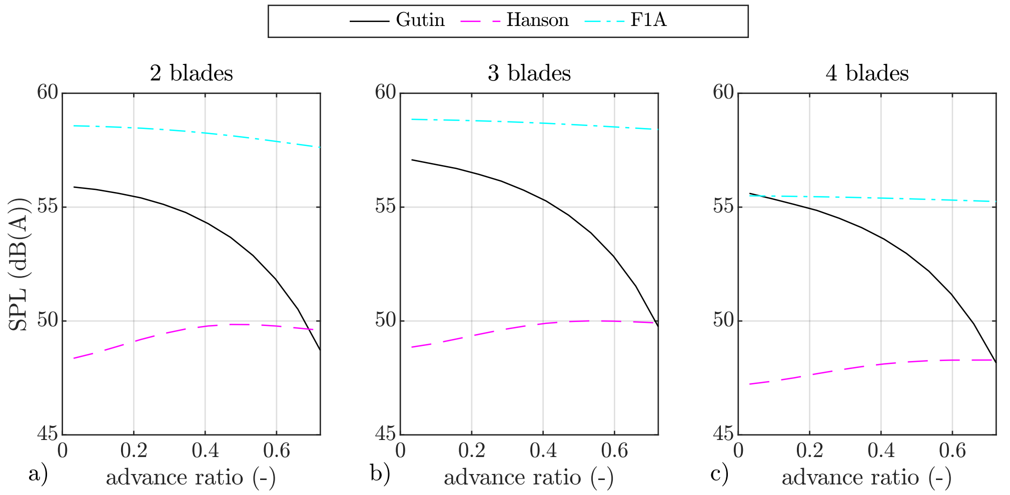

Figure D.10: Comparison of the tonal noise models for different blade numbers in overflight conditions for a variable advance ratios

E Additional Information about Design Procedures

Appendix E provides further information about the MIL design procedure and the MDO procedure. First, additional details on the comparison between the MIL-designed propeller and the reference propeller are provided. Second, a stepwise explanation of the MDO approach is given.

E.1 Comparison of Reference Propeller and Minimum Induced Loss Propeller

This appendix provides additional information about the assessment of the novel design procedure. The hard facts are stated in section 4.1, but the underlying simulation results are shown in the following three figures. The reference propeller is depicted by the solid black line, while the MIL design propeller is depicted by the magenta dashed line.

Fig. E.1 presents the static hover performance results. Diagram a) shows the thrust curve, diagram b) the torque predictions, and diagram c) the Figure of Merit. The comparison shows that the thrust matches perfectly over the complete operating range, while the torque is slightly reduced. This torque reduction leads to an increased Figure of Merit.

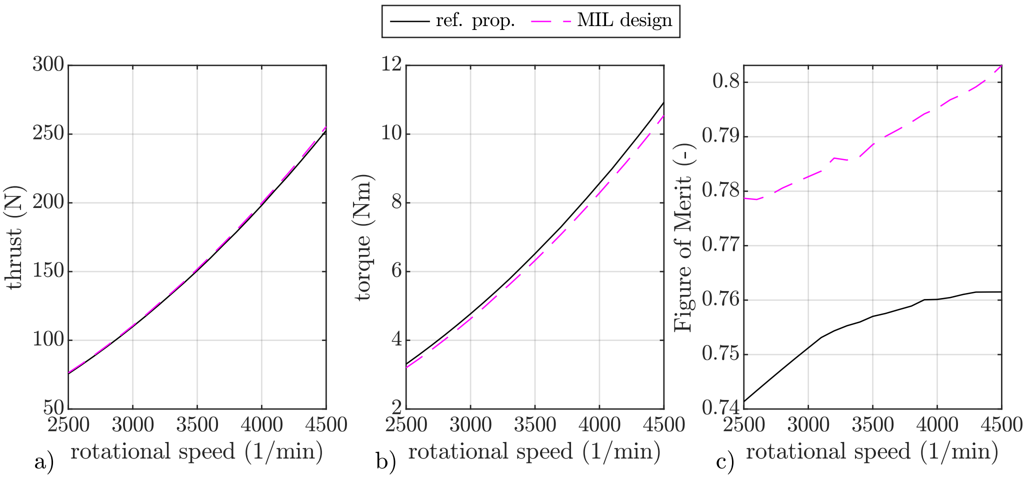

Figure E.1: Comparison of static aerodynamic performance in hover between the MIL and reference propeller

The second figure depicts the aerodynamic performance comparison for different wind speeds. Diagram a) shows the thrust coefficient, diagram b) the torque coefficient, and diagram c) the propulsive efficiency. The comparison reveals that the MIL propeller performance deteriorates at higher advance ratios, and the achievable maximum advance ratio is significantly reduced.

However, the propulsive efficiency remains the same up to an advance ratio of 0.2. Beyond this point, the efficiency degrades compared to that of the reference propeller.

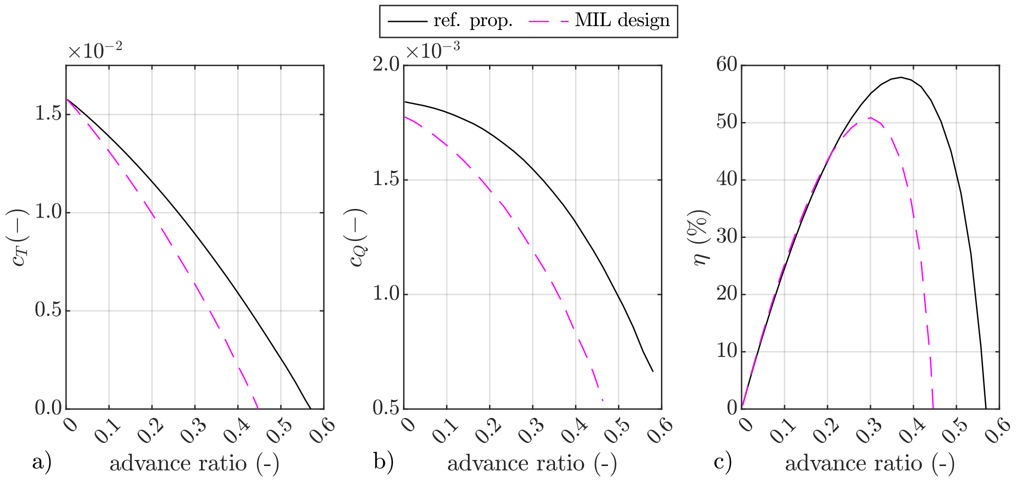

Figure E.2: Comparison of aerodynamic performance at different advance ratios between the MIL and reference propeller

In the last figure, the noise emissions of both propellers are decomposed into thickness, loading, broadband, and total noise components. The solid lines represent the reference propeller, while the dashed lines represent the MIL propeller. Fig. E.3 shows the SPL over the observer position for a normalized distance of 10 diameters.

The comparison of the loading noise (blue) shows that both propellers emit the same loading noise. The thickness noise (cyan) of the MIL propeller is 10 dB higher than that of the reference propeller. This increase is caused by the increased chord length of the MIL propeller compared to the reference propeller, even though the relative thickness is lower. On the other hand, the broadband noise (magenta) is slightly lower for the MIL propeller compared to the reference propeller.

The overall sound pressure level of the MIL propeller is increased by 2.4 dB at the 95° observer position. Far upstream and downstream, the MIL propeller is less noisy because broadband noise dominates in these regions.

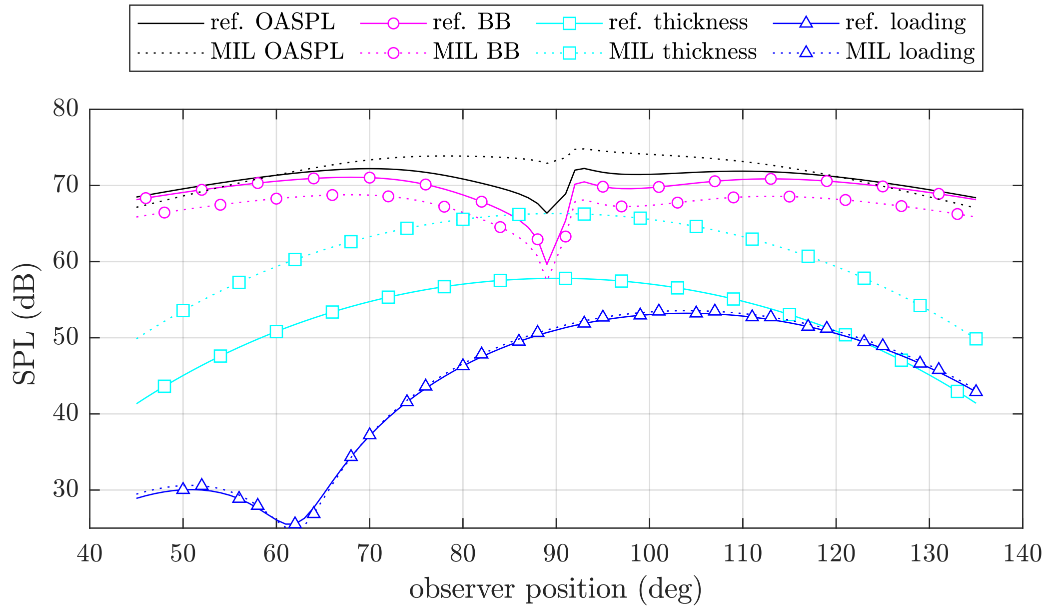

Figure E.3: Comparison of the noise emissions for the MIL and reference propeller in hover

E.2 Stepwise Explanation of the Multidisciplinary Optimisation Approach

Following enumeration presents a step-by-step description of the MDO approach with the mission analysis.

1 Define geometry using CST or MIL.
2 Check whether the geometry meets the geometric constraints.
    If the geometry does not meet the constraints, go to the last step.
3 Calculate blade mass.
4 Estimate motor mass.
5 Calculate new required thrust.
6 Within the mission analysis, the power consumption at each operating point is calculated.
    6.1 Define the lower and upper bounds of the rotational speed based on the blade tip Mach number limitations.
    6.2 Perform a parabolic fitting with different rotational speeds to find the matching thrust.
    6.3 Repeat this fitting until thrust converges within 1%.
        If the propeller does not generate sufficient thrust, go to the last step.
    6.4 In the case of a variable-pitch propeller, repeat this fitting for each pitch angle to find the minimal power consumption.
    6.5 Determine rotational speed, torque, shaft power, and propeller pitch.
7 Generate motor efficiency map using aerodynamic results.
8 Calculate motor efficiency for each operating point.
9 Calculate electric energy consumption.
10 Calculate noise emissions using aerodynamic properties.
11 Compute the weighting value between energy and noise emissions.
12 Perform genetic crossing, considering the weighting function, and restart from step 1.

F Additional Information about Optimisation Studies

This appendix provides additional information about the parameter variation within the single point MIL design study and the multidisciplinary optimsiation study.

First some additional information for the parameter variaon in section 5.1 are provided and second for the section 5.2.

F.1 Additional Information about the Influence of the Blade Number Variation on the Aeroacoustic Assessment

This supplementary information provides additional insights into the blade number variation. While not crucial for the main argumentation, it is helpful for classifying the results.

Fig. F.1 presents the blade pitch in diagram a), the effective AoA at 75% of the radius in diagram b), and the relative TE thickness at 75% of the radius in diagram c).

The blade pitch diagram clearly highlights the issue with the two-bladed propeller in hover conditions. To generate the required thrust, the two-bladed hover propeller requires a pitch of 4.5°, whereas most geometries are trimmed within 0.5°. The eight- and nine-bladed cruise propellers require negative blade pitch, as they generate excessive thrust due to their chord length reaching the lower bound of the parameter space.

The AoA distribution in diagram b) shows an increasing trend in hover, ranging from 3° for the three-bladed propeller to 4.5° for the nine-bladed propeller. For cruise, the AoA distribution follows a parabolic trend, peaking at 5.5° for the six-bladed geometry and decreasing to approximately 4° at both the upper and lower blade number limits.

The trend of the relative TE thickness at 75% of the radius aligns with the aspect ratio trend presented in fig. 5.1. The lowest TE thickness is 0.3%, while the highest reaches 5%.

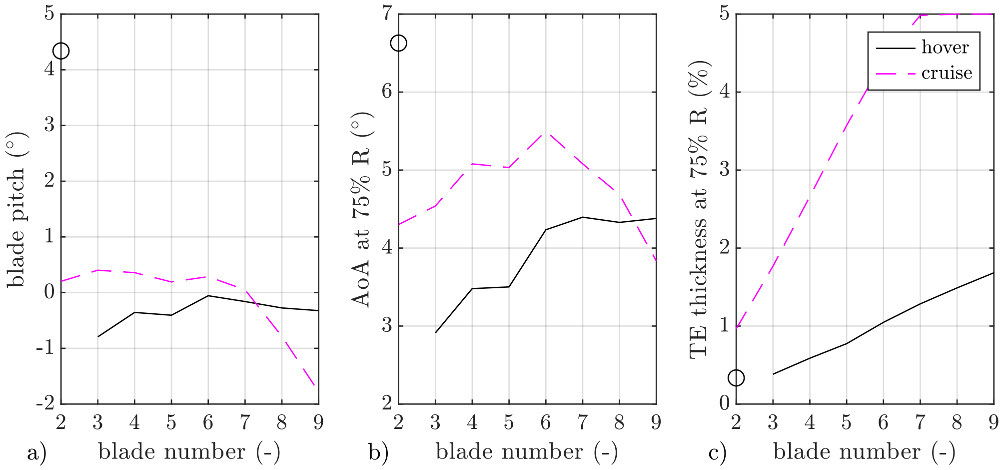

Figure F.1: Blade pitch, AoA and TE thickness as function of the blade number

Fig. F.2 provides a measure for blade volume and blade loading to classify tonal noise. Diagram a) presents the blade area multiplied by the number of blades at 75% of the radius as an indicator of blade volume. Since the 75% section is a two-dimensional representation, the volume is approximated by the total blade area at this section. This area or volume is relevant for thickness noise. Diagram b) depicts blade loading, which directly influences loading noise.

The propeller area at 75% radius ranges from 150 cm^2 to 25 cm^2 under hover conditions. For cruise designs, the area varies between 20 cm^2 and 7 cm^2. In the cruise designs, the propeller area remains nearly constant from the four- to the nine-bladed configuration.

For comparison, a DIN A4 page has an area of 625 cm^2, highlighting the extremely thin nature of the propeller blades. Even the three-bladed hover propeller, with a chord length of 17 cm, covers only a quarter of a DIN A4 page.

Blade loading decreases inversely proportional to the blade number, which results from the fixed design thrust in both cruise and hover conditions.

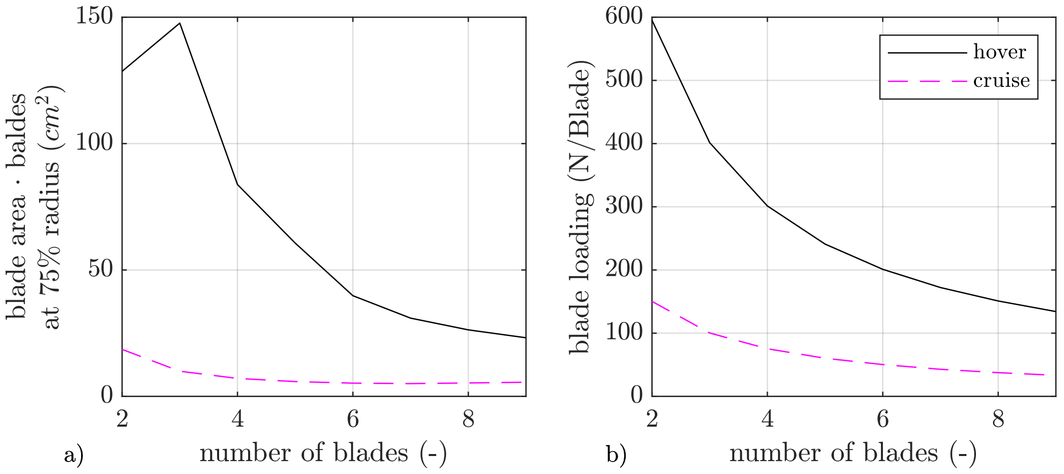

Figure F.2: Total blade area and loading as function of the blade number

F.2 Multidisciplinary Optimisation for the Reference Mission

Tab. F.1 provides additional information about the optimisation using the genetic algorithm. The presented values are also discussed in the main body but are summarised in this table for clarity.

Table F.1: Summary of detailed information about the optimisation process

Study	**Name**		**Number of Generations**	**Geometries found**	**Pareto Length**	**Fraction**
1	Baseline Optimisation		271	3352	26	0.8%
2	Broadband Noise		169	2479	43	1.7%
3	Acoustic Weighting	(A / D)	157 / 154	2035 / 2105	13 / 31	0.6% / 1.5%
4	Pitch System	(F / V)	157 / 127	2035 / 2127	13 / 20	0.6% / 0.9%
5	Mass Penalty	(F / V)	249 / 156	1763 / 3893	31 / 27	1.8% / 0.7%
6	Motor Efficiency	(F / V)	146 / 295	2289 / 3579	33 / 53	1.4% / 1.5%
	BSO	(F / V)	534 / 277	13250 / 4369	20 / 45	0.2% / 1.0%

Next, the mission geometries of the sweet spots from the mass penalty assessment in section 5.2.1.3 and the motor efficiency assessment in section 5.2.1.6 are presented for the sake of completeness.

Fig. F.3 shows the comparison of the geometries between fixed- and variable-pitch propeller with consideration of the system mass. The fixed pitch propeller is more slender than the variable pitch propeller. The root chord length is reduced by about 15cm, while the tip chord length is similar in both cases. Furthermore, the twist distribution of the fixed pitch propeller is approx. 5° lower than of the variable pitch propeller.

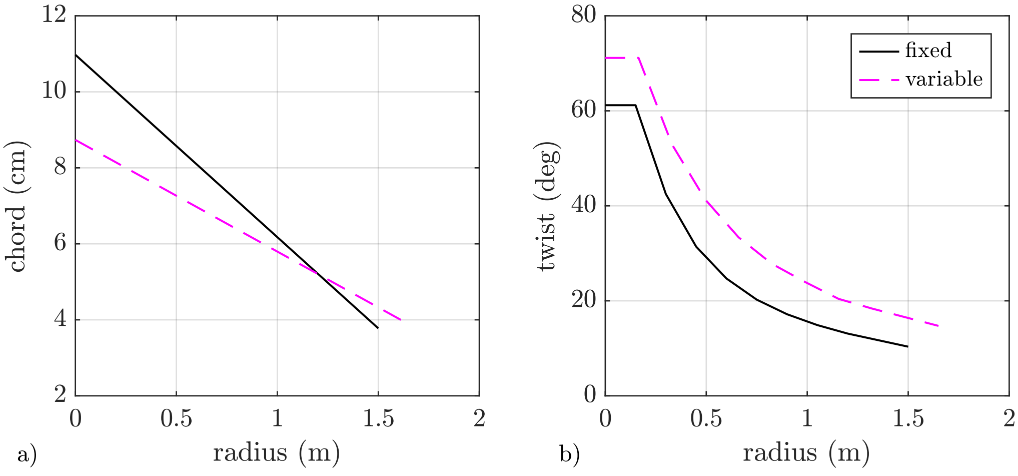

Figure F.3: Comparison of the sweet spot geometries between fixed and variable pitch propeller with consideration of mass penalties (Study 5)

Fig. F.4 shows the comparison of the geometries between fixed- and variable-pitch propeller with consideration of the motor efficiency map. However, the chord distribution of the variable pitch propeller changes significantly and has moved closer to the fixed pitch geometry. The twist distribution shown in diagram b) of F.4 are unchanged compared to diagram b) of F.3.

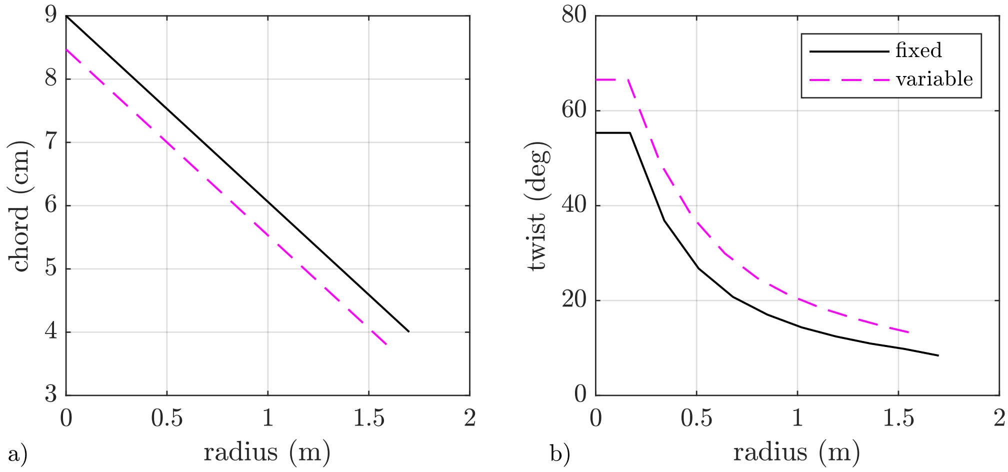

Figure F.4: Comparison of the sweet spot geometries between fixed and variable pitch propeller with consideration of mass and motor penalties (Study 6)

F.3 Insights in Final RANS Simulations

sThe optimisation of the parameter space results in a blade number of five in the fixed-pitch and eight in the variable-pitch case. Furthermore, the diameters are significantly larger than the diameter of the reference propeller. This combination leads to a problem in the CFD RANS simulations.

The curvature of the leading edge and the chord length define the required cell sizes on the blade surface. As the chord length and curvature are similar to the reference propeller, the cell size is similar. However, as the diameter and blade number increase, the overall computational effort increases significantly. A first estimation of the five-bladed propeller with a diameter of 3.4 m and an appropriate surface resolution results in 400 mio. cells. However, this is only the beginning of the mesh independence study. Even with access to the RWTH Aachen cluster CLAIX 2023, this propeller cannot be efficiently modelled with all blades.

Therefore, the CFD simulations are simplified. First, periodic boundaries are applied. The periodic boundaries significantly reduce the mesh size, especially for the eight-bladed variable-pitch propeller. The modelling effort increases, but the computational domain significantly decreases.

Appendix B shows that the periodic approach has worse convergence in the mesh independence study and results in lower thrust and torque compared to the other approaches. However, the overall prediction is within 10% relative to the MRF approach without periodic boundary conditions.

As the fixed- and variable-pitch propellers should be compared, both simulations are performed with the same base size relative to the diameter. Since the diameter of the variable-pitch propeller is smaller compared to the fixed-pitch propeller, the cell size decreases from the fixed- to the variable-pitch propeller. The mesh independence study is performed with the fixed-pitch propeller, as it requires more cells in the periodic approach.

Fig. F.5 shows that mesh independence is reached with 168 mio. cells. This results in a base size relative to the diameter of 18%. The same base size is applied to the variable-pitch propeller simulation.

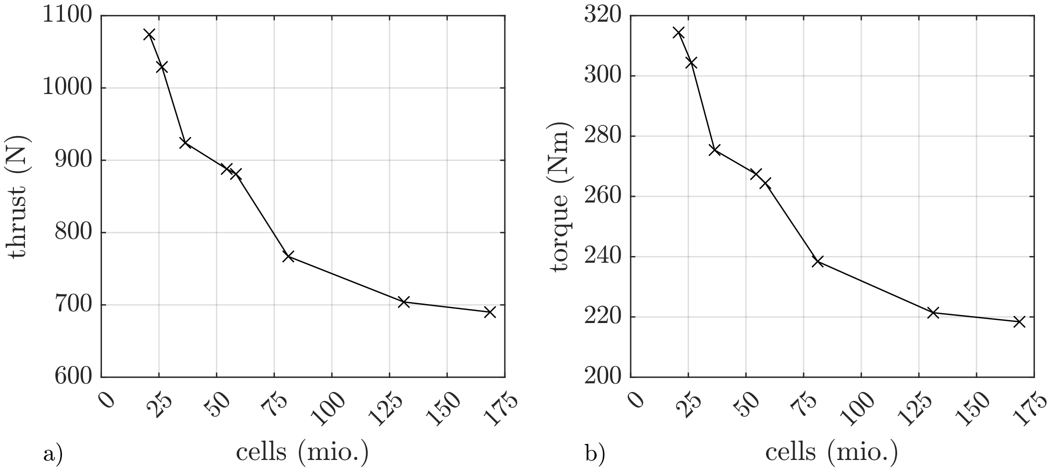

Figure F.5: Mesh independence study for the fixed-pitch propeller in the transition operating state